

**Colorimetric sensing of antibiotic residues in foods with
MXene and MXene-based nanozymes**

By
Weizheng Wang

A dissertation submitted in partial fulfillment of the requirements for the degree of

Doctor of Philosophy
(Biological System Engineering)

At the
UNIVERSITY OF WISCONSIN-MADISON
2023

Date of final oral examination: 06/29/2023

Sundaram Gunasekaran, Professor, Biological System Engineering

Jae-Hyuk Yu, Professor, Bacteriology

Filiz Yesilkoy, Assistant Professor, Biomedical Engineering

Tu-Anh Huynh, Assistant Professor, Food Science

ACKNOWLEDGMENTS

Firstly, words are far from enough to express my warmest gratitude and appreciation to my supervisor and chair of the dissertation committee, Professor Sundaram Gunasekaran, for his strong support, invaluable patience, and great wisdom. Upon the first meeting, you found the potential for great success in me, which I have not realized yet. Your dedicated involvement and consistent guidance shaped me and supported my accomplishments during my Ph.D. For all of these, I am greatly appreciative to have you as my major advisor.

I also take this opportunity to thank my dissertation committee members Professors Jae-Hyuk Yu, Filiz Yesilkoy, and Tu-Anh Huynh, for your consistent support, constructive advice, and insightful comments. In addition, I am grateful to Professor Yu for his support for my preliminary experiments with mycotoxins and providing the needed antibodies.

Many thanks also to the past and present colleagues in Professor Gunasekaran's lab: Drs. Omer Sadak, Jiehao Guan, M.U. Anu Prathap, Taeyun Kwon, Kaiyu He, Gozde Kabay, Khadija Malik, Deyler Castilla Caballero, and fellow students and visitors, Yaoqi Yin, Batul Kachwala, Hilary Urena Saborio, Kari Jordan, Dasol Choi, Yuanye Jiang, Awais Khan for their support and assistance, and I will always remember your friendship during my Ph.D. career. Special thanks to Yaoqi Yin for his collaboration and contribution, without which this thesis could not have been successfully completed. I am also grateful to undergraduate students Haoming Yu, Qiyuan Chen, Murtadha Albarrak, and Nick Schreiber for their help. I am also thankful to all staff in the Department of Biological Systems Engineering for their assistance during my Ph.D. career.

Finally, this dissertation is dedicated to all my family members, especially my loving parents, for their endless love, encouragement, and support and for raising me to be the person I am now.

Abstract

Colorimetric detection methods have attracted increasing attention recently and are now used for routine analysis in different areas due to their unique properties, including friendly expense, easy operation, miniaturization, fast results, and portability. Since antibiotics exhibit complex chemical structures and small sizes in the agri-food system and environment with low concentrations, developing a sensing system for antibiotics detection remains a considerable challenge, such as complicated sample pre-treatment requirements, sophisticated instruments, and highly qualified personnel that boost the detection cost. Moreover, after analysis, most sensing systems can only detect a certain antibiotic residue in the resource which may further reduce the detection efficiency. Hence, researchers have contributed to the multiple bio-recognizer and transducers investigations and studies.

Titanium carbide ($\text{Ti}_3\text{C}_2\text{T}_x$), known as MXene, is currently among the most attractive 2-dimensional (2D) nanomaterials worldwide for a wide range of applications involving (bio)-sensors, energy storage devices, clinical medication, pharmaceutical industries, etc., owing to their superior properties. This nanomaterial is found to mimic the catalytical behavior of horseradish peroxidase (HRP) in this dissertation that can catalyze the conversion of the enzymatic substrate to their final products and turns the solution color from white, transparent colorless to the corresponding color. Thanks to this technology, the goal of visual detection of multiple targets could come true.

In this dissertation, a sensing system was developed based on $\text{Ti}_3\text{C}_2\text{T}_x$ MXene and its derived hierarchical nanostructured enzyme nano-mimic known as nanozymes that can be used for colorimetric detection of different antibiotic residues in food materials.

To develop the multi-antibiotic sensing system, we first started to synthesize the few-layered- $\text{Ti}_3\text{C}_2\text{T}_x$ MXene (OFL-Ti-MN) that was selectively etched its bulky ceramic (MAX phase) by using the minimally intensive layer delamination (MILD) method. The fabricated OFL-Ti-MN was first explored with its enzymatic nano-mimic behavior by using a typical enzymatic system of hydrogen peroxide (H_2O_2) and 3,3',5,5'-tetramethylbenzidine (TMB) under optimal reaction condition. It can facilitate to trigger of the redox reaction between two substrates ($\text{H}_2\text{O}_2/\text{TMB}$) and help turn the white-transparent solution bluish-green. The affinity of OFL-Ti-MN against TMB is higher than that of HRP. On the contrary, the affinity of OFL-Ti-MN for H_2O_2 is much lower, resulting from the partial oxidation of fabrication OFL-Ti-MN and the vacancy defect of the OFL-Ti-MN Ti surface. However, the color change was inhibited as kanamycin (KAN) and tetracycline (TC) were introduced into this system (OFL-Ti-MN/TMB/ H_2O_2). Based on this strategy, an OFL-Ti-MN-based colorimetric method for KAN and TC detection was successfully architected, showing the limit of detection (LOD) of 15.28 nM and 615.28 nM for KAN and TC, respectively. The exploration of intrinsic peroxidase-mimic properties of OFL-Ti-MN uncovered the plausible mechanism of the inhibition effect of KAN and TC on color change. This provides an alternative way to detect antibiotics and opens the door to discovering the antibiotic function mechanism and extending the OFL-Ti-MN application (Chapters III & IV).

A hierarchical nanostructure of Au nanoparticle (Au NPs) doped layered $\text{Ti}_3\text{C}_2\text{T}_x$ MXene (L- $\text{Ti}_3\text{C}_2\text{T}_x$ NS) (MA2) was designed and synthesized via a facile one-step Au precursor ($\text{HAuCl}_4 \cdot 3\text{H}_2\text{O}$) was reduced directly on the surface of L- $\text{Ti}_3\text{C}_2\text{T}_x$ NS without adding extra reducing agents. The final MA2 nanocomposite shows the catalase-like properties in the TMB/ H_2O_2 system, with a significantly higher experimental affinity (~ 17 folds) to H_2O_2 than that of OFL-Ti-MN due to the synergic effect of Au NPs and L- $\text{Ti}_3\text{C}_2\text{T}_x$ NS. When ampicillin (AMP)

or penicillin G (Pen G) exists in the catalase nano-mimic system (MA2/TMB/H₂O₂), the bluish-green color does not appear, providing a great opportunity to manufacture a colorimetric method for AMP and Pen G detection. As a result, this sensing method showed LOD for AMP and Pen G detection as 7.51 nM and 68.9 nM, respectively, with a great linear relationship of 116.82 nM ~ 3.51 μM and 35.1 nM ~ 584 nM for AMP and Pen G, respectively. The proposed mechanism indicates that the MA2 can mimic the catalytic action of natural catalase in the presence of H₂O₂. Moreover, this further extended the investigation and application of MXene and MXene-based nanocomposites (Chapter V).

Table of Contents

ACKNOWLEDGMENTS	i
Abstract	ii
Table of Contents	v
List of Figures	viii
List of tables	xiii
Chapter I. Background information and research design	1
1.1. Conventional analytical methods	1
1.2. MXene-based nanomaterials	2
1.3. Antibiotics	4
1.4. Research design	5
1.5. References	7
Chapter II. Introduction and literature review for enzyme nano-mimic: Nanozyme-based sensor and biosensor for food and quality and safety*	9
Abstract	9
2.1. Introduction	9
2.2. Predominant catalytic mechanisms of nanozymes for biosensing	11
2.2.1. Peroxidase-like nanozyme	13
2.2.2. Oxidase-like nanozymes	19
2.3. Applications of nanozymes for sensing and biosensing	22
2.3.1. Detection of ions	22
2.3.2. Detection of foodborne pathogens and microbial metabolites	29
2.3.3. Detection of pesticide residues in food	35
2.3.4. Detection of other food contaminants	37
2.4. Summary and future perspectives	39
2.5. Appendix: Chapter II	42
2.6. References	43
Chapter III. 2D Oxygen-Terminated Few-Layered Ti₃C₂T_x MXene Nanosheets as Peroxidase-Mimic for Colorimetric Detection of Kanamycin*	52
Abstract	52
3.1. Introduction	52

3.2. Experimental section.....	55
3.2.1. Materials and reagents	55
3.2.2. MXene synthesis.....	55
3.2.3. Peroxidase-mimic kinetics of MXene	56
3.2.4. Colorimetric detection of KAN.....	57
3.2.5. Real sample detection	57
3.3. Results and discussion.....	58
3.3.1. MXene synthesis and characterization	58
3.3.2. Optimal condition and peroxidase-mimic kinetics of MXene enzyme nano- mimics	62
3.3.3. Mechanism of peroxidase-mimic property of OFL-Ti-MN	65
3.3.4. Colorimetric detection of KAN.....	68
3.3.5. Selectivity and detection of KAN in real samples	71
3.4. Conclusions	72
3.5. Appendix III.	74
3.6. References	85
Chapter IV. Nanozymatic degradation and simultaneous colorimetric detection of tetracycline*	90
Abstract	90
4.1. Introduction	90
4.2. Experimental section.....	93
4.2.1. Materials and reagents	93
4.2.2. Synthesis of FL-Ti₃C₂T_x	93
4.2.3. Characterization	93
4.2.4. Peroxidase-mimic behavior of Ti₃C₂T_x MXene.....	94
4.2.5. Colorimetric analysis of TC.....	95
4.3. Results and discussion.....	96
4.3.1. Synthesis and characterization of Ti₃C₂T_x MXene	96
4.3.2. pH and temperature effects on FL-Ti₃C₂T_x peroxidase activity.....	100
4.3.3. Physiochemical properties of FL-Ti₃C₂T_x nanosheets.....	101
4.3.4. The mechanism of peroxidase-mimic activity	103
4.3.5. Colorimetric detection for TC and its mechanism.....	106
4.3.6. Specificity and TC detection in real sample	109

4.4. Conclusions	110
4.5. Appendix IV.	112
4.6. References	124
Chapter V. Gold nanoparticles/MXene hierarchical nanostructure as a catalase mimic for colorimetric detection of ampicillin and penicillin G	128
Abstract	128
5.1. Introduction	128
5.2. Experiment section	131
5.2.1. Materials and methods	131
5.2.2. Pristine L-Ti ₃ C ₂ T _x NS nanosheet and MA colloidal solution preparation	131
5.2.3. Characterization of the instrument and properties	132
5.2.4. The catalyze-mimic activity of MA2 and the optimization process	133
5.2.5. Discrimination of AMP and Pen G	134
5.2.6. Real sample preparation	135
5.3. Results and discussion	135
5.3.1. Synthesis and characterization of MA2	135
5.3.2. Optimization of reaction condition and catalase-mimic kinetic of MA2	140
5.3.3. Mechanism of catalase-mimic activity of MA2	143
5.3.4. Colorimetric detection of AMP and Pen G	146
5.3.5. Selectivity and real sample application	149
5.4. Conclusions	151
5.5. Appendix V	152
5.6. References	163
Chapter VI	168
Conclusions and Future Prospects	168

List of Figures

Figure 2.1. Different fields of nanozyme-based biosensor applications. 11

Figure 2.2. **A.** Schematic of several common peroxidase and oxidase substrates that undergo oxidation in the presence of nanozyme and oxidizing agents: OPD: o-phenylenediamine; TMB: 3,3',5,5'-tetramethylbenzidine; ABTS: 2,2-azinobis(3-ethylbenzothiazoline-6-sulfonic acid) and AR: 10-acetyl-3,7-dihydroxyphenoxazine; **B.** Chemical structures of representative nanomaterials with intrinsic enzymatic properties: structures except graphene oxide are generated from: <https://www.chemtube3d.com>. **C(a).** Pt/Ag hybrid synthesized with DNA template serves as a peroxidase mimic, adapted with permission from [19] and **(b).** Color changes of different substrates after oxidation, adapted with permission from [20]. 12

Figure 2.3. **A.** Color change in three oxidase substrates catalyzed by Pt₇₂Co₂₈ nanoparticles, **B.** UV absorbance for TMBBox products undergoing catalysis of Pt-Co hybrid with various Pt/Co ratios; inset shows the facet of Pt₇₂Co₂₈, **C.** mechanism of Pt₇₂Co₂₈ for mimicking oxidase. Adapted with permission from [58] 21

Figure 2.4. **A(a)** Illustration of color “on/off” assay mechanism, **(b)** time profile with inset showing relationship between concentration of Hg²⁺ with UV absorbance at reaction time of 260 s, **(c)** absorbance of UV spectrum with increasing Hg²⁺ concentration, adapted with permission from [74]; **B (a)** Illustration of the impact of different ions on Fe₃O₄-DHCA peroxidase activity, **(b)** Schematic of mechanism of Fe₃O₄-DHCA with Zr⁴⁺ for PO₄³⁺ detection, **(c)** Relationship between UV absorbance and PO₄³⁺ concentration and inset showing concentration with conversion to logarithm, adapted with permission from [86] 27

Figure 2.5. **A(a).** Illustration of lateral flow assay for *E. coli* O157:H7; **(b)** Linear relationship between concentration of *E. coli* O157:H7 and color intensity; **(c)** Photograph of lateral flow assay with different concentrations of *E. coli* O157:H7, adapted with permission from [101]; **B (a)** Schematic for AFB1 detection mechanism based on electrochemical immunoassay using PtNPs/CoTPP/rGO-based biosensor and photo inset is electrochemical measurement device; **(b)** Current change with different concentrations of AFB1 and inset shows current vs. AFB1 linear relationship, adapted with permission from [104] 30

Figure 2.6. **A.** Illustration of nanoceria-based biosensing with dual mode-sensing platform technique, Adapted with permission from [123], **B (a)** Schematic of enzymatic competitive assay for the detection of organophosphates (OP), **(b)** fluorescent spectra for OP detection, (a-m: 0.5, 1, 2, 5, 10, 20, 50, 100, 200, 300, 400 and 500 nM, respectively), adapted with permission from [124] 36

Figure 2.7. **A.** Schematic illustration of color turn on/off for kanamycin detection; **B.** Selectivity test based on this immunoassay for different antibiotics detection; **C.** Relationship between peroxidase-like activity of gold nanoparticle-Ky2 aptamer and concentration of kanamycin, adapted with permission from [128] 38

Figure 3.1. **A.** Illustration of an OFL-Ti-MN synthesis process. **B.** SEM images of **(a)** and **(b)**. parent MAX phase precursor, **(c)-(f)**. synthesized OFL-Ti-MN..... 59

Figure 3.2. XRD patterns of **(a)** Ti_3AlC_2 powder and $\text{Ti}_3\text{C}_2\text{T}_x$ nanosheets and XPS survey scans of **(b)** Ti_3AlC_2 powder and $\text{Ti}_3\text{C}_2\text{T}_x$ nanosheets, high-resolution XPS spectra of $\text{Ti}_3\text{C}_2\text{T}_x$ nanosheets with curve fitting for **(c)** Ti 2p, **(d)** C 1s, **(e)** O 1s, and **(f)** F 1s..... 60

Figure 3.3. **(a)** UV-vis absorption spectra for TMB- H_2O_2 , MXene- H_2O_2 , MXene-TMB, and MXene/TMB- H_2O_2 reaction systems, **(b)** UV-vis absorption peak at 653 nm (A_{653}) of the solution after 15 min incubation in different pHs at 37 °C (solid line) and in pH 3.6 at different temperatures (dotted line). Steady-state kinetics assay of $\text{Ti}_3\text{C}_2\text{T}_x$ nanosheets in various enzyme substrate concentrations but with the other substrate concentration constant **(c)** varying TMB and **(e)** varying H_2O_2 and their corresponding double-reciprocal plots, **(d)** and **(f)**. 63

Scheme 3.1. **A:** Proposed redox reaction mechanism between two enzyme substrates in the presence of OFL-Ti-MN. **B:** Proposed mechanism of KAN detection by OFL-Ti-MN/ H_2O_2 /TMB bioassay system..... 67

Figure 3.4. **(a)** UV-vis absorption spectra of the OFL-Ti-MN/ H_2O_2 /TMB bioassay with different amounts of KAN, **(b)** Dynamic range for colorimetric detection of KAN. Inset: picture of the OFL-Ti-MN solutions indicating the color change with different KAN concentrations, and **(c)** a linear relationship between KAN concentration and change in absorption intensity 70

Figure 3.5. The OFL-Ti-MN/ H_2O_2 /TMB bioassay system for 18 different potential interferents and KAN analysis. Absorption values (A_{653}) relative to that of a blank for 18 potential interferents and KAN. Inset: pictures of the test samples. 71

Figure S3.1. FT-IR spectrum for synthesized OFL-Ti-MN 74

Figure S3.2. Reaction-time curves for TMB - H_2O_2 redox reaction between catalyzed by different concentrations of OFL-Ti-MN..... 75

Figure S3.3. Stability of OFL-Ti-MN nanosheets and horseradish peroxidase during storage at room temperature. Error bars represent standard deviations of three replacements..... 77

Figure S3.4. Change in UV-vis absorption peak at 653 nm (ΔA_{653}) as a function of time for free radical trapping experiment with different radical scavengers 78

Figure S3.5. Photographs for adding KAN in the different peroxidase-mimic systems in the presence of enzyme substrates. Note: OFL-Ti-MN: oxygen terminated few-layered Ti-based MXene nanosheets, Fe_3O_4 NPs: Fe_3O_4 nanoparticles, CuO/Grpox: CuO nanoparticle doped graphene oxide, PtNi NPs: PtNi nanoparticles 80

Figure S3.6. Optimization of mixing time for kanamycin and OFL-Ti-MN 81

.....	82
Figure S3.7. UV-vis scan of the OFL-Ti-MN/TMB/H ₂ O ₂ biosensing system with KAN=15.28 nM (this is the calculated LOD value for KAN detection).....	82
Figure 4.1. A. Schematic of FL-Ti ₃ C ₂ T _x nanosheet synthesis process. B. SEM micrographs of Ti ₃ AlC ₂ precursor surface (i) and cross-sectional view of prepared FL-Ti ₃ C ₂ T _x nanosheet at different magnifications (ii, iii).....	96
Figure 4.2. XRD spectrum and full scan XPS spectra for synthesized FL-Ti ₃ C ₂ T _x nanosheets and MAX phase (a, b), XPS spectra of Ti 2p, O 1s, C 1s, and F 1s for FL-Ti ₃ C ₂ T _x nanosheets, respectively (c-f).....	97
Figure 4.3. UV-vis absorbance spectra of TMB/H ₂ O ₂ , FL-Ti ₃ C ₂ T _x / H ₂ O ₂ , FL-Ti ₃ C ₂ T _x /TMB, and FL-Ti ₃ C ₂ T _x /TMB/ H ₂ O ₂ systems (a). The colorimetric performance of FL-Ti ₃ C ₂ T _x /TMB/H ₂ O ₂ system as a function of temperature at pH 3.6 (b) and as a function of reaction temperature at 37°C (c).....	101
Figure 4.4. Stability of FL-Ti ₃ C ₂ T _x and HRP when stored for 10 days at room temperature (a). UV-vis spectrum of FL-Ti ₃ C ₂ T _x MXene solution. Inset: plot of $\alpha h\nu$ vs. photon energy ($h\nu$) for band gap energy of MXene (b). Nyquist plots of FL-Ti ₃ C ₂ T _x in the dark (c).....	103
Scheme 4.1. A. Illustration of the biocatalytic chromogenic reaction between TMB and H ₂ O ₂ triggered by FL-Ti ₃ C ₂ T _x nanosheets. B. Two plausible pathways (pathway 1, top line in red and pathway 2, bottom line in purple) for TC degradation in the presence of FL-Ti ₃ C ₂ T _x and proposed structures of intermediate products (IP.1 through IP.17). The IPs enclosed in boxes are isomers or those possibly exist simultaneously.....	105
Figure 4.5. A. Photograph of the colour of the FL-Ti ₃ C ₂ T _x /TMB/H ₂ O ₂ solution with different TC concentrations, B. Change in A ₆₅₃ value from that of blank (ΔA_{653}) of FL-Ti ₃ C ₂ T _x bioassay with different amounts of TC (a) and calculated dynamic range and inset: the line (b).....	107
Figure S4.1. FT-IR spectrum of FL-Ti ₃ C ₂ T _x nanosheets.....	112
Figure S4.2. Raman spectra of MAX phase precursor and synthesized FL-Ti ₃ C ₂ T _x MXene nanosheets.....	113
Figure S4.3. Radical trapping experiment by using ascorbic acid, EDTA•2Na, and isopropanol for •O ₂ ⁻ , •OH, and h ⁺ scavenging.....	114
Figure S4.4. Optimization of mixing time for TC and FL-Ti ₃ C ₂ T _x nanosheets.....	115
Figure S4.5. Theoretically calculated LOD for TC analysis by FL-Ti ₃ C ₂ T _x nanosheets/TMB/H ₂ O ₂ system.....	116

- Figure S4.6.** Assay response to 11 potential interferents found in dairy products and/or water samples.....117
- Figure 5.1.** A. Scheme illustration of MA2 preparation process, B SEM surface morphology of (i) the MAX phase, (ii) and (iii) synthesized L-Ti₃C₂T_x NS with different magnifications, (iv)~(vi) prepared MA2 137
- Figure 5.2.** Characterization of MA2. (a). XRD pattern of MAX phase, L-Ti₃C₂T_x NS and MA2, (b). XPS full scan of MAX phase, L-Ti₃C₂T_x NS and MA2, High-resolution MA2 XPS spectra of (c). Ti 2p, (d). C 1s, (e). O 1s, (f). Au 4f. 139
- Figure 5.3.** (a). Optimization of volume ratio between L-Ti₃C₂T_x NS MXene and HAuCl₄•3H₂O. (b). The UV-Vis spectrum of the different reaction systems involving TMB+H₂O₂, L-Ti₃C₂T_x NS+TMB+H₂O₂, MA2+H₂O₂, MA2+TMB, and MA2+TMB+H₂O₂, (c). Effects of pH (blue) and temperature (red) on the MA2 catalytic activity, The steady-state kinetic curves of MA2 for enzyme-substrate H₂O₂ at fixed TMB concentration plotted by (d). Michalis-Menten equation and (e). Lineweave-Burk equation, (f). Long-term stability of MA2 and L-Ti₃C₂T_x NS MXene after being kept under room temperature for 30 days. 141
- Scheme 5.1.** A. Schematic illustration of a proposed mechanism in the MA2/TMB/H₂O₂ system, B. Schematic diagram of the mechanism of AMP and Pen G inhibitive effect on the MA2-triggered redox reaction between two substrates 145
- Figure 5.4.** (a). and (d). UV-Vis absorption spectra for AMP and Pen G detection, respectively, by the enzymatic nano-mimic system, (b). and (e). Detection range of designed colorimetric method for AMP and Pen G, respectively, inset: digital photos for the visualized color change of MA2/TMB/H₂O₂ system in the presence of a corresponding concentration of AMP and Pen G, respectively, Linear-relationships between β-lactam antibiotics concentrations ((c). AMP and (f). Pen G concentration) and the relative response of UV-Vis absorbance peak. 147
- Figure 5.5.** The selectivity experiment of MA2 towards 11 potential targets (35.05 μM). Lac: lactose, L-Ser: L-serine, L-Ala: L-alanine, Kan: kanamycin, TC: tetracycline..... 149
- Figure S5.1.** FT-IR spectra of MA2, L-Ti₃C₂T_x NS MXene, and MAX phase. 153
- Figure S5.2.** UV-Vis absorbance spectra of MA2 and L-Ti₃C₂T_x NS MXene. Inset: digital photo of concentrated MA2 (red) and L-Ti₃C₂T_x NS MXene solution (light grayish green). 154
- Figure S5.3.** The time-drive curve for redox reaction of TMB/H₂O₂ induced by various MA2 concentrations. 155
- Figure S5.4.** UV-Vis spectra for free radical-trapping experiment with various radical scavengers. LAA: L-ascorbic acid, EDTA•2Na: Ethylenediaminetetraacetic acid sodium salts. 158

Figure S5.5. Optimization experiment for an incubation time of β -lactam antibiotics and MA2
..... 159

Figure S5.6. Overnight experiment of the inhibition effect of AMP, Pen G and their mixture (1:1)
on the enzymatic nano-mimic system (MA2/TMB/H₂O₂). 161

List of tables

Table 2.1. Applications of nanozymes for colorimetric (unless noted otherwise) detection of ions	23
Table 2.2. Applications of nanozymes for colorimetric detection (unless noted otherwise) and quantification of foodborne pathogens and microbial metabolites.....	33
Table S2.1. Traditional enzyme application in biosensor for food analysis.....	42
Table S3.1. Different enzyme nano-mimics with their Michaelis -Menten constants (K_m) and maximum reaction rate (V_{max}) under optimized conditions.....	76
Table S3.2. Q-TOF-MS information and proposed structures of TMB and KAN.....	79
Table S3.3. Results for kanamycin (KAN) determination in three real samples.	83
Table S3.4. Kanamycin analysis method reported in the literature.....	84
Table S4.1. Performance metrics of our assay and some published methods for TC detection..	118
Table S4.2. QTOF MS information and proposed structures of TMB, TC, and TC degradation products.....	120
Table S4.3. Data for TC detection in tap water, honey, and skim milk samples.....	123
Table S5.1. Maximum residue limit of ampicillin and penicillin in milk	152
Table S5.2. Comparison of different catalase-like nano-mimics with their Michaelis-Menton kinetic parameters to H_2O_2 substrate	156
Table S5.3. Zeta potential of MA2 in different solutions.....	157
Table S5.4. Comparison of different methods for AMP and Pen G detection	160
Table S5.5. Results of AMP and Pen G detection in the real sample matrices	162

Chapter I. Background information and research design

1.1. Conventional analytical methods

As society develops rapidly, as well as the population explosion, the ecosystem, thus human health, is always affected by toxic agents, including synthetic polymer, heavy metal ions, anions, mycotoxins, pesticides, gases, pathogens, viruses, etc.[1]. The presence of a small amount of those toxicities may induce irreversible and deleterious damage to ecosystems and even human health. Early assessment and monitoring of those contaminants in the environment, agri-food systems, and the human body is paramountly substantial to enable the implementation of prevention strategies and clinical point-of-care.

Conventionally, the analytical methodologies focused more on the chromatography technology that is widely used worldwide. This is a quantitative method for highly stable and selective detection of antibiotics, mycotoxins, synthesized organic compounds, proteins, etc. As an example, liquid chromatography with mass spectroscopy (LC/MS) or high-performance liquid chromatography coupled with mass spectroscopy (HPLC/MS) is the most commonly employed analytical technique for biological, environmental, and food safety monitoring [2-4]. Nevertheless, complex sample pre-treatment procedures, cumbersome detection instruments, tedious operation processes, and high requirements for personnel significantly boost the expense of a single detection and limit the analysis application[5, 6].

Recently, tremendous efforts in analytical methods have been made towards novel sensing and biosensing device fabrication that possess portable, miniaturization, low cost, and rapid result properties. It is worth noting that the biosensing device is an extensive sensing strategy involving molecules with biological properties. Therefore, a typical biosensing device usually has three key components: an element that can specifically identify and capture the target (known as a bio-

recognition element), a transducer that can facilitate physiochemical information of target translation into the corresponding measurable signals, and a signal-display processor[7, 8]. Thanks to the fast development of nanotechnology, these strategies can come true. For example, a screen-printed electrode (SPE)-based electrochemical biosensor is one of the most favored biosensors owing to its high portability, low cost, flexible design, and ease of on-site testing. Typically, nanomaterials are modified on SPE working electrode (WE), which improves the surface activity of this biosensor owing to their higher surface-to-volume ratio and superior electrocatalytic properties[9]. When coupled with a unique biorecognition element (e.g., oligonucleotides, enzyme, antibody), the electrochemical biosensor is highly specific to a target and generates a measurable signal. Therefore, it can be widely applied in various areas for single-target detection, such as food quality and safety analysis, environment monitoring, and clinical diagnose[10-12]. Another active sensing strategy is to adopt magnetic nanoparticles (MNPs) for target analysis. A recent study on portable nuclear magnetic resonance (NMRs) biosensor assay opened a new door for NMR measurement systems in more *on-site* applications[13]. Foodborne pathogen (*E. Coli* O157:H7) was analyzed by this assay with a detection limit (LOD) of ~ 10 CFU/mL. However, the core shortcoming of the transduction mechanism based on the electrochemical and magnetic nature is reflected in the implementation of multiple targets within a single readout measurement. Hence, it is urgent to develop a sensing and biosensing method for multiple target analyses with those unique and advantagous properties of mordern sensor and biosensor device.

1.2. MXene-based nanomaterials

Since the first successful exfoliated single-layered graphene in 2004, an increasing attraction has been gained in the investigation and application of the various 2-dimensional (2D) nanomaterials due to their unique properties [14]. In recent decades, there have been multiple 2D

new nanomaterials beyond 2D graphene that have been synthesized and used worldwide. Innovative 2D transition metal carbide, nitride, and carbonitride nanomaterials have stood out since 2011 owing to their fascinating properties[15]. Later on, those nanomaterials were categorized as a new family named MXene. Typically the MXene is usually obtained from its bulky precursor MAX phase. Given the chemical and layered structures, the layered MXene has the denotation as $M_{n+1}X_nT_x$, where "M" presents the early transition metals such as Ti, Mo, etc., "X" is usually C and/or N atom, and "T" stands for functional groups that are newly formed after synthesis process. Experimentally, the surface composition of MXene (T_m in the denotation, such as -F, -O, -Cl, and -OH, etc.) may vary depending on various selective etching methods, which offer high metallic conductivity (~ 6000 - 8000 S/cm) and makes heterogeneous electron transfer process achievable *on site*[16, 17]. Besides, MXene has been reported to have relatively high stiffness with at least 500 GPa elastic constant based on density functional theory (DFT) computations[18]. As a result, MXene is increasingly performed in many applications, including biosensing, catalyst, antibacterial treatment, and chemical adsorption[19-21].

Layered titanium carbide nanomaterial (commonly $Ti_3C_2T_x$) is one of the most popular MXene, obtained from its MAX phase precursor (Ti_3AlC_2) via the manually shaking method that usually produces the less defective but larger single $Ti_3C_2T_x$ nanosheets[22]. In terms of the weaker bond of Ti-Al than the bond of Ti-C, fluoride-based etchants in strongly acidic conditions are usually used to selectively remove the Al interlayer without damaging the Ti-C bonds, achieving the separation goal of $Ti_3C_2T_x$ MXene from Ti_3AlC_2 precursor[23]. However, the side effect of this method may over-etched the surface composition, especially Ti single atom or several adjacent Ti atoms on the surface, leading to the single or cluster Ti atom defective vacancies[24]. In return, these newly created defects, due to their highly unstable and thus reactive characteristics, provide

exfoliated $Ti_3C_2T_x$ MXene nanosheet excellent reductivity[25]. Hence, this ability facilitates exfoliated $Ti_3C_2T_x$ MXene nanosheet to reduce the oxidizing reagents and even metal precursors much easier [26]. Furthermore, those defective vacancies can interact with those reduced metal ions and play an important role in supporting their growth *in-situ* [27]. In a word, all of these features can facilitate MXene's contribution to the sensing and biosensing area.

1.3. Antibiotics

The last several decades have evidenced the medical effectiveness of antibiotics that can be used in human illness treatment and applied in ecosystems and animals to enhance food safety and quality[28]. Nevertheless, the abuse of antibiotics usage can result in contamination in agri-food systems where the antibiotics cannot be naturally degraded or metabolized by animals, which may easily enter into the food supply chain[29]. An excessive amount of antibiotic residue in consumable food puts a high risk to the ecosystem and even human health, including environmental microbiome balance damage, human microbiome alteration, and increasing the drug resistance of bacteria inhibited in humans, etc.[30]. Besides, ingested antibiotic residues by human beings can also bioaccumulate, finally causing allergic reactions, disruption or intestinal flora, and other human health problems[31]. The antibiotic abuse phenomenon in farms is even worse since farmers usually use them to treat bovine mastitis. Those unmetabolized antibiotic residues enter dairy products easily. It is reported that the major available antibiotics remaining in cow milk include 1). the β -lactam family occurs around 36.54 % (such as amoxicillin, ampicillin, penicillin, etc.) and 2). Tetracycline family with 14.01 % [32]. Therefore, the USA Food and Drug Administration (FDA) and European Union (EU) have set the maximum residue limits (MRLs) as 5 ng/L~100 ng/L and 4 ng/L for β -lactams family, respectively, and 300 μ g/kg and 100 μ g/kg for tetracyclines, respectively [32-34]. Kanamycin is another available antibiotic remaining in the food,

which usually is used as an analysis target in the lab, though it is not a major concern in the market. Moreover, the EU set up the MRLs of kanamycin in milk with ~320 nM and ~214 nM set up by Korea Food and Drug Administration (KFDA) [35].

1.4. Research design

The tremendous revolutions in sensing and biosensing methods (electrochemical, colorimetric, fluorescent, etc.) occurring in recent decades are ascribed to the rapid development of nanotechnology, drastically promoting the performance of sensing and biosensing technologies concerning the sensitivity, portability, selectivity, etc. Of them, the nanomaterial with natural enzymatic behavior (known as nanozyme in some literature) is a rising star at the forefront of innovative sensing and biosensing applications. This revolutionary work on the sensor and biosensor has opened the door to establishing a facile and innovative sensing system for antibiotics detection in the dairy industry.

As a newborn 2D nanomaterial, $\text{Ti}_3\text{C}_2\text{T}_x$ -based MXene has recently attracted increasing attention. In this work, oxygen-terminated few-layered $\text{Ti}_3\text{C}_2\text{T}_x$ -based MXene (OFL-Ti-MN) was first recognized to function as peroxidase, named peroxidase nano-mimic, which can trigger the redox reaction between two typical enzymatic substrates, hydrogen peroxide (H_2O_2) and 3,3',5,5'-tetramethylbenzidine (TMB). Finally, bluish-green oxide TMB was generated and released into the solution, making the solution recognizably visible. Besides, because of the unique properties of layered $\text{Ti}_3\text{C}_2\text{T}_x$ -based MXene, this newborn 2D nanomaterial can reduce the Au precursor without any extra reducing agents. The obtained hierarchical Au/MXene nanocomposite (MA) has significantly increased enzymatic performance due to the synergistic effect of Au nanoparticles

and MXene. Taking advantage of these, both of these two enzyme nano-mimics were used in the sensor and biosensor for multiple targets detection with relatively high sensitivities.

The overall goal of this project aims to develop a low-cost, rapid, and portable colorimetric sensing strategy for multiple antibiotics detection in dairy products (e.g., milk). The specific objectives of this work are as follows:

1. Investigate the role of OFL-Ti-MN -based enzyme nano-mimic in the enzymatic system by exploring the mechanism and kinetics of the catalytic reaction.
2. Design the colorimetric bioassay based on the OFL-Ti-MN for kanamycin detection and explore its detection mechanism.
3. Study the OFL-Ti-MN/H₂O₂/TMB system for tetracycline detection and provide the detection mechanism.
4. Prepare the Au nanoparticles/layered Ti-based MXene nanocomposites in a one-step way.
5. Identify the Au nanoparticles/layered Ti-based MXene nanocomposites' performance in the enzymatic system and develop a colorimetric bioassay for ampicillin and penicillin G detection.

1.5. References

- [1] B. Liu, J. Zhuang, G. Wei, Recent advances in the design of colorimetric sensors for environmental monitoring, *Environmental Science: Nano* 7(8) (2020) 2195-2213.
- [2] D.M. Holstege, B. Puschner, G. Whitehead, F.D. Galey, Screening and mass spectral confirmation of β -lactam antibiotic residues in milk using LC-MS/MS, *Journal of agricultural and food chemistry* 50(2) (2002) 406-411.
- [3] L. Kantiani, M. Farré, D. Barceló, Analytical methodologies for the detection of β -lactam antibiotics in milk and feed samples, *TrAC Trends in Analytical Chemistry* 28(6) (2009) 729-744.
- [4] M. Vogeser, F. Kirchoff, Progress in automation of LC-MS in laboratory medicine, *Clinical biochemistry* 44(1) (2011) 4-13.
- [5] W. Wang, Y. You, S. Gunasekaran, LSPR-based colorimetric biosensing for food quality and safety, *Comprehensive Reviews in Food Science and Food Safety* 20(6) (2021) 5829-5855.
- [6] T. Kumar, S. Naik, S.E. Jujjavarappu, A critical review on early-warning electrochemical system on microbial fuel cell-based biosensor for on-site water quality monitoring, *Chemosphere* 291 (2022) 133098.
- [7] J. Goode, J. Rushworth, P. Millner, Biosensor regeneration: a review of common techniques and outcomes, *Langmuir* 31(23) (2015) 6267-6276.
- [8] W. Wang, S. Gunasekaran, MXene-Based Nucleic Acid Biosensors for Agricultural and Food Systems, *Biosensors* 12(11) (2022) 982.
- [9] X. Wang, Z. Zhang, G. Wu, C. Xu, J. Wu, X. Zhang, J. Liu, Applications of electrochemical biosensors based on functional antibody modified screen printed electrodes: A review, *Analytical Methods* (2021).
- [10] Y. Huang, J. Tan, L. Cui, Z. Zhou, S. Zhou, Z. Zhang, R. Zheng, Y. Xue, M. Zhang, S. Li, Graphene and Au NPs co-mediated enzymatic silver deposition for the ultrasensitive electrochemical detection of cholesterol, *Biosensors and Bioelectronics* 102 (2018) 560-567.
- [11] J. Zhou, X. Qiu, K. Su, G. Xu, P. Wang, Disposable poly (o-aminophenol)-carbon nanotubes modified screen print electrode-based enzyme sensor for electrochemical detection of marine toxin okadaic acid, *Sensors and Actuators B: Chemical* 235 (2016) 170-178.
- [12] K. Murtada, S. Jodeh, M. Zougagh, Á. Ríos, Development of an Aluminium Doped TiO₂ Nanoparticles-modified Screen Printed Carbon Electrode for Electrochemical Sensing of Vanillin in Food Samples, *Electroanalysis* 30(5) (2018) 969-974.
- [13] Y. Luo, E.C. Alocilja, Portable nuclear magnetic resonance biosensor and assay for a highly sensitive and rapid detection of foodborne bacteria in complex matrices, *Journal of biological engineering* 11(1) (2017) 1-8.
- [14] M. Naguib, O. Mashtalir, J. Carle, V. Presser, J. Lu, L. Hultman, Y. Gogotsi, M.W. Barsoum, Two-dimensional transition metal carbides, *ACS nano* 6(2) (2012) 1322-1331.
- [15] M. Naguib, M. Kurtoglu, V. Presser, J. Lu, J. Niu, M. Heon, L. Hultman, Y. Gogotsi, M.W. Barsoum, Two-dimensional nanocrystals produced by exfoliation of Ti₃AlC₂, *Advanced materials* 23(37) (2011) 4248-4253.
- [16] Q. Zhong, Y. Li, G. Zhang, Two-dimensional MXene-based and MXene-derived photocatalysts: Recent developments and perspectives, *Chemical Engineering Journal* 409 (2021) 128099.
- [17] X. Sang, Y. Xie, M.-W. Lin, M. Alhabeab, K.L. Van Aken, Y. Gogotsi, P.R. Kent, K. Xiao, R.R. Unocic, Atomic defects in monolayer titanium carbide (Ti₃C₂T_x) MXene, *ACS nano* 10(10) (2016) 9193-9200.

- [18] M. Kurtoglu, M. Naguib, Y. Gogotsi, M.W. Barsoum, First principles study of two-dimensional early transition metal carbides, *Mrs Communications* 2(4) (2012) 133-137.
- [19] D. Zhao, Z. Chen, W. Yang, S. Liu, X. Zhang, Y. Yu, W.-C. Cheong, L. Zheng, F. Ren, G. Ying, MXene (Ti₃C₂) vacancy-confined single-atom catalyst for efficient functionalization of CO₂, *Journal of the American Chemical Society* 141(9) (2019) 4086-4093.
- [20] Q. Peng, J. Guo, Q. Zhang, J. Xiang, B. Liu, A. Zhou, R. Liu, Y. Tian, Unique lead adsorption behavior of activated hydroxyl group in two-dimensional titanium carbide, *Journal of the American Chemical Society* 136(11) (2014) 4113-4116.
- [21] K. Rasool, M. Helal, A. Ali, C.E. Ren, Y. Gogotsi, K.A. Mahmoud, Antibacterial activity of Ti₃C₂T_x MXene, *ACS nano* 10(3) (2016) 3674-3684.
- [22] Q. Jiang, Y. Lei, H. Liang, K. Xi, C. Xia, H.N. Alshareef, Review of MXene electrochemical microsupercapacitors, *Energy Storage Materials* 27 (2020) 78-95.
- [23] Z. You, Y. Liao, X. Li, J. Fan, Q. Xiang, State-of-the-art recent progress in MXene-based photocatalysts: a comprehensive review, *Nanoscale* 13(21) (2021) 9463-9504.
- [24] K.R.G. Lim, M. Shekhiriev, B.C. Wyatt, B. Anasori, Y. Gogotsi, Z.W. Seh, Fundamentals of MXene synthesis, *Nature Synthesis* 1(8) (2022) 601-614.
- [25] A.n. Morales-García, F. Calle-Vallejo, F. Illas, MXenes: new horizons in catalysis, *ACS Catalysis* 10(22) (2020) 13487-13503.
- [26] J. Chen, Q. Huang, H. Huang, L. Mao, M. Liu, X. Zhang, Y. Wei, Recent progress and advances in the environmental applications of MXene related materials, *Nanoscale* 12(6) (2020) 3574-3592.
- [27] Y. Long, Y. Tao, T. Shang, H. Yang, Z. Sun, W. Chen, Q.H. Yang, Roles of metal ions in MXene synthesis, processing and applications: a perspective, *Advanced Science* 9(12) (2022) 2200296.
- [28] X. Yang, Z. Chen, W. Zhao, C. Liu, X. Qian, M. Zhang, G. Wei, E. Khan, Y.H. Ng, Y.S. Ok, Recent advances in photodegradation of antibiotic residues in water, *Chemical Engineering Journal* 405 (2021) 126806.
- [29] M. Bacanlı, N. Başaran, Importance of antibiotic residues in animal food, *Food and Chemical Toxicology* 125 (2019) 462-466.
- [30] Y. Ben, C. Fu, M. Hu, L. Liu, M.H. Wong, C. Zheng, Human health risk assessment of antibiotic resistance associated with antibiotic residues in the environment: A review, *Environmental research* 169 (2019) 483-493.
- [31] J.C. Paige, L. Tollefson, M.A. Miller, Health implications of residues of veterinary drugs and chemicals in animal tissues, *Veterinary Clinics of North America: Food Animal Practice* 15(1) (1999) 31-43.
- [32] S. Sachi, J. Ferdous, M.H. Sikder, S.A.K. Hussani, Antibiotic residues in milk: Past, present, and future, *Journal of advanced veterinary and animal research* 6(3) (2019) 315.
- [33] M. Khaskheli, R. Malik, M. Arain, A. Soomro, H. Arain, Detection of β -lactam antibiotic residues in market milk, *Pakistan Journal of Nutrition* 7(5) (2008) 682-685.
- [34] H. Sereshti, S.S. Jazani, N. Nouri, G. Shams, Dispersive liquid-liquid microextraction based on hydrophobic deep eutectic solvents: Application for tetracyclines monitoring in milk, *Microchemical Journal* 158 (2020) 105269.
- [35] N.-R. Ha, I.-P. Jung, I.-J. La, H.-S. Jung, M.-Y. Yoon, Ultra-sensitive detection of kanamycin for food safety using a reduced graphene oxide-based fluorescent aptasensor, *Scientific reports* 7 (2017) 40305.

Chapter II. Introduction and literature review for enzyme nano-mimic: Nanozyme-based sensor and biosensor for food and quality and safety*

Abstract

Nanozymes are a type of nanomaterials, both metallic and non-metallic, that can catalyze biochemical reactions just as natural enzymes do. Therefore, since their recent discovery in 2007, nanozymes are employed as nanoscale enzymatic mimics, which are now at the forefront of various biosensing applications. When compared with natural enzymes, nanozymes offer several advantages such as relatively higher stability, lower cost, easier modification, and inherently more efficient nanocatalytic properties. Past research on the structure and catalytic principles of nanozymes has brought into focus various developments of nanozyme-based biosensors. In this review, we introduce several typical nanozymes, primarily those belonging to the peroxidase and oxidase families. The enzyme-mimicking mechanisms of these nanozymes are presented, which primarily result in colorimetric signals suitable for simple and easy biosensing applications. Emphasis is placed on describing nanozyme-based biosensors that are used for detecting chemical contaminants, such as ions and pesticide residues, and biological contaminants, such as pathogens and biotoxins, that can compromise food quality and safety.

2.1. Introduction

Natural enzymes are powerful biocatalysts for substrate conversion due to their specific recognition abilities and relatively high catalytic activities under mild environmental conditions in most cases. These enzymes find ubiquitous uses in a myriad of laboratories and industries for performing biochemical reactions [1]. However, the use of natural enzymes is beset with such drawbacks as insufferable price, unstable structure, high sensitivity to external conditions, low

*Wang, W, Gunasekaran, S. (2020). Nanozyme-based biosensors for food quality and safety. *TrAC trends in analytical chemistry* **2020**, 126, 115841. Copyright Elsevier.

reusability, etc. [2, 3]. Therefore, numerous researches have been focused on finding appropriate substitutes for enzymes with similar active sites and catalytic properties. Some enzyme mimics include catalytic cyclodextrins, polymers, supramolecules, porphyrins, and dendrimers [4-7].

In 2007, Yan et al. reported the peroxidase enzyme-like activity of ferromagnetic nanoparticles (Fe_3O_4 NPs) and pointed out that with catalytic activity similar to that of protein/RNA which specifically acts as peroxidase enzyme in nature, inorganic NPs could directly trigger and accelerate the oxidation of peroxidase substrates in the presence of hydrogen peroxide (H_2O_2) [8]. Since then, several other NPs have been identified to have biocatalytic activity either alone or as hybrids in conjunction with other biomolecular ligands [9]. Wei and Wang coined the term 'nanozyme' to describe NPs that possess the ability to mimic enzymatic action [10]. In addition to good recognition and biocatalytic activity, nanozymes offer prolonged life and high stability all at a cost lower than that of natural enzymes [11]. Consequently, nanozymes are increasingly employed in many applications such as biosensing, cancer therapy, environmental protection, and antibacterial treatment [12-15].

Nanozyme-based biosensors (NBs) are popular in different areas, including food quality safety evaluation, clinical disease diagnosis, biological metabolite measurement, and environmental pollutant monitoring (**Figure 2.1**). To date, there has been only a limited review of information on NBs, especially focusing on food quality and safety [16, 17]. To fill this gap, herein we present a more comprehensive review of NBs in food analysis, along with the discussion on major catalytic mechanisms of nanozymes for biosensing.

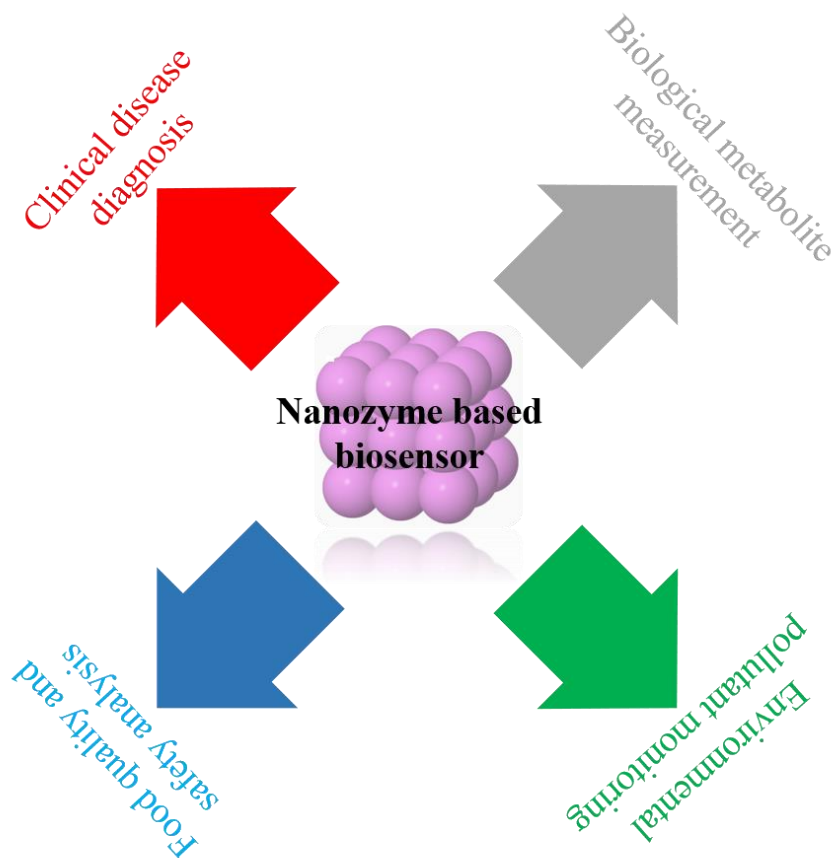


Figure 2.1. Different fields of nanozyme-based biosensor applications.

2.2. Predominant catalytic mechanisms of nanozymes for biosensing

Since the discovery of the first nanozyme (Fe_3O_4 NPs), hundreds of nanomaterials have been found to function as biocatalysts. According to the catalytic mechanisms the nanozymes mimic, two primary enzyme families have been identified: (1) oxidoreductases (e.g., oxidase and peroxidase) and (2) hydrolases (e.g., nuclease and protease) [18]. In this review, we primarily focus on the oxidoreductase family of nanozymes. The nanocomposites of NBs with several representative nanomaterials are shown in **Figure 2.2. A**, **2.2. B**. As **Figure 2.2. A** shown, though with the same enzymatic substrates, peroxidase-like nanozyme is more intended to identify and reduce H_2O_2 solution, while oxidase mimic nanozyme is more favor to trigger reduction of O_2 gas.

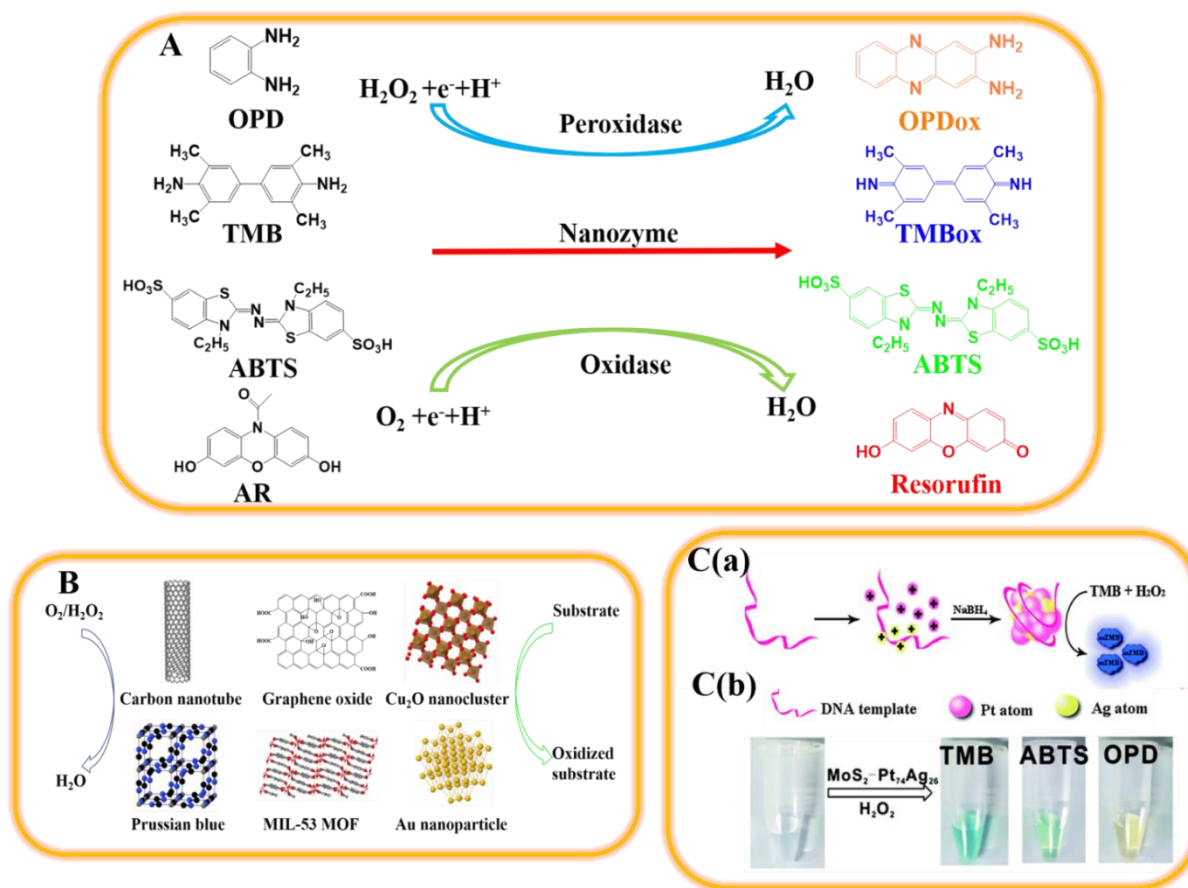


Figure 2.2. **A.** Schematic of several common peroxidase and oxidase substrates that undergo oxidation in the presence of nanozyme and oxidizing agents: OPD: o-phenylenediamine; TMB: 3,3',5,5'-tetramethylbenzidine; ABTS: 2,2-azinobis(3-ethylbenzothizoline-6-sulfonic acid) and AR: 10-acetyl-3,7-dihydroxyphenoxazine; **B.** Chemical structures of representative nanomaterials with intrinsic enzymatic properties: structures except graphene oxide are generated from: <https://www.chemtube3d.com>. **C(a).** Pt/Ag hybrid synthesized with DNA template serves as a peroxidase mimic, adapted with permission from [19] and **(b).** Color changes of different substrates after oxidation, adapted with permission from [20].

2.2.1. Peroxidase-like nanozyme

Currently, most NBs heavily depend on peroxidase-like nanozymes that could recognize and induce oxidation of peroxidase substrates in the presence of H_2O_2 , particularly for catalysis of o-phenylenediamine (OPD), 3,3',5,5'-tetramethylbenzidine (TMB), 2,2-azinobis(3-ethylbenzothiazoline-6-sulfonic acid) (ABTS), and 10-acetyl-3,7-dihydroxyphenoxazine (AR) into their corresponding oxidative products, orange OPDox, blue TMB_{ox}, green ABTS, and red resorufin, respectively (**Figure 2.2. A**) [21]. Due to the color change that accompanies the oxidative reaction, this mechanism provides the easiest way to qualitatively identify targets visually and the fastest way to quantify the concentration and/or level of the target analyte.

2.2.1.1. Non-metallic nanozymes

Several nanozymes are composed of carbon and its derivative nanomaterials, highlighting that carbon-based nanomaterials have superior peroxidase-like characteristics (**Figure 2.2. B**) [22, 23]. Mohammadpour et al. reported that carbon nanodots (CDs) can initiate the oxidation of TMB in the presence of H_2O_2 at 30 °C [24]. They found that absorbance of intermediate radical cations formed from CDs -TMB- H_2O_2 system has been observed at as same wavelength ($\lambda_{ads}=370\text{nm}$ and 653nm) as those released from TMB- H_2O_2 -horseradish peroxidase (HRP) system. Additionally, the magnitude of absorbance at two wavelengths has increased from 0.10 to 0.35 ($\lambda_{ads}=370\text{ nm}$) and from 0.05 to 0.20 ($\lambda_{ads}=653\text{ nm}$) during a reaction time of 1000 s. These results point out that the role of CDs in TMB oxidation is similar to that of peroxidase, which is to accelerate electron transfer from TMB to H_2O_2 molecules. Therefore, CDs largely increase the reaction rate of TMB oxidized by H_2O_2 . Additionally, this enzymatic catalysis is controlled by multiple environmental factors, such as pH, temperature and concentration of CDs, and H_2O_2 . Therefore, this is an

excellent example of zero-dimensional (0D) nanomaterials mimicking an enzyme action for supporting more future nanozyme applications.

Single-walled carbon nanohorns with a carboxylic group (SWCNH-COOHs) also possess peroxidase-like activity on TMB. An experimental study by Wang and Xu et al. provided strong evidence that the SWCNH-COOHs could remarkably accelerate the reaction between TMB and H_2O_2 [25]. In accordance with enzymatic kinetics, the catalytic reaction of SWCNH-COOHs follows the Michaelis-Menten equation, indicating that SWCNH-COOHs serves as peroxidase mimic. They also evaluated the robustness of SWCNH-COOHs and HRP, finding that SWCNH-COOHs are still capable to catalyze TMB- H_2O_2 redox reaction after incubation at a wide range pH (2~7) and temperature condition (20°C~80°C). These results suggest that SWCNH-COOHs might be a promising alternative one-dimensional (1D) peroxidase nano-mimetic in different bio-applications with a broader range of conditions.

Besides CD (0D) and SWCNH-COOHs (1D), several two-dimensional (2D) nanomaterials, especially graphene and graphene oxide (GO-COOHs) nanosheet, have been investigated for their enzyme-like characteristics [26]. Qu et al. studied the peroxidase-like activity of GO-COOH on TMB oxidation for glucose colorimetric detection in diluted blood and fruit juice sample matrixes [27]. To elucidate the mechanism of GO-COOH catalysis, kinetic studies of GO-COOH and HRP in TMB- H_2O_2 system were investigated independently, where slopes of line in Lineweaver–Burk plots were obtained based on two systems parallel to each other. This indicates the mechanism of GO-COOH catalysis is as same as that of HRP. In addition, peroxidase was reported following the ping-pong mechanism when they are initiating the redox reaction in the TMB- H_2O_2 system[28]. Combining the data of the steady-state kinetic study and the theoretical catalytic mechanism of peroxidase, the GO-COOH nanosheet was shown to obey the ping-pong mechanism when it

catalyzes TMB-H₂O₂ reaction [29]. During this catalysis, electrons from the valence bond of GO-COOH first transfer onto H₂O₂ molecules to produce •OH radicals once the GO-COOH surface electrostatically attaches to H₂O₂. The generated •OH radicals attract H⁺ in an acidic solution in terms of H-bond. And the peroxidase substrate, for example, TMB, is then adsorbed with GO-COOH, donating lone-pair electrons from -NH₂ group to GO-COOH nanosheet to mobilize GO-COOH nanostructures by enhancing the charge density of GO-COOH. After releasing lone-pair electrons, oxidized TMB turns the solution color blue. In this GO-COOH enzymatic catalysis, it is believed that nitrogen atom in peroxidase mimic-substrate reactions plays an important role in the electron transfer process of H₂O₂-substrate reaction. Hence, several groups took advantage of this finding, i.e., the role of the nitrogen atom, for improving the efficacy of TMB-H₂O₂ catalysis of GO-COOH based nanohybrids, for instance, GO-COOH coated by chitosan for colorimetric identification of glucose in human serum sample [30] or nitrogen-doped GO-COOH which could be useful for living cancer cells electrochemical recognition [31, 32]

2.2.1.2. Single metallic nanozymes

Nanozymes composed of single metallic nanomaterials are used in numerous areas. For example, nanozymes composed of transition metals, particularly transition metal oxides possess intrinsic peroxidase-like properties. The Fe₃O₄ NPs, widely reported as a successful nanozyme since 2007, were confirmed to behave like peroxidase in TMB catalysis [8, 33]. Data from steady-state kinetic and catalytic experiments suggest that the Fe₃O₄ NPs-TMB-H₂O₂ system also undergoes enzymatic catalysis, which follows the ping-pong catalytic mechanism of Fe₃O₄ NPs in TMB-H₂O₂ redox reaction [34]. As mentioned above, abundant generation of •OH radicals is ascribed to the exposure of H₂O₂ at Fe²⁺, which has higher peroxidase-like activity than Fe³⁺ ($k_{Fe^{2+}}=76$ L/mol·s, $k_{Fe^{3+}}=0.002$ L/mol·s) and follows the Fenton reaction (see Eqs. (1)-(8)) [35,

36]. The $\bullet\text{OH}$ radicals released from H_2O_2 would immediately bind with H^+ via hydrogen bonding, the resulting Fe^{2+} turns to Fe^{3+} which, at the same time, receives an electron from the $-\text{NH}_2$ group of TMB to form Fe^{2+} back, again. After donating an electron to Fe^{3+} , TMB is then oxidized to TMBox, eventually achieving a peroxidase-substrate reaction model. Herein, Fe_3O_4 NPs would be an alternative surrogate of natural enzymes in biosensing and other biomedical applications.



Besides Fe_3O_4 NPs, Cu nanocluster (Cu NC) also exhibits impressive catalytic oxidation reactions between H_2O_2 and TMB. Owing two possible distinct numbers of Cu atoms (5 atoms and 13 atoms) in the core, Cu NC shows an average size of $2.8 \pm 0.5\text{nm}$ with (1 1 1) planes of metallic Cu and indicates various degrees of oxidation state (0, +1 and +2) [37]. With these extrapolated nanostructures and their unique discrete electronic states, it performs better than HRP at near-neutral pH, which is beneficial for biosensing of targets that require neutral pH conditions [38]. In these reactions, Cu NC and O-O bond of H_2O_2 function as catalytic activity site and substrate site, respectively. Considerable amounts of $\bullet\text{OH}$ radicals are then rapidly created, which trigger TMB oxidation to TMBox. The excess reactive Cu^{2+} ion in the solution adsorbed at Cu NC

surface also improves the catalytic activity. Therefore, Cu NC would be a potential nanomaterial in biosensors for diagnostics, for example, glucose level determination *in vivo*.

Metal-organic frameworks (MOFs) are 3D synthetical crystalline complexes either composed of core-shell nanoarchitecture of several neutral or anionic organic linkers mutually connecting with a cluster of metal cation, or delicately arranged by repeat-blockers consisting of metal ions [39]. They can also serve as peroxidase mimics due to multivalent metal ions active sites (for instance, $\text{Fe}^{3+}/\text{Fe}^{2+}$, $\text{Cu}^{1+}/\text{Cu}^{2+}$) in their delicate nanostructures. Catalytic sites of MOFs are formed by the emerging occurrence of inorganic (normally metal ions)-organic molecular building block units, which are essential parts for peroxidase reaction achievement. In this regard, MOFs reveal perfect biocatalytic capability by mimicking the natural peroxidase [40]. Li et al. reported an inherent peroxidase-like behavior of Fe-MIL-88NH₂ in the TMB oxidation reaction in accordance with the ping-pong mechanism [41]. Based on the kinetic study and electron spin resonance data, they suggested that Fe-MIL-88NH₂ could first transfer electrons from Fe^{3+} to an adsorbent H₂O₂ molecule to break the O-O bond and create •OH radicals. Due to with lower Michaelis-Menten constant (K_m) to TMB ($K_m = 2.84 \times 10^{-4} \text{M}$) than HRP's ($K_m = 3.17 \times 10^{-4} \text{M}$), Fe-MIL-88NH₂ would have higher affinity to TMB than HRP does. Therefore, to compensate for the vacuum of outmost electrons orbital in Fe-MIL-88NH₂, lone pair electrons of -NH₂ in TMB would be dragged into the Fe-MIL-88NH₂ more rapidly by strong electronegative force. At last, colorless TMB is finally oxidized into blue TMB_{ox}. Hence, it is a promising nanomaterial of Fe-MIL-88NH₂ to be used for quick food composite detection and determination.

Moreover, noble metals such as Au, Pt, and Pd are always regarded as a kind of catalytic agents for accelerating numerous chemical reactions under a broad range of conditions [42]. By themselves, noble metals usually suffer from short life and instability when they are in complicated

experimental conditions. However, in conjunction with a protector or stabilizer, the life span of noble metals is significantly prolonged as well as the stability is largely improved. Surprisingly, both protector and stabilizer could also enhance the catalytic performance of noble metals remarkably on the redox reaction of peroxidase substrates [43]. For example, bovine serum albumin (BSA) was successfully employed to stabilize the Au cluster. This BSA-Au complex not only presents high peroxidase-like behavior over a broad temperature range but also offers properties such as striking robustness [44]. To further characterize the peroxidase activity of the BSA-Au cluster, a steady-state kinetic study was carried out. The K_m of the BSA-Au cluster was 125 times lower than that of HRP, i.e., the BSA-Au cluster was 125 times more favorable to TMB than HRP. Therefore, the ability of noble metals as peroxidase mimics cannot be overlooked.

2.2.1.3. Bi- or multi-metallic nanozymes

It has been reported that oxides of nanoalloys perform as peroxidase mimics by enhancing the reaction rate of peroxidase substrates [45-47]. $MnFe_2O_4$ NPs are an intriguing nanozyme in terms of its similarity of inherent structure with Mn^{2+} and Fe^{3+} active sites to that of peroxidases [48]. $MnFe_2O_4$ shows peroxidase-like activity toward TMB and OPD in the presence of H_2O_2 . Kinetic investigation of the Fenton reaction demonstrates that, because of its higher peroxidase activity compared with that of Fe^{3+} , Mn^{2+} plays a major role in TMB catalysis. Similar to the natural manganese peroxidase catalytic mechanism, $MnFe_2O_4$ NPs accelerate the rate of electron transfer from TMB to H_2O_2 , leading TMB to be oxidized into blue-colored TMB_{ox}. Additionally, inspired by the highly efficient synergy of HRP and manganese peroxidase in H_2O_2 decomposition, Bhattacharya et al. doped Mn^{2+} into mixed ferrite NPs ($Mn^II_xFe^II_{1-x}Fe^III_2O_4$ NPs) [49]. To explore the mechanism of $Mn^II_xFe^II_{1-x}Fe^III_2O_4$, they performed a steady-state kinetic study and found TMB

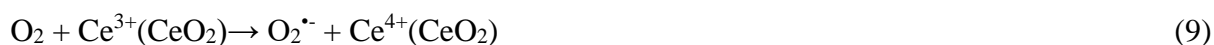
is more likely to be attached to $\text{Mn}^{\text{II}}_x\text{Fe}^{\text{II}}_{1-x}\text{Fe}^{\text{III}}_2\text{O}_4$ than to HRP. Afterwards, $\text{Mn}^{\text{II}}_x\text{Fe}^{\text{II}}_{1-x}\text{Fe}^{\text{III}}_2\text{O}_4$ has been used as a nanozyme in various applications, especially for biosensing.

Bi-noble metallic nanoalloys are also widely used as peroxidase-like nanozyme [50, 51]. Yang et al. used DNA as a template to synthesize Ag/Pt nanozyme (DNA-Ag/Pt), which exhibits high intrinsic peroxidase catalytic activity toward TMB [19]. Their experimental data suggest that intrinsic peroxidase activity is mainly attributed to Pt nanocomposite. While both DNA template and Ag serve as scaffolds to support the whole complex. Furthermore, higher electronic conductivity of Ag leads to improved electron movement throughout the nanozyme-substrate system, thus stimulating the catalysis capability of DNA-Ag/Pt in the oxidation of TMB, ORD, and ABTS in the presence of H_2O_2 (**Figure 2.2. C(a)**). To further enhance the enzymatic performance of Ag/Pt, Wang et al. decorated molybdenum disulfide (MoS_2) nanosheet by implanting $\text{Pt}_{74}\text{Ag}_{26}$ NPs [20]. They found that, at pH 4 and 50 °C, the enzymatic activity of $\text{Pt}_{74}\text{Ag}_{26}$ NPs was higher than those of Ag/Pt and MoS_2 nanosheet. Their results indicate that lone-pair electrons can easily transfer from the amino group of TMB to the H_2O_2 molecule mediated by MoS_2 - $\text{Ag}_{74}/\text{Pt}_{26}$ hybrid. As a result, H_2O_2 is decomposed into $\bullet\text{OH}$ radicals which attach to H^+ and the oxidized peroxidase substrates would appear after the deprotonation process (**Figure 2.2. C(b)**).

2.2.2. Oxidase-like nanozymes

Similar to natural oxidases, oxidase-like nanozymes can oxidize some organic substrates by reducing O_2 to generate H_2O_2 (**Figure 2.2. A**). Since Au has been proposed as an oxidase-like nanozymes, numerous nanomaterials have been reported as oxidase mimics for a variety of applications [52-54]. Wei et al. rationally synthesized nanoceria (cerium dioxide, CeO_2) which was confirmed as an oxidase mimetic in the catalytic reaction of TMB in the presence of O_2 [55]. Data from kinetic study and investigations of intermediates, elucidated that under the acidic condition,

the surface initially composed of $\text{Ce}^{3+}/\text{Ce}^{4+}$ of nanocerium firstly adsorbs O_2 , where Ce^{3+} immediately outputs the electron to adsorbed O_2 , assisting the generation of $\text{O}_2^{\bullet-}$ radicals and Ce^{4+} cations. At the same time, the high affinity of CeO_2 to TMB ($K_m=0.42$ mM) helps lone pair electrons easily transfer into $\text{Ce}^{4+}(\text{CeO}_2)$ NPs, leading Ce^{3+} cations to release and the solution color to change blue. On-site $\text{O}_2^{\bullet-}$ radicals released concomitantly re-oxidize Ce^{3+} to Ce^{4+} back, which, alternatively, directly oxidize TMB to TMB_{ox}, turning the solution color change blue as well (Eqs. 9-12) [55].



Wang et al. added that CeO_2 nanorods (CeO_2 NRs) with facet (1 1 0) have the highest oxidase activity among different synthesized samples, including polyhedral (1 1 1) and cubes (1 0 0) [56]. In this study, SO_4^{2-} ions are anchored in CeO_2 NRs to form CeO_2 NRs- SO_4^{2-} nanohybrid. This hybrid exhibited great affinity to O_2 molecules and fast electrons movement from $-\text{NH}_2$ of TMB to O_2 because of the strong electronegativity of SO_4^{2-} . As a result, the catalysis rate of the TMB- O_2 reaction is strikingly increased.

There is evidence that platinum-cobalt (PtCo) bimetallic NPs could stimulate the redox reaction of oxidase substrates with O_2 molecules [57]. Among different ratios of Pt/Co composites, $\text{Pt}_{72}\text{Co}_{28}$ with (1 1 1) facet serves the highest oxidase-like activity (**Figure 2.3. A, B**) [58]. The investigation of the mechanism uncovered that superoxide anion ($\text{O}_2^{\bullet-}$) is initially formed after electrons move from $\text{Pt}_{72}\text{Co}_{28}$ to surface adsorption O_2 , and instantly turned to HO_2^{\bullet} radicals by the protonation process. New HO_2^{\bullet} radicals in solution then either dissociate into O_{ads} and $\text{OH}^{\bullet}_{\text{ads}}$,

or are further reduced into OH^- , which concomitantly release plenty of hydroxyl radicals (**Figure 2.3. C**). As a result, three oxidase substrates, TMB, OPD and ARTS, loss their lone pair electrons to be oxidized into their corresponding oxidized species.

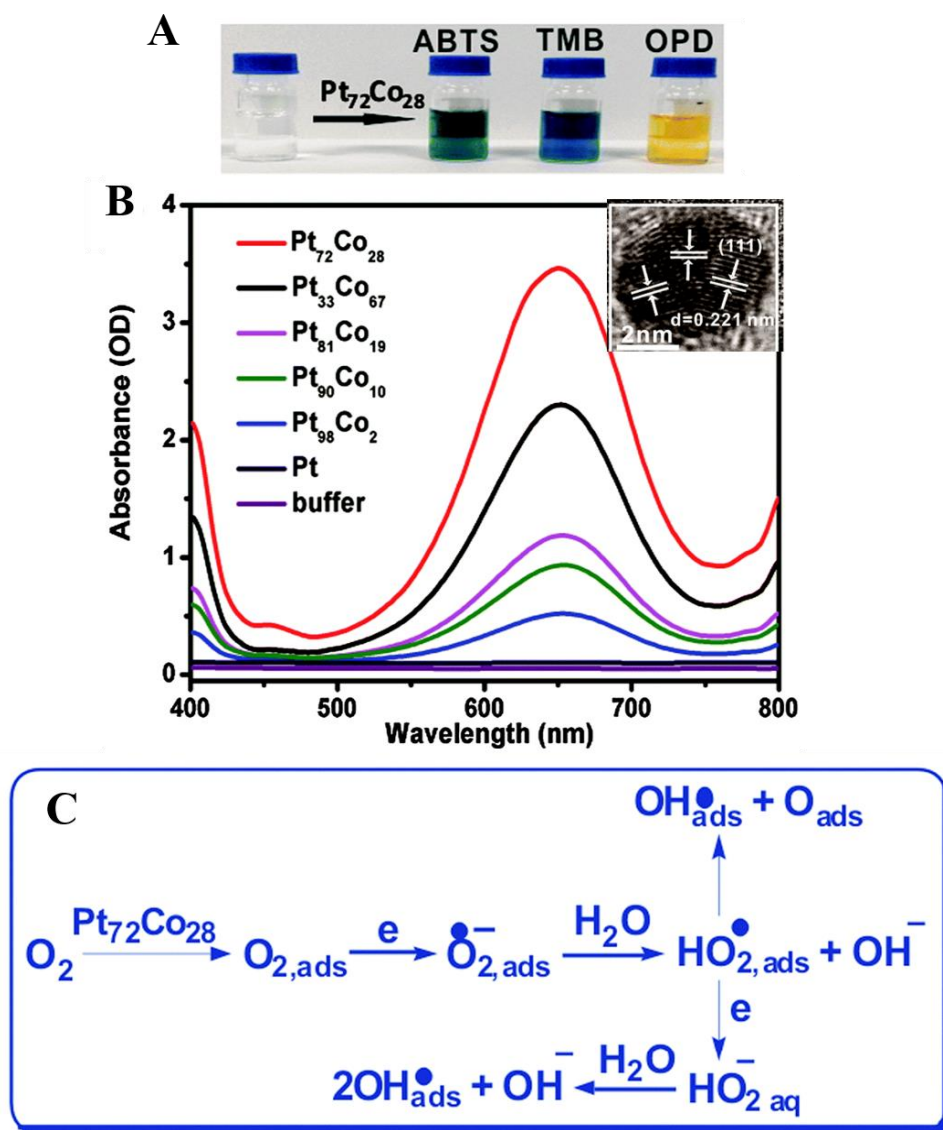


Figure 2.3. **A.** Color change in three oxidase substrates catalyzed by $\text{Pt}_{72}\text{Co}_{28}$ nanoparticles, **B.** UV absorbance for TMB products undergoing catalysis of Pt-Co hybrid with various Pt/Co ratios; inset shows the facet of $\text{Pt}_{72}\text{Co}_{28}$, **C.** mechanism of $\text{Pt}_{72}\text{Co}_{28}$ for mimicking oxidase.

Adapted with permission from [58]

2.3. Applications of nanozymes for sensing and biosensing

As an emerging class of enzyme-like nanomaterials, nanozymes rival other materials for biosensing applications. Biosensors comprising nanozyme provide highly accurate and precise sensing of various targets including Ebola virus, tumor cells, and glucose [59-61]. In this section, our focus is on biosensing applications relevant to food quality and safety monitoring.

2.3.1. Detection of ions

The detection of ions is a crucial event in the food field since it is necessary to be aware of their amounts in organisms, particularly in the human body. As successful surrogates of natural enzymes, nanozymes are broadly applied in a biosensing platform for various ions differentiation. A summary of NBs used for the detection of various cations (positively charged) and anions (negatively charged) is presented in **Table 2.1**.

Table 2.1. Applications of nanozymes for colorimetric (unless noted otherwise) detection of ions

Analyte ion	Nanozyme system	Enzyme mimicked	LOD	Linear range	Sample matrix	Ref.
Ag ⁺	Au cluster/bovine serum albumin (BSA)	Peroxidase	0.204 μ M	0.5~10 μ M	Lake water	[62]
	Pd nanoparticle/Histidine	Peroxidase	4.7 nM	30~300 nM	Environmental water samples	[63]
	Pt nanocubes/poly(vinylpyrrolidone)	Peroxidase	80 pM	10 ⁻² ~10 ⁴ nM	Tap-water	[64]
	zeolitic imidazolate frameworks-8/graphene oxide	Peroxidase	1.43 nM	2.0~5.0 nM	Yellow river water and human serum sample	[65]
Cu ²⁺	Ag/Pt nanocluster	Peroxidase	5.0 nM	10~100 nM	Lake water, Tap-water and pond water	[66]
	Histidine/Au nanocluster	Peroxidase	0.1 nM	1~100 nM	human serum sample	[67]
Fe ²⁺	C-dots/Mn ₃ O ₄ nanocomposite	Oxidase	0.03 μ M	0.03 ~ 0.83 μ M	—	[68]
	Molybdenum disulfide nanosheet (MoS ₂)	Peroxidase	7 nM	0.01~0.8 μ M	Lake water	[69]
	MoS ₂ nanosheet	#Peroxidase	3.5 nM	0.005~0.2 μ M	Lake water	[70]
Hg ²⁺	Au/Fe ₃ O ₄ /Graphene oxide (GO)	Peroxidase	0.15 nM	1~ 50 nM	Yellow river water	[71]
	Au/Fe ₃ O ₄ /GO-MoS ₂ aerogel	Peroxidase	3.279 nM	1~14 μ M	—	[72]
	Chitosan/Se nanoparticle	Oxidase	0.12 μ M	0.1 ~ 2.5 μ M	—	[73]
	Carbon nanodot	Peroxidase	23 nM	0~0.31 μ M	River water	[74]
	Citrate/Pt nanoparticle	Peroxidase	8.5 pM	0.01~4 nM	Tap water	[75]
	Mn ₃ O ₄ nanoparticle	Oxidase	18.9 nM	49.9~997.1 nM	Tap water, lake water, river water and wastewater	[76]

	Reduced GO/polyethylenimine/Pd nanoparticle	Peroxidase	(1) 0.39 nM in double distilled water (2) 10 nM in wastewater and human serum	0.1~25 nM	Wastewater and human serum	[77]
Pb ⁺	Au nanocluster	Peroxidase	2 μM	2~250 μM	Lake water	[78]
CN ⁻	Cobalt hydroxide/oxide-modified GO	#Peroxidase	22 nM	0.075 ~2.5 μM	Wastewater	[79]
F ⁻	CeO ₂	#Oxidase	1.8 μM	1.8 μM~1 mM	River lake	[80]
	Nanoceria	Oxidase	0.64 μM	0.64 ~100 μM	Lake water and toothpaste	[81]
NO ₂ ⁻	Histidine/Au nanocluster/rGO	*Oxidase	0.7 μM	2.5~5700 μM	Sausage	[82]
S ²⁻	β-casein/Pt nanoparticle	Peroxidase	0.8 nM	0.001 ~0.2 μM	Tap water and lake water	[83]
	Bare gold nanoparticle	Peroxidase	80 nM	0.5 ~10 μM	Tap water	[84]
	Bromide graphene	Peroxidase	25.3 μM	0.04~0.4 mM	River water and sewage water	[85]
PO ₄ ³⁻	3,4-dihydroxyhydrocinnamic acid /Fe ₃ O ₄ nanocubes (Fe ₃ O ₄ -DHCA)	Peroxidase	49.8 nM	0.066~33.3 μM	River water and tap water	[86]
	Fe ₃ O ₄ magnetic nanoparticles	Peroxidase	0.11 μM	0.2 ~ 200 μM	Drinking water, groundwater, and lake water	[87]

Fluorometry detection; *electrochemical detection

Cations are divided into essential and non-essential categories. Essential cations serve several necessary biofunctions in organisms at very low concentrations, such as (1). connective tissue support (Cu^{2+}): e.g. Cu deficiency leads cytochrome C oxidase level to decrease, which causes muscle weakness; (2). protein core active site ($\text{Fe}^{2+}/\text{Fe}^{3+}$) for helping O_2 transferring in humans: e.g. heme protein is always designated by protein with heme group which consists of the Fe ($\text{Fe}^{2+}/\text{Fe}^{3+}$) as coordination center; and (3). essential part of enzyme for CO_2 hydration (Zn^{2+}): e.g. carbonic anhydrase is composed of Zn^{2+} and His 64, which is mainly for CO_2 hydration in human body [88-90]. However, at excessive concentrations, they exhibit seriously acute toxicity to living systems. For example, rice growth inhibition (Fe^{2+}), vomiting, and diarrhea in humans (Al^{3+}) [91]. In this regard, it is important to measure their concentration in foodstuffs. Liu et al. designed a colorimetric biosensor using a nanozyme composed of Au NC and histidine biomolecule (His-Au NCs) for the detection of Cu^{2+} [67]. They believed that His-Au NC could largely induce the oxidation of TMB to blue color TMB_{ox} in the presence of H_2O_2 . Alternatively, with greater favorability to Cu^{2+} , His ligand of His-Au NCs selectively conjugate with free Cu^{2+} , so to dramatically constrain the intrinsic peroxidase property of the nanocomplex, thus inhibiting the oxidation of TMB- H_2O_2 . Ultimately, Cu^{2+} could be detected by measuring the change in the absorbance intensity of TMB solution. This biosensor exhibited a linear range between 1-100 nM with limit of detection (LOD) of 0.1 nM.

Recent findings show that free Fe^{2+} can remarkably enhance the MoS_2 nanosheet performance on OPD oxidation in the presence of H_2O_2 [69]. Ni et al. [70] took advantage of this synergistic effect in fabricating a biosensor for Fe^{2+} determination in lake water. Their biosensor can measure Fe^{2+} concentration in a wide concentration range (0.005 ~0.2 μM) with an LOD of 3.5 nM.

Non-essential cations are generally toxic to humans. For instance, Pb^{2+} is associated with headache and irritability at low level and even small amount of Hg^{2+} is capable of leading to neurotoxicity [92]. To avoid these adverse effects, it is important to determine their content in foodstuffs or water. Shamsipur et al. proposed to use CDs and cysteine (Cys) conjugates as nanomaterials to determine Hg^{2+} concentration in river water (**Figure 2.4. A (a)**) [74]. In fact, -S-group of Cys possesses fairly intensive hydrated electron (e^-_{aq}) decay ability (decay constant $\approx 8 \times 10^5 \text{ s}^{-1}$, i.e., $t_{1/2} \approx 1 \text{ } \mu\text{s}$), demonstrating which have striking electron restoration capability, resulting oxidation reaction to be prohibited [93]. Nevertheless, because Hg^{2+} biases towards Cys, the addition of Hg^{2+} shields the Cys surface, leading to decelerating the effect of Cys on CDs. As presented in **Figure 2.4. A (a)**, this behavior helps TMB oxidation to continue. Eventually, by measuring the intensity of UV-vis absorbance of TMB color, this kind of biosensor is capable to accurately detect $0 \sim 0.31 \text{ } \mu\text{M}$ Hg^{2+} in aquatic environment with LOD of 23 nM (**Figure 2.4. A(b, c)**). In addition, a highly sensitive NB was fabricated for Hg^{2+} measurement by applying Pt NPs capped with citrate, which exhibits an ability to catalyze Hg^{2+} over a concentration range of $0.01 \sim 4 \text{ nM}$ and LOD of 8.5 pM [75].

Anions are also important contaminants in foods, owing to the pollutants from advanced industrialization. For example, cyanide (CN^-), found in our natural aquatic environment, is a potent poison [94]. A finding indicates that with formation constant $\beta(\text{Co}(\text{CN})_4^{2-}) = 1.16 \times 10^{31} \text{ M}^{-4}$, CN^- is favorable towards the Co^{2+} for forming the anion compound $\text{Co}(\text{CN})_4^{2-}$ [95]. In this regard, an NB made of GO coated by cobalt hydroxide/oxide ($\text{CoO}_x\text{H-GO}$) system was manufactured for fluorometric assay for CN^- in wastewater [79]. During sensing, the $\text{CoO}_x\text{H-GO}$ nanocomposites are believed to catalyze the oxidation reaction of non-fluorescent AR to form a reddish color resorufin in the presence of H_2O_2 . Yet, the catalytic activity of $\text{CoO}_x\text{H-GO}$ nanocomposites would

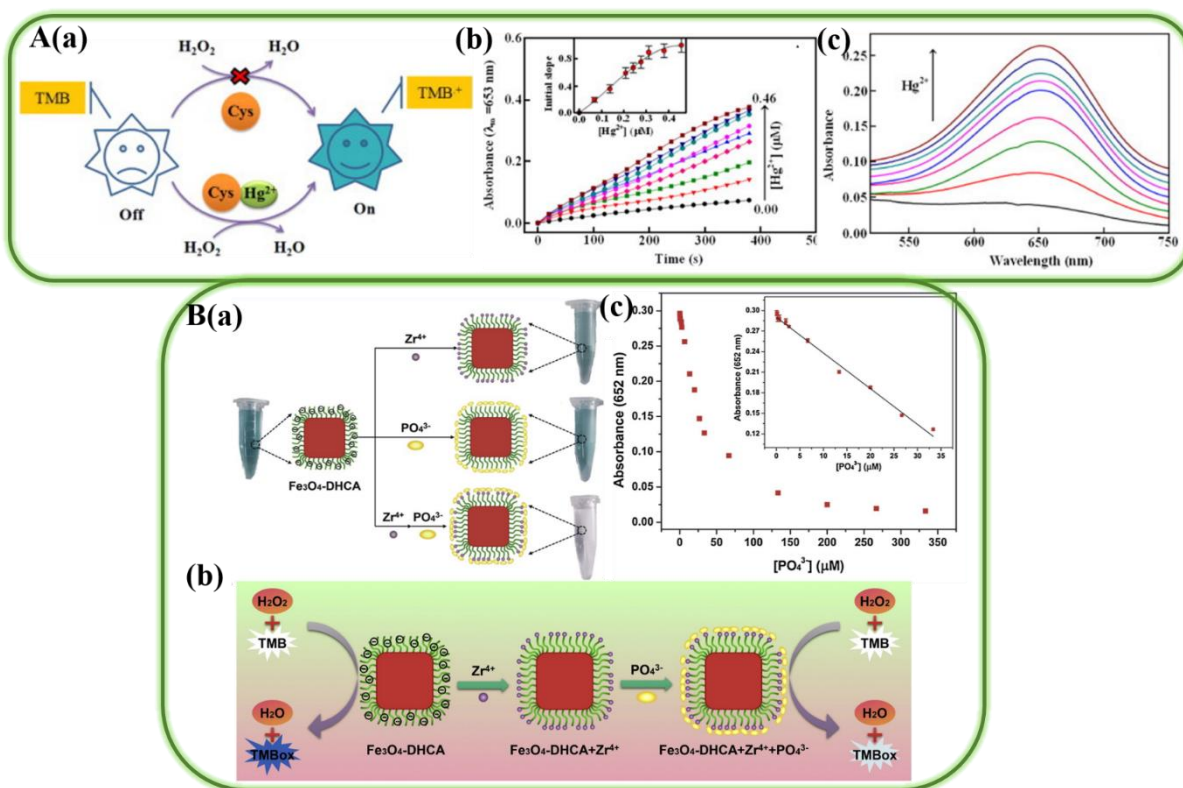


Figure 2.4. **A(a)** Illustration of color “on/off” assay mechanism, **(b)** time profile with inset showing the relationship between the concentration of Hg^{2+} with UV absorbance at a reaction time of 260 s, **(c)** absorbance of UV spectrum with increasing Hg^{2+} concentration, adapted with permission from [74]; **B (a)** Illustration of the impact of different ions on $\text{Fe}_3\text{O}_4\text{-DHCA}$ peroxidase activity, **(b)** Schematic of mechanism of $\text{Fe}_3\text{O}_4\text{-DHCA}$ with Zr^{4+} for PO_4^{3-} detection, **(c)** Relationship between UV absorbance and PO_4^{3-} concentration and inset showing concentration with conversion to logarithm, adapted with permission from [86]

be blocked by CN^- in terms of the preferable reaction between Co^{2+} and CN^- for forming $\text{Co}(\text{CN})_4^{2-}$, diminishing the red color intensity in the resulting solution. This sensor could quantitatively measure the CN^- concentration in a range of 75 nM~2.5 μM with an LOD of 22 nM.

The catalytic activity of $\text{CoO}_x\text{H-GO}$ nanocomposites is controlled by pH, concentration of H_2O_2 , and temperature. Additionally, due to the unique chemical structure of nanozyme, the enzymatic property of this nanocomposite is also affected by the thickness of GO, indicating that this kind of NBs could be fabricated as thin film probes, which could be employed as *in situ* CN^- biosensor.

Excessive $\text{NO}_2^-/\text{NO}_3^-$ and PO_4^{3-} are present in natural aquatic environments and in foods, leading to eutrophication in both natural environments and food products [96, 97]. Du et al. illustrated that His-Au NC modified by reduced graphene oxide (His-Au NC/rGO) can be used to measure NO_2^- in sausage with an LOD of $0.7 \mu\text{M}$ by means of an electrochemical method [82]. While PO_4^{3-} was colorimetrically detected by 3,4-dihydroxyhydrocinnamic acid conjugated with Fe_3O_4 nanocube ($\text{Fe}_3\text{O}_4\text{-DHCA}$), the signal of which was synergistically enhanced by Zr^{4+} [86]. In this NB, the intrinsic peroxidase behavior of $\text{Fe}_3\text{O}_4\text{-DHCA}$ in the TMB- H_2O_2 system is disturbed by PO_4^{3-} ions, caused by the priority reaction between the active site of $\text{Fe}_3\text{O}_4\text{-DHCA}$ (Fe) and PO_4^{3-} ions. The blue color of TMB remains after adding PO_4^{3-} anions in **Figure 2.4. B(a)** indicates that there are slight effects of PO_4^{3-} on the inhibitory activity, because of the less active site of $\text{Fe}_3\text{O}_4\text{-DHCA}$ exposure. On the contrary, no color showing in **Figure 2.4. B(a)** where there are Zr^{4+} and PO_4^{3-} both on the surface of $\text{Fe}_3\text{O}_4\text{-DHCA}$ indicates that Zr^{4+} cations would significantly enhance the prohibitive performance of PO_4^{3-} ions in $\text{Fe}_3\text{O}_4\text{-DHCA}$. As depicted in **Figure 2.4. B(b)**, Zr^{4+} ions are capable of electrostatically covering the surface of $\text{Fe}_3\text{O}_4\text{-DHCA}$ for enhancing the interacted areas of $\text{Fe}_3\text{O}_4\text{-DHCA}$. Furthermore, it could coordinate with PO_4^{3-} to protect the nanozyme from contacting with peroxidase substrates. With the synergistic inhibition behavior, as shown in **Figure 2.4. B(c)**, NB could detect PO_4^{3-} anion concentration in range of $0.066 \sim 33.3 \mu\text{M}$ with LOD of 49.3 nM . Therefore, it is an alternative NB for *in situ* detection of PO_4^{3-} .

2.3.2. Detection of foodborne pathogens and microbial metabolites

Foodborne pathogens and microbial metabolites are biological contaminants that adversely affect food safety. Enzyme-linked immunosorbent assay (ELISA) is prevalently used for various biochemical detections based on enzymatic reactions. As powerful surrogates of natural enzymes, nanozymes are now widely adopted in immunoassays. In contrast to the conventional ELISA, nanozyme immunoassays offer improved detection speed, higher sensitivity and stability under harsh conditions, and lower cost.

Escherichia coli O157:H7 is a major foodborne pathogen. Wan et al. measured *E. coli* O157:H7 concentration as low as 4.1 CFU/mL at pH 6.5 and 25 °C, by using hemin-concanavalin A hybrid nanoflowers based sandwich-structured immunoassay [98]. The authors further validated this approach by monitoring the occurrence of *E. coli* O157:H7 in milk sample to demonstrate the sensor's practical application. Lin et al. evaluated the performance of Pt-Au bimetallic nanozyme-based immunochromatographic assay for *E. coli* O157:H7 detection, which provided an LOD of 10^2 CFU/mL [99]. Moreover, a typical sandwich-type lateral flow assay with Pd-Pt nanozyme for colorimetric detection of *E. coli* O157:H7 has been proposed (**Figure 2.5. A**) [100]. Results from this colorimetric assay are obtained in just four minutes, but a longer time is needed due to the interference from other milk substrates. The linear range and LOD of this assay are 10^2 ~ 10^6 CFU/mL and 0.87×10^2 CFU/mL, respectively.

Listeria monocytogenes is another common foodborne pathogen that usually infects neurons and T-cell immune system in humans [101]. An investigation of a hybrid of Fe₃O₄ NC anchored aptamer showed that Fe₃O₄ NC serves as a signal amplification ligand for the colorimetric assay of *L. monocytogenes*. In this immunoassay, intercalation of Fe₃O₄ NC-aptamer into a sandwich-type biosensor exhibits a higher colorimetry response compared to BSA polymer-based biosensor.

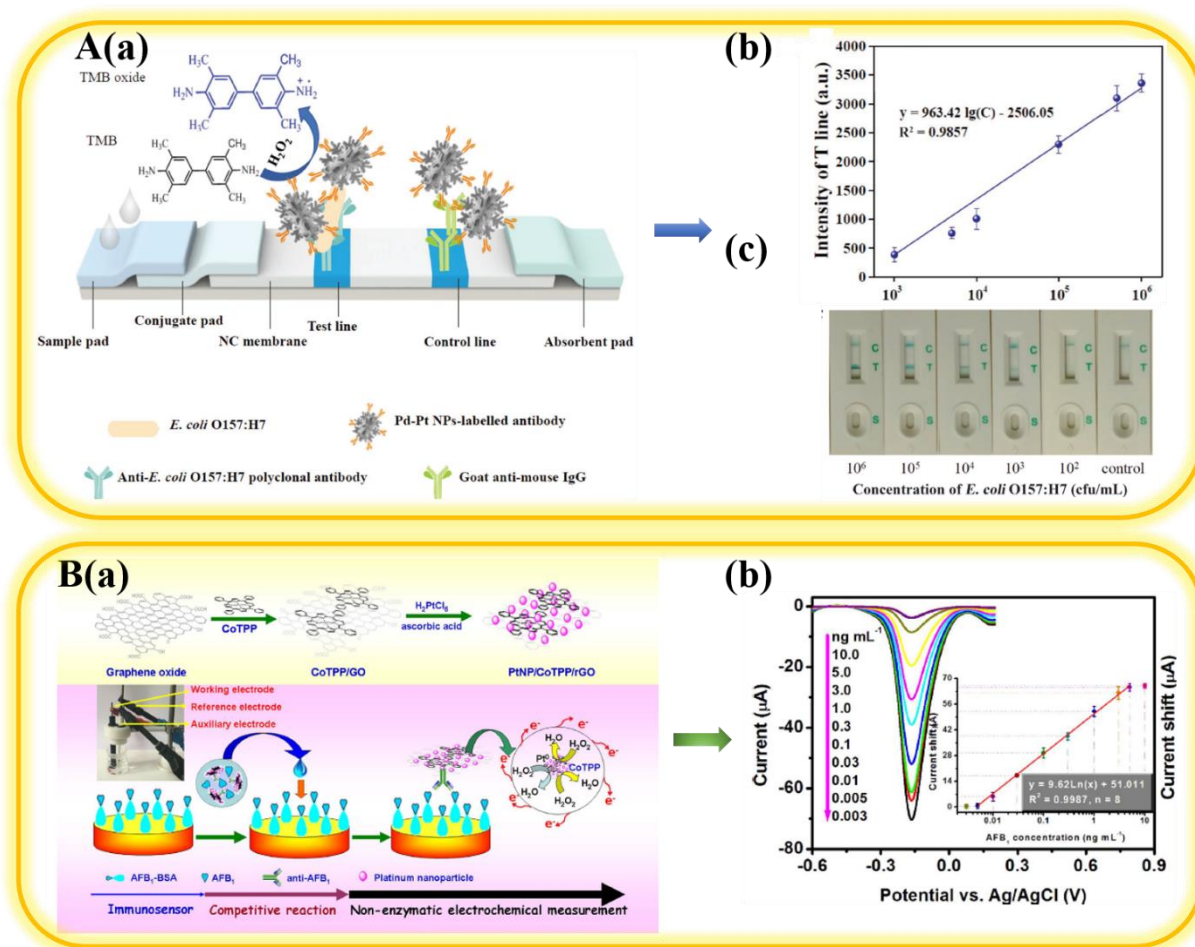


Figure 2.5. A(a). Illustration of lateral flow assay for *E. coli* O157:H7; (b) Linear relationship between concentration of *E. coli* O157:H7 and color intensity; (c) Photograph of lateral flow assay with different concentrations of *E. coli* O157:H7, adapted with permission from [101]; B (a) Schematic for AFB1 detection mechanism based on electrochemical immunoassay using PtNPs/CoTPP/rGO-based biosensor and photo inset is electrochemical measurement device; (b) Current change with different concentrations of AFB1 and inset shows current vs. AFB1 linear relationship, adapted with permission from [104]

In this case, a linear colorimetric response was obtained for the amount of *L. monocytogenes* in the range of $5.4 \times 10^3 \sim 10^8$ CFU/mL [102]. Besides Fe₃O₄ NC, BSA-MnO₂ NPs have a feasible

oxidase performance on color intensity enhancement for the detection of *L. monocytogenes* over a range of $10 \sim 10^6$ CFU/mL with an LOD of 10 CFU/mL. Interestingly, this NB (i.e., BSA-MnO₂ NP) could provide divergent assays for the detection of *L. monocytogenes*. For example, in the resulting aqueous solution, adding extra AuNPs would reduce TMB²⁺ back to TMB, promoting the aggregation of AuNPs, which turns the color of the resultant solution gold for secondary colorimetric detection [103].

Aflatoxin B1 (AFB1) is a product of secondary metabolism from *Aspergillus* species, which usually contaminates cereal crops, particularly rice, nuts, and corn. It was reported that AFB1 is responsible for multiple fetal aflatoxicosis outbreaks worldwide [105]. Immunoassays for AFB1 detection have received great attention. For example, a MnO₂ nanoflake-TMB system was applied for AFB1 colorimetric determination, which could accurately detect AFB1 concentration as low as 6.5 pg/mL with a linear range of 0.05 ~ 150 ng/mL at room temperature [106]. In addition, a peroxidase mimic of Co-porphyrin/Pt/rGO nanostructure (PtNP/CoTPP/rGO) based electrochromic immunosensor was developed to improve the detection sensitivity (**Figure 2.5. B(a)**). The conjugated PtNP/CoTPP/rGO is synthesized based on the π - π bond stacking interactions between GO nanosheet and Co-porphyrin. The redox reaction between the GO layer and H₂PtCl₆ provides Pt NPs at the rGO nanosheet. This nanocomplex was used for immobilizing anti-AFB1 antibodies and catalyzing redox reaction in the TMB-H₂O₂ system, which then amplifies electric signals by determining the change in color intensity. Consequently, an apparent increase in current was revealed in 25 min for AFB1 concentrations from 0.005 to 5 ng/mL. The LOD of this NB is about 1.5 pg/mL, which is much lower than the LOD Afforded by several commercial AFB1 kits (Quicking Biotech: 100 ppt; MyBioSource: 250 ppt) [107]. Data collected from testing peanuts

used as real samples demonstrated that this method would be a potential tool for detecting AFB1 for food safety monitoring.

Various nanozyme-based colorimetric immunoassays that are used for analyzing a variety of foodborne pathogens and microbial secondary metabolites in foodstuffs are summarized in **Table 2.2**.

Table 2.2. Applications of nanozymes for colorimetric detection (unless noted otherwise) and quantification of foodborne pathogens and microbial metabolites

Contaminant	Nanozyme system	Enzyme mimicked	LOD (CFU/mL) [§]	Linear range (CFU/mL) [§]	Sample matrix	Ref.
<i>C. jejuni</i>	Au@Pt NP	Peroxidase	10	10 ~ 10 ⁶	Milk sample	[108]
<i>E. sakazakii</i>	Fe ₃ O ₄ magnetic nanoparticles	Peroxidase	2	10 ~ 10 ⁵	Infant powder	[109]
<i>E. coli</i> , O157:H7	hemin-concanavalin A hybrid nanoflowers	Peroxidase	4.1	10 ~ 10 ⁶	Milk	[98]
	Pt-Au nanoparticle	Peroxidase	10 ²	10 ² ~ 10 ⁵	—	[99]
	Pd-Pt nanoparticle	Peroxidase	0.87*10 ²	10 ² ~ 10 ⁶	Milk	[100]
<i>E. coli</i> , O157:H7	Dopamine-Fe ₃ O ₄ nanoparticle	Peroxidase	10 ²	0~10 ⁴	—	[110]
<i>L. monocytogenes</i>	Fe ₃ O ₄ nanoparticles	Peroxidase	5.4*10 ³	5.4*10 ³ ~ 10 ⁸	Milk	[102]
	BSA-MnO ₂ nanoparticle	Oxidase	10	10 ~ 10 ⁶	Pork	[103]
	Au nanoparticles core/Ag nanocluster	Oxidase	10	10 ~ 10 ⁶	Pork	[111]
<i>P. aeruginosa</i>	Au nanoparticle	*Peroxidase	60	60 ~6*10 ⁷	—	[112]
<i>V. cholerae</i>	Fe ₃ O ₄ magnetic nanoparticles-polysaccharides	Peroxidase	10 ³	—	Drinking water and tap water	[113]
<i>V. parahaemolyticus</i>	Magnetic Fe ₃ O ₄ -MnO ₂ nanoparticle	Oxidase	10	10 ~10 ⁵	Oyster	[114]
Aflatoxin B1	MnO ₂ nanoflake	Oxidase	6.5 pg/mL	0.05~150 ng/mL	Peanut	[106]
	Co-Porphyrin/Pt/rGO Nanostructures	*Peroxidase	1.5 pg/mL	0.005 ~ 5 ng/mL	Peanut	[107]
Microcystin-LR	Cu(OH) ₂ nanocage	Peroxidase	6 ng/mL	0.007 ~75µg/mL	Lake and tap water	[115]
Ochratoxin A	MnO ₂ nanosheet	Oxidase	0.069 nM	1.25 ~250 nM	Grape juice	[116]
	MnCo ₂ O ₄ submicrosphere	Oxidase	0.08 ng/mL	0.1 ~ 10 ng/mL	Maize	[117]
Patulin	Ag NPs@Zn-MOF	#Peroxidase	0.06 µM	0.1 ~10 µM	Apple juice	[118]

<i>Staphylococcal enterotoxin B</i>	Au nanocluster-chitosan membrane	Peroxidase	1.0 pg/mL	1 ~ 700 ng/mL	Corn, flour and rice	[119]
Zearalenone	Au nanoparticle	Peroxidase	10 ng/mL	10 ~ 250ng/mL	Corn and corn oil	[120]

[§] CFU/mL unless noted otherwise; # Fluorometry detection; *electrochemical detection

2.3.3. Detection of pesticide residues in food

Residues of organophosphorus pesticides (OPs) in foodstuffs are frequently associated with chronic risk factors for cardiovascular diseases, cancers, nerve system damage, and reproduction system disruption [104]. OPs primarily remain in fresh fruits, vegetables, grains, and fish. Several NB are being developed for detecting OPs and other pesticide residues in food.

Methyl-paraoxon (MP), a type of OPs, could be detected by different NBs. Zhou et al. prepared an NB using polyacrylic acid-coated CeO₂ NPs (PAA-CeO₂ NPs) for detecting MP by taking advantage of MP's inhibitory effects on enzymatic catalysis. This involves the inhibition capability of MP against acetylthiocholine (ATCh) catalysis by acetylcholinesterase enzyme (AChE) in pH 8 buffer condition [121]. This NB was suitable for detecting MP concentrations ranging from 100 ~1000 ppb with an LOD of 26.73 ppb at acidic conditions and room temperature. Further, Wei et al. [122] prepared a nanoceria-based biosensor (NcRB) to show that nanoceria could directly bio-catalyze MP molecules to generate yellowish para-nitrophenol (p-NP) in the presence of H₂O₂ (**Figure 2.6. A**). By combining with the dual mode-sensing platform technique (DMSP-NcRB), color signals generated from DMSP-NcRB-MP-H₂O₂ system could be captured simultaneously by the platform composed of the smartphone-based and UV-spectroscopic method. By this dual way, the color intensity increased linearly from 0.42 ~ 42 μmol/L and the LOD of this approach was 0.42 μmol/L at alkaline condition. Employing this approach in real sample analysis, they demonstrated the feasibility of real-time and detection of MP using DMSP-NcRB.

Detection of other OPs, such as diazinon, glyphosate, and ethoprophos have also been reported using NBs [123-125]. For diazinon detection, Fe₃O₄ NPs @ZIF-8 nanohybrid, a peroxidase mimic, was used. This nanohybrid was synthesized by encapsulating Fe₃O₄ NPs in the cavities of porous ZIF-8, which is sensitive to recognize H₂O₂ that is an intermediate of a series of enzymatic

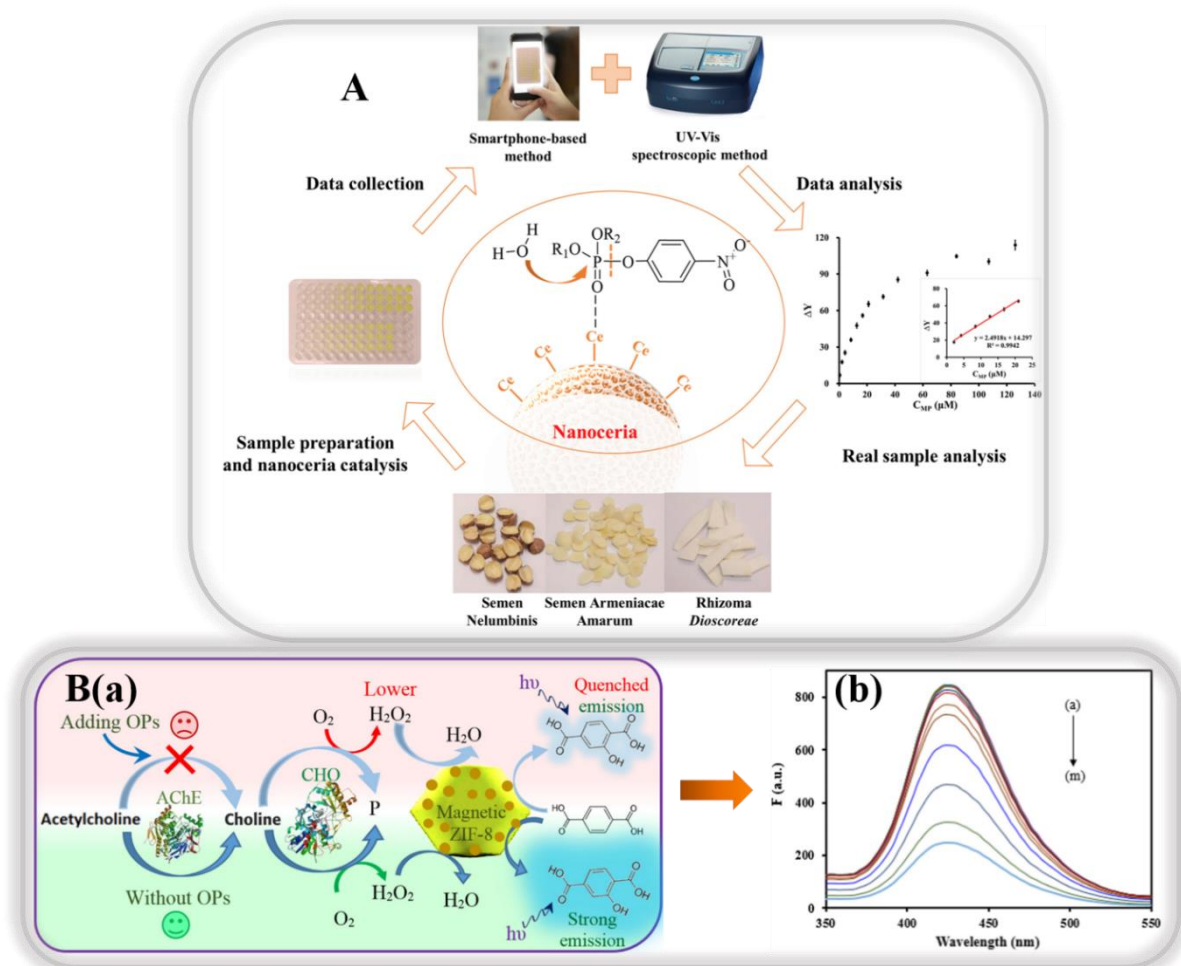


Figure 2.6. A. Illustration of nanoceria-based biosensing with dual mode-sensing platform technique, Adapted with permission from [123], **B (a)** Schematic of enzymatic competitive assay for the detection of organophosphates (OP), **(b)** fluorescent spectra for OP detection, (a-m: 0.5, 1, 2, 5, 10, 20, 50, 100, 200, 300, 400 and 500 nM, respectively), adapted with permission from [124]

reactions (**Figure 2.6. B(a)**) [123]. Whereas, diazinon would irreversibly inhibit the AChE enzymatic activity, which causes H_2O_2 molecules failure to release and TMBox to generate, thus significantly affecting the signal intensity. Consequently, as per the UV absorbance curve in **Figure**

2.6. B(b), increased diazinon concentration proportionally reduces the signal intensity in the range of 0.5~500 nM with an LOD of 0.2 nM.

A CuO/multi-walled carbon nanotube nanocomposite-based NB (CuO/MWCNT NB) was fabricated to fluorometrically analyze glyphosate in neutral pH aqueous solutions [124]. In this NB, CuO/MWCNT served as peroxidase for catalyzing the redox reaction of the H₂O₂– Amplex Red system, yielding the reddish resorufin. However, glyphosate protects this nanocomposite from contacting with the H₂O₂– Amplex Red system thus achieving to control the color intensity of the solution. As a result, CuO/MWCNT NB was able to detect glyphosate concentration in the range of 0.002~0.01 ppm with an LOD of 0.67 ppb.

2.3.4. Detection of other food contaminants

The detection of other food contaminants has also been reported using NBs. These contaminants include pharmaceutical drug residues and illegal food additives. Kanamycin, usually used in veterinary medicine, is found to associate with hearing problems, kidney toxicity, and allergic reactions in humans [126]. An "on/off" colorimetric assay composed of AuNPs was developed for kanamycin identification with relatively high selectivity [127]. As shown in **Figure 2.7. A**, aptamer (Ky2) prevents the AuNPs surface from coming in contact with the TMB-H₂O₂ system in the absence of kanamycin, inhibiting the enzymatic reaction. Initially, the Ky2 aptamer is designed to shield the AuNPs surface, suppressing the Au NPs to alter TMB in the H₂O₂ solution. The aptamer is then attracted by the addition kanamycin, resulting it to leave the surface of AuNPs to specifically coordinate with kanamycin. Due to the absence of Ky2, exposed Au species begins to catalyze TMB oxidation in the presence of H₂O₂, showing blue color in the solution. **Figure 2.7. C** indicates that saturation of AuNPs activity would appear after adding 100 nM of kanamycin.

This approach provides linear range for kanamycin detection from 1 ~ 100 nM with LOD of 1.49 nM.

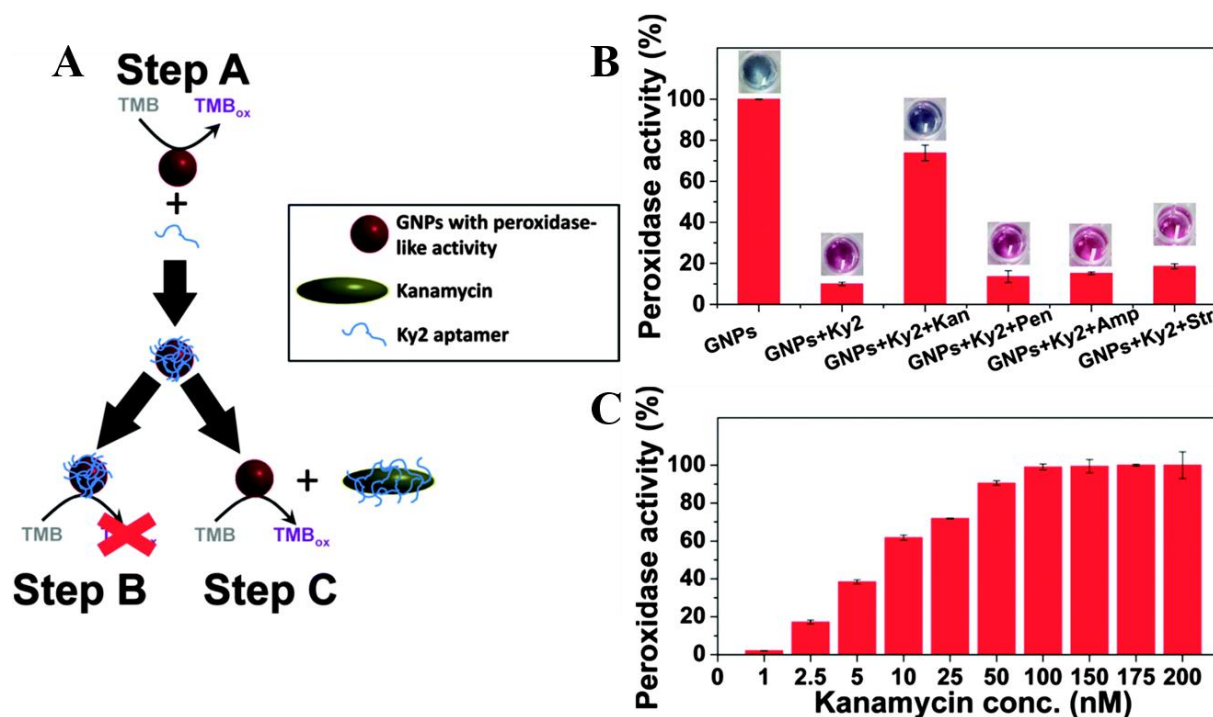


Figure 2.7. **A.** Schematic illustration of color turn on/off for kanamycin detection; **B.** Selectivity test based on this immunoassay for different antibiotics detection; **C.** Relationship between the peroxidase-like activity of gold nanoparticle-Ky2 aptamer and concentration of kanamycin, adapted with permission from [128]

Additionally, melamine was added illegally into dairy products for increasing the apparent nitrogen level which is typically used for indicating the protein level in dairy products, due to its relatively high nitrogen content [129]. It is proved to significantly exaggerate the intrinsic peroxidase property of AuNPs during the catalysis of the H₂O₂-TMB system [128]. By utilization

of the color intensity enhancement of the H₂O₂-TMB system in the presence of melamine, linear response in UV-vis spectra was from 0.001 ~0.8 μM with LOD of 0.2 nM.

2.4. Summary and future perspectives

The discovery of nanozymes has established an impressive bridge connecting nanomaterials and biological enzymes. This has facilitated great strides in tailoring enzyme mimics into nanoscale and at the same time, provided an alternative way for mediating different biological events.

Up to now, most nanozyme research is focused on oxidoreductase-type nanomaterials (e.g. oxidase, peroxidase, catalase, and superoxide dismutase). Despite all of them showing highly efficient catalytic rate, peroxidase-type, and oxidase-type are still the two most predominant nanozymes in the sensing area, due to their slightly more efficiency enzymatic catalysis performance than natural enzymes. Additionally, most NBs would be advantageous in their faster, more reliable, and rigidity for food safety analysis, compared to the traditional enzyme (Shown in **Appendix II, Table S2.1.**), ascribed to their inherent nanomaterial properties. Therefore, in this review, we have highlighted various practical applications of nanozymes, especially in food systems.

The exciting future for nanozymes is nonetheless beset with some challenges. The nanozyme as an emerging enzyme mimic has lower densities of active sites, which decreases its enzymatic activity in catalytic reactions as well as lower the turnover number for peroxidase substrate conversion [130]. Additionally, one difficulty is to identify the accurate active site and thus for investigating the origin of catalytic activity, due to heterogeneous elemental composition and facet nanoarchitecture exposed by several nanozymes and their synthesis. Therefore, optimization of the

nanostructure of nanozymes and their sizes play essential roles in catalytic activity precise analysis before any further exploration and research on the nanozyme catalytic capability.

Apparently, with the exception of detecting ions, most nanozymes lack the ability of specific recognition, as traditional enzymes are, leading them impossible to analyze macromolecules and even organelles individually. In other words, if nanozymes would be adopted to fabricate biosensors for macromolecules or organelles detection, it is necessary to join other biomolecules which are capable to specifically identifying those targets (e.g. antibodies or natural enzymes). Hence, the next step after nanozyme nanostructure optimization is to mimic enzyme structures to improve the nanozyme's specificity, which would be a promising way to simplify the NB fabrication procedure and largely decrease cost.

Most of the currently developed NBs highly rely on the colorimetric assay for food safety monitoring. While this bodes well for simple detection, colorimetric detection has its limitation for many foods that can mask visual signals making the detection difficult and even inaccurate. Food materials are complex systems, which contain considerable interfering chemicals. Therefore, different signaling assays combination, such as dual colorimetric-digital approaches, lateral flow strip utilization, etc., should be investigated to establish suitable NBs for each step of the food supply chain with a facile, rapid, and economical detection system to ensure food safety. This should be the future direction for further developing nanozymes suitable for biosensing in the food industry.

Besides applying in biosensing in the food safety area, nanozyme is also a promising enzyme mimic to be adopted in biosensors for other areas of determination, for example, hormone signal transduction system in cells, enzyme catalytic activity, DNA transcription, and even nerve signal transmission. However, before achieving those goals in the future, researchers should pay more

attention to the nanozyme itself biosafety and bioavailability. Despite various available research on nanozyme properties and applications, compared to traditional enzymes, those studies are still rather limited. Therefore, more investigations in the future should be done to solve issues and explore more applications of nanozyme.

2.5. Appendix: Chapter II.

Table S2.1. Traditional enzyme application in biosensor for food analysis

Contaminant	Traditional enzyme					Nanozyme				
	Name	LOD	Operational stability	Time to response	Ref.	Name	LOD	Operational stability	Time to response	Ref.
Hg ²⁺	Glucose oxidase	1 ng/mL	pH 6.0; Room temperature	20 min for incubation	[131]	Citrate/Pt nanoparticle	8.5 pM	Room temperature	10 min for response	[75]
CN ⁻	Tyrosinase	0.1 nM	pH 6.0; Room temperature	>10 min for incubation	[132]	Cobalt hydroxide/oxide-modified GO	22 nM	pH 3~11; Temperature range (20 °C ~ 100 °C)	2h for response	[79]
<i>Escherichia coli</i> , O157	Peroxidase	10 ³ CFU/mL	pH 7.4; Room temperature	~24 h	[133]	hemin-concanavalin A hybrid nanoflowers	4.1 CFU/mL	pH: 6.5; Temperature of 25 °C	90 min for incubation	[98]
Aflatoxin B1	AChE	2 ng/mL	pH 7.4; Room temperature	~ 10 min	[134]	Co-Porphyrin/Pt/rGO Nanostructures	1.5 pg/mL	pH 7.0; Room temperature	~ 25 min	[107]
Methyl-paraoxon	AChE	500 nM	pH 7.5; Room temperature	20 min for incubation	[135]	Nanoceria	0.42 μM	pH 10; Temperature range (4 °C ~ 60 °C)	<1 min for incubation	[122]
Glyphosate	horseradish peroxidase	1.7 μg/L	pH 6.1; Temperature of 22 °C	20 min for incubation	[136]	CuO/MWCNT	0.67 ppb	pH 7.2; Room temperature	120 min for incubation	[124]

2.6. References

- [1] C. Mateo, J.M. Palomo, G. Fernandez-Lorente, J.M. Guisan, R. Fernandez-Lafuente, Improvement of enzyme activity, stability and selectivity via immobilization techniques, *Enzyme and microbial technology* 40(6) (2007) 1451-1463.
- [2] S. Nisha, S.A. Karthick, N. Gobi, A review on methods, application and properties of immobilized enzyme, *Chemical Science Review and Letters* 1(3) (2012) 148-155.
- [3] M. Misson, H. Zhang, B. Jin, Nanobiocatalyst advancements and bioprocessing applications, *Journal of the Royal Society Interface* 12(102) (2015) 20140891.
- [4] E.M.M. Del Valle, Cyclodextrins and their uses: a review, *Process biochemistry* 39(9) (2004) 1033-1046.
- [5] G. Wulff, Enzyme-like catalysis by molecularly imprinted polymers, *Chemical reviews* 102(1) (2002) 1-28.
- [6] Z. Dong, Q. Luo, J. Liu, Artificial enzymes based on supramolecular scaffolds, *Chemical Society Reviews* 41(23) (2012) 7890-7908.
- [7] J. Kofoed, J.-L. Reymond, Dendrimers as artificial enzymes, *Current opinion in chemical biology* 9(6) (2005) 656-664.
- [8] L. Gao, J. Zhuang, L. Nie, J. Zhang, Y. Zhang, N. Gu, T. Wang, J. Feng, D. Yang, S. Perrett, Intrinsic peroxidase-like activity of ferromagnetic nanoparticles, *Nature nanotechnology* 2(9) (2007) 577.
- [9] Y. Zhou, B. Liu, R. Yang, J. Liu, Filling in the gaps between nanozymes and enzymes: challenges and opportunities, *Bioconjugate chemistry* 28(12) (2017) 2903-2909.
- [10] H. Wei, E. Wang, Nanomaterials with enzyme-like characteristics (nanozymes): next-generation artificial enzymes, *Chemical Society Reviews* 42(14) (2013) 6060-6093.
- [11] M.K. Masud, J. Kim, M.M. Billah, K. Wood, M.J.A. Shiddiky, N.-T. Nguyen, R.K. Parsapur, Y.V. Kaneti, A.A. Alshehri, Y.G. Alghamidi, Nanoarchitected peroxidase-mimetic nanozymes: mesoporous nanocrystalline α - or γ -iron oxide?, *Journal of Materials Chemistry B* (2019).
- [12] H. Wang, K. Wan, X. Shi, Recent advances in nanozyme research, *Advanced Materials* (2018) 1805368.
- [13] J. Wu, X. Wang, Q. Wang, Z. Lou, S. Li, Y. Zhu, L. Qin, H. Wei, Nanomaterials with enzyme-like characteristics (nanozymes): next-generation artificial enzymes (II), *Chemical Society Reviews* 48(4) (2019) 1004-1076.
- [14] V. Singh, V. Kumar, S. Kashyap, A.V. Singh, V. Kishore, M. Sitti, P.S. Saxena, A. Srivastava, Graphene oxide synergistically enhances antibiotic efficacy in vancomycin-resistant staphylococcus aureus, *ACS Applied Bio Materials* 2(3) (2019) 1148-1157.
- [15] K. Fan, J. Xi, L. Fan, P. Wang, C. Zhu, Y. Tang, X. Xu, M. Liang, B. Jiang, X. Yan, In vivo guiding nitrogen-doped carbon nanozyme for tumor catalytic therapy, *Nature communications* 9(1) (2018) 1440.
- [16] Q. Wang, H. Wei, Z. Zhang, E. Wang, S. Dong, Nanozyme: An emerging alternative to natural enzyme for biosensing and immunoassay, *TrAC Trends in Analytical Chemistry* 105 (2018) 218-224.
- [17] X. Zhang, D. Wu, X. Zhou, Y. Yu, J. Liu, N. Hu, H. Wang, G. Li, Y. Wu, Recent progress on the construction of nanozymes-based biosensors and their applications to food safety assay, *TrAC Trends in Analytical Chemistry* (2019) 115668.
- [18] Y. Huang, J. Ren, X. Qu, Nanozymes: classification, catalytic mechanisms, activity regulation, and applications, *Chemical reviews* 119(6) (2019) 4357-4412.

- [19] C. Zheng, A.-X. Zheng, B. Liu, X.-L. Zhang, Y. He, J. Li, H.-H. Yang, G. Chen, One-pot synthesized DNA-templated Ag/Pt bimetallic nanoclusters as peroxidase mimics for colorimetric detection of thrombin, *Chemical Communications* 50(86) (2014) 13103-13106.
- [20] S. Cai, Q. Han, C. Qi, Z. Lian, X. Jia, R. Yang, C. Wang, Pt 74 Ag 26 nanoparticle-decorated ultrathin MoS₂ nanosheets as novel peroxidase mimics for highly selective colorimetric detection of H₂O₂ and glucose, *Nanoscale* 8(6) (2016) 3685-3693.
- [21] X. Wang, Y. Hu, H. Wei, Nanozymes in bionanotechnology: from sensing to therapeutics and beyond, *Inorganic Chemistry Frontiers* 3(1) (2016) 41-60.
- [22] B. Garg, T. Bisht, Carbon nanodots as peroxidase nanozymes for biosensing, *Molecules* 21(12) (2016) 1653.
- [23] H. Sun, Y. Zhou, J. Ren, X. Qu, Carbon nanozymes: enzymatic properties, catalytic mechanism, and applications, *Angewandte Chemie International Edition* 57(30) (2018) 9224-9237.
- [24] M. Shamsipur, A. Safavi, Z. Mohammadpour, Indirect colorimetric detection of glutathione based on its radical restoration ability using carbon nanodots as nanozymes, *Sensors and Actuators B: Chemical* 199 (2014) 463-469.
- [25] S. Zhu, X.-E. Zhao, J. You, G. Xu, H. Wang, Carboxylic-group-functionalized single-walled carbon nanohorns as peroxidase mimetics and their application to glucose detection, *Analyst* 140(18) (2015) 6398-6403.
- [26] X. Wang, W. Guo, Y. Hu, J. Wu, H. Wei, Carbon-Based Nanomaterials for Nanozymes, *Nanozymes: Next Wave of Artificial Enzymes*, Springer 2016, pp. 7-29.
- [27] Y. Song, K. Qu, C. Zhao, J. Ren, X. Qu, Graphene oxide: intrinsic peroxidase catalytic activity and its application to glucose detection, *Advanced Materials* 22(19) (2010) 2206-2210.
- [28] D.J. Porter, H.J. Bright, The mechanism of oxidation of nitroalkanes by horseradish peroxidase, *Journal of Biological Chemistry* 258(16) (1983) 9913-9924.
- [29] J.A. Nicell, Kinetics of horseradish peroxidase-catalysed polymerization and precipitation of aqueous 4-chlorophenol, *Journal of Chemical Technology & Biotechnology: International Research in Process, Environmental AND Clean Technology* 60(2) (1994) 203-215.
- [30] G.-L. Wang, X. Xu, X. Wu, G. Cao, Y. Dong, Z. Li, Visible-light-stimulated enzymelike activity of graphene oxide and its application for facile glucose sensing, *The Journal of Physical Chemistry C* 118(48) (2014) 28109-28117.
- [31] Y. Hu, X.J. Gao, Y. Zhu, F. Muhammad, S. Tan, W. Cao, S. Lin, Z. Jin, X. Gao, H. Wei, Nitrogen-doped carbon nanomaterials as highly active and specific peroxidase mimics, *Chemistry of Materials* 30(18) (2018) 6431-6439.
- [32] J. Xi, C. Xie, Y. Zhang, L. Wang, J. Xiao, X. Duan, J. Ren, F. Xiao, S. Wang, Pd nanoparticles decorated N-doped graphene quantum dots@ N-doped carbon hollow nanospheres with high electrochemical sensing performance in cancer detection, *ACS applied materials & interfaces* 8(34) (2016) 22563-22573.
- [33] Z. Zhang, X. Wang, X. Yang, A sensitive choline biosensor using Fe₃O₄ magnetic nanoparticles as peroxidase mimics, *Analyst* 136(23) (2011) 4960-4965.
- [34] N. Wang, L. Zhu, D. Wang, M. Wang, Z. Lin, H. Tang, Sono-assisted preparation of highly-efficient peroxidase-like Fe₃O₄ magnetic nanoparticles for catalytic removal of organic pollutants with H₂O₂, *Ultrasonics Sonochemistry* 17(3) (2010) 526-533.
- [35] S. Wang, A comparative study of Fenton and Fenton-like reaction kinetics in decolourisation of wastewater, *Dyes and Pigments* 76(3) (2008) 714-720.

- [36] X.-Q. Zhang, S.-W. Gong, Y. Zhang, T. Yang, C.-Y. Wang, N. Gu, Prussian blue modified iron oxide magnetic nanoparticles and their high peroxidase-like activity, *Journal of Materials Chemistry* 20(24) (2010) 5110-5116.
- [37] N. Goswami, A. Giri, M.S. Bootharaju, P.L. Xavier, T. Pradeep, S.K. Pal, Copper quantum clusters in protein matrix: potential sensor of Pb²⁺ ion, *Analytical chemistry* 83(24) (2011) 9676-9680.
- [38] L. Hu, Y. Yuan, L. Zhang, J. Zhao, S. Majeed, G. Xu, Copper nanoclusters as peroxidase mimetics and their applications to H₂O₂ and glucose detection, *Analytica chimica acta* 762 (2013) 83-86.
- [39] S.R. Batten, N.R. Champness, X.-M. Chen, J. Garcia-Martinez, S. Kitagawa, L. Öhrström, M. O'Keefe, M.P. Suh, J. Reedijk, Terminology of metal-organic frameworks and coordination polymers (IUPAC Recommendations 2013), *Pure and Applied Chemistry* 85(8) (2013) 1715-1724.
- [40] I. Nath, J. Chakraborty, F. Verpoort, Metal organic frameworks mimicking natural enzymes: a structural and functional analogy, *Chemical Society Reviews* 45(15) (2016) 4127-4170.
- [41] Y.L. Liu, X.J. Zhao, X.X. Yang, Y.F. Li, A nanosized metal-organic framework of Fe-MIL-88NH₂ as a novel peroxidase mimic used for colorimetric detection of glucose, *Analyst* 138(16) (2013) 4526-4531.
- [42] W. Zang, G. Li, L. Wang, X. Zhang, Catalytic hydrogenation by noble-metal nanocrystals with well-defined facets: a review, *Catalysis Science & Technology* 5(5) (2015) 2532-2553.
- [43] B. Liu, J. Liu, Surface modification of nanozymes, *Nano Research* 10(4) (2017) 1125-1148.
- [44] X.-X. Wang, Q. Wu, Z. Shan, Q.-M. Huang, BSA-stabilized Au clusters as peroxidase mimetics for use in xanthine detection, *Biosensors and Bioelectronics* 26(8) (2011) 3614-3619.
- [45] M. Zhao, J. Huang, Y. Zhou, X. Pan, H. He, Z. Ye, X. Pan, Controlled synthesis of spinel ZnFe₂O₄ decorated ZnO heterostructures as peroxidase mimetics for enhanced colorimetric biosensing, *Chemical Communications* 49(69) (2013) 7656-7658.
- [46] H. Liu, C. Gu, W. Xiong, M. Zhang, A sensitive hydrogen peroxide biosensor using ultra-small CuInS₂ nanocrystals as peroxidase mimics, *Sensors and Actuators B: Chemical* 209 (2015) 670-676.
- [47] B. Wang, P. Ju, D. Zhang, X. Han, L. Zheng, X. Yin, C. Sun, Colorimetric detection of H₂O₂ using flower-like Fe₂(MoO₄)₃ microparticles as a peroxidase mimic, *Microchimica Acta* 183(11) (2016) 3025-3033.
- [48] V. Figueroa-Espi, A. Alvarez-Paneque, M. Torrens, A.J. Otero-Gonzalez, E. Reguera, Conjugation of manganese ferrite nanoparticles to an anti Sticholysin monoclonal antibody and conjugate applications, *Colloids and Surfaces A: Physicochemical and Engineering Aspects* 387(1-3) (2011) 118-124.
- [49] D. Bhattacharya, A. Baksi, I. Banerjee, R. Ananthkrishnan, T.K. Maiti, P. Pramanik, Development of phosphonate modified Fe_{1-x}MnxFe₂O₄ mixed ferrite nanoparticles: novel peroxidase mimetics in enzyme linked immunosorbent assay, *Talanta* 86 (2011) 337-348.
- [50] Y. Zhang, X. Pang, D. Wu, H. Ma, Z. Yan, J. Zhang, B. Du, Q. Wei, A robust electrochemiluminescence immunoassay for carcinoembryonic antigen detection based on a microtiter plate as a bridge and Au@Pd nanorods as a peroxidase mimic, *Analyst* 141(1) (2016) 337-345.
- [51] W. He, X. Wu, J. Liu, X. Hu, K. Zhang, S. Hou, W. Zhou, S. Xie, Design of AgM bimetallic alloy nanostructures (M= Au, Pd, Pt) with tunable morphology and peroxidase-like activity, *Chemistry of Materials* 22(9) (2010) 2988-2994.

- [52] M. Comotti, C. Della Pina, R. Matarrese, M. Rossi, The catalytic activity of “naked” gold particles, *Angewandte Chemie International Edition* 43(43) (2004) 5812-5815.
- [53] D. Jiang, D. Ni, Z.T. Rosenkrans, P. Huang, X. Yan, W. Cai, Nanozyme: new horizons for responsive biomedical applications, *Chemical Society Reviews* (2019).
- [54] M. Liang, X. Yan, Nanozymes: From New Concepts, Mechanisms, and Standards to Applications, *Accounts of chemical research* 52(8) (2019) 2190-2200.
- [55] H. Cheng, S. Lin, F. Muhammad, Y.-W. Lin, H. Wei, Rationally modulate the oxidase-like activity of nanoceria for self-regulated bioassays, *Acs Sensors* 1(11) (2016) 1336-1343.
- [56] L. Huang, W. Zhang, K. Chen, W. Zhu, X. Liu, R. Wang, X. Zhang, N. Hu, Y. Suo, J. Wang, Facet-selective response of trigger molecule to CeO₂ {1 1 0} for up-regulating oxidase-like activity, *Chemical Engineering Journal* 330 (2017) 746-752.
- [57] Z. Wang, Y. Zhang, E. Ju, Z. Liu, F. Cao, Z. Chen, J. Ren, X. Qu, Biomimetic nanoflowers by self-assembly of nanozymes to induce intracellular oxidative damage against hypoxic tumors, *Nature communications* 9(1) (2018) 3334.
- [58] S. Cai, C. Qi, Y. Li, Q. Han, R. Yang, C. Wang, PtCo bimetallic nanoparticles with high oxidase-like catalytic activity and their applications for magnetic-enhanced colorimetric biosensing, *Journal of Materials Chemistry B* 4(10) (2016) 1869-1877.
- [59] D. Duan, K. Fan, D. Zhang, S. Tan, M. Liang, Y. Liu, J. Zhang, P. Zhang, W. Liu, X. Qiu, Nanozyme-strip for rapid local diagnosis of Ebola, *Biosensors and Bioelectronics* 74 (2015) 134-141.
- [60] X. Wang, L. Qin, M. Zhou, Z. Lou, H. Wei, Nanozyme sensor arrays for detecting versatile Analytes from small molecules to proteins and cells, *Analytical chemistry* 90(19) (2018) 11696-11702.
- [61] J. Sun, C. Li, Y. Qi, S. Guo, X. Liang, Optimizing colorimetric assay based on V₂O₅ nanozymes for sensitive detection of H₂O₂ and glucose, *Sensors* 16(4) (2016) 584.
- [62] Y. Chang, Z. Zhang, J. Hao, W. Yang, J. Tang, BSA-stabilized Au clusters as peroxidase mimetic for colorimetric detection of Ag⁺, *Sensors and Actuators B: Chemical* 232 (2016) 692-697.
- [63] W. Zhang, X. Niu, S. Meng, X. Li, Y. He, J. Pan, F. Qiu, H. Zhao, M. Lan, Histidine-mediated tunable peroxidase-like activity of nanosized Pd for photometric sensing of Ag⁺, *Sensors and Actuators B: Chemical* 273 (2018) 400-407.
- [64] Z. Gao, G.G. Liu, H. Ye, R. Rauschendorfer, D. Tang, X. Xia, Facile colorimetric detection of silver ions with picomolar sensitivity, *Analytical chemistry* 89(6) (2017) 3622-3629.
- [65] C.-r. Li, J. Hai, L. Fan, S.-l. Li, B.-d. Wang, Z.-y. Yang, Amplified colorimetric detection of Ag⁺ based on Ag⁺-triggered peroxidase-like catalytic activity of ZIF-8/GO nanosheets, *Sensors and Actuators B: Chemical* 284 (2019) 213-219.
- [66] W.U. Liang-Liang, Q. Zhi-Juan, X.I.E. Zheng-Jun, Y.-Y. Zhang, P. Chi-Fang, Colorimetric Detection of Copper Ions Based on Surface Modification of Silver/Platinum Cluster Nanozyme, *Chinese Journal of Analytical Chemistry* 45(4) (2017) 471-476.
- [67] Y. Liu, D. Ding, Y. Zhen, R. Guo, Amino acid-mediated ‘turn-off/turn-on’ nanozyme activity of gold nanoclusters for sensitive and selective detection of copper ions and histidine, *Biosensors and Bioelectronics* 92 (2017) 140-146.
- [68] F. Honarasa, F. Peyravi, H. Amirian, C-dots/Mn₃O₄ nanocomposite as an oxidase nanozyme for colorimetric determination of ferrous ion, *Journal of the Iranian Chemical Society* (2019) 1-6.

- [69] Y. Wang, J. Hu, Q. Zhuang, Y. Ni, Enhancing sensitivity and selectivity in a label-free colorimetric sensor for detection of iron (II) ions with luminescent molybdenum disulfide nanosheet-based peroxidase mimetics, *Biosensors and Bioelectronics* 80 (2016) 111-117.
- [70] J. Hu, Q. Zhuang, Y. Wang, Y. Ni, Label-free fluorescent catalytic biosensor for highly sensitive and selective detection of the ferrous ion in water samples using a layered molybdenum disulfide nanozyme coupled with an advanced chemometric model, *Analyst* 141(5) (2016) 1822-1829.
- [71] S. Zhang, H. Li, Z. Wang, J. Liu, H. Zhang, B. Wang, Z. Yang, A strongly coupled Au/Fe₃O₄/GO hybrid material with enhanced nanozyme activity for highly sensitive colorimetric detection, and rapid and efficient removal of Hg²⁺ in aqueous solutions, *Nanoscale* 7(18) (2015) 8495-8502.
- [72] L. Zhi, W. Zuo, F. Chen, B. Wang, 3D MoS₂ composition aerogels as chemosensors and adsorbents for colorimetric detection and high-capacity adsorption of Hg²⁺, *ACS Sustainable Chemistry & Engineering* 4(6) (2016) 3398-3408.
- [73] H. Cao, J. Xiao, H. Liu, Enhanced oxidase-like activity of selenium nanoparticles stabilized by chitosan and application in a facile colorimetric assay for mercury (II), *Biochemical Engineering Journal* 152 (2019) 107384.
- [74] Z. Mohammadpour, A. Safavi, M. Shamsipur, A new label free colorimetric chemosensor for detection of mercury ion with tunable dynamic range using carbon nanodots as enzyme mimics, *Chemical Engineering Journal* 255 (2014) 1-7.
- [75] G.-W. Wu, S.-B. He, H.-P. Peng, H.-H. Deng, A.-L. Liu, X.-H. Lin, X.-H. Xia, W. Chen, Citrate-capped platinum nanoparticle as a smart probe for ultrasensitive mercury sensing, *Analytical chemistry* 86(21) (2014) 10955-10960.
- [76] J. Wang, J. Wang, P. Zhou, H. Tao, X. Wang, Y. Wu, Oligonucleotide-induced regulation of the oxidase-mimicking activity of octahedral Mn₃O₄ nanoparticles for colorimetric detection of heavy metals, *Microchimica Acta* 187(2) (2020) 99.
- [77] S. Zhang, D. Zhang, X. Zhang, D. Shang, Z. Xue, D. Shan, X. Lu, Ultratrace naked-eye colorimetric detection of Hg²⁺ in wastewater and serum utilizing mercury-stimulated peroxidase mimetic activity of reduced graphene oxide-PEI-Pd nanohybrids, *Analytical chemistry* 89(6) (2017) 3538-3544.
- [78] H. Liao, G. Liu, Y. Liu, R. Li, W. Fu, L. Hu, Aggregation-induced accelerating peroxidase-like activity of gold nanoclusters and their applications for colorimetric Pb²⁺ detection, *Chemical Communications* 53(73) (2017) 10160-10163.
- [79] C.-W. Lien, B. Unnikrishnan, S.G. Harroun, C.-M. Wang, J.-Y. Chang, H.-T. Chang, C.-C. Huang, Visual detection of cyanide ions by membrane-based nanozyme assay, *Biosensors and Bioelectronics* 102 (2018) 510-517.
- [80] D. Li, S.L. Garisto, P.-J.J. Huang, J. Yang, B. Liu, J. Liu, Fluorescent detection of fluoride by CeO₂ nanozyme oxidation of Amplex red, *Inorganic Chemistry Communications* 106 (2019) 38-42.
- [81] B. Liu, Z. Huang, J. Liu, Boosting the oxidase mimicking activity of nanoceria by fluoride capping: rivaling protein enzymes and ultrasensitive F⁻ detection, *Nanoscale* 8(28) (2016) 13562-13567.
- [82] L. Liu, J. Du, W.-e. Liu, Y. Guo, G. Wu, W. Qi, X. Lu, Enhanced His@ AuNCs oxidase-like activity by reduced graphene oxide and its application for colorimetric and electrochemical detection of nitrite, *Analytical and bioanalytical chemistry* 411(10) (2019) 2189-2200.

- [83] Y. Liu, Y. Zheng, D. Ding, R. Guo, Switching peroxidase-mimic activity of protein stabilized platinum nanozymes by sulfide ions: substrate dependence, mechanism, and detection, *Langmuir* 33(48) (2017) 13811-13820.
- [84] H.-H. Deng, S.-H. Weng, S.-L. Huang, L.-N. Zhang, A.-L. Liu, X.-H. Lin, W. Chen, Colorimetric detection of sulfide based on target-induced shielding against the peroxidase-like activity of gold nanoparticles, *Analytica chimica acta* 852 (2014) 218-222.
- [85] S. Singh, K. Mitra, A. Shukla, R. Singh, R.K. Gundampati, N. Misra, P. Maiti, B. Ray, Brominated graphene as mimetic peroxidase for sulfide ion recognition, *Analytical chemistry* 89(1) (2016) 783-791.
- [86] X. Li, B. Liu, K. Ye, L. Ni, X. Xu, F. Qiu, J. Pan, X. Niu, Highly sensitive and specific colorimetric detection of phosphate by using Zr (IV) to synergistically suppress the peroxidase-mimicking activity of hydrophilic Fe₃O₄ nanocubes, *Sensors and Actuators B: Chemical* 297 (2019) 126822.
- [87] C. Chen, L. Lu, Y. Zheng, D. Zhao, F. Yang, X. Yang, A new colorimetric protocol for selective detection of phosphate based on the inhibition of peroxidase-like activity of magnetite nanoparticles, *Analytical Methods* 7(1) (2015) 161-167.
- [88] D. Danks, Copper deficiency in humans, *Annual review of nutrition* 8(1) (1988) 235-257.
- [89] J. Liang, W. Lipscomb, Hydration of CO₂ by carbonic anhydrase: intramolecular proton transfer between Zn²⁺-bound H₂O and histidine 64 in human carbonic anhydrase II, *Biochemistry* 27(23) (1988) 8676-8682.
- [90] D.L. Nelson, A.L. Lehninger, M.M. Cox, *Lehninger principles of biochemistry*, Macmillan2008.
- [91] M. Jaishankar, T. Tseten, N. Anbalagan, B.B. Mathew, K.N. Beeregowda, Toxicity, mechanism and health effects of some heavy metals, *Interdisciplinary toxicology* 7(2) (2014) 60-72.
- [92] P.B. Tchounwou, C.G. Yedjou, A.K. Patlolla, D.J. Sutton, Heavy metal toxicity and the environment, *Molecular, clinical and environmental toxicology*, Springer2012, pp. 133-164.
- [93] G.E. Adams, P. Wardman, Free radicals in biology: the pulse radiolysis approach, *Free radicals in biology*. Vol. III1977.
- [94] G. Lakatos, E. Fleit, I. Mészáros, Ecotoxicological studies and risk assessment on the cyanide contamination in Tisza river, *Toxicology letters* 140 (2003) 333-342.
- [95] E. Avşar, B. Başaran, Formation of cyanide complexes of cobalt (II) and manganese (II), *Polyhedron* 6(10) (1987) 1909-1912.
- [96] A.J.P. Smolders, L.P.M. Lamers, E. Lucassen, G. Van der Velde, J.G.M. Roelofs, Internal eutrophication: how it works and what to do about it—a review, *Chemistry and ecology* 22(2) (2006) 93-111.
- [97] X. Xue, A.E. Landis, Eutrophication potential of food consumption patterns, *Environmental science & technology* 44(16) (2010) 6450-6456.
- [98] K.-Y. Wang, S.-J. Bu, C.-J. Ju, C.-T. Li, Z.-Y. Li, Y. Han, C.-Y. Ma, C.-Y. Wang, Z. Hao, W.-S. Liu, Hemin-incorporated nanoflowers as enzyme mimics for colorimetric detection of foodborne pathogenic bacteria, *Bioorganic & medicinal chemistry letters* 28(23-24) (2018) 3802-3807.
- [99] T. Jiang, Y. Song, T. Wei, H. Li, D. Du, M.-J. Zhu, Y. Lin, Sensitive detection of *Escherichia coli* O157: H7 using Pt–Au bimetal nanoparticles with peroxidase-like amplification, *Biosensors and Bioelectronics* 77 (2016) 687-694.

- [100] J. Han, L. Zhang, L. Hu, K. Xing, X. Lu, Y. Huang, J. Zhang, W. Lai, T. Chen, Nanozyme-based lateral flow assay for the sensitive detection of *Escherichia coli* O157: H7 in milk, *Journal of dairy science* 101(7) (2018) 5770-5779.
- [101] J.M. Farber, P.I. Peterkin, *Listeria monocytogenes*, a food-borne pathogen, *Microbiology and Molecular Biology Reviews* 55(3) (1991) 476-511.
- [102] L. Zhang, R. Huang, W. Liu, H. Liu, X. Zhou, D. Xing, Rapid and visual detection of *Listeria monocytogenes* based on nanoparticle cluster catalyzed signal amplification, *Biosensors and Bioelectronics* 86 (2016) 1-7.
- [103] Y. Liu, J. Wang, C. Zhao, X. Guo, X. Song, W. Zhao, S. Liu, K. Xu, J. Li, A multicolorimetric assay for rapid detection of *Listeria monocytogenes* based on the etching of gold nanorods, *Analytica chimica acta* 1048 (2019) 154-160.
- [104] P. Nicolopoulou-Stamati, S. Maipas, C. Kotampasi, P. Stamatis, L. Hens, Chemical pesticides and human health: the urgent need for a new concept in agriculture, *Frontiers in public health* 4 (2016) 148.
- [105] M. Peraica, B. Radić, A. Lucić, M. Pavlović, Toxic effects of mycotoxins in humans, *Bulletin of the World Health Organization* 77(9) (1999) 754.
- [106] W. Lai, Q. Wei, M. Xu, J. Zhuang, D. Tang, Enzyme-controlled dissolution of MnO₂ nanoflakes with enzyme cascade amplification for colorimetric immunoassay, *Biosensors and Bioelectronics* 89 (2017) 645-651.
- [107] J. Shu, Z. Qiu, Q. Wei, J. Zhuang, D. Tang, Cobalt-porphyrin-platinum-functionalized reduced graphene oxide hybrid nanostructures: a novel peroxidase mimetic system for improved electrochemical immunoassay, *Scientific reports* 5 (2015) 15113.
- [108] Z. Dehghani, M. Hosseini, J. Mohammadnejad, B. Bakhshi, A.H. Rezayan, Colorimetric aptasensor for *Campylobacter jejuni* cells by exploiting the peroxidase like activity of Au@Pd nanoparticles, *Microchimica Acta* 185(10) (2018) 448.
- [109] L. Zhang, Y. Chen, N. Cheng, Y. Xu, K. Huang, Y. Luo, P. Wang, D. Duan, W. Xu, Ultrasensitive detection of viable *Enterobacter sakazakii* by a continual cascade nanozyme biosensor, *Analytical chemistry* 89(19) (2017) 10194-10200.
- [110] S. Mumtaz, L.-S. Wang, S.Z. Hussain, M. Abdullah, Z. Huma, Z. Iqbal, B. Cieran, V.M. Rotello, I. Hussain, Dopamine coated Fe₃O₄ nanoparticles as enzyme mimics for the sensitive detection of bacteria, *Chemical Communications* 53(91) (2017) 12306-12308.
- [111] Y. Liu, J. Wang, X. Song, K. Xu, H. Chen, C. Zhao, J. Li, Colorimetric immunoassay for *Listeria monocytogenes* by using core gold nanoparticles, silver nanoclusters as oxidase mimetics, and aptamer-conjugated magnetic nanoparticles, *Microchimica Acta* 185(8) (2018) 360.
- [112] R. Das, A. Dhiman, A. Kapil, V. Bansal, T.K. Sharma, Aptamer-mediated colorimetric and electrochemical detection of *Pseudomonas aeruginosa* utilizing peroxidase-mimic activity of gold NanoZyme, *Analytical and bioanalytical chemistry* 411(6) (2019) 1229-1238.
- [113] R. Thiramanas, K. Jangpatarapongsa, P. Tangboriboonrat, D. Polpanich, Detection of *Vibrio cholerae* using the intrinsic catalytic activity of a magnetic polymeric nanoparticle, *Analytical chemistry* 85(12) (2013) 5996-6002.
- [114] Y. Liu, C. Zhao, X. Song, K. Xu, J. Wang, J. Li, Colorimetric immunoassay for rapid detection of *Vibrio parahaemolyticus*, *Microchimica Acta* 184(12) (2017) 4785-4792.
- [115] W. Liu, C. Gan, W. Chang, A. Qileng, H. Lei, Y. Liu, Double-integrated mimic enzymes for the visual screening of Microcystin-LR: Copper hydroxide nanozyme and G-quadruplex/hemin DNAzyme, *Analytica chimica acta* 1054 (2019) 128-136.

- [116] F. Tian, J. Zhou, B. Jiao, Y. He, A nanozyme-based cascade colorimetric aptasensor for amplified detection of ochratoxin A, *Nanoscale* (2019).
- [117] L. Huang, K. Chen, W. Zhang, W. Zhu, X. Liu, J. Wang, R. Wang, N. Hu, Y. Suo, J. Wang, ssDNA-tailorable oxidase-mimicking activity of spinel MnCo₂O₄ for sensitive biomolecular detection in food sample, *Sensors and Actuators B: Chemical* 269 (2018) 79-87.
- [118] N. Bagheri, A. Khataee, B. Habibi, J. Hassanzadeh, Mimetic Ag nanoparticle/Zn-based MOF nanocomposite (AgNPs@ ZnMOF) capped with molecularly imprinted polymer for the selective detection of patulin, *Talanta* 179 (2018) 710-718.
- [119] X. Xie, F. Tan, A. Xu, K. Deng, Y. Zeng, H. Huang, UV-induced peroxidase-like activity of gold nanoclusters for differentiating pathogenic bacteria and detection of enterotoxin with colorimetric readout, *Sensors and Actuators B: Chemical* 279 (2019) 289-297.
- [120] S. Sun, R. Zhao, S. Feng, Y. Xie, Colorimetric zearalenone assay based on the use of an aptamer and of gold nanoparticles with peroxidase-like activity, *Microchimica Acta* 185(12) (2018) 535.
- [121] S.-X. Zhang, S.-F. Xue, J. Deng, M. Zhang, G. Shi, T. Zhou, Polyacrylic acid-coated cerium oxide nanoparticles: an oxidase mimic applied for colorimetric assay to organophosphorus pesticides, *Biosensors and Bioelectronics* 85 (2016) 457-463.
- [122] J. Wei, L. Yang, M. Luo, Y. Wang, P. Li, Nanozyme-assisted technique for dual mode detection of organophosphorus pesticide, *Ecotoxicology and environmental safety* 179 (2019) 17-23.
- [123] N. Bagheri, A. Khataee, J. Hassanzadeh, B. Habibi, Sensitive biosensing of organophosphate pesticides using enzyme mimics of magnetic ZIF-8, *Spectrochimica Acta Part A: Molecular and Biomolecular Spectroscopy* 209 (2019) 118-125.
- [124] Y.-C. Chang, Y.-S. Lin, G.-T. Xiao, T.-C. Chiu, C.-C. Hu, A highly selective and sensitive nanosensor for the detection of glyphosate, *Talanta* 161 (2016) 94-98.
- [125] G. Guan, L. Yang, Q. Mei, K. Zhang, Z. Zhang, M.-Y. Han, Chemiluminescence switching on peroxidase-like Fe₃O₄ nanoparticles for selective detection and simultaneous determination of various pesticides, *Analytical chemistry* 84(21) (2012) 9492-9497.
- [126] N.-R. Ha, I.-P. Jung, I.-J. La, H.-S. Jung, M.-Y. Yoon, Ultra-sensitive detection of kanamycin for food safety using a reduced graphene oxide-based fluorescent aptasensor, *Scientific reports* 7 (2017) 40305.
- [127] T.K. Sharma, R. Ramanathan, P. Weerathunge, M. Mohammadtaheri, H.K. Daima, R. Shukla, V. Bansal, Aptamer-mediated 'turn-off/turn-on' nanozyme activity of gold nanoparticles for kanamycin detection, *Chemical communications* 50(100) (2014) 15856-15859.
- [128] P. Ni, H. Dai, Y. Wang, Y. Sun, Y. Shi, J. Hu, Z. Li, Visual detection of melamine based on the peroxidase-like activity enhancement of bare gold nanoparticles, *Biosensors and Bioelectronics* 60 (2014) 286-291.
- [129] C. Xiu, K.K. Klein, Melamine in milk products in China: Examining the factors that led to deliberate use of the contaminant, *Food Policy* 35(5) (2010) 463-470.
- [130] Y. Lin, J. Ren, X. Qu, Catalytically active nanomaterials: a promising candidate for artificial enzymes, *Accounts of chemical research* 47(4) (2014) 1097-1105.
- [131] H. Mohammadi, M. El Rhazi, A. Amine, A.M.O. Brett, C.M.A. Brett, Determination of mercury (II) by invertase enzyme inhibition coupled with batch injection analysis, *Analyst* 127(8) (2002) 1088-1093.
- [132] D. Shan, C. Mousty, S. Cosnier, Subnanomolar cyanide detection at polyphenol oxidase/clay biosensors, *Analytical chemistry* 76(1) (2004) 178-183.

- [133] B.W. Blais, J. Leggate, J. Bosley, A. Martinez-Perez, Comparison of fluorogenic and chromogenic assay systems in the detection of *Escherichia coli* O157 by a novel polymyxin-based ELISA, *Letters in applied microbiology* 39(6) (2004) 516-522.
- [134] I.B. Rejeb, F. Arduini, A. Arvinte, A. Amine, M. Gargouri, L. Micheli, C. Bala, D. Moscone, G. Palleschi, Development of a bio-electrochemical assay for AFB1 detection in olive oil, *Biosensors and Bioelectronics* 24(7) (2009) 1962-1968.
- [135] S.V. Dzyadevych, A.P. Soldatkin, V.N. Arkhypova, V. Anna, J.-M. Chovelon, C.A. Georgiou, C. Martelet, N. Jaffrezic-Renault, Early-warning electrochemical biosensor system for environmental monitoring based on enzyme inhibition, *Sensors and Actuators B: Chemical* 105(1) (2005) 81-87.
- [136] E.A. Songa, O.A. Arotiba, J.H.O. Owino, N. Jahed, P.G.L. Baker, E.I. Iwuoha, Electrochemical detection of glyphosate herbicide using horseradish peroxidase immobilized on sulfonated polymer matrix, *Bioelectrochemistry* 75(2) (2009) 117-123.

Chapter III. 2D Oxygen-Terminated Few-Layered $Ti_3C_2T_x$ MXene Nanosheets as Peroxidase-Mimic for Colorimetric Detection of Kanamycin*

Abstract

Nanomaterials-based bioinspired enzyme mimics are gaining increased attention as alternatives to biocatalysts. Herein, we report synthesizing oxygen-terminated few-layered titanium-based MXene nanosheets (OFL-Ti-MN). OFL-Ti-MN possesses horseradish peroxidase (HRP) activity in catalyzing the oxidation of colorless 3,3',5,5'-tetramethylbenzidine (TMB) in the presence of hydrogen peroxide (H_2O_2), which turns the solution color bluish-green. The solution color fades quickly when kanamycin (KAN) is added to this system. This reaction indicates that KAN can prevent color change in the OFL-Ti-MN/TMB- H_2O_2 system. Based on this strategy, we developed an OFL-Ti-MN-based colorimetric sensor to detect and quantify KAN. The sensor exhibited a dynamic range from 15.28 nM to 46.14 μ M and a calculated limit of detection (LOD) of 15.28 nM. From the insight gained from the peroxidase-mimic property of OFL-Ti-MN, we proposed a mechanism for the inhibition effect of KAN on peroxidase and peroxidase-mimic enzymes. The proposed mechanism can potentially help elucidate the reasons for the antibacterial function of KAN and its side effects in humans.

3.1. Introduction

Natural enzymes play an essential role in substrate conversion with their high specificities and abilities to enhance reaction rates. Nevertheless, several disadvantages, such as high cost, low stability, poor reusability, etc., limit the use of enzymes [1]. With the advent of nanotechnology, numerous unique properties of nanomaterials such as antibacterial, photocatalytic, and magnetic have been discovered and applied [2-6]. Since 2007, the enzyme-mimic property of nanomaterials

*Wang, W., Yin, Y., Gunasekaran, S., (2022). Oxygen-terminated few-layered $Ti_3C_2T_x$ MXene nanosheets as peroxidase-mimic nanozyme for colorimetric detection of kanamycin. *Biosensors and Bioelectronics* **2022**, 114774. Copyright Elsevier.

has been recognized as various nanomaterials that can induce enzymatic catalysis with great recognition ability either on their own or by forming complexes with other molecules [7]. These nanomaterials that possess enzymatic functions similar to those of natural enzymes are known as enzyme nanoparticle mimics (nano-mimics) (also called “nanozymes”) [8, 9]. Compared to natural enzymes, enzyme nano-mimics are more stable, have a longer life cycle, and are less expensive [10]. As a result, enzyme nano-mimics are widely explored for use in various applications, including biosensing, illness treatment, environmental protection, etc. [11].

MXene is synthesized from a layer-structured MAX phase bulk ceramic, which is denoted as $M_{n+1}AX_n$, where "M" is the early transition metal (e.g., Ti, Mo, Cr, Zr, etc.), "A" represents the atoms located in group 13 or 14 of the periodic table (e.g., Al, Si, etc.), and "X" is usually C and/or N atoms [12]. However, the "A" layer can be removed by etchants, i.e., hydrogen fluoride (HF) or a mixture of lithium fluoride (LiF) and hydrochloric acid (HCl), and during the process, "T" atoms (such as -F, -O, -Cl, and -OH) are anchored on the surface of the remaining MAX phase structure. So, MXene, the complete etched product of the MAX phase, is denoted as $M_{n+1}X_nT_m$. The surface composition (i.e., T_m in the MXene notation) may vary according to the chemical etching method, which affords MXene high metallic conductivity (~6000-8000 S/cm) and makes heterogeneous electron (e^-) transfer achievable on-site [13]. The most common MXene, $Ti_3C_2T_x$, is synthesized from Ti_3AlC_2 bulk ceramic by the minimally intensive layer delamination (MILD) method, where manual shaking can yield less defective and larger single $Ti_3C_2T_x$ nanoflakes [14, 15]. Typically, fluoride-based etchants in strongly acidic conditions (HF solution or fluoride salts in highly concentrated HCl solution) are used to exfoliate single- or ultrathin multiple-layered MXene, but this can create single or a cluster of vacancy defects on the Ti layers due to single or several adjacent Ti atoms being etched-off [16]. These highly unstable and reactive vacancies provide

layered MXene with relatively high reductivity. Therefore, MXene can reduce oxidizing agents and even metal salt precursors without any reducing agents[17]. In addition, vacancy defects provide exfoliated MXene accommodation for those single metal products [18]. Besides, since various chemical atoms and groups (-F, -Cl, -OH, etc.) are grown on the etched aluminum (Al) sites during the etching process, electrochemical absorption of MXene to oxidizing agents or metal salt precursors is improved, and the electron transfer is hastened. These unique features make MXene a new catalytic nanomaterial and an ideal candidate for biosensing.

The overuse of antibiotics to treat cows for bovine mastitis can contaminate raw milk with antibiotic residues that are highly resistant to heat sterilization and easily transfer into dairy products [19]. Antibiotic residues can cause allergic reactions, disrupt intestinal flora, and other severe human health problems [20]. Furthermore, the excess use of antibiotics can create antibiotic resistance and facilitate the entrance of resistant pathogens into the food chain. Kanamycin (KAN) is a common aminoglycoside antibiotic used in foods since it is inexpensive and possesses excellent antibacterial activity. Excessive KAN consumption can induce human nephrotoxicity, neurotoxicity, and ototoxicity [21]. Therefore, the European Union (EU) and Korea Food and Drug Administration (KFDA) have established maximum residue limits (MRLs) of KAN in milk as ~320 nM and ~214 nM, respectively [22].

We synthesized oxygen-terminated few-layered titanium-based MXene nanosheets (OFL-Ti-MN) in a controllable way and determined their peroxidase-mimic kinetics. The reduction of the 3,3',5,5'-tetramethylbenzidine (TMB)-H₂O₂ system mediated by MXene turned the color of the sample solution from clear to bluish-green; however, in the presence of KAN, the color change faded quickly. We used the ability of KAN to interfere with this color-change reaction as the basis and designed a colorimetric biosensor to detect and measure KAN in several real sample matrices.

3.2. Experimental section

3.2.1. Materials and reagents

H₂O₂ solution (30%) was purchased from ACROS Organics. MAX phase was obtained from Nano-Mall Technology Co. Ltd, Hangzhou, China. Ampicillin and penicillin G were supplied from Scientific Inc. Kanamycin sulfate was purchased from Bio Basic Company. Moreover, amoxicillin was supplied from Chem-Impex Int'l Inc. Honey, and skimmed milk was purchased from a local supermarket. All other chemicals were of analytical grade and were obtained from Sigma-Aldrich. De-ionized (DI) water (18 MΩ cm) was used to prepare buffer solutions.

3.2.2. MXene synthesis

Due to the strong covalent bonding between the early transition metal and C/N atoms, most MXene can be obtained via selective exfoliation from its parent MAX phase by HF or fluoride salt-based mixtures [23]. So most MXene nanosheets are synthesized via the MILD method using LiF etchant [13]. Briefly, 7.5 M LiF and 9 M HCl were mixed at room temperature and stirred for 10 min to prepare the etchant. Then, the MAX phase (Ti₃AlC₂) was added to the etchant slowly, stirring at room temperature for 24 h. The resulting acidic mixture was centrifuged (4000 rpm for 5 min) and rinsed with DI water multiple times until the pH of the final mixture was greater than 5.0. After discarding the precipitate, a dark-green supernatant, filled with protective N₂ gas, was collected and ultrasonicated for 2 h. The final thin MXene film was carefully collected via vacuum filtering and freeze-drying. The collected sample was kept under a protective N₂ environment and stored at room temperature.

The surface morphology of synthesized OFL-Ti-MN was studied by a field emission scanning electron microscope (FE-SEM, LEO Gemini 1530) with a 4.7-mm working distance. Fourier

transform-infrared (FT-IR, Spectrum 100, Perkin Elmer) and X-ray photoelectron (XPS, Thermo Scientific K-Alpha) spectroscopies were carried out to characterize the chemical composition of MXene. X-ray diffraction of the samples was performed (XRD, Bruker D8 Discovery) with Cu K α radiation and a scan rate of 20° min⁻¹ within the 2 θ range from 20° to 80° per step. The optical character of the nanozymatic system was studied by ultraviolet-visual spectroscopy (UV-vis, Lambda 35, PerkinElmer).

3.2.3. Peroxidase-mimic kinetics of MXene

The peroxidase-mimic kinetics of MXene was measured through the oxidation of TMB in the presence of hydrogen peroxide (H₂O₂) and MXene catalyst in acetate buffer (pH 3.6) [24]. This redox reaction was incubated in a water bath for 15 min, and chromogenic TMB products were analyzed with a typical UV-vis absorbance peak at 635 nm (A_{635}). Mass spectrometry (Bruker Maxis Ultra-High Resolution Quadrupole Time-of-Flight MS) (Q-TOF-MS) was used in positive ionization mode to determine the mass of the bluish-green product. To determine the optimal reaction conditions, the prepared MXene was dissolved in acetate buffer (0.2 M, pH 3.0~ pH 5.5) to prepare 50 μ g/mL MXene suspensions. Next, 1.2 mL of the prepared MXene suspension was added to a solution of 100 μ L TMB substrate (5 mM) plus 200 μ L 30% H₂O₂. The redox reaction was analyzed for 5 s via UV-vis spectroscopy during the incubation at 30 °C ~70 °C in a water bath.

The steady-state kinetics of the MXene assay was determined. To 50 μ g/mL MXene suspensions, TMB (0.143~3.571 mM) and H₂O₂ (0.81~3.29 M) were added. This mixture was incubated at 37 °C for 15 min, during which A_{635} was recorded every 5 s. The kinetics analysis was performed under optimal reaction conditions based on the Michaelis-Menten equation (Eq. (5)) and its double-reciprocal Lineweaver-Burk plot (Eq. (6)) [25]:

$$V_0 = \frac{V_{max}[S]}{K_m + [S]} \quad (5)$$

$$\frac{1}{V_0} = \frac{K_m}{V_{max}} \left(\frac{1}{[S]} + \frac{1}{K_m} \right) \quad (6)$$

Where V_0 = initial reaction velocity; K_m = Michaelis-Menten constant, which measures the affinity of enzyme nano-mimics to substrates, the higher the K_m , the weaker affinity between enzyme nano-mimics and enzymatic substrate and vice versa; V_{max} = maximum enzymatic reaction velocity; and $[S]$ = substrate concentration, respectively.

To perform the free radical-trapping experiment, L-ascorbic acid (LAA), ethylenediaminetetraacetic acid disodium salt (EDTA•2Na), and isopropanol (IPA) were mixed with MXene buffer solution (0.2 M acetic acid buffer) at a final concentration of 1 mM in the light condition for superoxide anion ($\bullet\text{O}_2^-$), hydroxyl radicals ($\bullet\text{OH}$), and hole (h^+) capture [26]. After adding TMB and H_2O_2 , their UV-vis absorption spectra were collected at 37 °C.

3.2.4. Colorimetric detection of KAN

For the colorimetric detection of KAN, 2.5 mg/mL MXene stock suspension was diluted in DI water to prepare a 20 $\mu\text{g/mL}$ test suspension. To the prepared MXene suspension, KAN samples of concentrations 15.38 to 46.14 μM were mixed and mildly shaken for 10 min at room temperature. To this 100 μL , TMB (5 mM), and 200 μL H_2O_2 (30 %) were added, followed by incubation at 37 °C for 15 min. The final solution was analyzed via UV-vis spectroscopy.

3.2.5. Real sample detection

Tap water, honey, and skim milk were selected as real matrices to detect and measure KAN concentration. KAN was mixed with tap water directly and vortexed for 10 min to prepare spiked water samples. To prepare spiked honey and skim milk samples, a published method was adopted

with slight modifications [27, 28]. For spiked honey, KAN was added to 1 g honey dissolved in 10 mL DI water. The prepared mixture was filtered with a 0.22- μm syringe filter and stored overnight at room temperature. For spiked skim milk, KAN was dissolved in DI water and was added to 10 mL of skim milk. The pH of this mixture was adjusted to 4.6 using hydrogen acetate (HAc, 20 %, v/v) to denature and precipitate milk proteins at their isoelectric point. After holding at 45 °C for 30 min, the samples were centrifuged at 14,000 rpm for 15 min, and the precipitate was removed. The collected supernatant was diluted with DI water (100 \times) and filtered with a 0.22- μm syringe filter. The KAN-spiked skim milk filtrate was stored in a refrigerator at 4 °C until further experiments.

All experiments were repeated three times, and the measured values are reported as mean \pm standard deviation.

3.3.Results and discussion

3.3.1. MXene synthesis and characterization

A schematic of the OFL-Ti-MN preparation method is presented in **Figure 3.1. A**. As shown, the LiF/HCl mixture removes Al interlayers and facilitates delamination. The surface of the MAX precursor observed in SEM micrographs (**Figure 3.1. B (a, b)**) reveals numerous larger than 10 μm pebble-like structures. **Figure 3.1. B (c, d)** are SEM images at different magnifications, which show the large surface area of MXene nanosheets. Additionally, as shown in the cross-sectional SEM images (**Figure 3.1. B (e, f)**), the as-synthesized oxygen-terminated MXene (OTM) comprises only a few layers, each with an average thickness of less than 80 nm, which further exposes a large surface area to the external environment. These unique properties help the OTM entrap a large number of substrate molecules and enhance their enzymatic catalytic performance.

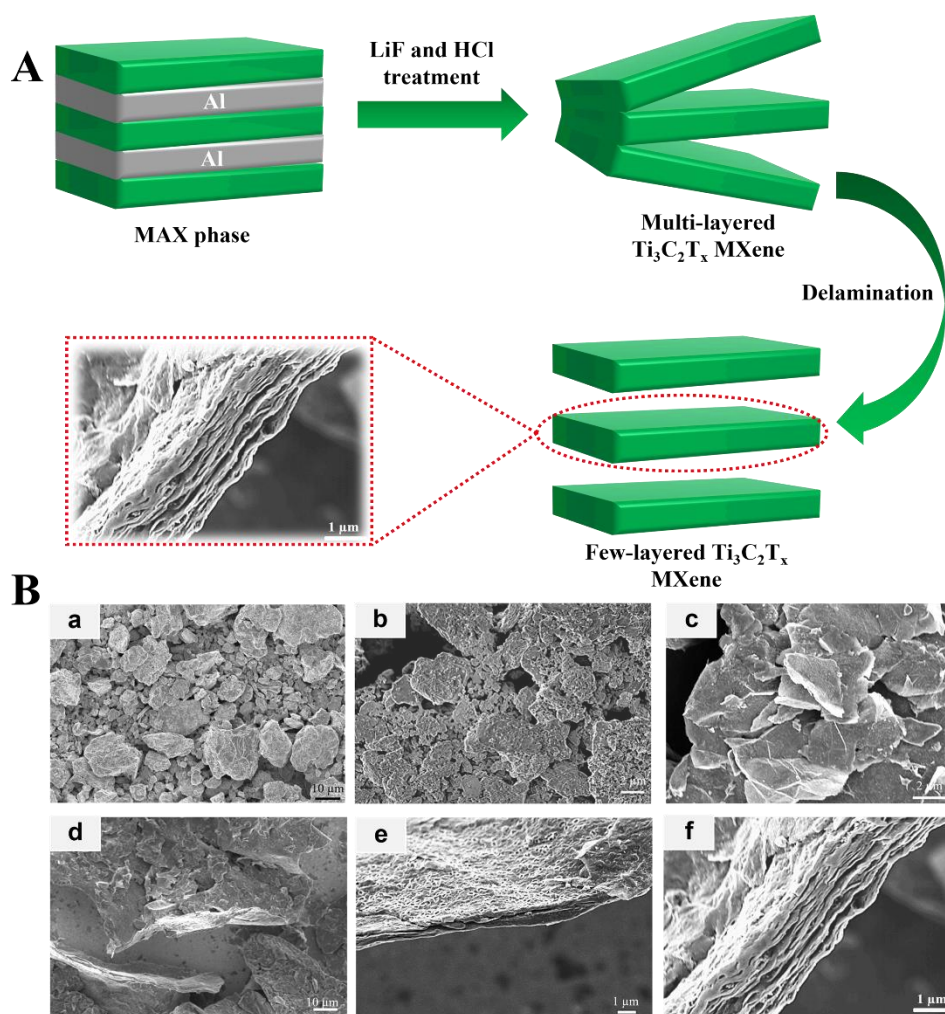


Figure 3.1. A. Illustration of an OFL-Ti-MN synthesis process. B. SEM images of (a) and (b). parent MAX phase precursor, (c)-(f). synthesized OFL-Ti-MN

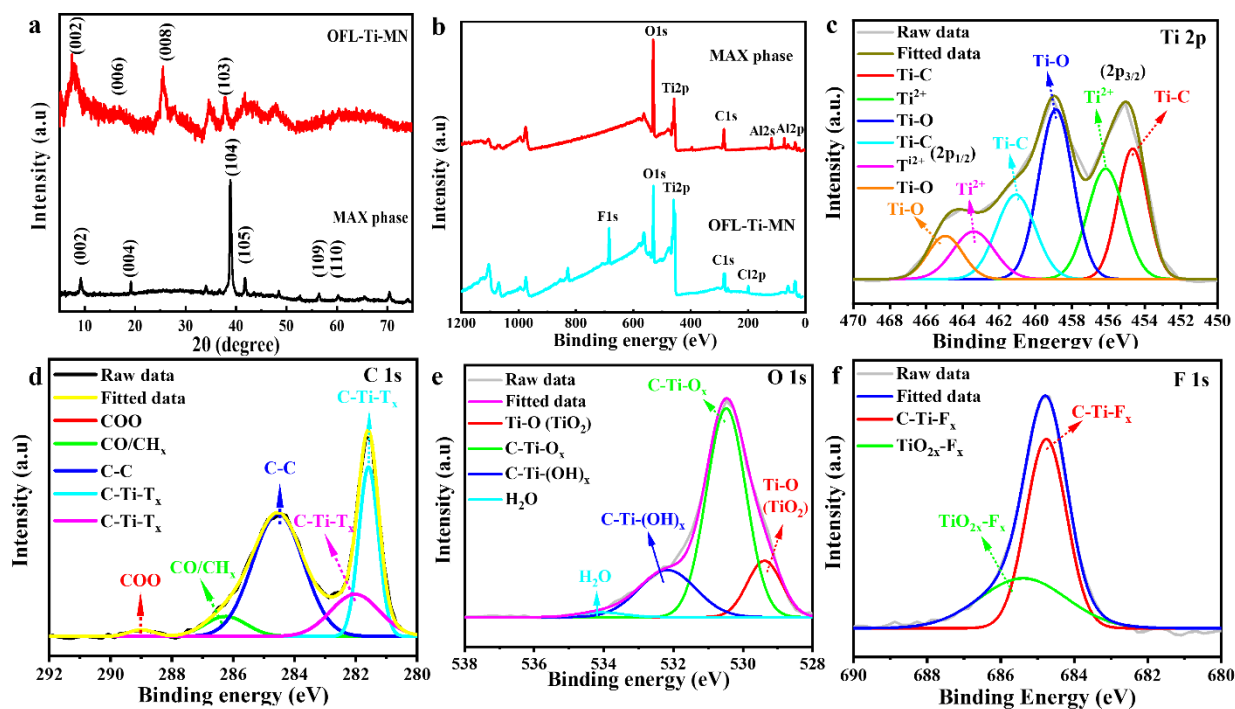


Figure 3.2. XRD patterns of (a) Ti_3AlC_2 powder and $\text{Ti}_3\text{C}_2\text{T}_x$ nanosheets and XPS survey scans of (b) Ti_3AlC_2 powder and $\text{Ti}_3\text{C}_2\text{T}_x$ nanosheets, high-resolution XPS spectra of $\text{Ti}_3\text{C}_2\text{T}_x$ nanosheets with curve fitting for (c) Ti 2p, (d) C 1s, (e) O 1s, and (f) F 1s.

The XRD pattern of the MAX phase (**Figure 3.2. (a)**) is mainly used to evaluate the occurrence of the impurity phase of Ti_3AlC_2 powder. When Ti_3AlC_2 powder was added to the LiF/HCl mixture, bubbles appeared continually, indicating the occurrence of a chemical reaction. The exfoliated MXene nanosheets exhibited significantly weakened peaks except for a sharp peak (006) around $2\theta = 26^\circ$. Non-basal plane peak (104) of the MAX phase centered at $2\theta = 39^\circ$ almost disappeared owing to the successful exhaustion of the Al layer from $\text{Ti}_3\text{C}_2\text{T}_x$ [29]. Typically, diffraction peaks (002) and (110), centered respectively at $2\theta = 9.22^\circ$ and $2\theta = 60.36^\circ$, are identified to verify the purity of the MAX phase [30]. The (002) peak for the synthesized MXene nanosheets has shifted from 9.22° to 7.89° as a result of the randomness of delaminated flakes' orientation, suggesting

that the interlayer distance of $\text{Ti}_3\text{C}_2\text{T}_x$ is approximately 1.136 nm based on the Bragg equation [31]. These data confirm that Al atoms were successfully etched off after the LiF/HCl treatment.

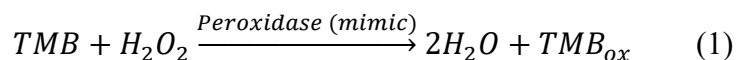
The XPS spectra (**Figure 3.2. (b)**) show peaks at binding energy (BE) values of 458 eV and 284 eV for the synthesized MXene nanosheets and MAX phase corresponding to Ti 2p and C 1s, respectively, indicating that both MXene nanosheets and MAX phase are composed of Ti and C atoms [32]. The O 1s, F 1s, and Cl 2p peaks appear predominantly at BEs 532 eV, 685 eV, and 198 eV, respectively, due to LiF/HCl treatment and atoms anchoring MXene nanosheets [33]. Peaks of Al 2s and Al 2p are seen in the MAX phase spectrum at 119 eV and 74 eV, respectively, and are not observed in the MXene spectrum, supporting that Al atoms have been completely etched off of MXene [32]. The high-resolution Ti 2p spectrum (**Figure 3.2. (c)**) was fitted into two fixed areas with a ratio of 2:1 separated by BE of 5.6 eV, comprised of three pairs of $2p_{1/2} - 2p_{3/2}$ doublets. The $2p_{3/2}$ region components are assigned to Ti-C, Ti^{2+} , and Ti-O at BEs 454.6 eV, 456.1 eV, and 458.8 eV, respectively [34, 35]. In the C 1s region (**Figure 3.2. (d)**), there are two peaks centered at BEs 281.6 eV and 282.5 eV associated with C-Ti, while three peaks with their BEs at 284.6 eV, 286.9 eV, and 288.8 eV corresponded with C-Ti, C-C, CO/ CH_x , and COO, respectively, in agreement with earlier reports [34, 36]. So, the basic framework of $\text{Ti}_3\text{C}_2\text{T}_x$ has been successfully constructed. The O 1s spectrum (**Figure 3.2. (e)**) can be deconvoluted into four peaks corresponding to Ti-O (529.4 eV), C-Ti-O_x (530.4 eV), C-Ti-(OH)_x (532.1 eV), and adsorbed water (534.1 eV)[36, 37]. The existence of different oxygen-containing bonds confirms that O₂ has largely oxidized the MXene surface during the synthesis due to the high reductivity of MXene. Major peaks in the F 1s spectrum (**Figure 3.2. (f)**) are of C-Ti-F_x and TiO_{2x}-F_x, centered at BEs 684.8 eV and 685.5 eV, respectively [36]. Adsorption of water molecules and the F-containing

group indicate that the surface of MXene terminates various functional groups and enhances the ability of its surface chemical modification.

The FT-IR survey spectrum of OTM (**Figure S3.1.**) shows dips at 1000 and 1217 cm^{-1} , corresponding to O_2 and possible C-F vibration owing to the presence of F based on XPS spectra. While two dips at 1368 and 1638 cm^{-1} are assigned to water molecular and C=O bonding, respectively. The presence of -OH groups is confirmed at 2945 and 3300 cm^{-1} [38, 39]. Hence the FT-IR results further confirm that the MXene layers are oxidized by O_2 molecules during their synthesis.

3.3.2. Optimal condition and peroxidase-mimic kinetics of MXene enzyme nano-mimics

OTM was first found to act as a peroxidase mimic in the TMB- H_2O_2 system. The general oxidation process of substrates such as TMB by H_2O_2 can be depicted as:



The above equation shows that H_2O_2 can oxidize TMB in an enzymatic or nanozymatic system, such as the Fe_3O_4 -TMB- H_2O_2 [40]. When oxidized, the solution acquires a bluish-green tinge due to the color of the oxidized TMB product (TMB_{ox}), which produces a UV-vis absorption peak at 653 nm [41]. Thus, the UV-vis absorbance peak at 653 nm appearing when OFL-Ti-MN was present in the system (**Figure 3.3. (a)**) confirms that OFL-Ti-MN acts as a peroxidase-mimic and oxidizes TMB in the presence of H_2O_2 .

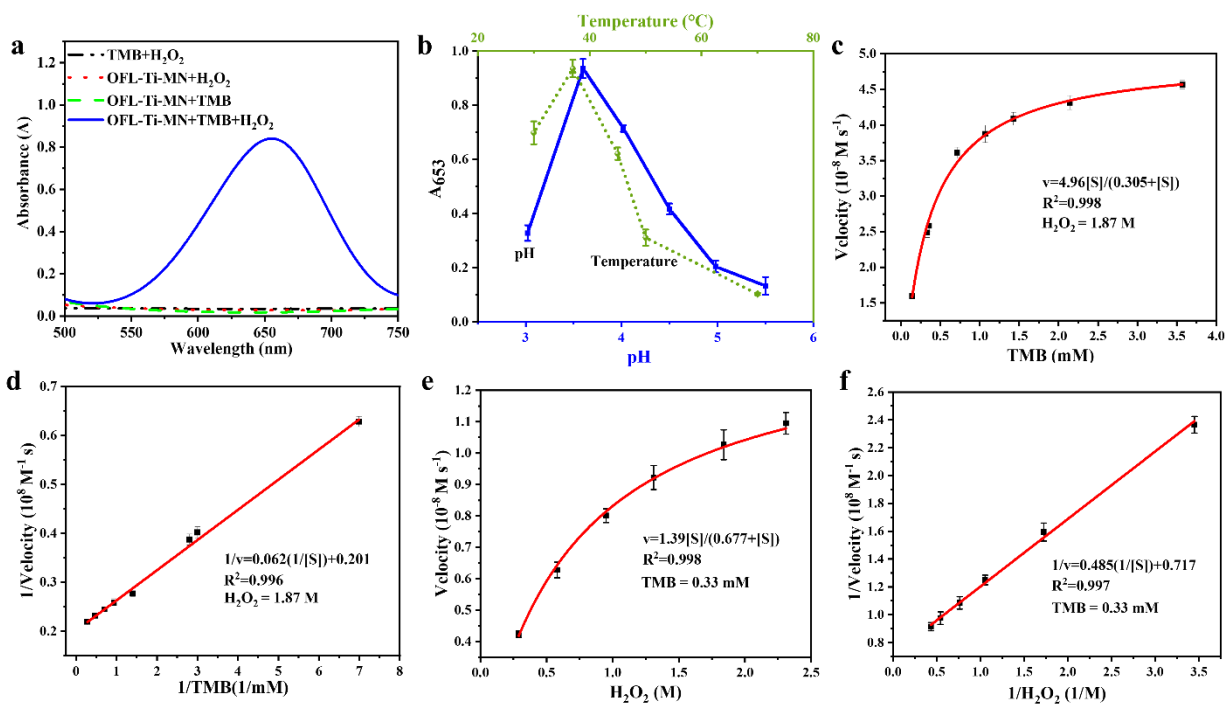


Figure 3.3. (a) UV-vis absorption spectra for TMB-H₂O₂, MXene-H₂O₂, MXene-TMB, and MXene/TMB-H₂O₂ reaction systems, (b) UV-vis absorption peak at 653 nm (A₆₅₃) of the solution after 15 min incubation in different pHs at 37 °C (solid line) and in pH 3.6 at different temperatures (dotted line). Steady-state kinetics assay of Ti₃C₂T_x nanosheets in various enzyme-substrate concentrations but with the other substrate concentration constant (c) varying TMB and (e) varying H₂O₂ and their corresponding double-reciprocal plots, (d) and (f).

We optimized the pH and temperature (**Figure 3.3. (b)**) for the best peroxidase-mimic catalytic performance of OFL-Ti-MN. The most substantial absorbance peak of the OFL-Ti-MN/TMB-H₂O₂ system was observed at pH 3.6. It has been reported that the decomposition of H₂O₂ by transition metals or their oxides follows the base-like decomposition in the acidic condition[42]. Theoretically, the peroxidase enzyme (or its enzyme nano-mimics) preferably breaks O-O bond of adsorbed H₂O₂ (H₂O₂^{*}) to produce •OH-adsorbed surface of OFL-Ti-MN (OH^{*}) in acidic

conditions, resulting from the low energy barrier of the first decomposition step of H_2O_2 at a lower pH (0.57 eV). Additionally, the point of zero charge (pH_{pzc}) value of MXene is about 3.0, providing MXene with acidic nature, which helps it attract positively charged H_2O_2 ($\text{pK}_a = 11.6$) at pH 3.6 [43, 44]. Hence, pH 3.6 was chosen for subsequent experiments [45].

To measure the temperature effect on the peroxidase catalytic property of OFL-Ti-MN, reactions were performed at different temperatures. Based on the observed A_{653} maximum (**Figure 3.3. (b)**), 37 °C was chosen as the best temperature for OTM catalytic activity. The time-dependent change in A_{653} indicated that the catalytic activity increased significantly with increasing OTM concentration (Fig. S2).

The investigation of peroxidase reaction kinetics of OFL-Ti-MN enzyme nano-mimics followed the Michaelis-Menten model, exhibiting a hyperbolic relationship between the concentration of TMB/ H_2O_2 and reaction rate (**Figure 3.3. (c, e)**). The K_m and V_{max} values of OFL-Ti-MN for enzymatic substrates (TMB and H_2O_2) were determined from the Lineweaver-Burk double reciprocal plots (**Figure 3.3. (d, f)**). The K_m value for OFL-Ti-MN against TMB (0.305 mM) is lower than that for horseradish peroxidase (HRP) (0.434 mM)[46], which indicates that OFL-Ti-MN has a higher affinity to TMB than HRP. The kinetics of different peroxidase-mimics were compared based on their Michaelis-Menten constants for reactions with TMB and H_2O_2 (**Table S3.1.**). Among the many peroxidase nano-mimics, the K_m of OFL-Ti-MN against H_2O_2 is the highest (0.677 M), probably due to 1) Severe oxidation of MXene during etching, confirmed by XPS, where the O atom contributes to 43.04%. In this regard, Ti vacancy defects such as (Ti-O) or (C-Ti-O) offset the reductivity of MXene, resulting in a lower affinity to the H_2O_2 and 2) H_2O_2 molecules first gain e^- from OFL-Ti-MN as they attach to Ti vacancy defects, releasing hydroxyl groups to anchor on site. As a result, some H_2O_2 molecules are consumed before

oxidation of TMB, suggesting that it is necessary to add higher H₂O₂ concentration to reach half V_{max} of TMB oxidation, namely, increasing the K_m of the TMB reaction. The V_{max} of OFL-Ti-MN with TMB (4.96*10⁻⁸ M s⁻¹) is higher than those for several other enzyme nano-mimics (**Table S3.1.**), indicating that OFL-Ti-MN is more favorable to oxidizing TMB.

The long-term stability of OFL-Ti-MN and HRP was compared by monitoring their performance in catalyzing the TMB-H₂O₂ reaction after storing them for 40 days at room temperature (**Figure S3.3.**). The activity was calculated as:

$$Activity (\%) = \frac{A_{653}(t)}{A_{653}(0)} * 100 \quad (2)$$

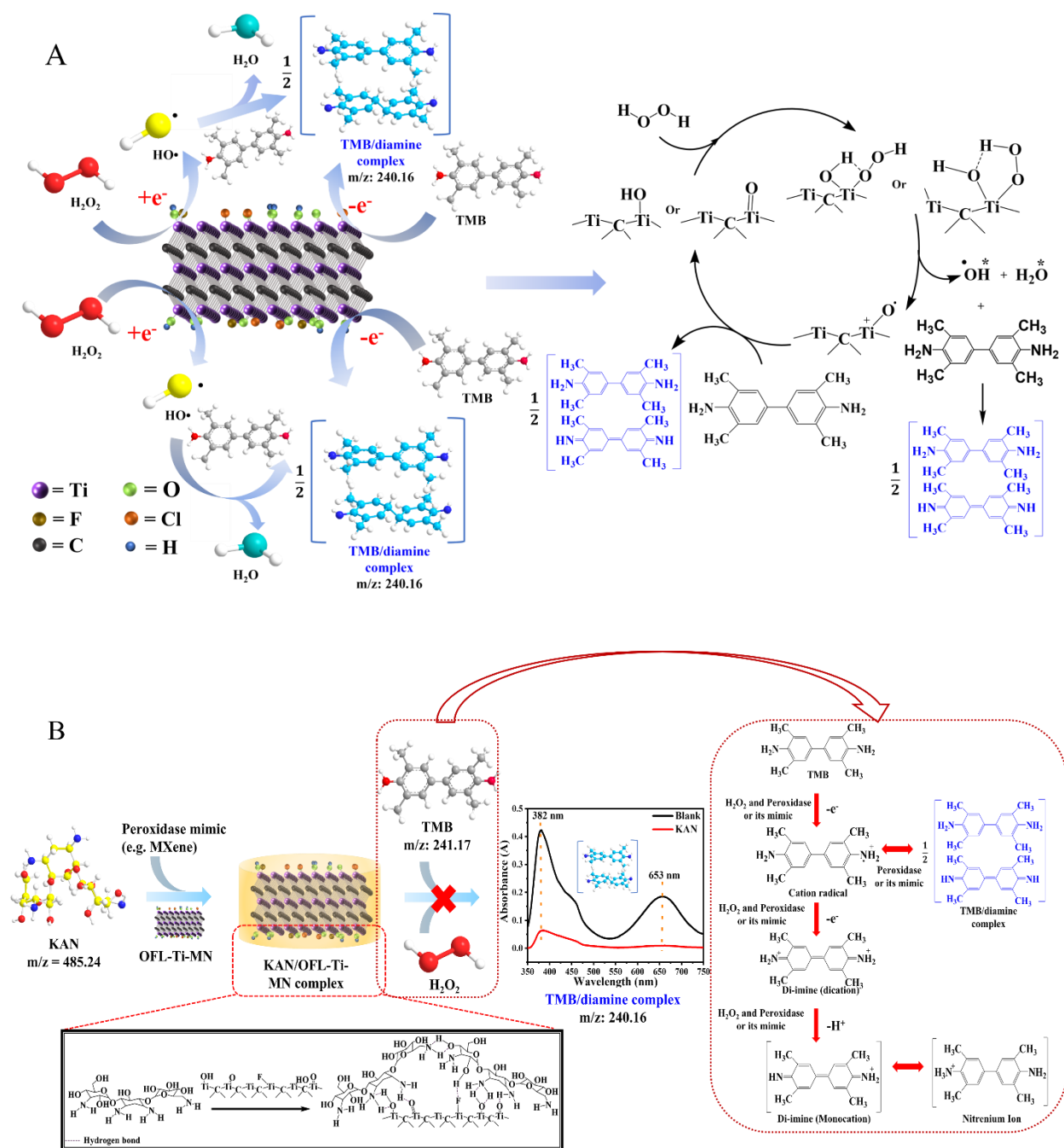
where A₆₅₃ (t) and A₆₅₃ (0) are UV-vis absorbance peaks of the reaction system kept at room temperature for t days and 0 days (i.e., fresh), respectively. Our results indicate that OFL-Ti-MN remained more stable for longer. For example, after 15 days, the catalytic ability of OFL-Ti-MN was over 92%, while that of HRP was about 12.2% (**Figure S3.3.**).

3.3.3. Mechanism of peroxidase-mimic property of OFL-Ti-MN

We propose a mechanism (**Scheme 3.1. A**) for the OFL-Ti-MN-mediated catalytic reaction based on our data and other evidence, although we are still uncertain about some structural details. At first, after adding H₂O₂ to the OFL-Ti-MN dispersion, the nucleophilic H₂O₂ molecules with a positive charge (pK_a = 11.6) are more favorably adsorbed on the surface of OFL-Ti-MN (pK_{pzc} = 3.0) in the acidic condition (pH 3.6) with lower adsorption energy compared with water molecules. This forces the electrophilic MXene surface to be attacked by adsorbed H₂O₂* to form hydroperoxyl ligands (OOH*) on Ti atoms in a conjugation -OH and Ti=O group (**Scheme 3.1. A**, right)[47, 48]. These ligands also form hydrogen bonds with other polar groups on the Ti atoms (-F, -OH, =O, etc.), which in turn stabilize the OOH* on the OFL-Ti-MN surface. As mentioned

previously, Ti-Al bonds are impaired by etching with a highly corrosive and acidic etchant (LiF/HCl). Meanwhile, some adjacent Ti atoms anchored in the sublayers (Ti1 and Ti3) are also etched-off, leaving several single or clusters of Ti vacancies[49]. These unstable vacancy defects presenting high nucleophilicity and proton affinity can donate e^- to adsorbed OOH^* ligands, breaking the O-O bond on the OFL-Ti-MN surface. And then, reactive oxygen species (ROS) are generated in the solution. Multiple radical scavengers were employed to ascertain the main ROS released, including LAA, EDTA•2Na, and IPA. The results show (**Figure S3.4.**), A_{653} values for a solution with IPA were very small even after 15 min incubation in a water bath, illustrating that $\bullet OH$ is a crucial ROS product released in the solution as the reduction reaction occurs in H_2O_2 . During this process, generated ROS is mostly $\bullet OH^*$, which preferably captures the H^+ protonated by a hydrogen donor (in our case, TMB) to produce H_2O molecules[50].

The color of the EDTA•2Na solution is almost transparent and clear, as can be gleaned from its lower A_{653} value compared to those of the blank and LAA solutions (**Figure S3.4.**). This indicates an essential role of h^+ in a catalytic reaction. It is possible that TMB molecules also anchor on the surface of OFL-Ti-MN via hydrogen bonding with polar groups of OFL-Ti-MN (-F, -OH, =O, etc.) since there is a high affinity between OFL-Ti-MN and TMB molecules ($K_m=0.335$ mM). Thus, over-donating e^- defects leaving h^+ in the Ti sublayers of the MXene gain free e^- from $-NH_2$ in several TMB molecules by electronegative force (**Scheme 3.1. A**). Meanwhile, TMB may protonate to adsorb oxygen radicals ($\bullet O^*$) on the Ti atoms. Consequently, TMB cation radicals are released. Since cation radicals are unstable, they immediately turn to TMB/diamine complex with mass/charge (m/z) = 240.16 as added H^+ in the positive ion mode of Q-TOF-MS spectra (**Scheme 3.1. A** and **Table S3.2.**), ultimately turning the aqueous solution bluish-green. This is also in agreement with published results on TMB oxidation products[51].



Scheme 3.1. A: Proposed redox reaction mechanism between two enzyme substrates in the presence of OFL-Ti-MN. **B:** Proposed mechanism of KAN detection by OFL-Ti-MN/ H_2O_2 /TMB bioassay system

3.3.4. Colorimetric detection of KAN

Since KAN can effectively suppress the clear to bluish-green color change in the OFL-Ti-MN/TMB-H₂O₂ system, it is possible to detect the presence of KAN colorimetrically. To determine the mechanism of KAN detection, we used mass spectrum (m/z) to determine the supposed chemical structure of the final products (**Table S3.2.**). The data show that the TMB/diamine complex associated with H⁺ was present in the OFL-Ti-MN/TMB-H₂O₂ system, the color of which was also tested by measuring A₆₅₃. Nevertheless, as KAN was added to the solution, neither color was seen, nor any adduct was found in the MS spectra. The Q-TOF-MS produced [KAN+H⁺] positive ions at expected $m/z = 485.24$, illustrating that KAN was still in the final solution. Therefore, we propose a mechanism for KAN detection as depicted in **Scheme 3.1. B** (on left). We suppose intermolecular hydrogen bonds are formed between KAN hydroxyl or amino groups and the polar group (=O, -OH, and F)-modified surface of OFL-Ti-MN, constructing the fundamental infrastructures of nanomaterial-KAN complex [52]. Then, two adjacent KAN molecules attract each other via hydrogen bonding associated with the abundant hydroxyl and amino groups of the KAN scaffold and form a network [53]. Therefore, there is no space for H₂O₂ molecules to be adsorbed on the OFL-Ti-MN nor any hydrogen binding sites available for the TMB molecules. This network shields the OFL-Ti-MN surface and blocks it from being attacked by an enzyme substrate (**Scheme 3.1. B**, on right) [54]. As a result, there is no blue-colored TMB/diamine complex produced in the solution. Based on the experimental results, we calculated that about 40 μ M KAN could completely inactivate the enzymatic activity of 20 μ g/mL OFL-Ti-MN.

We also tested the effect of three other reported enzyme nano-mimics, Fe₃O₄ nanoparticles, CuO-doped graphene oxide, and PtNi nanoparticles, with KAN (**Figure S3.5.**) and found that KAN can inhibit the color change of these enzyme nano-mimics systems. As has been reported

previously, KAN chelates with transition metals (e.g., Cu(II), Fe(II), Co(II), etc.) via -NH₂ and -OH groups, producing transition metal-KAN complex compounds[55, 56].

Metalloenzymes account for multiple biological activities in all living species. Published results show that aminoglycoside molecules may modify metalloenzymes by sequestering the enzyme (metalloprotein/metalloenzyme) with multiple amino nitrogen and deprotonated alcoholic oxygen. In fact, they can chelate the metal ion center of biomolecules to produce a metal-aminoglycoside complex [57]. Finally, these complexes generate ROS in the cellular environment, which damages cells and induces ototoxicity in the inner ear [58]. Therefore, our proposed mechanism of colorimetric KAN detection can also shed some light at the molecular level on the antibacterial function of KAN and its side effects on humans.

Based on this color-change reaction, we developed methods for qualitative and quantitative analyses of KAN. The mixing time of KAN and OFL-Ti-MN was optimized before KAN measurement (**Figure S3.6.**). The relative response (RR, %) was calculated as:

$$RR = \frac{A_{653(t)}}{A_{653(0)}} * 100 \quad (3)$$

Where $A_{653(0)}$ and $A_{653(t)}$ are A_{653} values at 0 and t min, respectively, the lowest point RR value indicates that KAN reaches its maximum inhibition effect on the peroxidase-mimic solution in 10 min of mixing (**Figure S3.6.**).

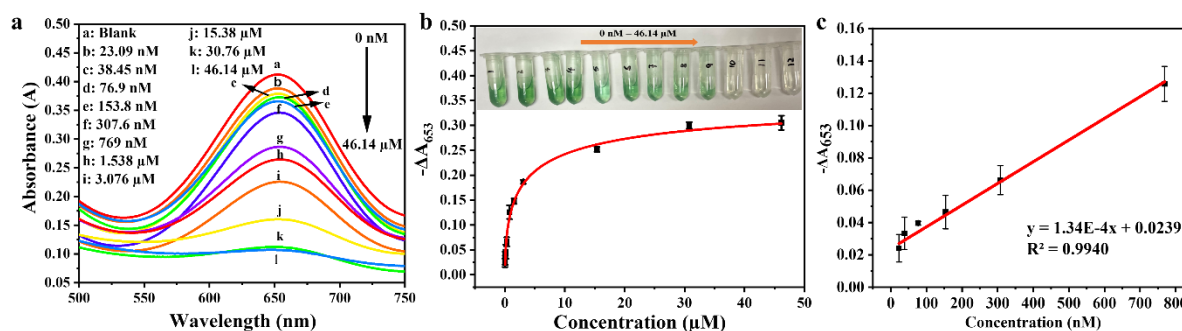


Figure 3.4. (a) UV-vis absorption spectra of the OFL-Ti-MN/H₂O₂/TMB bioassay with different amounts of KAN, (b) Dynamic range for colorimetric detection of KAN. Inset: picture of the OFL-Ti-MN solutions indicating the color change with different KAN concentrations, and (c) a linear relationship between KAN concentration and change in absorption intensity

According to UV-vis survey spectra of the OFL-Ti-MN/TMB-H₂O₂-KAN system (**Figure 3.4. (a)**), the absorbance peak of oxidized TMB declined gradually as KAN concentration increased from 23.09 nM to 46.14 μM. The dynamic activity range of this bioassay was calculated as:

$$-\Delta A_{653} = -(A_{653(\text{wk})} - A_{653(\text{nk})}) \quad (4)$$

where $A_{653(\text{wk})}$ and $A_{653(\text{nk})}$ are A_{653} values of OFL-Ti-MN/TMB-H₂O₂ with and without KAN, respectively. The calculated dynamic range is fairly wide, from 15.28 nM to 46.14 μM KAN. Inset in **Figure 3.4. (b)** shows the fading of the bluish-green color with increasing KAN concentration. Hence, it is possible to determine the KAN concentration semi-quantitatively with the naked eye. The sensor response is also highly linear ($R^2 = 0.9956$) in the KAN concentration range from 23.09 nM to 769 nM (**Figure 3.4. (c)**) [59]. The calculated limit of detection (LOD) of this colorimetric sensor was 15.28 nM (**Figure S3.7.**), which is much lower than the MRLs for KAN in milk per the EU (~320 nM) and KFDA (~214 nM)[22] regulations. The A_{653} value was then experimentally

obtained with 15.28 nM KAN to verify the sensor sensitivity at the estimated LOD value (**Figure S3.7**).

3.3.5. Selectivity and detection of KAN in real samples

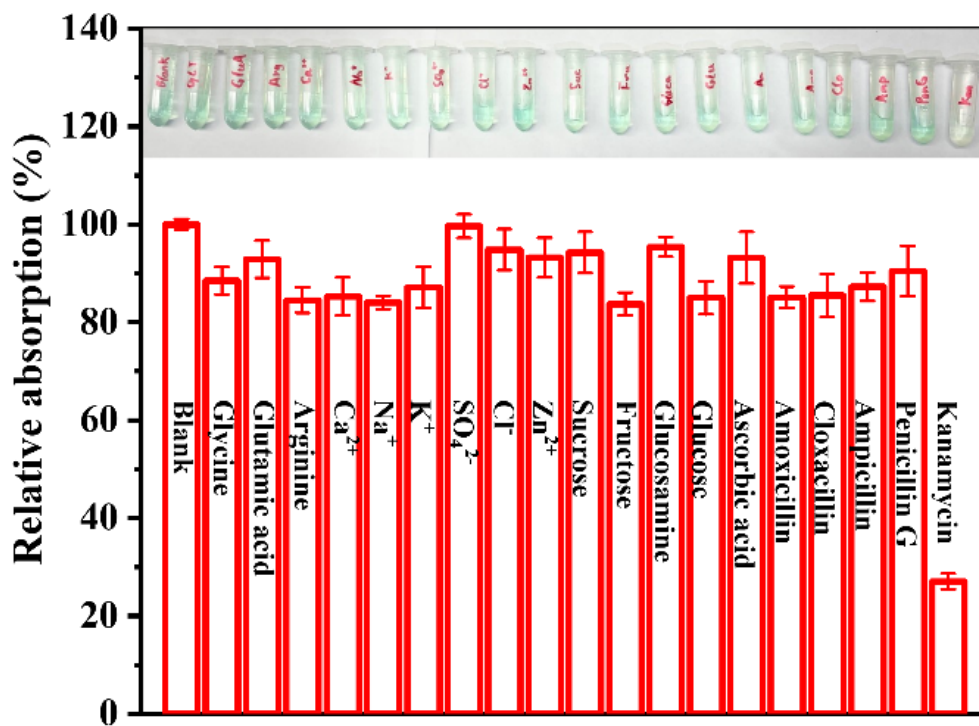


Figure 3.5. The OFL-Ti-MN/H₂O₂/TMB bioassay system for 18 different potential interferents and KAN analysis. Absorption values (A_{653}) relative to that of a blank for 18 potential interferents and KAN. Inset: pictures of the test samples.

The selectivity of this OFL-Ti-MN-based KAN sensor was measured by spiking milk and honey samples with KAN and different potential interferents, such as ions, sugars, vitamin C, amino acids, and antibiotics. As shown in **Figure 3.5**. (top), the intensity of the bluish-green color of samples with interferents is much stronger than that containing KAN. To quantify the sensor specificity, relative absorption (RA, %) values were calculated as:

$$RA = \frac{A_{653}(\text{analyte})}{A_{653}(\text{blank})} * 100 \quad (5)$$

Where $A_{653(\text{analyte})}$ and $A_{653(\text{blank})}$ are A_{653} values with different analytes and blank, respectively.

The lower the RA value, the higher the inhibition effect of the target on the OFL-Ti-MN nanozymatic system color change. Based on the data in Fig. 5, the RA value of KAN is significantly lower compared to those of other interferents. This confirms that the OFL-Ti-MN-based nanozymatic sensing system has excellent selectivity toward KAN.

KAN-spiked tap water, honey, and skim milk samples were tested to assess the practical application of the sensor. The recovery of spiked KAN ranged from 96.9 % to 108.8 % (**Table S3.3.**). The recovery values higher than 100%, especially in skim milk samples, are possibly due to their complex nature, where some protein interaction may affect the sensor response. Overall, these results illustrate the excellent performance of our OFL-Ti-MN-based colorimetric biosensing system.

3.4. Conclusions

In summary, the 2D OFL-Ti-MN was synthesized and verified to possess high peroxidase-mimic activity in the TMB- H_2O_2 system. With the peroxidase catalytic activity, the OFL-Ti-MN can facilitate to release $\bullet\text{OH}$ radicals in the presence of H_2O_2 molecules, oxidizing the TMB molecules to generate bluish-green TMBox products, thus altering the color of the test solution. Like the natural peroxidase, the catalytic performance of OFL-Ti-MN is highly dependent on the environmental pH, temperature, and reaction time. However, when KAN was added to this system, the electron transfer was blocked due to the hydrogen bonds formed between KAN and the surface of OFL-Ti-MN and chelation of KAN to the transition metal (e.g., Ti), resulting in the prevention of the redox reaction between the enzyme substrates (TMB/ H_2O_2). We employed the inhibitory effect of KAN on the color-change reaction in the OFL-Ti-MN/TMB- H_2O_2 system for colorimetric

measurement of KAN within 15 min. Though the LOD of our assay (15.3 nM) is higher than that of some other published ones, our method meets the MRLs of KAN required by different international organizations. Besides, our method is rapid (results shown within 15 min), easy to perform, and fairly inexpensive as it does not require immunological agents. In addition, the results offer a fundamental description of KAN in inhibiting peroxidase activity. These advantages make our method suitable for routine testing of KAN in real food matrices, with excellent specificity and sensibility. Further, this investigation opens the door to studies of other peroxidase-mimic nanostructures based on 2D OFL-Ti-MN with their applications in other organic chemical analyses.

3.5. Appendix III.

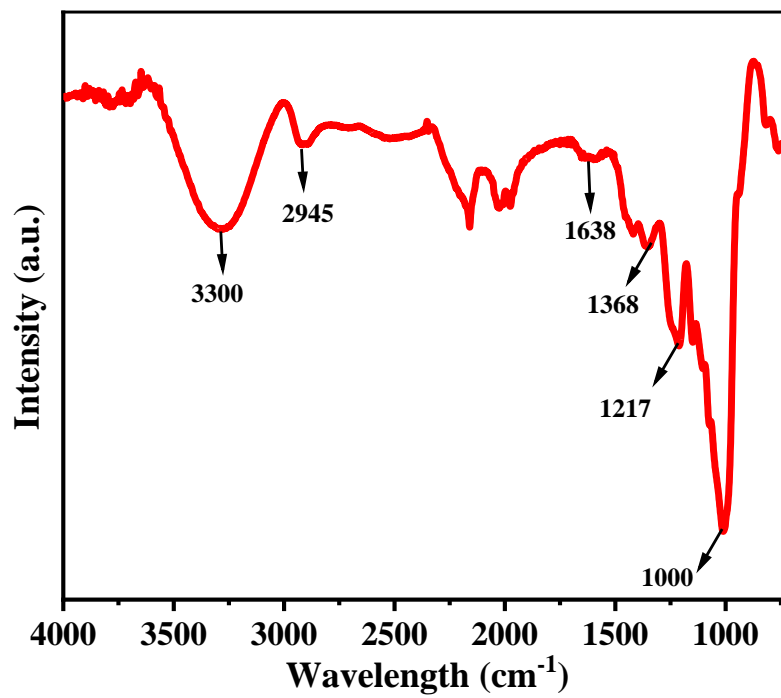


Figure S3.1. FT-IR spectrum for synthesized OFL-Ti-MN

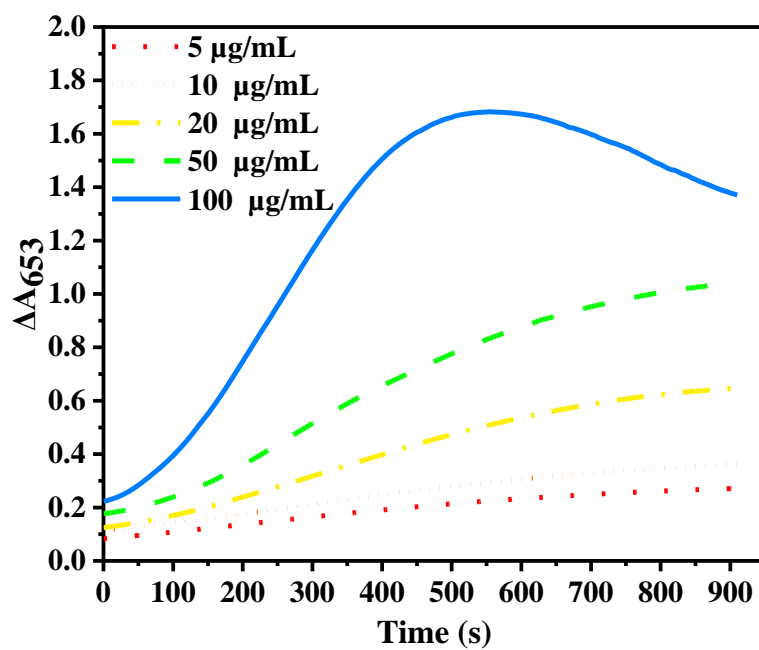


Figure S3.2. Reaction-time curves for TMB - H_2O_2 redox reaction catalyzed by different concentrations of OFL-Ti-MN

Table S3.1. Different enzyme nano-mimics with their Michaelis -Menten constants (K_m) and maximum reaction rate (V_{max}) under optimized conditions.

Enzyme-mimic	Substrate	K_m (mM)	$V_{max} * 10^{-8}$ ($M \cdot s^{-1}$)	Ref.
CuNPs	TMB	1.05	3.97	[60]
	H ₂ O ₂	31.26	26.4	
dBSA-Hem-AuNCs	TMB	0.52	2.47	[61]
	H ₂ O ₂	0.84	1.4	
Fe-MIL-88B	TMB	15	4	[62]
	H ₂ O ₂	17	6.7	
Pd/N-S-CS	TMB	1.44	24.1	[63]
	H ₂ O ₂	42.7	38.9	
Cu-Ag/rGO	TMB	0.63	4.25	[64]
	H ₂ O ₂	8.62	7.02	
FePt-Au HNPs	TMB	0.445	24.67	[65]
	H ₂ O ₂	0.0185	0.6894	
PRGI/Pt	TMB	2.37	97.1	[66]
	H ₂ O ₂	3.56	36.6	
3NiV-400	TMB	0.437	3.14	[67]
	H ₂ O ₂	15	2.02	
LaFeO ₃	TMB	0.427	73.01	[68]
	H ₂ O ₂	0.209	172.47	
Co ₄ S ₃ /Co(OH) ₂ HNTs	TMB	1.33	46.6	[69]
HRP	TMB	0.434	10	[40]
	H ₂ O ₂	3.700	8.710	
OFL-Ti-MN	TMB	0.305	4.96	This work
	H ₂ O ₂	677	1.39	

Note. NP: nanoparticles, dBSA: disassembled bovine serum albumin, Hem: Hemin, NC: nanocluster, HRP: horseradish peroxidase, Fe-MIL-88B: iron-based metal-organic framework, Pd/N-S-CS: Pd nanoparticles supported on nitrogen, sulfur-doped three-dimensional hierarchical nanostructures, HNPs: hybrid nanoparticles, PRGI/Pt: polyethylenimine-protected reduced graphene oxide anchoring iron oxide, 3NiV-400: 2D Ni-V mixed metal oxide, HNTs: hybrid nanotubes

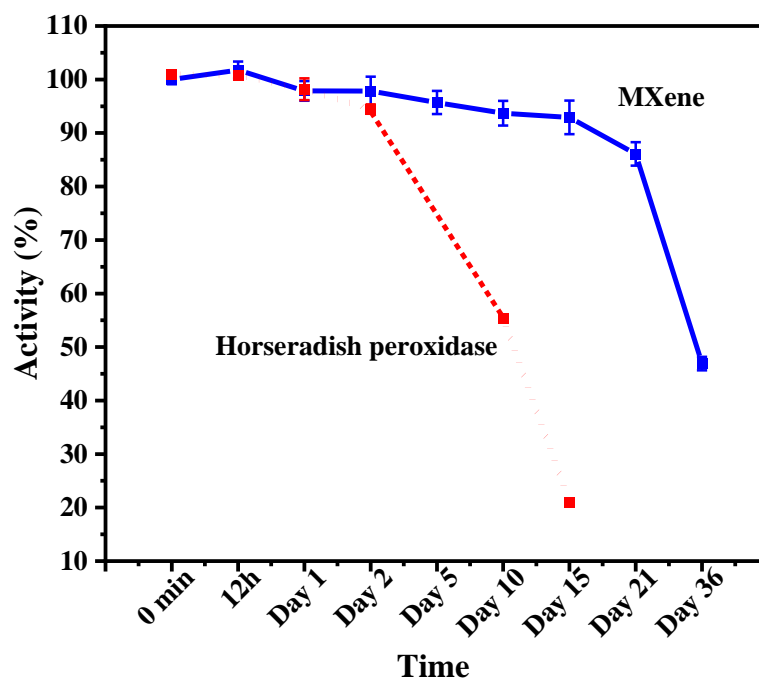


Figure S3.3. Stability of OFL-Ti-MN nanosheets and horseradish peroxidase during storage at room temperature. Error bars represent standard deviations of three replacements

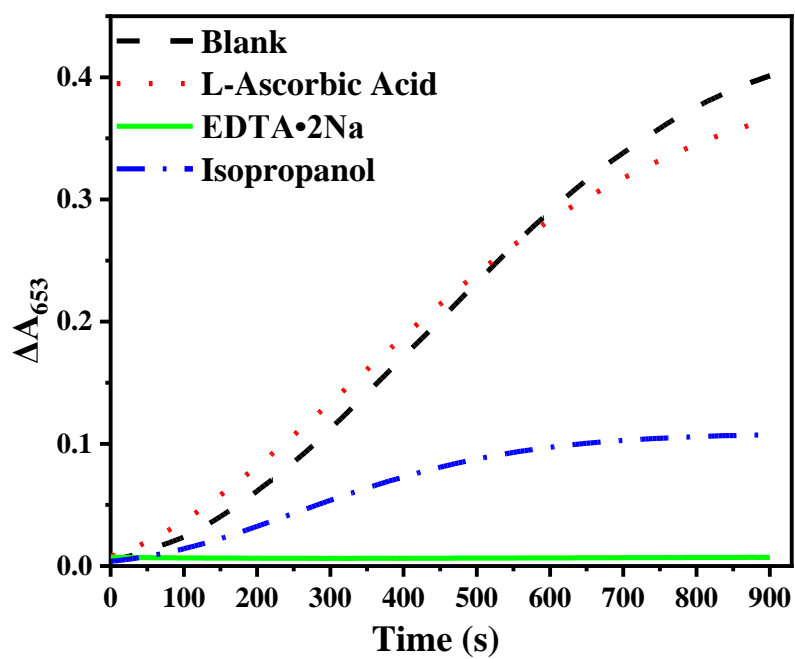
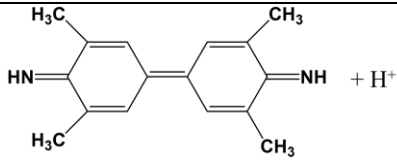
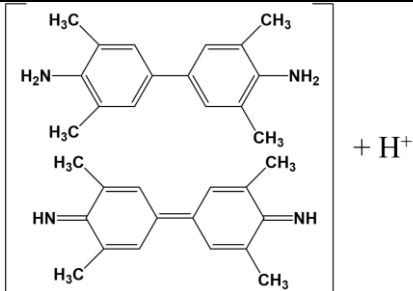
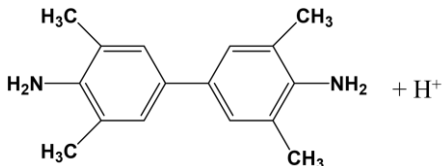
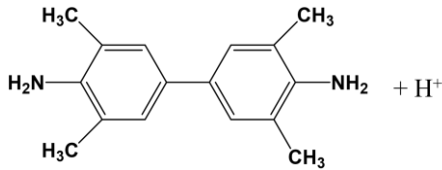
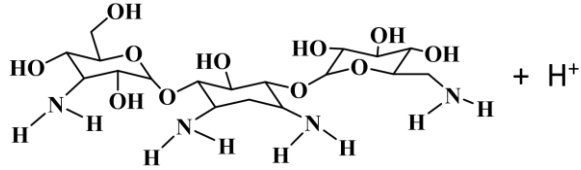


Figure S3.4. Change in UV-vis absorption peak at 653 nm (ΔA_{653}) as a function of time for free radical trapping experiment with different radical scavengers

Table S3.2. Q-TOF-MS information and proposed structures of TMB and KAN

Sample	m/z	Supposed structure
Blank	239.15	 <p>Di-imine</p>
	240.16	 <p>TMB / diamine complex</p>
	241.16	 <p>TMB</p>
KAN added in OFL-Ti-MN enzyme nano-mimics system	241.16	 <p>TMB</p>
	485.24	 <p>KAN</p>

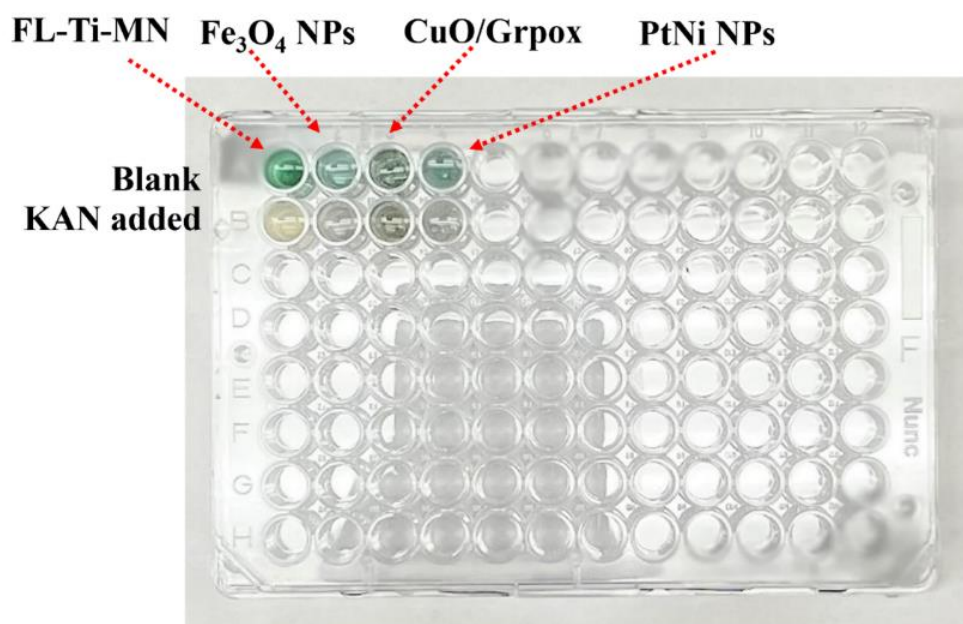


Figure S3.5. Photographs for adding KAN in the different peroxidase-mimic systems in the presence of enzyme substrates. Note: OFL-Ti-MN: oxygen terminated few-layered Ti-based MXene nanosheets, Fe_3O_4 NPs: Fe_3O_4 nanoparticles, CuO/Grpox: CuO nanoparticle doped graphene oxide, PtNi NPs: PtNi nanoparticles

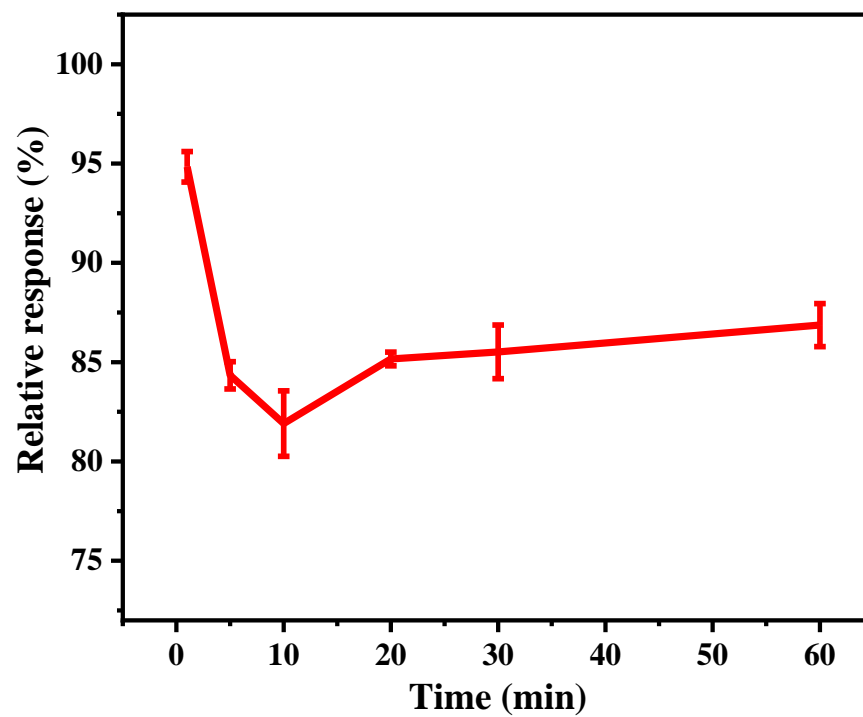


Figure S3.6. Optimization of mixing time for kanamycin and OFL-Ti-MN

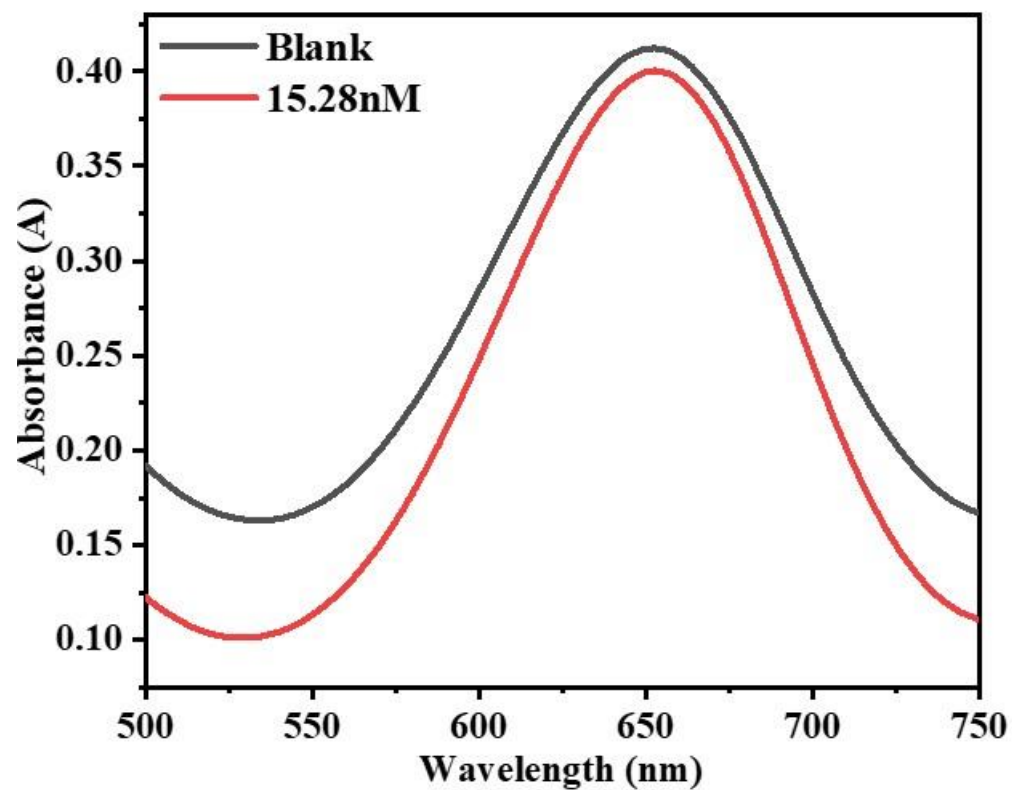


Figure S3.7. UV-vis scan of the OFL-Ti-MN/TMB/H₂O₂ biosensing system with KAN=15.28 nM (this is the calculated LOD value for KAN detection).

Table S3.3. Results for kanamycin (KAN) determination in three real samples.

Target	Sample	Spiked (μM)	Found (μM)	SD (% , n=3) *	Recovery (%)**
KAN	Tap water	0.05	0.0484	0.99	96.91
		0.10	0.0987	2.99	99.10
	Honey	0.05	0.0505	2.78	101.04
		0.10	0.102	4.63	102.22
	Skim milk	0.05	0.0541	1.23	108.21
		0.10	0.108	3.92	108.84

*: SD(% n=3): Standard Deviation in triplicate experiment

** : Recovery (%) = $C_{\text{found}}/C_{\text{spike}} * 100\%$

Table S3.4. Kanamycin analysis method reported in the literature

Analysis method	Biorecognition or its mimic element	LOD*	Linear range	Ref.**
Colorimetry	Aptamer	4.6 pM	0.01 ~ 100 nM	[70]
Electrochemistry	Aptamer and horseradish peroxidase	9.1 fg/mL	0.05 pg/mL ~ 10 ng/mL	[71]
Fluorescence	Aptamer	1 nM	5 ~ 50 nM	[72]
Potentiometry	Aptamer	0.05 pM	0.05 ~ 30 pM	[73]
Cantilever assay	Aptamer	50 μ M	100 μ M ~ 10 mM	[74]
Luminescence	Aptamer	143 nM	0.2 ~ 150 μ M	[75]
Fluorescence	Aptamer	59 nM	0.1 ~ 20 μ M	[76]
Colorimetry	OFL-Ti-MN	15 nM	23.09 ~ 769 nM	This work

*: LOD: Limit of detection

**: Ref. Reference

3.6. References

- [1] M. Misson, H. Zhang, B. Jin, Nanobiocatalyst advancements and bioprocessing applications, *Journal of the Royal Society Interface* 12(102) (2015) 20140891.
- [2] M.A. Mahdi, S.R. Yousefi, L.S. Jasim, M. Salavati-Niasari, Green synthesis of DyBa₂Fe₃O₇. 988/DyFeO₃ nanocomposites using almond extract with dual eco-friendly applications: Photocatalytic and antibacterial activities, *International Journal of Hydrogen Energy* 47(31) (2022) 14319-14330.
- [3] S.R. Yousefi, H.A. Alshamsi, O. Amiri, M. Salavati-Niasari, Synthesis, characterization and application of Co/Co₃O₄ nanocomposites as an effective photocatalyst for discoloration of organic dye contaminants in wastewater and antibacterial properties, *Journal of Molecular Liquids* 337 (2021) 116405.
- [4] S.R. Yousefi, O. Amiri, M. Salavati-Niasari, Control sonochemical parameter to prepare pure Zn₀. 35Fe₂. 65O₄ nanostructures and study their photocatalytic activity, *Ultrasonics sonochemistry* 58 (2019) 104619.
- [5] S.R. Yousefi, A. Sobhani, M. Salavati-Niasari, A new nanocomposite superionic system (CdHgI₄/HgI₂): synthesis, characterization and experimental investigation, *Advanced Powder Technology* 28(4) (2017) 1258-1262.
- [6] S.R. Yousefi, A. Sobhani, H.A. Alshamsi, M. Salavati-Niasari, Green sonochemical synthesis of BaDy₂ NiO₅/Dy₂ O₃ and BaDy₂ NiO₅/NiO nanocomposites in the presence of core almond as a capping agent and their application as photocatalysts for the removal of organic dyes in water, *RSC advances* 11(19) (2021) 11500-11512.
- [7] W. Wang, S. Gunasekaran, Nanozymes-based biosensors for food quality and safety, *TrAC trends in analytical chemistry* 126 (2020) 115841.
- [8] H. Wei, E. Wang, Nanomaterials with enzyme-like characteristics (nanozymes): next-generation artificial enzymes, *Chemical Society Reviews* 42(14) (2013) 6060-6093.
- [9] W. Wang, S. Gunasekaran, Potential Toxicology of Nanozymes, *Nanzymes*, CRC Press 2021, pp. 377-401.
- [10] M.K. Masud, J. Kim, M.M. Billah, K. Wood, M.J.A. Shiddiky, N.-T. Nguyen, R.K. Parsapur, Y.V. Kaneti, A.A. Alshehri, Y.G. Alghamidi, Nanoarchitected peroxidase-mimetic nanozymes: mesoporous nanocrystalline α - or γ -iron oxide?, *Journal of Materials Chemistry B* (2019).
- [11] H. Wang, K. Wan, X. Shi, Recent advances in nanozyme research, *Advanced Materials* (2018) 1805368.
- [12] X. Zhan, C. Si, J. Zhou, Z. Sun, MXene and MXene-based composites: synthesis, properties and environment-related applications, *Nanoscale Horizons* 5(2) (2020) 235-258.
- [13] X. Sang, Y. Xie, M.-W. Lin, M. Alhabeab, K.L. Van Aken, Y. Gogotsi, P.R. Kent, K. Xiao, R.R. Unocic, Atomic defects in monolayer titanium carbide (Ti₃C₂T_x) MXene, *ACS nano* 10(10) (2016) 9193-9200.
- [14] M. Shekhirev, J. Busa, C.E. Shuck, A. Torres, S. Bagheri, A. Sinitskii, Y. Gogotsi, Ultralarge Flakes of Ti₃C₂T_x MXene via Soft Delamination, *ACS nano* (2022).
- [15] B. Singh, R. Bahadur, S. Neekhara, M. Gandhi, R. Srivastava, Hydrothermal-assisted synthesis and stability of multifunctional MXene nanobipyramids: structural, chemical, and optical evolution, *ACS Applied Materials & Interfaces* 13(2) (2021) 3011-3023.
- [16] Z. Li, Y. Cui, Z. Wu, C. Milligan, L. Zhou, G. Mitchell, B. Xu, E. Shi, J.T. Miller, F.H. Ribeiro, Reactive metal-support interactions at moderate temperature in two-dimensional niobium-carbide-supported platinum catalysts, *Nature Catalysis* 1(5) (2018) 349-355.

- [17] A.n. Morales-García, F. Calle-Vallejo, F. Illas, MXenes: new horizons in catalysis, *ACS Catalysis* 10(22) (2020) 13487-13503.
- [18] Y. Zhang, L. Wang, N. Zhang, Z. Zhou, Adsorptive environmental applications of MXene nanomaterials: a review, *RSC advances* 8(36) (2018) 19895-19905.
- [19] T.M. Wassenaar, Use of antimicrobial agents in veterinary medicine and implications for human health, *Critical reviews in microbiology* 31(3) (2005) 155-169.
- [20] J.C. Paige, L. Tollefson, M.A. Miller, Health implications of residues of veterinary drugs and chemicals in animal tissues, *Veterinary Clinics of North America: Food Animal Practice* 15(1) (1999) 31-43.
- [21] G.M. Musiime, A.C. Seale, S.G. Moxon, J.E. Lawn, Risk of gentamicin toxicity in neonates treated for possible severe bacterial infection in low- and middle-income countries: systematic review, *Tropical medicine & international health* 20(12) (2015) 1593-1606.
- [22] N.-R. Ha, I.-P. Jung, I.-J. La, H.-S. Jung, M.-Y. Yoon, Ultra-sensitive detection of kanamycin for food safety using a reduced graphene oxide-based fluorescent aptasensor, *Scientific reports* 7 (2017) 40305.
- [23] M. Alhabeb, K. Maleski, B. Anasori, P. Lelyukh, L. Clark, S. Sin, Y. Gogotsi, Guidelines for synthesis and processing of two-dimensional titanium carbide (Ti₃C₂T_x MXene), *Chemistry of Materials* 29(18) (2017) 7633-7644.
- [24] B. Jiang, D. Duan, L. Gao, M. Zhou, K. Fan, Y. Tang, J. Xi, Y. Bi, Z. Tong, G.F. Gao, Standardized assays for determining the catalytic activity and kinetics of peroxidase-like nanozymes, *Nature protocols* 13(7) (2018) 1506-1520.
- [25] X. Liu, J. Yang, J. Cheng, Y. Xu, W. Chen, Y. Li, Facile preparation of four-in-one nanozyme catalytic platform and the application in selective detection of catechol and hydroquinone, *Sensors and Actuators B: Chemical* 337 (2021) 129763.
- [26] Y. Wang, L. Rao, P. Wang, Z. Shi, L. Zhang, Photocatalytic activity of N-TiO₂/O-doped N vacancy g-C₃N₄ and the intermediates toxicity evaluation under tetracycline hydrochloride and Cr (VI) coexistence environment, *Applied Catalysis B: Environmental* 262 (2020) 118308.
- [27] Y. Tang, Y. Hu, P. Zhou, C. Wang, H. Tao, Y. Wu, Colorimetric detection of kanamycin residue in foods based on the aptamer-enhanced peroxidase-mimicking activity of layered WS₂ nanosheets, *Journal of Agricultural and Food Chemistry* 69(9) (2021) 2884-2893.
- [28] J. Liu, J. Zeng, Y. Tian, N. Zhou, An aptamer and functionalized nanoparticle-based strip biosensor for on-site detection of kanamycin in food samples, *Analyst* 143(1) (2018) 182-189.
- [29] M. Naguib, M. Kurtoglu, V. Presser, J. Lu, J. Niu, M. Heon, L. Hultman, Y. Gogotsi, M.W. Barsoum, Two-dimensional nanocrystals produced by exfoliation of Ti₃AlC₂, *Advanced materials* 23(37) (2011) 4248-4253.
- [30] M. Shekhirev, C.E. Shuck, A. Sarycheva, Y. Gogotsi, Characterization of MXenes at every step, from their precursors to single flakes and assembled films, *Progress in Materials Science* 120 (2021) 100757.
- [31] W. Feng, H. Luo, S. Zeng, C. Chen, L. Deng, Y. Tan, X. Zhou, S. Peng, H. Zhang, Ni-modified Ti₃C₂ MXene with enhanced microwave absorbing ability, *Materials Chemistry Frontiers* 2(12) (2018) 2320-2326.
- [32] T.B. Limbu, B. Chitara, J.D. Orlando, M.Y.G. Cervantes, S. Kumari, Q. Li, Y. Tang, F. Yan, Green synthesis of reduced Ti₃C₂T_x MXene nanosheets with enhanced conductivity, oxidation stability, and SERS activity, *Journal of Materials Chemistry C* 8(14) (2020) 4722-4731.

- [33] L. Zhao, Z. Wang, Y. Li, S. Wang, L. Wang, Z. Qi, Q. Ge, X. Liu, J.Z. Zhang, Designed synthesis of chlorine and nitrogen co-doped Ti₃C₂ MXene quantum dots and their outstanding hydroxyl radical scavenging properties, *Journal of Materials Science & Technology* 78 (2021) 30-37.
- [34] W.Y. Chen, X. Jiang, S.-N. Lai, D. Peroulis, L. Stanciu, Nanohybrids of a MXene and transition metal dichalcogenide for selective detection of volatile organic compounds, *Nature communications* 11(1) (2020) 1-10.
- [35] Y.T. Liu, P. Zhang, N. Sun, B. Anasori, Q.Z. Zhu, H. Liu, Y. Gogotsi, B. Xu, Self-assembly of transition metal oxide nanostructures on MXene nanosheets for fast and stable lithium storage, *Advanced Materials* 30(23) (2018) 1707334.
- [36] S. Shah, T. Habib, H. Gao, P. Gao, W. Sun, M. Green, M. Radovic, Template-free 3D titanium carbide (Ti₃C₂T_x) MXene particles crumpled by capillary forces, *Chemical Communications* 53(2) (2017) 400-403.
- [37] A. Pazniak, P. Bazhin, N. Shplis, E. Kolesnikov, I. Shchetinin, A. Komissarov, J. Polcak, A. Stolin, D. Kuznetsov, Ti₃C₂T_x MXene characterization produced from SHS-ground Ti₃AlC₂, *Materials & Design* 183 (2019) 108143.
- [38] B. Rashid, A. Anwar, S. Shahabuddin, G. Mohan, R. Saidur, N. Aslfattahi, N. Sridewi, A Comparative Study of Cytotoxicity of PPG and PEG Surface-Modified 2-D Ti₃C₂ MXene Flakes on Human Cancer Cells and Their Photothermal Response, *Materials* 14(16) (2021) 4370.
- [39] E. Lee, A. VahidMohammadi, B.C. Prorok, Y.S. Yoon, M. Beidaghi, D.-J. Kim, Room temperature gas sensing of two-dimensional titanium carbide (MXene), *ACS applied materials & interfaces* 9(42) (2017) 37184-37190.
- [40] L. Gao, J. Zhuang, L. Nie, J. Zhang, Y. Zhang, N. Gu, T. Wang, J. Feng, D. Yang, S. Perrett, Intrinsic peroxidase-like activity of ferromagnetic nanoparticles, *Nature nanotechnology* 2(9) (2007) 577.
- [41] D. Zhu, H. Chen, C. Huang, G. Li, X. Wang, W. Jiang, K. Fan, H₂O₂ Self-Producing Single-Atom Nanozyme Hydrogels as Light-Controlled Oxidative Stress Amplifier for Enhanced Synergistic Therapy by Transforming "Cold" Tumors, *Advanced Functional Materials* (2022) 2110268.
- [42] J. Li, W. Liu, X. Wu, X. Gao, Mechanism of pH-switchable peroxidase and catalase-like activities of gold, silver, platinum and palladium, *Biomaterials* 48 (2015) 37-44.
- [43] M. Jeon, B.-M. Jun, S. Kim, M. Jang, C.M. Park, S.A. Snyder, Y. Yoon, A review on MXene-based nanomaterials as adsorbents in aqueous solution, *Chemosphere* 261 (2020) 127781.
- [44] K. Liu, K. Yan, G. Sun, Mechanism of H₂O₂/bleach activators and related factors, *Cellulose* 26(4) (2019) 2743-2757.
- [45] Q. Chen, S. Li, Y. Liu, X. Zhang, Y. Tang, H. Chai, Y. Huang, Size-controllable Fe-N/C single-atom nanozyme with exceptional oxidase-like activity for sensitive detection of alkaline phosphatase, *Sensors and Actuators B: Chemical* 305 (2020) 127511.
- [46] X. Zhou, M. Wang, J. Chen, X. Xie, X. Su, Peroxidase-like activity of Fe-N-C single-atom nanozyme based colorimetric detection of galactose, *Analytica Chimica Acta* 1128 (2020) 72-79.
- [47] C.M. Lousada, A.J. Johansson, T. Brinck, M. Jonsson, Mechanism of H₂O₂ decomposition on transition metal oxide surfaces, *The Journal of Physical Chemistry C* 116(17) (2012) 9533-9543.

- [48] C.W. Yoon, K.F. Hirsekorn, M.L. Neidig, X. Yang, T.D. Tilley, Mechanism of the decomposition of aqueous hydrogen peroxide over heterogeneous TiSBA15 and TS-1 selective oxidation catalysts: insights from spectroscopic and density functional theory studies, *ACS Catalysis* 1(12) (2011) 1665-1678.
- [49] D. Zhao, Z. Chen, W. Yang, S. Liu, X. Zhang, Y. Yu, W.-C. Cheong, L. Zheng, F. Ren, G. Ying, MXene (Ti₃C₂) vacancy-confined single-atom catalyst for efficient functionalization of CO₂, *Journal of the American Chemical Society* 141(9) (2019) 4086-4093.
- [50] Y. Huang, J. Ren, X. Qu, Nanozymes: classification, catalytic mechanisms, activity regulation, and applications, *Chemical reviews* 119(6) (2019) 4357-4412.
- [51] S. Gu, S. Risse, Y. Lu, M. Ballauff, Mechanism of the Oxidation of 3, 3', 5, 5' - Tetramethylbenzidine Catalyzed by Peroxidase-Like Pt Nanoparticles Immobilized in Spherical Polyelectrolyte Brushes: A Kinetic Study, *ChemPhysChem* 21(5) (2020) 450-458.
- [52] J. Hu, L. Yang, X. Cheng, Y. Li, Y. Cheng, Aminoglycoside-Based Biomaterials: From Material Design to Antibacterial and Gene Delivery Applications, *Advanced Functional Materials* 31(36) (2021) 2103718.
- [53] J.M. Dieterich, U. Gerstel, J.-M. Schröder, B. Hartke, Aggregation of Kanamycin A: dimer formation with physiological cations, *Journal of molecular modeling* 17(12) (2011) 3195-3207.
- [54] P.D. Josephy, Oxidative activation of benzidine and its derivatives by peroxidases, *Environmental health perspectives* 64 (1985) 171-178.
- [55] W. Szczepanik, P. Kaczmarek, J. Sobczak, W. Bal, K. Gatner, M. Jeżowska-Bojczuk, Copper (II) binding by kanamycin A and hydrogen peroxide activation by resulting complexes, *New Journal of Chemistry* 26(10) (2002) 1507-1514.
- [56] M. Jospe-Kaufman, L. Siomin, M. Fridman, The relationship between the structure and toxicity of aminoglycoside antibiotics, *Bioorganic & medicinal chemistry letters* 30(13) (2020) 127218.
- [57] M. Yang, S.A. Tomellini, Non-derivatization approach to high-performance liquid chromatography–fluorescence detection for aminoglycoside antibiotics based on a ligand displacement reaction, *Journal of Chromatography A* 939(1-2) (2001) 59-67.
- [58] W.-J. Wu, S.-H. Sha, J. Schacht, Recent advances in understanding aminoglycoside ototoxicity and its prevention, *Audiology and Neurotology* 7(3) (2002) 171-174.
- [59] W. Wang, F. Chen, Y. Wang, L. Wang, H. Fu, F. Zheng, L. Beecher, Optimization of reactions between reducing sugars and 1-phenyl-3-methyl-5-pyrazolone (PMP) by response surface methodology, *Food chemistry* 254 (2018) 158-164.
- [60] N. Wang, B. Li, F. Qiao, J. Sun, H. Fan, S. Ai, Humic acid-assisted synthesis of stable copper nanoparticles as a peroxidase mimetic and their application in glucose detection, *Journal of materials chemistry B* 3(39) (2015) 7718-7723.
- [61] S. Li, L. Zhang, Y. Jiang, S. Zhu, X. Lv, Z. Duan, H. Wang, In-site encapsulating gold “nanowires” into hemin-coupled protein scaffolds through biomimetic assembly towards the nanocomposites with strong catalysis, electrocatalysis, and fluorescence properties, *Nanoscale* 9(41) (2017) 16005-16011.
- [62] Z. Xu, L.-l. Long, Y.-q. Chen, M.-L. Chen, Y.-H. Cheng, A nanozyme-linked immunosorbent assay based on metal–organic frameworks (MOFs) for sensitive detection of aflatoxin B₁, *Food Chemistry* 338 (2021) 128039.
- [63] W. Shi, H. Fan, S. Ai, L. Zhu, Pd nanoparticles supported on nitrogen, sulfur-doped three-dimensional hierarchical nanostructures as peroxidase-like catalysts for colorimetric detection of xanthine, *RSC Advances* 5(41) (2015) 32183-32190.

- [64] G. Darabdhara, B. Sharma, M.R. Das, R. Boukherroub, S. Szunerits, Cu-Ag bimetallic nanoparticles on reduced graphene oxide nanosheets as peroxidase mimic for glucose and ascorbic acid detection, *Sensors and Actuators B: Chemical* 238 (2017) 842-851.
- [65] Y. Ding, B. Yang, H. Liu, Z. Liu, X. Zhang, X. Zheng, Q. Liu, FePt-Au ternary metallic nanoparticles with the enhanced peroxidase-like activity for ultrafast colorimetric detection of H₂O₂, *Sensors and Actuators B: Chemical* 259 (2018) 775-783.
- [66] L. Liu, B. Du, C. Shang, J. Wang, E. Wang, Construction of surface charge-controlled reduced graphene oxide-loaded Fe₃O₄ and Pt nanohybrid for peroxidase mimic with enhanced catalytic activity, *Analytica chimica acta* 1014 (2018) 77-84.
- [67] C. Chen, Y. Wang, Z. Yang, D. Zhang, Layered double hydroxide derived ultrathin 2D Ni-V mixed metal oxide as a robust peroxidase mimic, *Chemical Engineering Journal* 369 (2019) 161-169.
- [68] L. Chen, J. Yang, W. Chen, S. Sun, H. Tang, Y. Li, Perovskite mesoporous LaFeO₃ with peroxidase-like activity for colorimetric detection of gallic acid, *Sensors and Actuators B: Chemical* 321 (2020) 128642.
- [69] J. Wang, Y. Wang, D. Zhang, C. Chen, Intrinsic oxidase-like nanoenzyme Co₄S₃/Co (OH)₂ hybrid nanotubes with broad-spectrum antibacterial activity, *ACS Applied Materials & Interfaces* 12(26) (2020) 29614-29624.
- [70] X. Zhu, L. Tang, J. Wang, B. Peng, X. Ouyang, J. Tan, J. Yu, H. Feng, J. Tang, Enhanced peroxidase-like activity of boron nitride quantum dots anchored porous CeO₂ nanorods by aptamer for highly sensitive colorimetric detection of kanamycin, *Sensors and Actuators B: Chemical* 330 (2021) 129318.
- [71] W. Huang, Y. Zhou, D. Zhan, G. Lai, Homogeneous biorecognition reaction-induced assembly of DNA nanostructures for ultrasensitive electrochemical detection of kanamycin antibiotic, *Analytica Chimica Acta* 1154 (2021) 338317.
- [72] T. Ye, Y. Peng, M. Yuan, H. Cao, J. Yu, Y. Li, F. Xu, A "turn-on" fluorometric assay for kanamycin detection by using silver nanoclusters and surface plasmon enhanced energy transfer, *Microchimica Acta* 186(1) (2019) 1-8.
- [73] Y. Yao, C. Jiang, J. Ping, Flexible freestanding graphene paper-based potentiometric enzymatic aptasensor for ultrasensitive wireless detection of kanamycin, *Biosensors and Bioelectronics* 123 (2019) 178-184.
- [74] X. Bai, H. Hou, B. Zhang, J. Tang, Label-free detection of kanamycin using aptamer-based cantilever array sensor, *Biosensors and Bioelectronics* 56 (2014) 112-116.
- [75] K.-H. Leung, H.-Z. He, D.S.-H. Chan, W.-C. Fu, C.-H. Leung, D.-L. Ma, An oligonucleotide-based switch-on luminescent probe for the detection of kanamycin in aqueous solution, *Sensors and Actuators B: Chemical* 177 (2013) 487-492.
- [76] Y.-P. Xing, C. Liu, X.-H. Zhou, H.-C. Shi, Label-free detection of kanamycin based on a G-quadruplex DNA aptamer-based fluorescent intercalator displacement assay, *Scientific reports* 5(1) (2015) 1-8.

Chapter IV. Nanozymatic degradation and simultaneous colorimetric detection of tetracycline*

Abstract

Tetracycline (TC) is a broad-spectrum antibiotic that can enter and accumulate in the human body via the food chain. Even in small concentrations, TC can cause several malignant health effects. We developed a system to simultaneously degrade the presence of TC in food matrices using titanium carbide MXene (FL-Ti₃C₂T_x). The FL-Ti₃C₂T_x exhibited biocatalytic property that activates hydrogen peroxide (H₂O₂) molecules in 3, 3', 5, 5'-tetramethylbenzidine (TMB) environment. During the FL-Ti₃C₂T_x reaction, the catalytic products released turn the color of the H₂O₂/TMB system bluish-green. However, when TC is present, the bluish-green color does not appear. Via quadrupole time-of-flight mass spectrometry, we found that the TC is degraded by FL-Ti₃C₂T_x / H₂O₂ in preference to H₂O₂/TMB redox reaction, which intervenes in the color change. Hence, we developed a colorimetric assay to detect TC with a LOD of 615.38 nM and proposed two TC degradation pathways that facilitate the highly sensitive colorimetric bioassay.

4.1. Introduction

The abuse of antibiotics for the antibacterial treatment of livestock and humans has been reported to deteriorate the natural ecosystem, especially water resources, and ultimately threaten human health via the food chain. Tetracycline (TC), a broad-spectrum antibiotic, is one of the most detected antibiotics in the environment of dairy products. For instance, TC was found at 11.16 ng/L in drinking water resources and in 14% of all cases of antibiotics detected in milk products worldwide [1]. Nevertheless, as it is hardly degraded in the natural environment, TC can stay in agri-food resources for a long time. Besides,

*Wang, W., Yin, Y., Gunasekaran, S., (2023). Nanozymatic degradation and simultaneous colorimetric detection of tetracycline. *Food Chemistry*, 136607, Copyright Elsevier.

difficulty in absorption and metabolization *in vivo* helps TC enter via the food chain and accumulate in the human body easily [2]. The accumulation of TC, even in small concentrations, can cause several malignant effects on human health, such as hepatotoxicity and genotoxicity [3]. Therefore, the United States Food and Drug Administration (USFDA) has set the maximum residue limits (MRLs) for tetracyclines in raw milk as 676 nM [4].

TC detection has been mainly based on traditional methods, such as high-performance liquid chromatography (HPLC), antimicrobial bioassay, and liquid chromatography-tandem mass spectrometry (LC-MS-MS) [5]. Though highly sensitive and selective, these methods are time-consuming, expensive, and laborious, which limits their applications *on-site* [6]. Besides, those methods cannot degrade TC after analysis. As a result, TC is usually released into the waste stream after analysis, which requires a further step for TC degradation before the waste stream is permitted to enter the environment. There are some efforts put into the photodegradation of TC, such as Fe-based MOFs, Ag/TiO₂ nanocomposites, etc. [7, 8]. However, they are only used for TC degradation, which are not able to monitor the concentration of TC in the agri-food system. Therefore, a method that can both detect and degrade TC is highly desirable.

Enzyme nano-mimics are nanomaterials with natural enzymatic properties. They are gaining increasing attention due to their excellent intrinsic catalytic ability, high stability, low cost, and prolonged life cycle [9]. Many enzyme nano-mimics are being explored for qualitative and quantitative measurement of multiple biomolecules by triggering the reactions between the enzymatic substrates [10].

Recently, MXenes have been recognized as a new 2D nanomaterial family that affords excellent physical and chemical properties, i.e., electrical conductivity, good reducibility,

etc. Among the MXenes, titanium carbide (Ti_3C_2) has been popular since it exhibits electrical conductivity ($6500 \text{ S}\cdot\text{cm}^{-1}$) comparable to that of carbon nanotubes [11]. Ti_3C_2 is exfoliated from its parent bulk ceramic MAX phase precursor (Ti_3AlC_2) by selective Al element etching[12]. Due to the strong acid-involved etching process, i.e., using highly concentrated HF, atom deficiency derived from Ti atom(s) removal on the Ti layer surface can offer excellent reducibility to Ti_3C_2 . Moreover, depending on the type of etchant used, there are different surface terminations of Ti_3C_2 , i.e., -F, -O, -OH, etc., contributing to the T_x symbol in the MXene denotation ($\text{Ti}_3\text{C}_2\text{T}_x$) [13]. These help $\text{Ti}_3\text{C}_2\text{T}_x$ in being a promising catalyst for biosensing and toxins degradation applications.

We synthesized a few-layered $\text{Ti}_2\text{C}_2\text{T}_x$ (FL- $\text{Ti}_2\text{C}_2\text{T}_x$) MXene via the minimally intensive layer delamination (MILD) method. The FL- $\text{Ti}_2\text{C}_2\text{T}_x$ is used as a peroxidase mimic for catalyzing the redox reaction between two 3,3',5,5'-tetramethylbenzidine (TMB) and hydrogen peroxide (H_2O_2), turning a colorless sample solution bluish green. However, the bluish-green color disappears when TC is introduced into this system. Based on this, we developed a colorimetric biosensor for the detection of TC and proposed a mechanism for the detection of TC. We found that TC is degraded by H_2O_2 in the presence of FL- $\text{Ti}_2\text{C}_2\text{T}_x$ in preference to the TMB oxidation reaction, which prevents the color change from occurring. Hence, this nanozymatic catalytic mechanism facilitates the degradation of TC and simultaneously its colorimetric detection in real matrices.

4.2. Experimental section

4.2.1. Materials and reagents

H₂O₂ solution (30%) was purchased from ACROS Organics. MAX phase precursor was obtained from Nano-Mall Technology Co. Ltd, China. Two β -lactams antibiotics (penicillin G and ampicillin) were obtained from Scientific Inc. In addition, amoxicillin was purchased from Chem-Impex International Inc. Skim milk was purchased from a local supermarket. Other chemicals not explicitly mentioned here are of analytical grade obtained from Sigma-Aldrich. Buffer solutions were prepared using deionized (DI) water (18 M Ω .cm).

4.2.2. Synthesis of FL-Ti₃C₂T_x

FL-Ti₃C₂T_x was exfoliated from the Ti₃AlC₂ MAX phase using lithium fluoride salt (LiF) solution for selective etching Al interlayer [12]. Briefly, an etchant mixture was first prepared by dissolving 0.8 g LiF into 10 mL concentrated hydrogen chloride (HCl, 9 M) and mixed at 22 °C for 10 min. Next, 0.5 g Ti₃AlC₂ precursor was gradually added to this acidic solution, continuously being kept at 22 °C for one day. The suspension was rinsed with DI water and centrifuged five times until the final solution reached pH > 6.0. Then, the supernatant containing multi-layer Ti₃C₂T_x was collected and ultrasonicated for 3 h under N₂ protection. Finally, a dark FL-Ti₃C₂T_x powder was obtained after freeze-drying.

4.2.3. Characterization

A field emission scanning electron microscope (LEO1530, Gemini FE-SEM) was used to observe the surface morphology of FL-Ti₃C₂T_x MXene. The chemical composition and structure of FL-Ti₃C₂T_x MXene were investigated by X-ray photoelectron spectroscopy (XPS) (Thermo Scientific K-Alpha) and Fourier transform-infrared (FT-IR, Spectrum 100,

Perkin Elmer) spectroscopy. The X-ray diffraction (XRD) pattern and UV-vis absorbance peak were studied by a Bruker D8 Discovery X-ray diffractometer equipped with Cu K α radiation and ultraviolet-visual (UV-vis) spectroscopy with a spectrometer (Lambda 35, PerkinElmer), respectively. Electrochemical analysis was performed in dark and light conditions in an electrochemical workstation (CH-660D, CH Instrument Inc.) with an Ag/AgCl (3 M KCl) reference electrode, a platinum counter electrode, and a carbon working electrode. Electrochemical impedance spectroscopy (EIS) was also performed in the frequency range of 1 Hz to 100 kHz at open circuit potential.

4.2.4. Peroxidase-mimic behavior of Ti₃C₂T_x MXene

The peroxidase mimic activity of FL-Ti₃C₂T_x MXene was investigated in the TMB and H₂O₂ system. Typically, synthesized FL-Ti₃C₂T_x MXene was first dissolved in the DI water to prepare a 4 mg/mL FL-Ti₃C₂T_x stock solution. Next, 10 μ L FL-Ti₃C₂T_x stock solution was transferred into a curvet and diluted 100-fold by different pH buffer solutions (0.2 M sodium acetate/acetic acid buffer) ranging from 3.0 to 6.0 to prepare 40 μ g/mL FL-Ti₃C₂T_x MXene solution. The prepared MXene suspension was transferred to a mixture of 5 mM TMB (100 μ L) and 200 μ L H₂O₂ (30%) solution, running under a water bath (12°C ~ 70°C) for 15 min.

The free radical trapping experiment was conducted in solutions of ethylenediaminetetraacetic acid disodium salt (EDTA•2Na), L-ascorbic acid (LAA), and isopropanol (IPA) separately mixed with Ti₃C₂T_x/TMB/H₂O₂ under optimal conditions for hole (h⁺), superoxide anion (\bullet O₂⁻), and hydroxyl radicals (\bullet OH) capture, respectively [14].

4.2.5. Colorimetric analysis of TC

Colorimetric detection of TC was performed with a FL-Ti₃C₂T_x-containing enzymatic system. First, Ti₃C₂T_x powders were dissolved in the DI water to prepare a 4 mg/mL stock solution. Next, 1 mL 2.5 mg/mL FL-Ti₃C₂T_x solution was prepared by activating the stock solution (4 mg/mL) in the buffer solution (0.2 M sodium acetate/acetic acid buffer). 8 μ L of 2.5 mg/mL Ti₃C₂T_x solution was then diluted into 1 mL of 20 μ g/mL via DI water, which was reacted with different amounts of TC under room temperature for 10 min. Next, a mixture of TMB (5 mM, 100 μ L) and 200 μ L H₂O₂ (30 %) were transferred into the above mixture and reacted for 15 min in a water bath set at 37 °C. The UV-vis absorption value of the final mixture at 653 nm was recorded as A₆₅₃. Bruker Maxis ultra-high resolution quadrupole time-of-flight mass spectrometry (QTOF MS) was employed in positive ionization mode to analyze the mass/charge (m/z) of various TC degradation products.

To determine the TC concentration in real food and environmental matrices, tap water and skim milk samples spiked with TC were tested [15]. Tap water was vortexed rigorously after spiking with 4 and 8 μ M TC for 10 min and was in the ultrasonic water bath for 30 mins. The final solution was ready to be used. For the TC-spiking of skim milk, milk diluted by DI water (1:10) was spiked with 4 and 8 μ M TC, which then was added with 20 % acetic acid (v/v) to adjust pH to 4.6 to denature and precipitate milk proteins. Next, protein precipitates were removed by centrifuging at 14,000 rpm for 15 min, which was then filtered by a 0.22- μ m syringe filter. All measurements were conducted in triplicate.

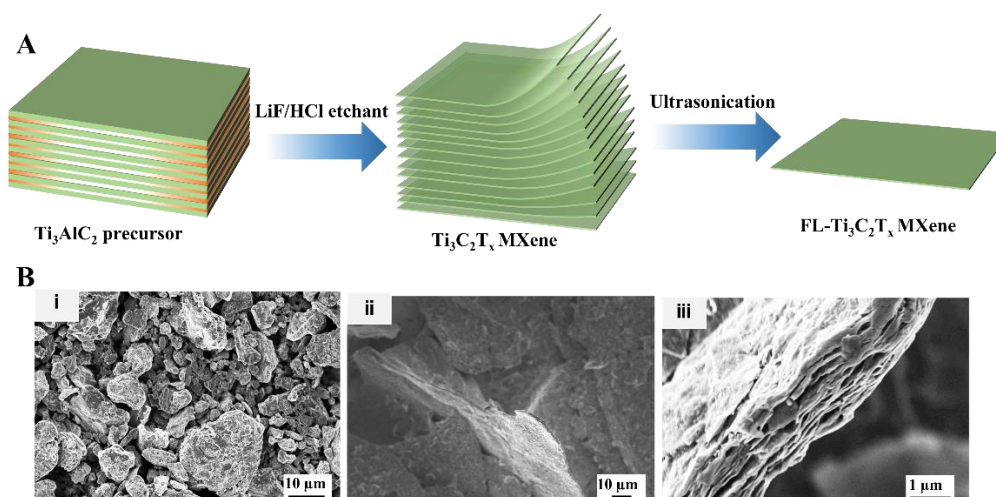


Figure 4.1. A. Schematic of FL- $\text{Ti}_3\text{C}_2\text{T}_x$ nanosheet synthesis process. B. SEM micrographs of Ti_3AlC_2 precursor surface (i) and cross-sectional view of prepared FL- $\text{Ti}_3\text{C}_2\text{T}_x$ nanosheet at different magnifications (ii, iii).

4.3. Results and discussion

4.3.1. Synthesis and characterization of $\text{Ti}_3\text{C}_2\text{T}_x$ MXene

Figure 4.1. A is a schematic representation of the FL- $\text{Ti}_3\text{C}_2\text{T}_x$ MXene preparation process. The microstructure of the Ti_3AlC_2 precursor (**Figure 4.1. B(i)**) shows randomly distributed several anomalous pebble-like particles ($>10\ \mu\text{m}$) on the surface. SEM images of FL- $\text{Ti}_3\text{C}_2\text{T}_x$ show that the nanosheets are uniformly spaced and distributed with a large specific surface area, suggesting effective layer separation (**Figure 4.1. B(ii, iii)**). According to **Figure 4.1. B(ii)**, the surface area of etched FL- $\text{Ti}_3\text{C}_2\text{T}_x$ nanosheets was further expanded and exposed to the ambient conditions, benefiting from the few ultrathin layers collected after the exfoliation of multilayered $\text{Ti}_3\text{C}_2\text{T}_x$ MXene (**Figure 4.1. B(iii)**). Therefore, these unique features afford FL- $\text{Ti}_3\text{C}_2\text{T}_x$ nanosheets the ability to entrap a large amount of substrate to facilitate their enzymatic-mimic activities.

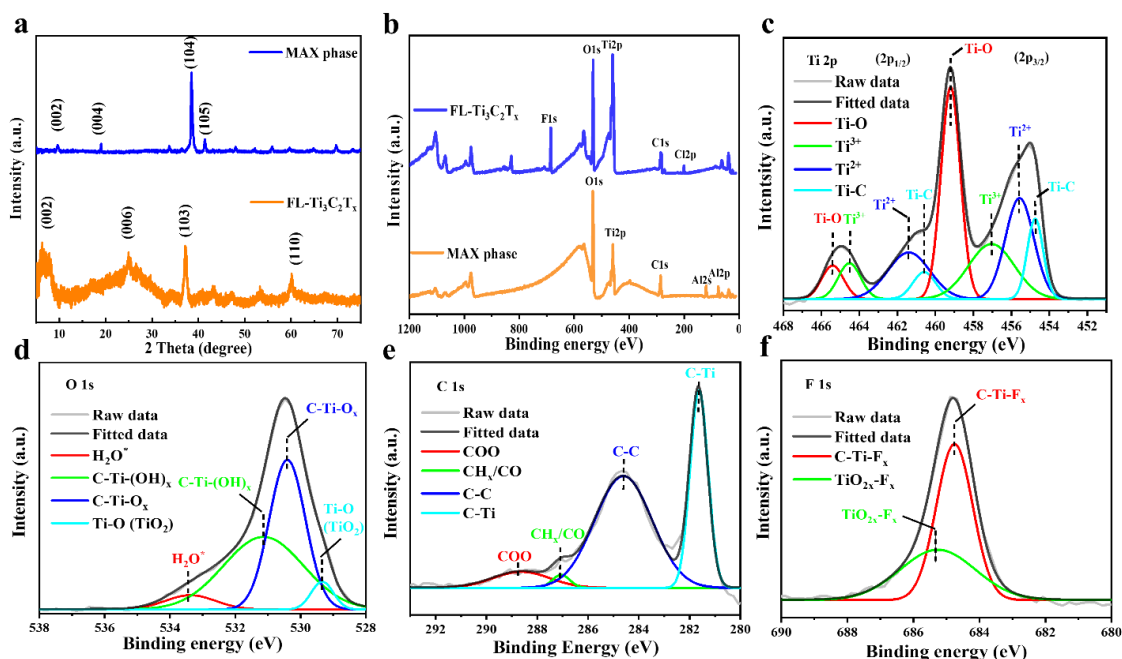


Figure 4.2. XRD spectrum and full scan XPS spectra for synthesized FL-Ti₃C₂T_x nanosheets and MAX phase (a, b), XPS spectra of Ti 2p, O 1s, C 1s, and F 1s for FL-Ti₃C₂T_x nanosheets, respectively (c-f).

The crystalline patterns of exfoliated FL-Ti₃C₂T_x and the MAX phase precursor were determined by the XRD. As seen in **Figure 4.2. (a)**, a significant sharp peak, identified as the (104) index in the MAX phase spectrum at $2\theta = 38.84^\circ$, indicates the high quality of the MAX phase precursor [16]. On the contrary, there is no obvious diffraction peak at (104) in the FL-Ti₃C₂T_x after LiF/HCl treatment, ascribed to the highly effective Al interlayer etching. Meanwhile, a broader (002) peak observed at $2\theta = 6.4^\circ$ in the FL-Ti₃C₂T_x pattern is caused by the loss of crystallinity and expanded interlayer space after exfoliation [17]. According to Bragg law, the interlayer d-spacing of FL-Ti₃C₂T_x is calculated to be around 13.88 Å [18]. These results confirm that the Al interlayer has been etched off completely. The intercalated Li⁺ ions cause the exfoliated FL-Ti₃C₂T_x flakes to

expand their interlayer spacing, which can eliminate the potential for re-stacking of the FL-Ti₃C₂T_x flakes.

The XPS survey spectrum was used to analyze the chemical states and surface composition of the MAX phase and fabricated FL-Ti₃C₂T_x nanosheets. According to **Figure 4.2. (b)**, the full scan XPS spectrum for elemental components of the MAX phase and prepared FL-Ti₃C₂T_x MXene nanosheets shows the existence of C 1s and Ti 2p at binding energy (BE) of 284 eV and 458 eV, respectively. These two elemental peaks prove that the MAX phase and FL-Ti₃C₂T_x MXene are mainly composed of Ti and C elements. However, XPS spectra of the MAX phase and prepared FL-Ti₃C₂T_x MXene nanosheets contain O 1s, caused by the partial oxidization of O₂ during either storage or the FL-Ti₃C₂T_x MXene fabrication process. Further, XPS results of FL-Ti₃C₂T_x show, when compared to XPS of the the MAX phase, two additional prominent peaks centered at BE of 685 eV and 198 eV, associated with F 1s and Cl 2p peaks, respectively, possibly owing to the etchant mixture used during etching [19].

Additionally, no Al 2s and Al 2p peaks were seen in the XPS scan of FL-Ti₃C₂T_x nanosheets, which supports that the Al interlayer has been completely etched off. Ti 2p XPS spectrum (**Figure 4.2. (c)**) was separated into two areas with a ratio of 2:1 as 2p_{1/2} and 2p_{3/2} regions composed of four pairs of doublets. In the 2p_{3/2} region, four signals centered at BEs of 459.2 eV, 457.0 eV, 455.6 eV, and 454.7 eV are recognized as Ti-O, Ti³⁺, Ti²⁺, and Ti-C, respectively[20]. In parallel, three types of Ti-O bonding in the O 1s spectrum (**Figure 4.2. (d)**) are centered at BE of 531.1 eV, 530.5 eV, and 529.4 eV, corresponding to C-Ti-(OH)_x, C-Ti-O_x, and Ti-O (TiO₂), respectively [21]. It is noted that most existing O elements are in the form of Ti-O (TiO₂) or C-Ti-O_x based on the O spectrum, indicating

that the FL-Ti₃C₂T_x MXene nanosheets also possess the catalytic properties of TiO₂ [22]. In **Figure 4.2. (e)**, the C 1s region of prepared FL-Ti₃C₂T_x nanosheets exhibits four peaks, COO, CH_x/CO, C-C, and C-Ti, with their corresponding BEs of 288.6 eV, 287.0 eV, 284.5 eV, and 281.4 eV. Based on the Ti 2p and C 1s spectrum, MXene has been obtained with Ti₃C₂ as its scaffold. Whereas, the emerging oxygen-related bonds in the above spectrum confirm that interlayers of FL-Ti₃C₂T_x have largely reacted with O₂ during the preparation process owing to the high reductivity of MXene [23]. This was verified by the FT-IR spectra which show the existence of a large quantity of oxygen-related bonds.

The presence of two adsorption peaks in the FL-Ti₃C₂T_x MXene spectrum centered at 3317 cm⁻¹ and 1351 cm⁻¹ (**Appendix IV, Figure S4.1.**) reveals the presence of -OH groups, led by the adsorption of H₂O molecules on the surface of FL-Ti₃C₂T_x nanosheets and growth of -OH groups on carbon or metallic Ti layers [24]. Moreover, a bond between oxygen at 1000 cm⁻¹ and a double bond of C=O at 1638 cm⁻¹ is observed in the FT-IR spectrum [25]. The bond vibration of C-F (1219 cm⁻¹) was analyzed by the FT-IR (verified by XPS spectra of **Figure 4.2. (f)**), which was mainly caused by the LiF/HCl etching process. These functional groups (-F, -OH, =O, etc.) terminated on the surface of FL-Ti₃C₂T_x nanosheets can help enhance the catalytic performance of MXene in the enzymatic environment and later for TC degradation.

Raman spectra of MAX phase precursor and FL-Ti₃C₂T_x nanosheets are compared in **Figure S4.2. (Appendix IV)** Modes I, II, and III located around 260 cm⁻¹, 400 cm⁻¹, and 625 cm⁻¹ are critical features for the MAX phase, in agreement with the previous literature [26]. Specifically, peak I is associated with Ti-Al vibration, while peaks II and III are caused by Ti-C vibration[27]. In comparison, peak I is not observed in Raman spectra of FL-Ti₃C₂T_x nanosheets, indicating that the Al layer was removed during the etching.

Additionally, it is common in layered MXene structures to have their surface undisturbed after Al etching, given the evidence of broad peaks II and III with low intensity in FL-Ti₃C₂T_x nanosheets [28]. It is worth noting that a predominate peak at 150 cm⁻¹ indicates the oxidized FL-Ti₃C₂T_x formation after the etching process [26]. In the 1100 cm⁻¹ to 1700 cm⁻¹ region, two more legible Raman scattering peaks at 1358 cm⁻¹ and 1597 cm⁻¹, assigned as the D band and G band of more disordered graphitic carbon, were revealed in MXene after LiF-HCl etching [29].

4.3.2. pH and temperature effects on FL-Ti₃C₂T_x peroxidase activity

Oxidation of TMB by H₂O₂ is usually triggered by peroxidase, which releases bluish-colored reaction products in the solution, which can be measured by UV/vis absorption at a wavelength of 653 nm (A₆₅₃) [9]. We discovered that the FL-Ti₃C₂T_x nanosheets, acting as a peroxidase nano-mimic, can trigger the oxidation of TMB in the H₂O₂ environment [30]. According to **Figure 4.3. (a)**, A₆₅₃ values of the TMB+H₂O₂, TMB+MXene, and H₂O₂+MXene systems were negligible. However, when FL-Ti₃C₂T_x MXene nanosheets were present along with TMB and H₂O₂ system, a substantial A₆₅₃ reading was obtained. This demonstrates the peroxidase-mimicking ability of FL-Ti₃C₂T_x MXene.

The optimal temperature and pH conditions for this nanozymatic reaction were determined (**Figure 4.3. (b, c)**). Based on the A₆₅₃ values, 37 °C was found optimal at pH 3.6, where a strongly acidic environment subjects H₂O₂ to a base-like decomposition in the presence of the metals or their oxides [31]. It has been theoretically calculated that O-O single bond of adsorbed H₂O₂ (H₂O₂^{*}) tends to be broken at low pH by the peroxidase enzyme or its mimic owing to the weak energy barrier of 0.57 eV, directly releasing two adsorbed OH (OH^{*}) or OH radical (•OH) on the surface of peroxidase or its mimic (in our

case, FL-Ti₃C₂T_x nanosheets)[31]. Besides, the negative charge of MXene is ascribed to its point of zero charge (pK_{pzc}) value between 2 to 3, improving the attraction to positively charged H₂O₂ (pKa = 11.6 ~ 11.7) at pH 3.6 [32, 33]. Therefore, pH 3.6 was determined as the optimal pH condition for the catalytic activity of FL-Ti₃C₂T_x nanosheets.

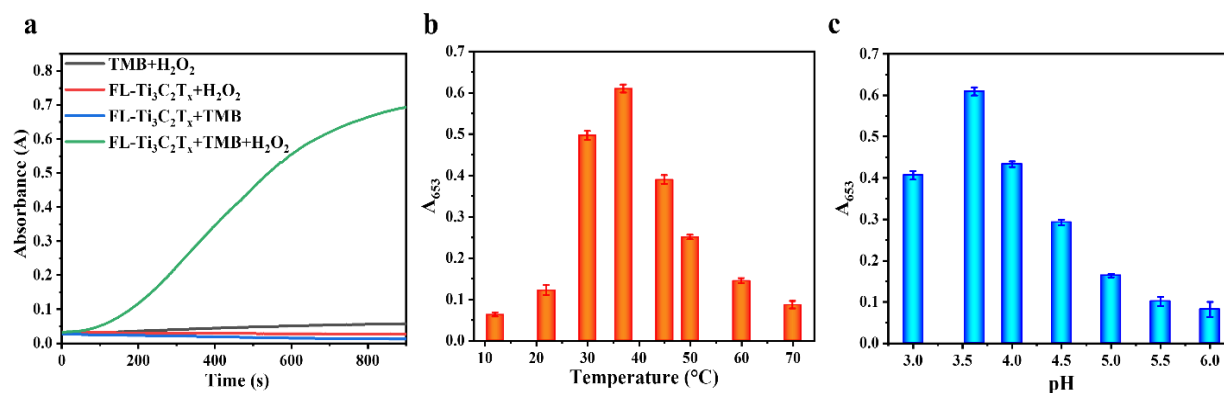


Figure 4.3. UV-vis absorbance spectra of TMB/H₂O₂, FL-Ti₃C₂T_x/ H₂O₂, FL-Ti₃C₂T_x /TMB, and FL-Ti₃C₂T_x /TMB/ H₂O₂ systems (a). The colorimetric performance of FL-Ti₃C₂T_x/TMB/H₂O₂ system as a function of temperature at pH 3.6 (b) and as a function of reaction temperature at 37°C (c).

4.3.3. Physiochemical properties of FL-Ti₃C₂T_x nanosheets

The HRP and FL-Ti₃C₂T_x nanosheets were stored at room temperature in the dark for 10 days in PBS and acetic acid/sodium acetate buffer, respectively. Their residual enzymatic performances were compared and recorded to study the storage stability (**Figure**

4.4. (a)). The percentage activity (%) was calculated as follows:

$$\text{Percentage activity} = \frac{A_{653}(t)}{A_{653}(0)} * 100$$

where $A_{653}(0)$ and $A_{653}(t)$ are respectively A_{653} values of the enzymatic system at '0' and 't' days of storage at room temperature. Based on **Figure 4.4. (a)**, even after 10 days of storage, the peroxidase-mimic behavior of FL-Ti₃C₂T_x nanoflakes remained at 89.1%, which is much higher than that of HRP (41.1%), indicating that FL-Ti₃C₂T_x nanoflakes are more stable than HRP.

According to previous reports, titanium carbide (Ti₃C₂) cannot generate e⁻/h⁺ pairs by utilizing visible light since it is not a semiconductor. However, with various surface modifications (-F, -O, and -OH), MXene can be converted into a nanomaterial with semiconducting properties, the band gap of which mainly depends on the surface functional group [34]. The band-gap energy of MXenes has been measured and calculated according to the Tauc plot [35]:

$$(\alpha h\nu) = A(h\nu - E_g)^2$$

Where, α = absorption coefficient (cm⁻¹), h = Planck's constant (6.6261×10^{-34} J s or 4.1357×10^{-15} eV s), ν = light frequency (s⁻¹), A = constant for indirect transition, and E_g = band energy (eV). **Figure 4.4. (b)** reveals the UV-vis spectrum for MXene analysis, and according to the Tauc plot (inset in **Figure 4.4. (b)**), the band-gap of FL-Ti₃C₂T_x nanosheets is 2.04 eV, in agreement with the TiO₂/Ti₃C₂ nanocomposites [35]. This illustrates that the multiple functional groups terminate on the surface of nanosheets, affording the MXene we synthesized semiconducting properties.

The charge transfer resistances of FL-Ti₃C₂T_x measured in the dark and solar light conditions via EIS are presented in **Figure 4.4. (c)**. The diameter of the semicircle in the Nyquist plot is smaller for FL-Ti₃C₂T_x nanosheets in solar light than in the dark, suggesting

that the e^- was excited from the valence band by the energy of the light photons to fill the empty conduction band and finally leaving the original state as h^+ .

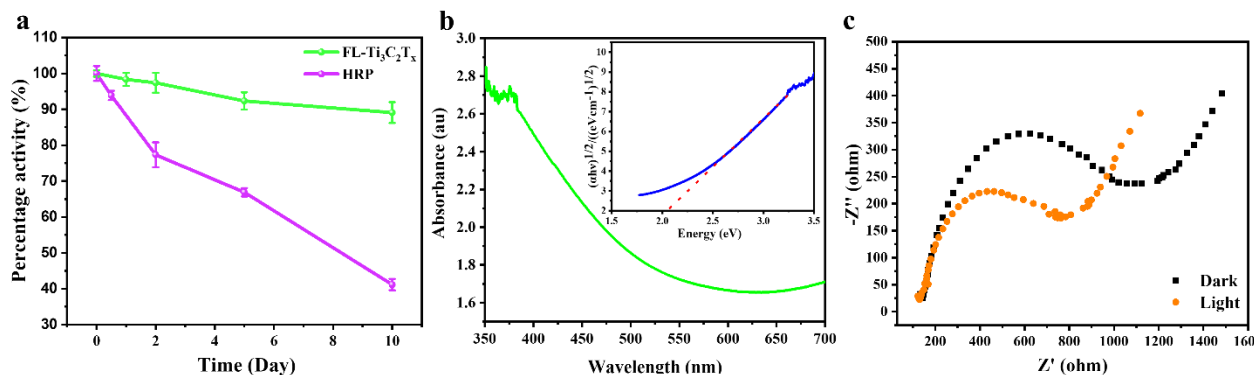


Figure 1.4. Stability of FL-Ti₃C₂T_x and HRP when stored for 10 days at room temperature (a). UV-vis spectrum of FL-Ti₃C₂T_x MXene solution. Inset: plot of $\alpha h\nu$ vs. photon energy ($h\nu$) for band gap energy of MXene (b). Nyquist plots of FL-Ti₃C₂T_x in the dark (c).

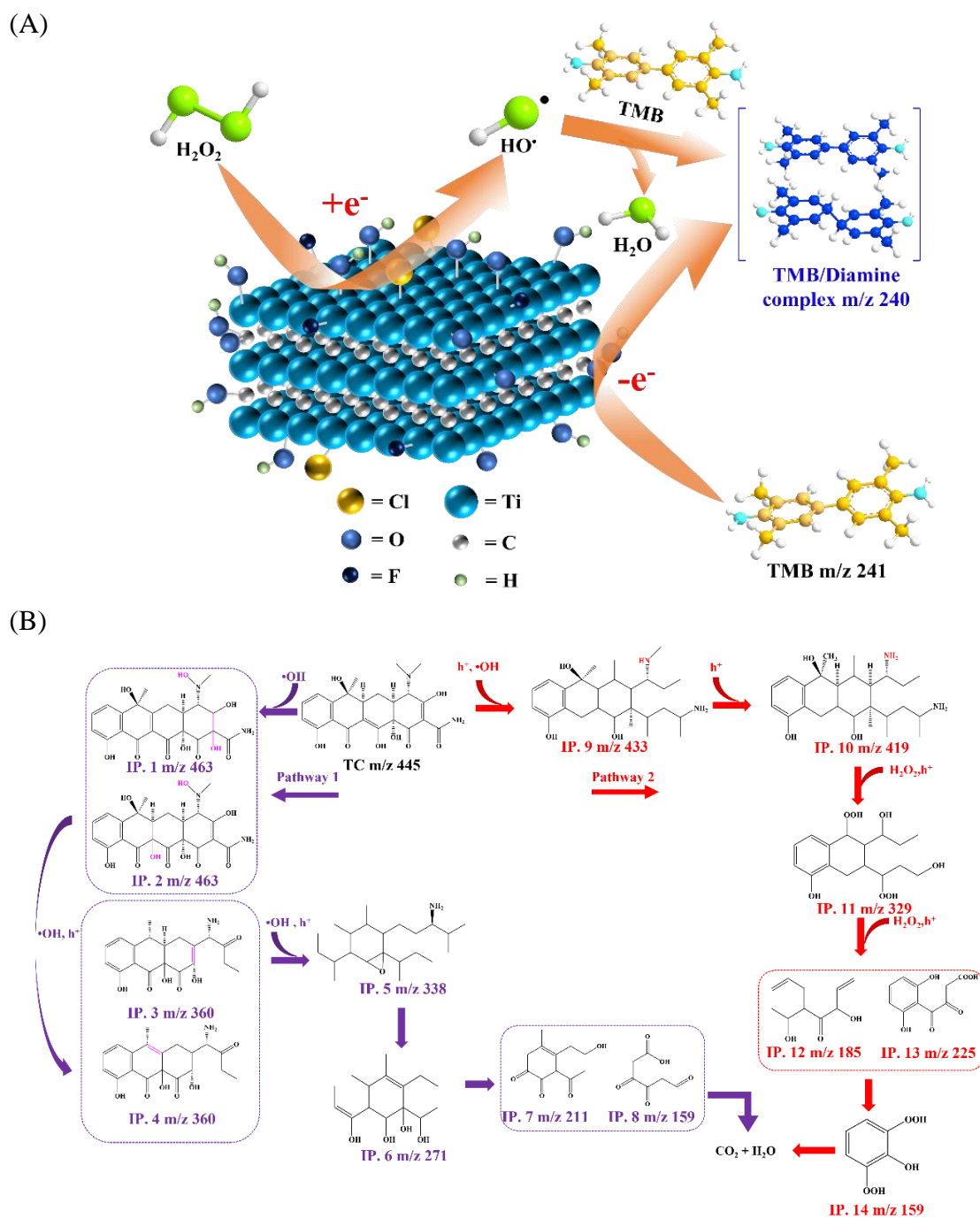
4.3.4. The mechanism of peroxidase-mimic activity

Following our previous study and other reports, we proposed a mechanism for the enzymatic role of FL-Ti₃C₂T_x nanosheets in the TMB/H₂O₂ system, although uncertainty remains in some chemical structure details (**Scheme 4.1. A**) [30]. Initially, the negatively charged surface of FL-Ti₃C₂T_x nanosheets ($pK_{pzc} = 2\sim 3$) is preferably attracted to the added nucleophilic H₂O₂ molecules with a positive charge ($pK_a = 11.7$) in the low-pH environment (pH 3.6) due to lower adsorption energy than that of H₂O molecules. As H₂O₂ molecules are adsorbed on the surface of FL-Ti₃C₂T_x nanosheets, they are irreversibly activated to a hydroperoxyl ligand on the Ti layer in the form of a Ti-OOH intermediate [36, 37]. Moreover, these -OOH ligands are further stabilized by hydrogen bonds formed between other polar groups terminated on the Ti surface or C interlayers (-F, -OH, =O, etc.)

and themselves. O-O bonds are then broken by the Ti surface, where some unstable vacancy defects with high nucleophilic properties are presented after the etching process and donate multiple e^- to -OOH ligands as proton affinity [38]. Therefore, this reaction releases large amounts of reactive oxygen species (ROS) into the solution. Meanwhile, the surface of FL- $Ti_3C_2T_x$ nanosheets may also conjugate with TMB via strong hydrogen bonds between amine groups of TMB and polar groups (-F, =O, etc.) present on the surface of FL- $Ti_3C_2T_x$ nanosheets.

To determine the specific ROS and factor in the solution, a radical trapping experiment was designed using EDTA•2Na, IPA, and LAA radical scavengers that are responsible for the h^+ , •OH, •O²⁻ entrapped, respectively. As seen in **Figure S4.3. (Appendix IV)**, there is a UV-vis absorption peak with lower intensity for the IPA sample compared with that of the LAA or blank solution, illustrating that the •OH is the major ROS in the solution after the reduction reaction of H₂O₂. A UV-vis absorption peak with no apparent intensity was observed in the EDTA•2Na sample, which demonstrates that h^+ plays an essential role in the subsequent catalytic reactions (**Appendix IV, Figure S4.3.**).

The regeneration event of the e^-/h^+ carrier occurs on the surface of FL- $Ti_3C_2T_x$ nanosheets after the surface gains e^- from the amine group of TMB. In addition to offsetting the defects left after over-donating e^- , TMB may also donate H^+ to adsorbed oxygen species (•O*) on the surface of FL- $Ti_3C_2T_x$ nanosheets. As a result, H₂O molecules are generated after the •OH or •O* accepts H^+ protonated from the H donor (TMB) [39]. Meanwhile, TMB molecules are irreversibly oxidized to form pools of TMB cation radicals and TMB/diamine complex, finally turning the solution color bluish-green.



Scheme 4.1. A. Illustration of the biocatalytic chromogenic reaction between TMB and H_2O_2 triggered by FL- $\text{Ti}_3\text{C}_2\text{T}_x$ nanosheets. B. Two plausible pathways (pathway 1, top line in red and pathway 2, bottom line in purple) for TC degradation in the presence of FL- $\text{Ti}_3\text{C}_2\text{T}_x$ and proposed structures of intermediate products (IP.1 through IP.17). The IPs enclosed in boxes are isomers or those possibly exist simultaneously.

4.3.5. Colorimetric detection for TC and its mechanism

We recognized the ability of TC to inhibit the redox reaction between TMB/H₂O₂ triggered by FL-Ti₃C₂T_x nanosheets and hence to prohibit the solution color change. Based on this strategy, a colorimetric bioassay was applied to detect TC. In this assay, TC is first incubated with FL-Ti₃C₂T_x nanosheets in the sample solution for 0 to 60 min. The time for incubating TC and the prepared FL-Ti₃C₂T_x nanosheets was optimized (**Appendix IV, Figure S4.4**). The relative response (RR, %) was calculated as:

$$RR = \frac{A_{653(t)}}{A_{653(0)}} * 100$$

Where, A_{653(t)} and A₆₅₃₍₀₎ are A₆₅₃ values after "t" and "0" min, respectively. The RR value decreased significantly with incubation time for the first 10 min (**Appendix IV, Figure S4.4**), and then it leveled off, indicating that the inhibition effect of TC on the enzymatic system almost reached the maximum. Therefore, 10 min was selected as TC incubation time. Digital images of solution color with an increasing amount of TC from 0 μM to 230.77 μM added are shown in **Figure 4.5. A**. It is also possible to semi-quantitatively visualize the solution color change with naked eyes since the color of the peroxidase mimic and its enzyme substrates solution faded as the concentration of TC increased. When the concentration of TC was higher than 46.15 μM, the color change of the solution can be recognized from the original one. The detection was confirmed by UV-vis spectra (**Figure 4.5. B(a) and (b)**). The dynamic range was a linear function of the difference between A₆₅₃ values with and without TC, i.e., ΔA₆₅₃.

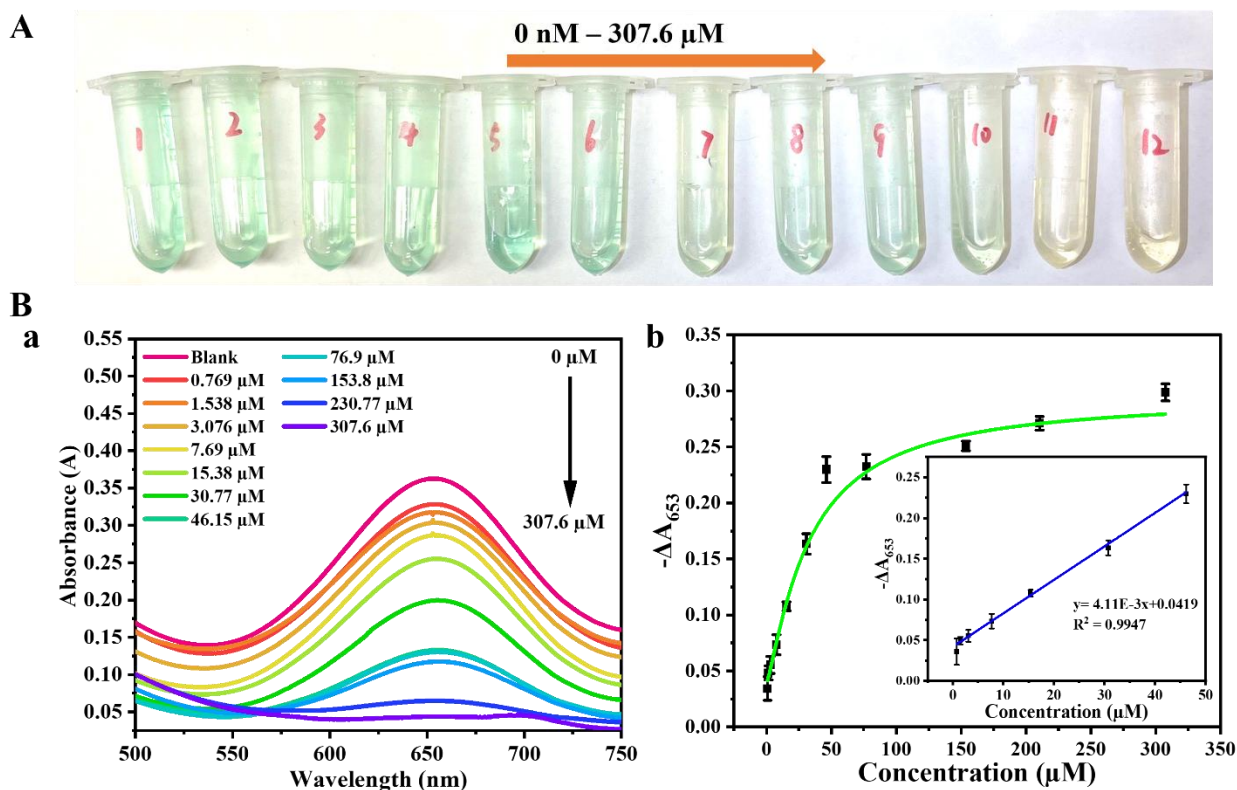


Figure 4.5. A. Photograph of the color of the FL-Ti₃C₂T_x/TMB/H₂O₂ solution with different TC concentrations, B. Change in A₆₅₃ value from that of blank (ΔA_{653}) of FL-Ti₃C₂T_x bioassay with different amounts of TC (a) and calculated dynamic range and inset: the line (b).

The TC colorimetric detection has a wide dynamic range from 0.769 μM to 307.6 μM. There was a linear relationship between added TC concentration and A₆₅₃ from 0.769 μM to 46.15 μM with R² as 0.9947 (**Figure 5.5. (b)**, inset). The calculated limit of detection (LOD) of 615.4 nM was experimentally verified (**Appendix IV, Figure S5.5.**). This LOD value is lower than the MRL (of 676 nM) set by the US FDA, though higher than the MRL (of 225 nM) set by the EU [4]. The performance metrics of our assay are better than those of other published methods (**Appendix IV, Table S4.1.**). The LOD of our method is lower

than some other published methods. However, unlike other methods, ours is the only method that can simultaneously degrade TC and provide a colorimetric indication of its presence.

According to previous reports, TC can be photo-catalytically oxidized in the presence of titanium dioxide (TiO_2) or TiO_2 -based semiconductors under sunlight [8, 14]. As mentioned earlier, our exfoliated FL- $\text{Ti}_3\text{C}_2\text{T}_x$ flakes are partially oxidized during etching or storage, which renders the surface of the Ti layer in the form of TiO_2 . Hence, the FL- $\text{Ti}_3\text{C}_2\text{T}_x$ we synthesized is believed to possess the same catalytic properties as TiO_2 . In this, $\bullet\text{OH}$, $\bullet\text{O}_2^-$, and even h^+ are three possible active entities that play a critical role in TC degradation [40, 41]. QTOF MS was carried out to detect intermediate products (IP) during the degradation of TC mediated by FL- $\text{Ti}_3\text{C}_2\text{T}_x$ nanosheets.

Per earlier reports of TC degradation triggered by TiO_2 and our QTOF MS data [40-43], we propose two plausible ways to further explore the mechanism of TC detection, including dehydration, dealkylation, hydroxylation, and substitution in the presence of FL- $\text{Ti}_3\text{C}_2\text{T}_x$ and H_2O_2 (**Scheme 4.1.B** and **Appendix IV, Table S4.2.**). Briefly, in pathway 1, TC molecules with m/z of 445 (in the form of $[\text{TC}+\text{H}]^+$ in QTOF MS) are first oxidized by $\bullet\text{OH}$ radicals to produce hydroxylated isomers ($m/z=463$), which are then quickly transferred to several intermediates either via substitution or dehydration processes, forming IP. 3 – IP. 4. The open ring product IP. 5 ($m/z=338$) is further oxidized to release IP. 6 ($m/z=271$), which are further transferred to several small pieces, IP.7 ($m/z=211$) and IP.8 ($m/z=159$). Finally, these products are degraded into CO_2 and H_2O . In pathway 2, TC molecules are oxidized and dealkylated starting from the methyl group ($-\text{CH}_3$) located in the tertiary amine group. The intermediate product IP. 9 ($m/z=433$) quickly reduced into

IP. 10 with $m/z=419$. The release of IP. 10 opens its rings by the synergistic behavior of H_2O_2 and h^+ to produce IP. 11 ($m/z=329$), IP. 12 ($m/z=185$), and IP. 13 ($m/z=225$) and IP. 14 ($m/z=159$). These open-ring IPs were further degraded into CO_2 and H_2O in the solution. According to the mechanism of the TC degradation, $\bullet\text{OH}$ is the major ROS released in the solution ascribed to e^- of generated OH^- from $-\text{OOH}$ ligand donation to $\text{FL-Ti}_3\text{C}_2\text{T}_x$ nanosheets (**Appendix IV, Figure S4.3.**). However, due to the existence of TC, the preference of $\bullet\text{OH}$ is to share the e^- with TC forming a covalent bond between TC and $\bullet\text{OH}$, blocking the $\bullet\text{OH}$ from reacting toward TMB directly (**Scheme 4.1. B**, pathway 1) [42]. Further research is needed to elucidate the potential reasons why the generated $\bullet\text{OH}$ radicals react with TC in preference to TMB.

Additionally, the generation of h^+ carriers leads to the opening of the IP rings, which helps IP ultimately transform into CO_2 and H_2O [43]. As stated earlier, the h^+ has been determined in the $\text{EDTA}\cdot 2\text{Na}$ enzymatic system (**Appendix IV, Figure S4.3.**). Nevertheless, h^+ has less impact on TC degradation compared with $\bullet\text{OH}$, attributed to the short illumination time during detection. In contrast, $\bullet\text{O}_2^-$ was not observed in the solution even as the $\text{FL-Ti}_3\text{C}_2\text{T}_x$ nanosheets were added with H_2O_2 since there was comparative absorbance intensity to that from blank solution, measured in the LAA solution, in agreement with the previous reports (**Appendix IV, Figure S4.3.**) [44]. Therefore, $\bullet\text{O}_2^-$ was not a key factor for TC degradation.

4.3.6. Specificity and TC detection in real sample

The specificity of the $\text{FL-Ti}_3\text{C}_2\text{T}_x$ nanosheets-based sensing method was tested against 11 potential interferents in dairy and/or water samples with a concentration of $100\ \mu\text{M}$, including amino acids, ions, sugars, and other antibiotics (amoxicillin, penicillin G, and ampicillin). As

observed in **Figure S4.6. (Appendix IV)**, the color of the TC sample is much lighter than that of other interferent samples. The TC sample color is rather yellowish attributed to its original color as the TC concentration increases. The bluish-green color change can be quantified by the A_{653} value. To numerically measure the sensor selectivity, relative absorption (%) values were calculated:

$$\text{Relative absorption} = \frac{A_{653(\text{interferent})}}{A_{653(\text{blank})}} * 100$$

Where, $A_{653(\text{blank})}$ and $A_{653(\text{interferent})}$ are A_{653} values for the blank and solutions with interferents, respectively. This data set confirms that the FL-Ti₃C₂T_x MXene-mediated enzymatic system exhibits good specificity toward TC.

TC-spiked tap water and skim milk were employed as real sample testing of the assay (**Appendix IV, Table S4.3.**). The recoveries of TC in these real matrices ranged from 96.54 % and 104.02 % with relative standard deviation (RSD) values less than 5 %, which attests that our enzyme nano-mimics assay is highly suitable for the detection of TC in environmental and food samples.

4.4. Conclusions

FL-Ti₃C₂T_x, synthesized from Ti₃AlC₂ precursor via HF-HCl etching, exhibited high peroxidase-mimic activity in TMB/H₂O₂ system. The FL-Ti₃C₂T_x nanosheets trigger a reduction reaction in H₂O₂ molecules to release key ROS species (\bullet OH) for the subsequent TMB oxidation reaction, which turns the solution color bluish-green. However, in the presence of TC, the oxidation of TC, by the released \bullet OH from H₂O₂ and h⁺ carriers of FL-Ti₃C₂T_x nanosheets, occurs before the oxidation of TMB, which inhibits the color change

of the sample solution. This competitive behavior of TC in the FL-Ti₃C₂T_x /TMB/H₂O₂ system was used to fabricate a colorimetric biosensor for the detection and quantification of TC with a low LOD of 615.4 nM. Our titanium carbide MXene assay proved successful when tested in TC-spiked real food matrices of tap water and skim milk with excellent selectivity and sensitivity. Moreover, our results support that environmentally benign degradation of TC simultaneously facilitates its colorimetric detection.

4.5. Appendix IV.

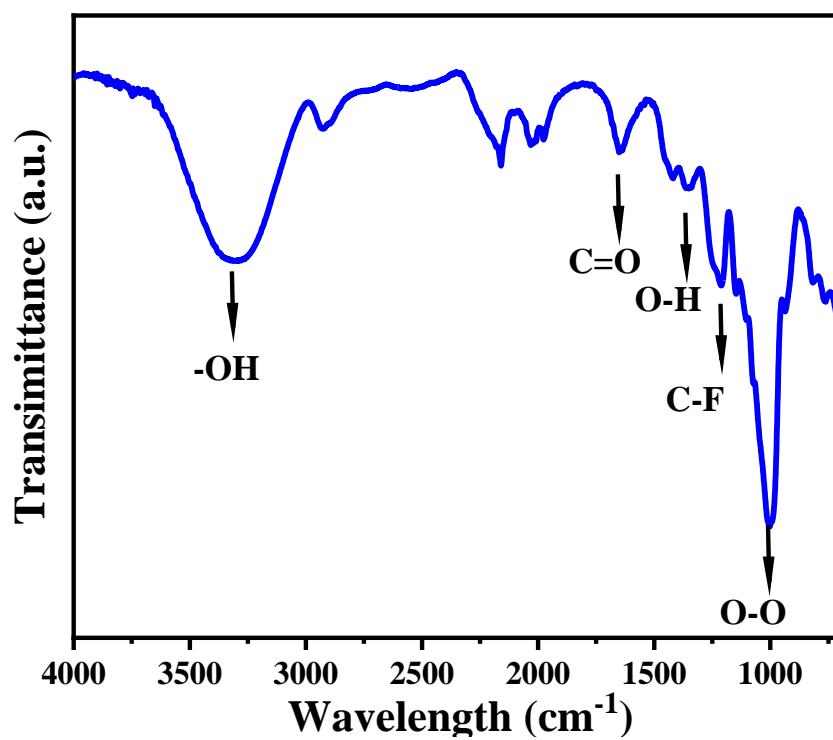


Figure S4.1. FT-IR spectrum of FL-Ti₃C₂T_x nanosheets.

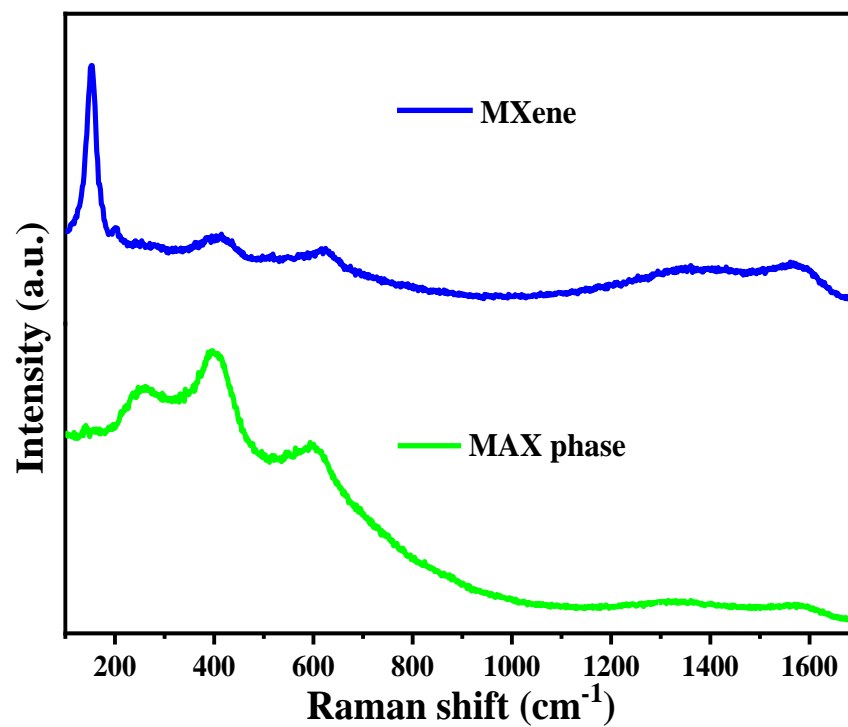


Figure S4.2. Raman spectra of MAX phase precursor and synthesized FL-Ti₃C₂T_x MXene nanosheets.

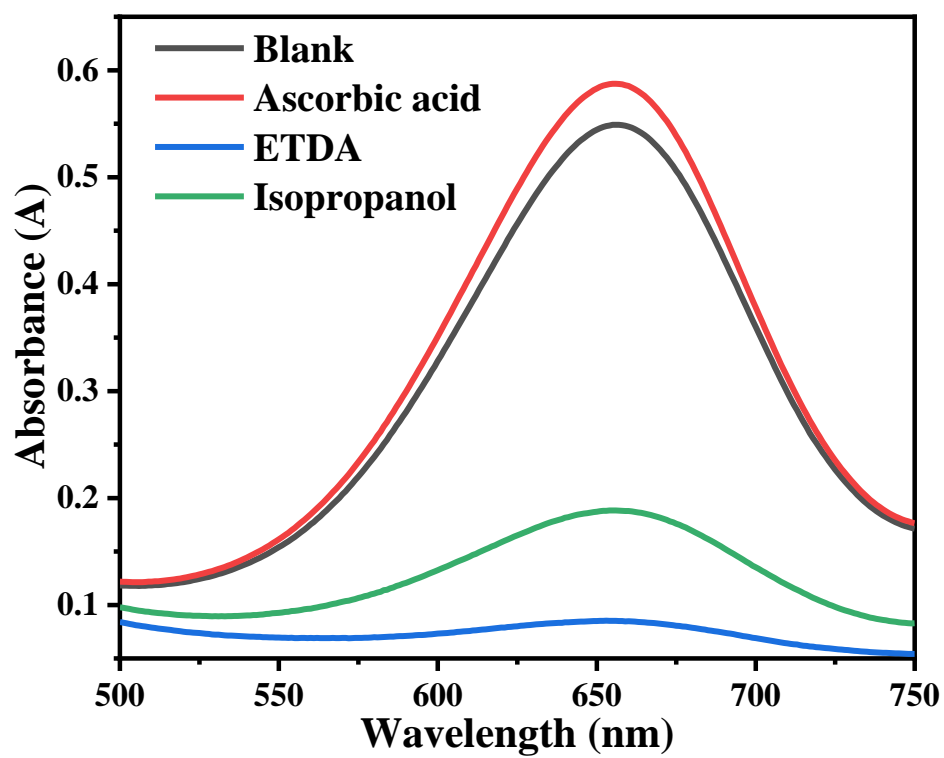


Figure S4.3. Radical trapping experiment by using ascorbic acid, EDTA•2Na, and isopropanol for $\bullet\text{O}_2^-$, $\bullet\text{OH}$, and h^+ scavenging

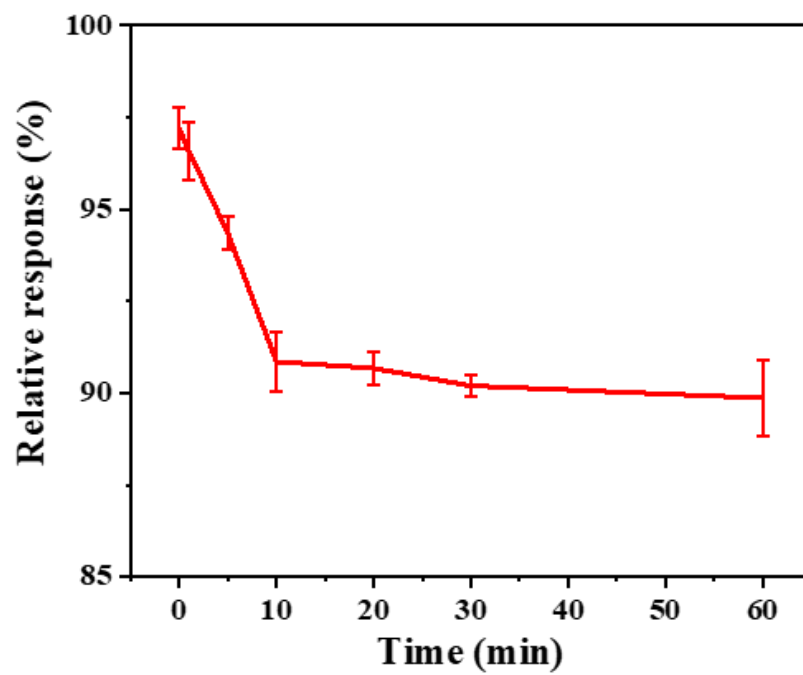


Figure S4.4. Optimization of mixing time for TC and FL-Ti₃C₂T_x nanosheets

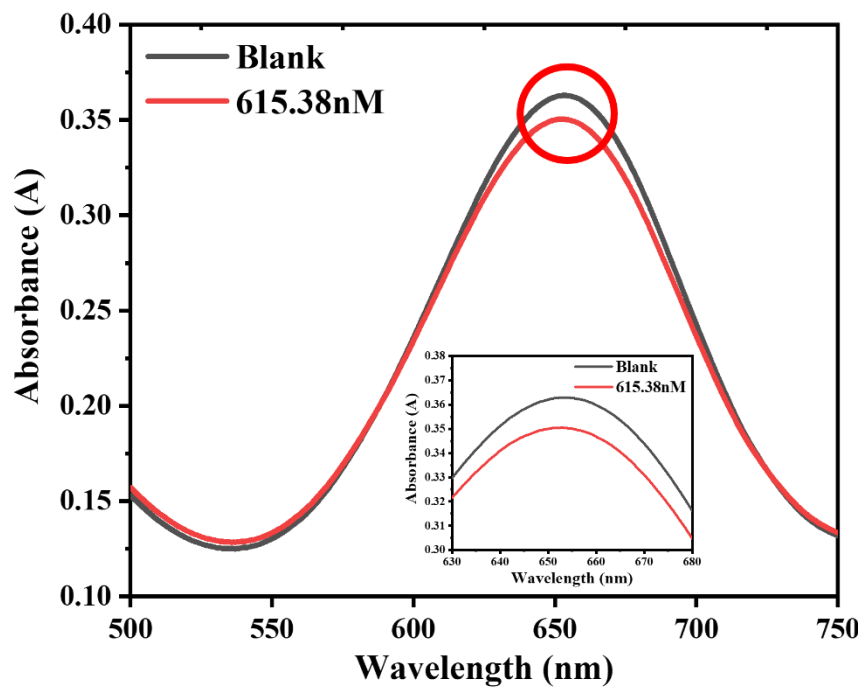


Figure S4.5. Theoretically calculated LOD for TC analysis by FL-Ti₃C₂T_x nanosheets/TMB/H₂O₂ system

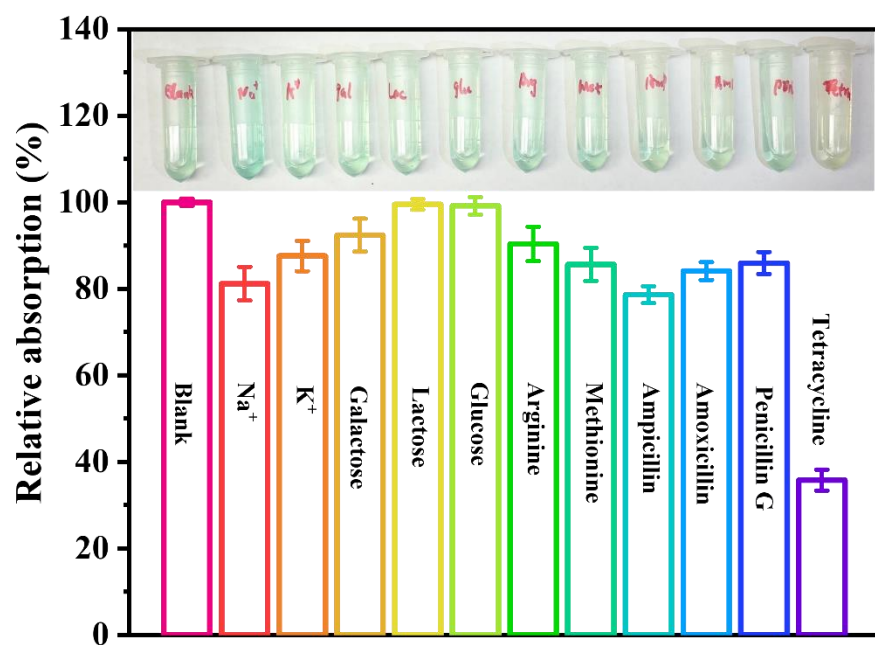


Figure S4.6. Assay response to 11 potential interferents found in dairy products and/or water samples.

Table S4.1. Performance metrics of our assay and some published methods for TC detection

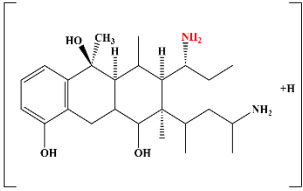
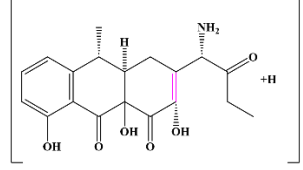
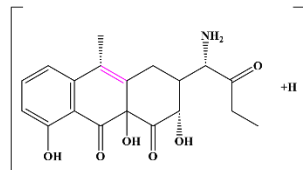
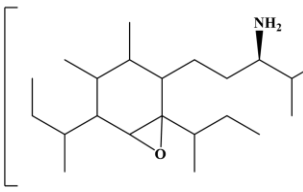
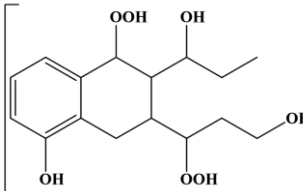
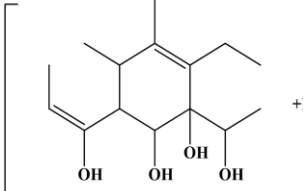
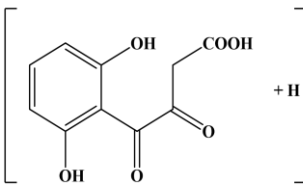
Detection method	Nanomaterial used	Linear range (μM) ^a	LOD (μM) ^b	Ref
Fluorescence	Carbon dots	0.5 ~ 6.0	0.33	[45]
	MIP/CdTe QD ^c	70 ~ 2.2*10 ³	8.8	[46]
	NH ₂ -MIL-53(Al) ^d	1.5 ~ 70	0.92	[47]
	CQD@MSNs ^e	0 ~ 100	5.19	[48]
	AC@Au-Cit-Eu ^f	0.05 ~ 9.5	11.2*10 ⁻³	[49]
	Nanoclay (Atta)/carbon dots (CDs)	0.025 ~ 20	8.7*10 ⁻³	[50]
	NAC@Ag NCs ^g	1.12 ~ 230	0.47	[51]
	Eu-based MOF	0.05 ~ 60	3*10 ⁻³	[52]
Colorimetric	D-Trp-OMe@AuNCs/TMB/H ₂ O ₂ ^h	1.5 ~ 30.0	0.20	[53]
	DSMIP@Mn ₃ O ₄ ⁱ	0.5 ~ 150	0.1	[54]
	Fe ₃ O ₄ @MIP ^j	2 ~ 225	0.4	[55]
	Cu-doped-g-C ₃ N ₄ nanocomposite	0.28 ~ 10	0.086	[56]
	PCC ^k	4.5 ~ 168.75	2.70	[57]

	FL-Ti ₃ C ₂ T _x TMB/H ₂ O ₂	nanosheets/	0.77 ~ 46.14	0.62	This work
--	---	-------------	--------------	------	--------------

Note: a and b. calculated after unit transfer. c. composite of imprinted polymethacrylates and CdTe quantum dots, d. NH₂-MIL-53(Al) as metal-organic framework (MOF) nanosheets doped with Eu³⁺, e., mesoporous silica nanosphere composed of carbon quantum dots. f. aminoclay/Au nanocomplexes modified citric acid and Eu³⁺, g. Ag(0)@Ag(I)-N-acetyl-L-cysteine@Ag nanocluster, h. D-tryptophane methyl ester capped gold nanoclusters, i. imprinted polymer with Mn₃O₄ enzyme nano-mimics, j. Fe₃O₄ nanocomposites in molecularly imprinted polymer, k. phosphate with anion exchange on the surface of vaterite-phase calcium carbonate particles,

Table S4.2. QTOF MS information and proposed structures of TMB, TC, and TC degradation products

Name/TC degradation intermediate product (IP) number per Scheme 2)	Mass/Charge (m/z)	Supposed structure(s)
TMB / diamine complex	240	
TMB	241	
Tetracycline (TC)	445	
IP.1 or IP.2	463	<p>Or</p>
IP.9	433	

IP.10	419	
IP.3 or IP.4	360	 <p>Or</p> 
IP.5 or IP.11	338	
IP. 11	329	
IP.6	271	
IP. 13	225	

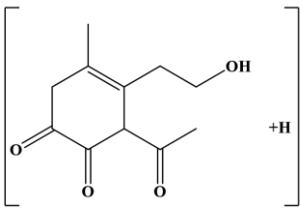
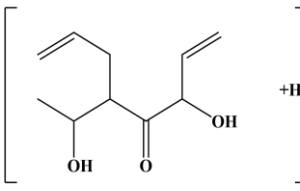
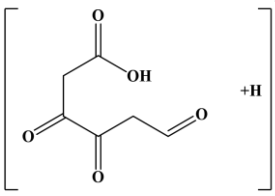
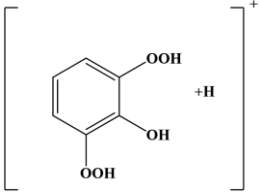
IP.7	211	
IP.12	185	
IP.8 or IP. 14	159	 <p data-bbox="824 894 854 926">or</p> 

Table S4.3. Data for TC detection in tap water, honey, and skim milk samples.

Sample	TC spiked (μM)	TC found (μM)	Recovery (%) [*]	RSD (% , n=3)
Tap water	4	3.91	97.79	2.60
	8	7.72	96.54	1.60
Skim milk	4	4.03	100.87	4.38
	8	8.32	104.02	1.92

^{*}Recovery (%) = $(C_{\text{found}} / C_{\text{spike}}) * 100$

4.6. References

- [1] S. Sachi, J. Ferdous, M.H. Sikder, S.A.K. Hussani, Antibiotic residues in milk: Past, present, and future, *Journal of advanced veterinary and animal research* 6(3) (2019) 315.
- [2] X. Chen, J. Xu, Y. Li, L. Zhang, N. Bi, J. Gou, T. Zhu, L. Jia, A novel intelligently integrated MOF-based ratio fluorescence sensor for ultra-sensitive monitoring of TC in water and food samples, *Food Chemistry* 405 (2023) 134899.
- [3] J. Scaria, K. Anupama, P. Nidheesh, Tetracyclines in the environment: An overview on the occurrence, fate, toxicity, detection, removal methods, and sludge management, *Science of The Total Environment* 771 (2021) 145291.
- [4] X. Chen, J. Che, Nitrogen and sulfur co-doped carbon dots derived from granatums and ammonium persulfate to detect tetracyclines in milk, *Food Chemistry Advances* (2022) 100112.
- [5] L. Lan, Y. Yao, J. Ping, Y. Ying, Recent advances in nanomaterial-based biosensors for antibiotics detection, *Biosensors and Bioelectronics* 91 (2017) 504-514.
- [6] J. Xu, B. Zhang, L. Jia, N. Bi, T. Zhao, Metal-enhanced fluorescence detection and degradation of tetracycline by silver nanoparticle-encapsulated halloysite nano-lumen, *Journal of hazardous materials* 386 (2020) 121630.
- [7] Y. Zhang, J. Zhou, X. Chen, L. Wang, W. Cai, Coupling of heterogeneous advanced oxidation processes and photocatalysis in efficient degradation of tetracycline hydrochloride by Fe-based MOFs: Synergistic effect and degradation pathway, *Chemical Engineering Journal* 369 (2019) 745-757.
- [8] S. Zhao, J. Chen, Y. Liu, Y. Jiang, C. Jiang, Z. Yin, Y. Xiao, S. Cao, Silver nanoparticles confined in shell-in-shell hollow TiO₂ manifesting efficiently photocatalytic activity and stability, *Chemical Engineering Journal* 367 (2019) 249-259.
- [9] W. Wang, S. Gunasekaran, Nanozymes-based biosensors for food quality and safety, *TrAC trends in analytical chemistry* 126 (2020) 115841.
- [10] W. Wang, S. Gunasekaran, Potential Toxicology of Nanozymes, *Nanozymes*, CRC Press 2021, pp. 377-401.
- [11] X. Zhang, Z. Zhang, Z. Zhou, MXene-based materials for electrochemical energy storage, *Journal of energy chemistry* 27(1) (2018) 73-85.
- [12] M. Alhabeb, K. Maleski, B. Anasori, P. Lelyukh, L. Clark, S. Sin, Y. Gogotsi, Guidelines for synthesis and processing of two-dimensional titanium carbide (Ti₃C₂T_x MXene), *Chemistry of Materials* 29(18) (2017) 7633-7644.
- [13] Y. Pei, X. Zhang, Z. Hui, J. Zhou, X. Huang, G. Sun, W. Huang, Ti₃C₂TX MXene for sensing applications: recent progress, design principles, and future perspectives, *ACS nano* 15(3) (2021) 3996-4017.
- [14] Y. Wang, L. Rao, P. Wang, Z. Shi, L. Zhang, Photocatalytic activity of N-TiO₂/O-doped N vacancy g-C₃N₄ and the intermediates toxicity evaluation under tetracycline hydrochloride and Cr (VI) coexistence environment, *Applied Catalysis B: Environmental* 262 (2020) 118308.
- [15] Y. Tang, Y. Hu, P. Zhou, C. Wang, H. Tao, Y. Wu, Colorimetric detection of kanamycin residue in foods based on the aptamer-enhanced peroxidase-mimicking activity of layered WS₂ nanosheets, *Journal of Agricultural and Food Chemistry* 69(9) (2021) 2884-2893.
- [16] X. Liu, Y. Qiu, D. Jiang, F. Li, Y. Gan, Y. Zhu, Y. Pan, H. Wan, P. Wang, Covalently grafting first-generation PAMAM dendrimers onto MXenes with self-adsorbed AuNPs for use as a functional nanoplatform for highly sensitive electrochemical biosensing of cTnT, *Microsystems & nanoengineering* 8(1) (2022) 1-15.

- [17] W. Wang, S. Gunasekaran, MXene-Based Nucleic Acid Biosensors for Agricultural and Food Systems, *Biosensors* 12(11) (2022) 982.
- [18] W. Feng, H. Luo, S. Zeng, C. Chen, L. Deng, Y. Tan, X. Zhou, S. Peng, H. Zhang, Ni-modified Ti₃C₂ MXene with enhanced microwave absorbing ability, *Materials Chemistry Frontiers* 2(12) (2018) 2320-2326.
- [19] A.E. Ghazaly, H. Ahmed, A.R. Rezk, J. Halim, P.O. Persson, L.Y. Yeo, J. Rosen, Ultrafast, one-step, salt-solution-based acoustic synthesis of Ti₃C₂ MXene, *ACS nano* 15(3) (2021) 4287-4293.
- [20] J. Choi, Y.J. Kim, S.Y. Cho, K. Park, H. Kang, S.J. Kim, H.T. Jung, In situ formation of multiple schottky barriers in a Ti₃C₂ MXene film and its application in highly sensitive gas sensors, *Advanced Functional Materials* 30(40) (2020) 2003998.
- [21] J.H. Ciou, S. Li, P.S. Lee, Ti₃C₂ MXene paper for the effective adsorption and controllable release of aroma molecules, *Small* 15(38) (2019) 1903281.
- [22] Z. Wang, Z. Xu, H. Huang, X. Chu, Y. Xie, D. Xiong, C. Yan, H. Zhao, H. Zhang, W. Yang, Unraveling and regulating self-discharge behavior of Ti₃C₂T_x MXene-based supercapacitors, *ACS nano* 14(4) (2020) 4916-4924.
- [23] A.C. Khot, T.D. Dongale, J.H. Park, A.V. Kesavan, T.G. Kim, Ti₃C₂-based MXene oxide nanosheets for resistive memory and synaptic learning applications, *ACS Applied Materials & Interfaces* 13(4) (2021) 5216-5227.
- [24] Y. Li, X. Zhou, J. Wang, Q. Deng, M. Li, S. Du, Y.-H. Han, J. Lee, Q. Huang, Facile preparation of in situ coated Ti₃C₂T_x/Ni_{0.5}Zn_{0.5}Fe₂O₄ composites and their electromagnetic performance, *Rsc Advances* 7(40) (2017) 24698-24708.
- [25] W. Wu, C. Wang, C. Zhao, D. Wei, J. Zhu, Y. Xu, Facile strategy of hollow polyaniline nanotubes supported on Ti₃C₂-MXene nanosheets for high-performance symmetric supercapacitors, *Journal of Colloid and Interface Science* 580 (2020) 601-613.
- [26] A. Iqbal, N.M. Hamdan, Investigation and Optimization of Mxene Functionalized Mesoporous Titania Films as Efficient Photoelectrodes, *Materials* 14(21) (2021) 6292.
- [27] L. Cheng, Q. Chen, J. Li, H. Liu, Boosting the photocatalytic activity of CdLa₂S₄ for hydrogen production using Ti₃C₂ MXene as a co-catalyst, *Applied Catalysis B: Environmental* 267 (2020) 118379.
- [28] R. Syamsai, P. Kollu, S.K. Jeong, A.N. Grace, Synthesis and properties of 2D-titanium carbide MXene sheets towards electrochemical energy storage applications, *Ceramics International* 43(16) (2017) 13119-13126.
- [29] R. Lotfi, M. Naguib, D.E. Yilmaz, J. Nanda, A.C. Van Duin, A comparative study on the oxidation of two-dimensional Ti₃C₂ MXene structures in different environments, *Journal of Materials Chemistry A* 6(26) (2018) 12733-12743.
- [30] W. Wang, Y. Yin, S. Gunasekaran, Oxygen-terminated few-layered Ti₃C₂T_x MXene nanosheets as peroxidase-mimic nanozyme for colorimetric detection of kanamycin, *Biosensors and Bioelectronics* (2022) 114774.
- [31] J. Li, W. Liu, X. Wu, X. Gao, Mechanism of pH-switchable peroxidase and catalase-like activities of gold, silver, platinum and palladium, *Biomaterials* 48 (2015) 37-44.
- [32] K. Liu, K. Yan, G. Sun, Mechanism of H₂O₂/bleach activators and related factors, *Cellulose* 26(4) (2019) 2743-2757.
- [33] A. Shahzad, K. Rasool, W. Miran, M. Nawaz, J. Jang, K.A. Mahmoud, D.S. Lee, Two-dimensional Ti₃C₂T_x MXene nanosheets for efficient copper removal from water, *ACS Sustainable Chemistry & Engineering* 5(12) (2017) 11481-11488.

- [34] Z. You, Y. Liao, X. Li, J. Fan, Q. Xiang, State-of-the-art recent progress in MXene-based photocatalysts: a comprehensive review, *Nanoscale* 13(21) (2021) 9463-9504.
- [35] Q. Liu, X. Tan, S. Wang, F. Ma, H. Znad, Z. Shen, L. Liu, S. Liu, MXene as a non-metal charge mediator in 2D layered CdS@Ti₃C₂@TiO₂ composites with superior Z-scheme visible light-driven photocatalytic activity, *Environmental Science: Nano* 6(10) (2019) 3158-3169.
- [36] D.T. Bregante, N.E. Thornburg, J.M. Notestein, D.W. Flaherty, Consequences of confinement for alkene epoxidation with hydrogen peroxide on highly dispersed group 4 and 5 metal oxide catalysts, *Acs Catalysis* 8(4) (2018) 2995-3010.
- [37] C.M. Lousada, A.J. Johansson, T. Brinck, M. Jonsson, Mechanism of H₂O₂ decomposition on transition metal oxide surfaces, *The Journal of Physical Chemistry C* 116(17) (2012) 9533-9543.
- [38] D. Zhao, Z. Chen, W. Yang, S. Liu, X. Zhang, Y. Yu, W.-C. Cheong, L. Zheng, F. Ren, G. Ying, MXene (Ti₃C₂) vacancy-confined single-atom catalyst for efficient functionalization of CO₂, *Journal of the American Chemical Society* 141(9) (2019) 4086-4093.
- [39] N.V. Maksimchuk, G.M. Maksimov, V.Y. Evtushok, I.D. Ivanchikova, Y.A. Chesalov, R.I. Maksimovskaya, O.A. Kholdeeva, A. Sole-Daura, J.M. Poblet, J.J. Carbo, Relevance of protons in heterolytic activation of H₂O₂ over Nb (V): Insights from model studies on nb-substituted polyoxometalates, *ACS Catalysis* 8(10) (2018) 9722-9737.
- [40] S. Wu, H. Hu, Y. Lin, J. Zhang, Y.H. Hu, Visible light photocatalytic degradation of tetracycline over TiO₂, *Chemical Engineering Journal* 382 (2020) 122842.
- [41] T. Zhang, Y. Liu, Y. Rao, X. Li, D. Yuan, S. Tang, Q. Zhao, Enhanced photocatalytic activity of TiO₂ with acetylene black and persulfate for degradation of tetracycline hydrochloride under visible light, *Chemical Engineering Journal* 384 (2020) 123350.
- [42] L. Ren, W. Zhou, B. Sun, H. Li, P. Qiao, Y. Xu, J. Wu, K. Lin, H. Fu, Defects-engineering of magnetic γ -Fe₂O₃ ultrathin nanosheets/mesoporous black TiO₂ hollow sphere heterojunctions for efficient charge separation and the solar-driven photocatalytic mechanism of tetracycline degradation, *Applied Catalysis B: Environmental* 240 (2019) 319-328.
- [43] Z. Xie, Y. Feng, F. Wang, D. Chen, Q. Zhang, Y. Zeng, W. Lv, G. Liu, Construction of carbon dots modified MoO₃/g-C₃N₄ Z-scheme photocatalyst with enhanced visible-light photocatalytic activity for the degradation of tetracycline, *Applied Catalysis B: Environmental* 229 (2018) 96-104.
- [44] K. Rasool, M. Helal, A. Ali, C.E. Ren, Y. Gogotsi, K.A. Mahmoud, Antibacterial activity of Ti₃C₂T_x MXene, *ACS nano* 10(3) (2016) 3674-3684.
- [45] J. Xue, N.-N. Li, D.-M. Zhang, C.-F. Bi, C.-G. Xu, N.-N. Shi, X. Zhang, Y.-H. Fan, One-step synthesis of a carbon dot-based fluorescent probe for colorimetric and ratiometric sensing of tetracycline, *Analytical Methods* 12(42) (2020) 5097-5102.
- [46] J.-L. Chen, Determination of tetracycline using imprinted polymethacrylates along with fluorescent CdTe quantum dots on plastic substrates, *Microchimica Acta* 184(5) (2017) 1335-1343.
- [47] J. Chen, Y. Xu, S. Li, F. Xu, Q. Zhang, Ratio fluorescence detection of tetracycline by a Eu³⁺/NH₂-MIL-53 (Al) composite, *RSC advances* 11(4) (2021) 2397-2404.
- [48] J. Zheng, Y. Yang, K. Cheng, J. Ma, P. Yu, Mesoporous silica nanoparticles encapsulated carbon quantum dots for detection of tetracycline, *Journal of Materials Science: Materials in Electronics* (2022) 1-12.

- [49] J. Xu, R. Chen, L. Jia, X. Shen, T. Zhao, L. Su, S. Guo, T. Ma, B. Zhang, Q. Guo, Janus applications: A multifunctional nano-platform with integrated visual detection and photodegradation of tetracyclines, *Applied Surface Science* 484 (2019) 1-10.
- [50] L. Jia, R. Chen, J. Xu, L. Zhang, X. Chen, N. Bi, J. Gou, T. Zhao, A stick-like intelligent multicolor nano-sensor for the detection of tetracycline: The integration of nano-clay and carbon dots, *Journal of hazardous materials* 413 (2021) 125296.
- [51] Y. Zhang, M. Lv, P. Gao, G. Zhang, L. Shi, M. Yuan, S. Shuang, The synthesis of high bright silver nanoclusters with aggregation-induced emission for detection of tetracycline, *Sensors and Actuators B: Chemical* 326 (2021) 129009.
- [52] Y. Zhao, Q. Wang, H. Wang, H. Zhangsun, X. Sun, T. Bu, Y. Liu, W. Wang, Z. Xu, L. Wang, Europium-based metal-organic framework containing characteristic metal chains: a novel turn-on fluorescence sensor for simultaneous high-performance detection and removal of tetracycline, *Sensors and Actuators B: Chemical* 334 (2021) 129610.
- [53] Y. Song, J. Qiao, W. Liu, L. Qi, Enhancement of gold nanoclusters-based peroxidase nanozymes for detection of tetracycline, *Microchemical Journal* 157 (2020) 104871.
- [54] Y. Chen, Y. Xia, Y. Liu, Y. Tang, F. Zhao, B. Zeng, Colorimetric and electrochemical detection platforms for tetracycline based on surface molecularly imprinted polyionic liquid on Mn₃O₄ nanozyme, *Biosensors and Bioelectronics* 216 (2022) 114650.
- [55] B. Liu, H. Zhu, R. Feng, M. Wang, P. Hu, J. Pan, X. Niu, Facile molecular imprinting on magnetic nanozyme surface for highly selective colorimetric detection of tetracycline, *Sensors and Actuators B: Chemical* 370 (2022) 132451.
- [56] Y. Shen, Y. Wei, Z. Liu, C. Nie, Y. Ye, Engineering of 2D artificial nanozyme-based blocking effect-triggered colorimetric sensor for onsite visual assay of residual tetracycline in milk, *Microchimica Acta* 189(6) (2022) 1-11.
- [57] P. Yukhajon, T. Somboon, S. Sansuk, Enhanced adsorption and colorimetric detection of tetracycline antibiotics by using functional phosphate/carbonate composite with nanoporous network coverage, *Journal of Environmental Sciences* 126 (2023) 365-377.

Chapter V. Gold nanoparticles/MXene hierarchical nanostructure as a catalase mimic for colorimetric detection of ampicillin and penicillin G

Abstract

Ampicillin (AMP) and penicillin G (PenG) are the two common β -lactam antibiotics used to fight bacterial infections in livestock. Excessive use of these leads to animal products tainted with trace amounts of antibiotic residues. Consumption of foods contaminated with antibiotics can cause their accumulation in our bodies and pose threats to our health. We developed a colorimetric assay to detect the presence of these AMP and PenG in real matrices using a hierarchical nanostructure material composed of layered titanium carbide MXene nanosheets ($\text{Ti}_3\text{C}_2\text{T}_x$) decorated with gold nanoparticles (AuNPs). The AuNPs were directly grown on the MXene nanosheets via a facile method, which significantly enhanced the catalase-like enzyme activity of MXene. The $\text{Ti}_3\text{C}_2\text{T}_x/\text{AuNPs}$ nanocomposite catalyzed the enzymatic substrate 3,3',5,5'-tetramethylbenzidine (TMB) to its oxidized form in the presence of hydrogen peroxide, and the reaction products turned the sample solution greenish blue. However, this color-change reaction does not occur when AMP and/or PenG is present in the solution. Our assay performed well with wide dynamic ranges and low limits of detection (LOD), respectively 68.9 nM to 70.1 μM and 7.51 nM for AMP and 7.51 nM to 35.05 μM and 68.9 nM for PenG. We hypothesized and experimentally verified that superoxide anions ($\text{O}_2^{\bullet-}$) generated play a critical role in the catalysis of AMP and PenG. Our results may help develop a simple and inexpensive colorimetric sensor for the routine detection of AMP and PenG in food samples.

5.1. Introduction

The discovery of antibiotics and subsequent use as veterinary medicines for treating animal diseases are among the greatest achievements in medical history[1]. However, excessive

antibiotics used to keep animals healthy resulted in a large amount of antibiotic residue in the food products and environment, threatening the ecosystem and human health. The emerging antibiotic-resistant bacteria in the aquatic environment are one of the biggest challenges to ecological health[2]. Antibiotic-resistant genes are another critical concern since they are spread among microorganisms and distributed widely from humans and animals to environmental water resources[3]. Ampicillin (AMP) and penicillin G (Pen G), known with a unique β -lactam ring, are the oldest and most commonly used antibiotics worldwide as a result of their low cost and effectiveness in preventing bacterial infection in livestock[4]. Nevertheless, overconsumption of them by the human body from food can lead to allergic reactions, kidney impairment, etc[5]. Consequently, to prevent the negative impact of AMP and Pen G on the agri-food system and the human body, especially in dairy products, different authorities have set their maximum residue limit (MRL) in the milk (shown in Table S1)[6]. Therefore, developing a portable, highly sensitive, and multi-target sensing system is urgently needed to implement appropriate preventive strategies at the dairy sources before those enter the food chain, thus alleviating the disastrous healthy issue and economic loss.

Current AMP and Pen G detection methods rely more on high-performance liquid chromatography (HPLC), surface-enhanced Raman spectroscopy (SERS), fluorescence immunoassay, etc[7]. Most of these technologies suffer disadvantages, such as high costs, time-consuming, laborious sample preparation, and tedious analysis process, limiting their practical *on-site* applications[8]. Moreover, some can measure only one specific antibiotic type each time, greatly lowering the detection efficiency. Consequently, it is still important to obtain a simple, high-efficiency, cost-effective, and portable sensing system for the residue of AMP and Pen G in dairy product determination.

Enzymatic nano-mimic, in some literature known as "nanozyme," are nanomaterials that can mimic natural enzymes to convert the enzymatic substrates, turning colorless solution visibly[9]. To date, numerous nanomaterials have been identified to possess this specific property, such as metal-organic framework (MOF)s, metal oxide, N-doped graphene, etc.[10]. With their intrinsic catalytic property, long life cycle, and low cost, they are now applied in various areas, such as biosensors, cancer therapy, drug delivery, etc[11].

Titanium carbide nanosheet ($\text{Ti}_3\text{C}_2\text{T}_x$) nanomaterials, also known as MXene, gain increasing attention worldwide as an emerging family of 2D nanomaterials owing to their mechanical strength, high photoelectronic properties, large surface area, excellent surface modification, etc., and wide applications, such as biosensor, photocatalyst, etc.[12-14]. Due to the metallic bond involved, especially Ti-Al, electron injection is necessary to increase bond length and decrease the bond strength. In addition to electron injection, ion intercalation can also facilitate to increase in the interlayer space between each MXene sheet in the precursor, thus helping the exfoliation effect on the A layer. Strong acid or acid/salt mixtures are often adopted to selectively remove the Al interlayer, obtaining anisotropic MXene, i.e., HF, HCl/LiF, etc. [15]. These etching processes can modify the surface of MXene with various terminated groups denoted as T_x in the MXene denotation, including -F -Cl, -O, -OH, etc., stabilizing the structure of MXene. Alternatively, the strong acidic etching environment still creates the vacancy of defects of the Ti layer, providing the MXene with relatively high reducibility. These can make the $\text{Ti}_3\text{C}_2\text{T}_x$ MXene a relatively high reducing agent candidate to directly reduce oxidizing agents, especially dissolved oxygen (O_2), during storage. Besides, MXene itself has a relative-low affinity to H_2O_2 , lowering its catalytic activity[16]. Hence, we took advantage of the excellent reducibility and reactive surface of $\text{Ti}_3\text{C}_2\text{T}_x$ MXene, which can reduce the metal salt precursor without adding any extra reducing agent, to

synthesize the gold nanoparticle (Au NPs)/MXene (MA2) hierarchical nanostructure for colorimetric sensor development.

Herein, we successfully selectively removed the Al interlayer of the MAX phase to synthesize L-Ti₃C₂T_x NS. Then the prepared MXene is capable of reducing the tetra-chloroauric (III) acid trihydrate (HAuCl₄•3H₂O) in one step to generate the MA2. It was found as a catalase-mimic nanomaterial to trigger the redox reaction in the enzymatic system composed of hydron peroxide (H₂O₂) and 3,3',5,5'-tetramethylbenzidine (TMB), finally changing the colorless solution to the greenish-blue. Nevertheless, the greenish-blue color of the solution does not appear as AMP and/or Pen G are added to the system. According to this, we designed and developed a colorimetric sensor for both AMP and Pen G detection in the solution and measured them in the real sample matrices.

5.2. Experiment section

5.2.1. Materials and methods

All chemicals received and used here were of analytical grade without any further purification. MAX phase powder was from Nano-Mall Technology Co. Ltd, China. 30% H₂O₂ solution was provided by ACROS Organics. In addition, two target antibiotics (AMP and Pen G) were successfully purchased from Scientific Inc. Real sample metric, skim milk, was obtained from the local grocery store. Other chemicals not explained specifically were purchased from Sigma-Aldrich. Deionized (DI) water (18 MΩ.cm) was used for various solution preparation.

5.2.2. Pristine L-Ti₃C₂T_x NS nanosheet and MA colloidal solution preparation

Scheme 5.1.A depicts the synthesis process of L-Ti₃C₂T_x NS and MA nanocomposites. L-Ti₃C₂T_x NS was obtained via the minimally intensive layer delamination (MILD) method[17]. First, 0.5 g Ti₃AlC₂ MAX phase clay was slowly added into the 10 mL 7.5 M HCl and 0.8 g LiF mixture

and stirred for 24 h under room temperature. Then, the as-obtained acidic suspension was rinsed with several cycles by adding DI water, centrifugation at 4,000 rpm (10 min), and decantation until the pH value of the supernatant reached 5.0. Next, after the last washing cycle, the grayish-black swollen sediment was collected and redispersed into 10 mL DI water, followed by N₂ gas flow for mixture deoxidation. The as-prepared mixture was then sonicated in the ice water bath for 40 mins and centrifugation for another 1 h (4,000 rpm). The final obtained supernatant composed of L-Ti₃C₂T_x NS was kept and freeze-dried, which was used for the following experiment.

MA hierarchical-structure nanocomposite was synthesized in a one-step, self-assembled way[18]. Briefly, as-synthesized pristine L-Ti₃C₂T_x NS (4 mg/mL) colloidal solution was added with 10 mM HAuCl₄•3H₂O in 50 mL centrifuge tube at different volume ratios (Ti₃C₂T_x MXene: HAuCl₄•3H₂O) labeled as MA1 (1:1), MA2 (1:2), MA3 (2:1), MA4 (5:1), MA5 (1:5), MA6 (1:10), which then was sonicated in an ice water bath for 45 min. Second, the reddish brown suspension was then washed with DI water, followed by centrifugation (5,000 rpm, 15 min) several times. The final precipitate was collected and dissolved in 5 mL DI water, which was then freeze-dried for further use. The 1:2 volume ratio (Ti₃C₂T_x MXene and HAuCl₄•3H₂O) was tested to provide the MA with the best catalytic performance in H₂O₂/TMB system (**Figure 5.3. a**) (Eq.1). Therefore, the MA2 was used for the following experiment.

$$\Delta A_{653} = A_{653(2400)} - A_{653(0)} \quad (1)$$

Where $A_{653(2400)}$ and $A_{653(0)}$ are the intensity of UV-Vis absorbance peak of the enzyme nano-mimic system (MA/TMB/H₂O₂) reaction at 2400 s and 0 s, respectively.

5.2.3. Characterization of the instrument and properties

The surface morphologies of the as-obtained sample studies were recorded by a Schottky-type field-emission scanning electron microscope (FE-SEM, Zeiss LEO 1530-1) with a working

distance of 3.2 mm. All samples' X-ray diffraction (XRD) pattern was investigated using an X-ray diffractometer (Bruker D8 discovery) with Cu-K α radiation in a 20°/min scan rate within 20° to 80° of 2θ per cycle. The chemical structure and composition of L-Ti₃C₂T_x NS and MA2 were carried out through X-ray photoelectron spectroscopy (XPS, Thermo K alpha) equipped with a micro-focused monochromatic Al K α X-ray source and Spectrum 100 Fourier transform infrared (FT-IR, Perkin Elmer). Lambda 35 ultraviolet-visual spectroscopy (UV-Vis, Perkin Elmer) was employed to characterize the optical properties of all prepared samples. The Zeta potential of the MA2 colloidal solution was studied via Brookhaven's NanoBrook 90Plus Nanoparticle Size analyzer.

5.2.4. The catalyze-mimic activity of MA2 and the optimization process

The measurement of the catalyze-mimic activity of MA2 was performed using H₂O₂/TMB system in the acetic buffer (0.2 M NaAc buffer) under room temperature[19]. 120 μ g/mL of MA2 was prepared in 800 μ L NaAc buffer (pH 3.6) and mixed with 1% H₂O₂ and 5 mM TMB. The redox reaction was incubated in 33 °C water for 40 min, and the oxidized TMB (TMB_{ox}) products were measured via UV-Vis spectrometry at 653 nm of absorbance wavelength (A_{653}).

The optimal reaction conditions were determined as follows. As-prepared MA2 was added into NaAc buffer with various pH (3.0 - 6.0) to obtain 120 μ g/mL MA2 colloidal solution. Then, the MA solution was mixed with 20 μ L of 1% H₂O₂ and 10 μ L of 5 mM TMB, which was analyzed for 5s by UV-Vis spectroscopy equipped with a home-made water bath with temperatures ranging from 10 °C to 50 °C for 40 mins.

Steady-state kinetic analysis was evaluated at a fixed concentration of MA2 (120 μ g/mL in 800 μ L NaAc buffer) by varying the TMB (0.018 mM – 4.39 mM) or H₂O₂ (2 – 190 mM)

concentrations under optimal conditions. The UV-Vis data were recorded per 5s, which was then plotted according to enzyme kinetic theory (Eq. 2 and Eq. 3)[20].

$$V = \frac{V_{max}[S]}{K_m + [S]} \quad (2)$$

$$\frac{1}{V} = \frac{K_m}{V_{max}} \left(\frac{1}{[S]} + \frac{1}{K_m} \right) \quad (3)$$

Where V is the initial conversion rate of substrate, K_m means the Michaelis-Menten kinetic constant, which is used for the affinity of MA2 to substrate measurement, the higher MA2 affinity to a substrate has the lower value of K_m and vice versa; [S] and V_{max} represent the substrate concentration and the maximum conversion rate, respectively.

The reactive oxygen radicals (ROS)-capturing experiment was performed under optimal conditions in the different radical scavengers involved systems, including L-ascorbic acid (LAA), isopropanol (ISO), and ethylenediaminetetraacetic acid salt (EDTA•2Na), for superoxide anion ($\bullet O_2^-$), hydroxyl radical ($\bullet OH$), hole (h^+) scavenging, respectively[21]. The absorbance peaks of final solutions were observed at 653 nm from UV-Vis.

5.2.5. Discrimination of AMP and Pen G

To detect the AMP and Pen G, 4 mg/mL MA2 stock solution in DI water was prepared, which then was diluted with 800 μ L NaAc buffer (pH. 3.6) to obtain 120 μ g/mL suspension. This suspension was then mixed with AMP or Pen G solution with final concentrations (116.82 nM – 70.1 μ M) or (23.36 nM – 35.05 μ M), respectively, and incubated in the shaker at room temperature for 10 mins. Next, the mixture was added with 10 μ L TMB (5 mM) and 20 μ L 1% H_2O_2 , incubating in the water bath (33 °C) for 40 min. Finally, the absorbance peak of the reacted solutions was measured by UV-Vis spectrometry at 653 nm absorbance wavelength (A_{653}).

5.2.6. Real sample preparation

The applicability of the developed colorimetric sensor was validated for AMP and Pen G analysis in skim milk and tap water. For AMP and Pen G detection in tap water, the tap water was collected directly from the tap tube, which was used for dissolving AMP and Pen G to prepare spiked water samples, followed by filtering with a 0.22 μm filter membrane. The pretreatment of skim milk was based on the previous method with slight modifications[22]. 20 mL skim milk was spiked with appropriate amounts of AMP or Pen G, shaking for 5 min to obtain the homogenous solution. Then 20% acetic acid (HAc, v/v) was slowly added until the solution pH was 4.6 for milk proteins denaturation and precipitation at their isoelectric point. The prepared sample was then run at 45 °C for 45 min, followed by centrifugation (10,000 rpm, 15 min). The clear supernatant was collected, which was purified with a 0.22 μm filter and then diluted with methanol (100-fold). The AMP or Pen G milk sample was kept in the 4 °C refrigerator for further use.

All measurement experiment was triplicated, with the measure data noted as mean value \pm standard deviation (SD).

5.3. Results and discussion

5.3.1. Synthesis and characterization of MA2

In this work, Au NPs were deposited *in situ* and grown on the surface of L-Ti₃C₂T_x NS without any extra reducing agents (**Figure 5.1. A**)[18]. As shown in **Figure 5.1. A**, HCl/LiF mixture was adopted as an etchant to etch off Al atoms from the MAX phase. As a result, single or several neighboring Ti atoms from the Ti lattice were knocked out in such a strong reaction environment and left the single or cluster vacancy defects on the Ti layer[23]. In return, these defective formations affect the stability of the Ti layer, providing L-Ti₃C₂T_x NS with higher reducibility.

With the aid of the intrinsic high reducibility of L-Ti₃C₂T_x NS, the self-assembled MA2 hierarchical nanostructure can be achieved.

Additionally, the surface morphology of as-synthesized MA2 was confirmed by SEM, compared with that of L-Ti₃C₂T_x NS and MAX phase. It can be seen in **Figure 5.1. B(i)** that the surface of the MAX phase sample comprises multiple irregular pebble-like ceramic materials with diameters larger than 5 μm. The cross-sectional SEM photograph (**Figure 5.1. B(ii) and (iii)**) reveals the well-ordered lamellar structures that are stacks of several single-layer flakes with an average thickness of ~30 nm. This behavior further the exposure surface area L-Ti₃C₂T_x NS to the ambient environment. The high magnification of MA2 surface microstructure observed in SEM shows that MA2 retains well with multiple spherical Au NPs loaded and distributed into several Au NPs clusters both on the surface and interlayers, evidencing that Au NPs were successfully deposited and grown in the L-Ti₃C₂T_x NS (**Figure 5.1. B(iv)-(vi)**). This unique property facilitates the MA2 with more active sites for more enzymatic substrate capture, thus improving its catalysis performance.

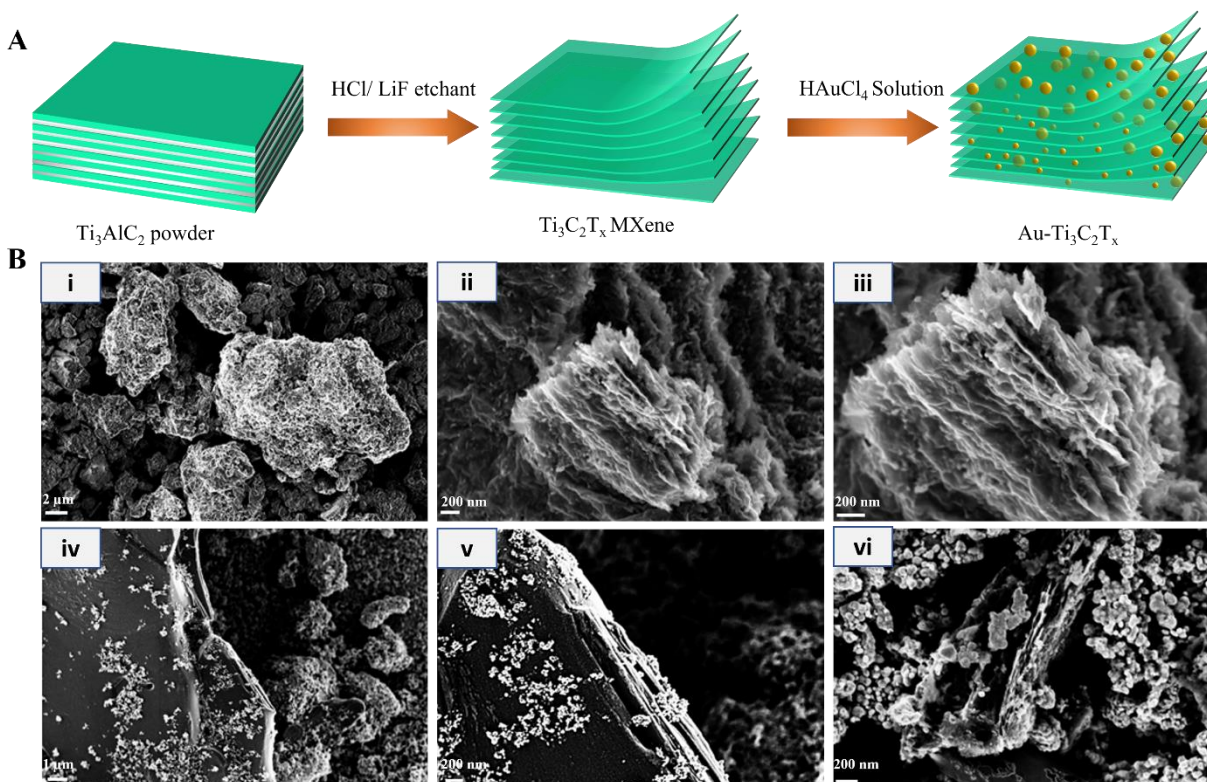


Figure 5.1. A. Schematic illustration of MA2 preparation process, B SEM surface morphology of (i) the MAX phase, (ii) and (iii) synthesized $L-Ti_3C_2T_x$ NS with different magnifications, (iv)~(vi) prepared MA2

As the interspace and purity of MXene largely influenced the size and shape of Au NPs throughout the interlayer, we further determined the internal structure of MA2 via XRD. According to **Figure 5.2. (a)**, (002) peak is centered at $2\theta = 9.64^\circ$ in the MAX phase where no impurity exists in the MAX phase particles[24]. A broader (002) peak is characteristic of the exfoliated $L-Ti_3C_2T_x$ NS, with its center shifted from $2\theta = 9.64^\circ$ to $2\theta = 7.98^\circ$, suggesting enlarged interplanar spacing from 9.167\AA to 11.071\AA in terms of Bragg law[25]. The (111), (200), (220), and (311) peaks in the XRD spectrum of MA2 emerge with corresponding centers at $2\theta = 38.23^\circ$, $2\theta = 44.48^\circ$, $2\theta = 64.60^\circ$, and $2\theta = 77.74^\circ$, respectively owing to successful Au NPs and $L-Ti_3C_2T_x$ NS hybridization.

Subsequently, XPS was employed to determine the surface elemental composition and chemical states of each sample. The F 1s and O 1s peaks with binding energy (BE) 684.8 eV and 531.1 eV, respectively, appear in full scan XPS spectrums of L-Ti₃C₂T_x NS and MA2 owing to the HCl/LiF etching process when those atoms replaced the etched Al interlayer (**Figure 5.2. (b)**) [26]. Also, Al 2s and Al 2p peaks are not observed in both L-Ti₃C₂T_x NS and MA2 XPS spectrums, suggesting the Al interlayer is successfully etched off. Au 4f XPS spectroscopy observed confirms Au NPs on the surface of L-Ti₃C₂T_x NS. In the high-resolution Ti 2p of MA2 XPS spectroscopy, two distinct major peaks at 464.1 eV and 458.3 eV result from a spin-orbital splitting, associating with the Ti 2p_{1/2} and Ti 2p_{3/2}, respectively (**Figure 5.2. (c)**) [27]. These two region components are derived from Ti-O (464.5 eV) and Ti-C (463.9 eV and 458.4 eV) species, in agreement with previous reports[28]. The deconvoluted C 2s region (**Figure 5.2. (d)**) is composed of four peaks centered at 288.2 eV (-COO), 285.5 eV (CO/CH_x), 284.2 eV (C-C), and 282.4 eV (C-Ti-T_x) [29]. These results confirm that the fundamental architecture of 2D MA2 nanocomposites has been successfully established. In **Figure 5.2. (e)**, there are three peaks with BE 531.8 eV, 531.2 eV, and 529.7 eV, corresponding to Ti-C-(OH)_x, C-Ti-O_x, and Ti-O(TiO₂), respectively, proving an insight into the oxidation of L-Ti₃C₂T_x NS (**Figure 5.2. (f)**) [30]. The unique Au 4f region is divided into two signals with BE 87.4 eV and 83.8 eV, assigned as Au 4f_{5/2} and Au 4f_{7/2}, respectively. The 3.6 eV of spin-orbit coupling energy gap indicates that the L-Ti₃C₂T_x NS has successfully bonded with Au(0)[31].

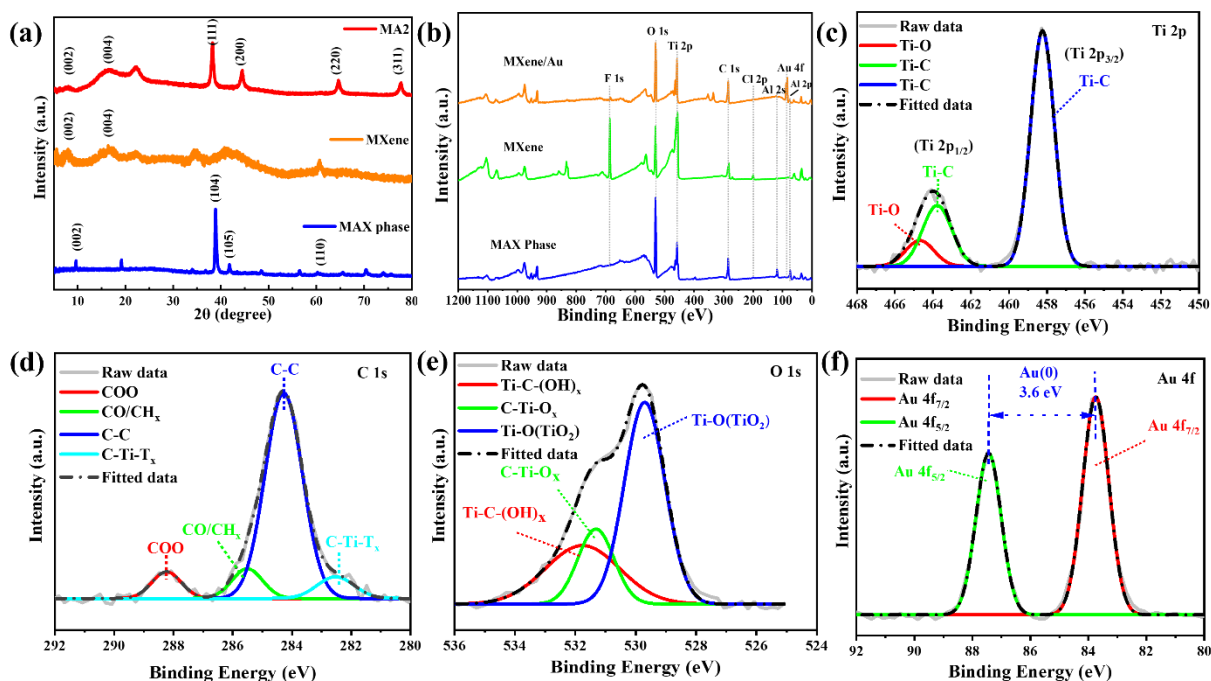
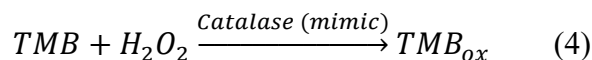


Figure 5.2. Characterization of MA2. (a). XRD pattern of MAX phase, L-Ti₃C₂T_x NS and MA2, (b). XPS full scan of MAX phase, L-Ti₃C₂T_x NS and MA2, High-resolution MA2 XPS spectra of (c). Ti 2p, (d). C 1s, (e). O 1s, (f). Au 4f.

Chemical bonds of the L-Ti₃C₂T_x NS were further proved by FT-IR (**Appendix V, Figure S5.1.**), where dips at 780 cm⁻¹ and 1080 cm⁻¹ are associated with Ti-O bending and Ti-O-C stretching, respectively [32]. Several dips at 1374 cm⁻¹ and 1764 cm⁻¹ correspond to the molecular water and C = O bonding. The relatively broad dip area appears around 2400 – 3000 cm⁻¹ due to the presence of hydroxyl group and hydrogen bond[33]. Further, the UV-Vis absorption spectrum shows an apparent wide peak of Au NPs (~553 nm), and the inset photo shows the highly concentrated MA2 (dark red) and L-Ti₃C₂T_x NS (black) solution, which confirms the change in the local refractive index of L-Ti₃C₂T_x NS, indicating that the Au NPs have successfully deposited on the L-Ti₃C₂T_x NS (**Appendix V, Figure S5.2.**)[34].

5.3.2. Optimization of reaction condition and catalase-mimic kinetic of MA2

Catalase can induce the redox reaction between the TMB and H₂O₂, producing the blue TMB_{ox} in the solution, the process of which is shown in Eq. 4.



Different systems were performed to confirm that MA2 can work as catalase with high enzymatic kinetic and activity, and final products were measured by UV-Vis spectrometer (Shown in **Figure 5.3. (a)**). When MA2 was present in the H₂O₂/TMB system, the color of the solution slowly turned blue, along with small bubbles generated slowly and intermittently, indicating blue TMB oxide and the production of oxygen gas (O₂). Per our previous publication, a fewer-layer Ti-based MXene can work as peroxidase-mimic, which can also turn the solution blue as a result of the environment composed of a large amount of H₂O₂ and TMB[16]. Nonetheless, only the MA2 group with significant diluted H₂O₂ and TMB concentrations can produce the blue color. This result demonstrates that MA2 can function as an enzyme in the presence of H₂O₂ and TMB, and the hierarchical nanostructure of MA2 with Au NPs and L-Ti₃C₂T_xNS synergic effect significantly boosts the enzymatic kinetics of the MA2. Further, the catalytic performance of MA2 increases significantly with increasing time and the amount of MA2 (**Appendix V, Figure S5.3**).

pH- and temperature-dependent stabilities were investigated for reaction condition optimization (**Figure 5.3. (b)**). As the blue short dash-dot line shows, the most sensitive response to enzymatic substrates was measured at pH 3.6, which was used as the optimal pH in this work. The catalytic ability of MA2 investigated under various temperatures ranging from 10 °C to 50 °C states that 33 °C was the best temperature as the most intense absorbance peak of MA2/TMB/H₂O₂ system was observed in UV-Vis spectrometer (shown in red-solid line in **Figure 5.3. (b)**).

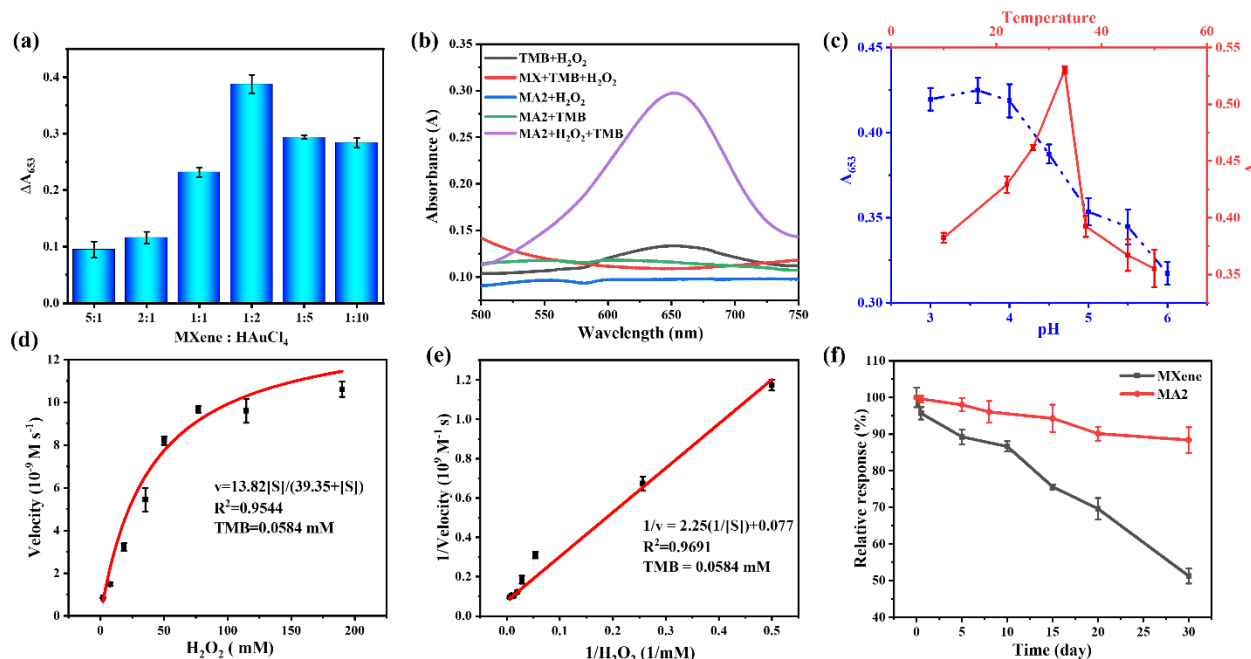


Figure 5.3. (a). Optimization of volume ratio between L-Ti₃C₂T_x NS MXene and HAuCl₄•3H₂O. (b). The UV-Vis spectrum of the different reaction systems involving TMB+H₂O₂, L-Ti₃C₂T_x NS+TMB+H₂O₂, MA2+H₂O₂, MA2+TMB, and MA2+TMB+H₂O₂, (c). Effects of pH (blue) and temperature (red) on the MA2 catalytic activity, The steady-state kinetic curves of MA2 for enzyme-substrate H₂O₂ at fixed TMB concentration plotted by (d). Michaelis-Menten equation and (e). Lineweaver-Burk equation, (f). Long-term stability of MA2 and L-Ti₃C₂T_x NS MXene after being kept under room temperature for 30 days.

The catalase-like kinetic of hierarchical nanostructure MA2 executed in the classical chromogenic system (H₂O₂/TMB) follows the typical Michaelis-Menten curve, depicting the hyperbolic relationship between the concentration of enzymatic substrates (TMB or H₂O₂) and velocity (**Figure 5.3. (c) and (e)**). Two steady-state parameters, K_m and V_{max}, were measured by its double reciprocal curve (Lineweaver-Burk) (**Figure 5.3. (d) and (f)**). K_m value, identified as the enzyme affinity to a substrate, was determined as 39.35 mM of MA2 against H₂O₂, which is

lower than that of catalase, with emphasis on the better affinity of MA2 against H₂O₂ (**Appendix V, Table S5.2.**). It is worth noting that the MA2 has ~17 folds lower K_m values for H₂O₂ than that of L-Ti₃C₂T_x NS (0.677 M), in emphasis that the synergistic effect of Au and L-Ti₃C₂T_x NS is capable of significantly increasing the affinity of MA2 against H₂O₂ (**Appendix V, Table S5.2.**). **Table S5.2 (Appendix V)** also compares the K_m values of some selected catalase-mimic nanomaterial for H₂O₂, where the K_m of most catalase-mimics is higher than that of MA2(**Appendix V, Table S5.2.**). Based on these results, it is indicative that MA2 has a higher affinity to enzymatic substrates than other catalase-mimics. Therefore, MA2 can trigger the catalytic reaction in the few amounts of H₂O₂ and TMB solution, turning the white transparent color blue (**Figure 5.3.(a)**).

The long-term stable performance of MA2 and L-Ti₃C₂T_x NS was carried out by triggering the redox reaction between H₂O₂ and TMB under their own optimal conditions during their room-temperature storage period (30 days) (**Figure 5.3. (f)**). The relative response (%) was measured as Eq. 5:

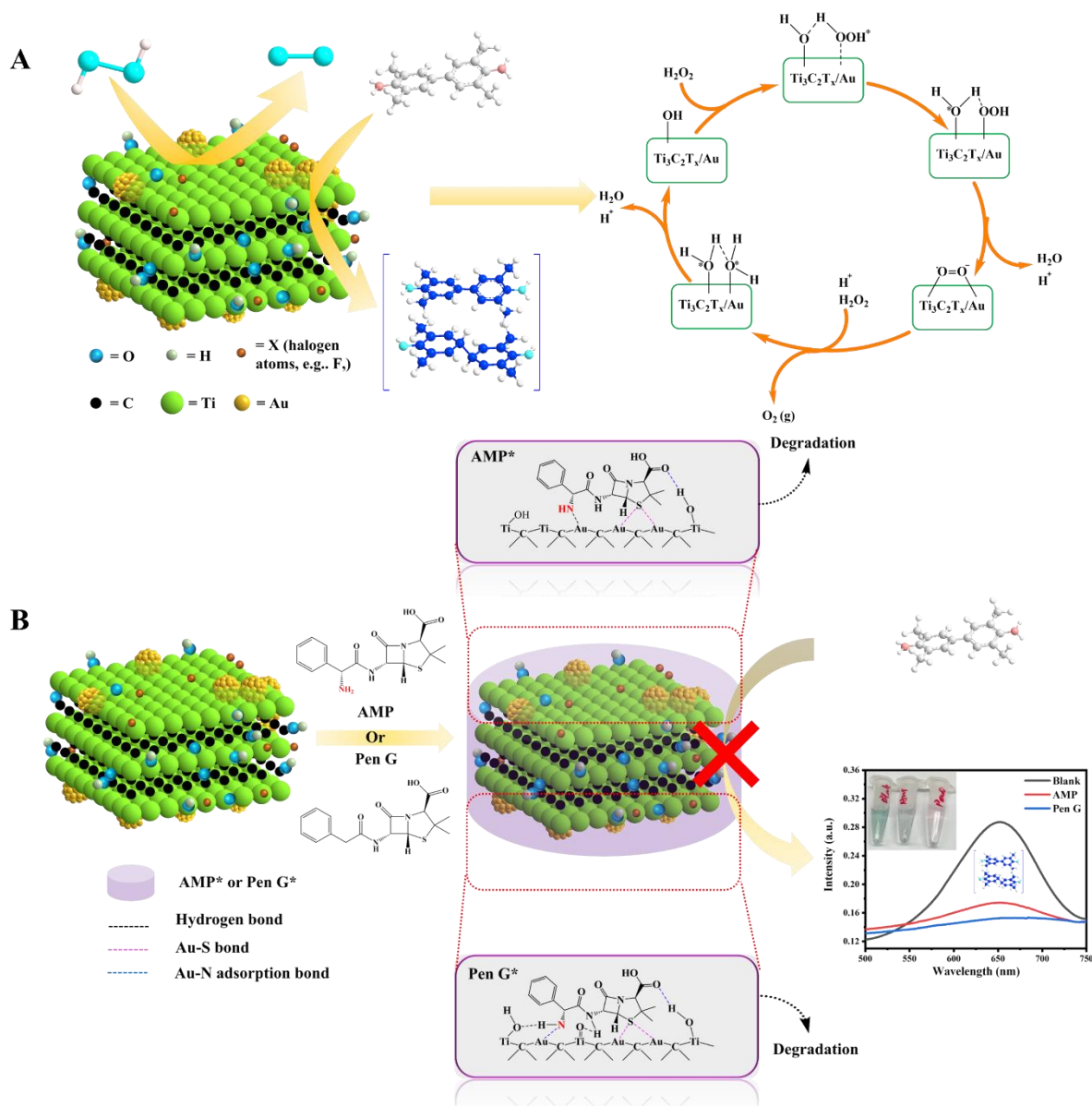
$$\text{Relative response (\%)} = \frac{A_{653}(t)}{A_{653}(i)} * 100\% \quad (5)$$

Where A₆₅₃(t) and A₆₅₃(i) are the absorbance intensity of the H₂O₂/TMB solution in the presence of t-storage-time and fresh nanomaterials, respectively. Excellent stability of MA2 was obtained after it was stored for 20 days, with the remaining 90.13% of catalytic performance in H₂O₂/TMB (Shown in **Figure 5.3. (f)**). High stability of MA2 occurs due to the relatively low zeta potential of -32.86 mV in buffer prevents the MA2 aggregation by considerably strong inter-nanomaterial repulsion force (shown in **Appendix V, Table S5.3.**)[35].

5.3.3. Mechanism of catalase-mimic activity of MA2

In accordance with our observation and investigation, **Scheme 5.1. A** exhibits the proposed mechanism of the catalase-mimic performance of MA2. However, it is hard to predict this with detailed information, which should be further studied. As previous XPS and FTIR data shown, hierarchical MA2 nanocomposites were oxidized by oxygen since oxidized L-Ti₃C₂T_x NS reactant was used, where multiple O-related groups terminated on the surface of L-Ti₃C₂T_x NS as well as MA2. Furthermore, the negative zeta potential value of MA2 indicates that the slipping plane of MA2 particles was covered with pre-adsorption of OH⁻ [36]. As the H₂O₂ was introduced into the MA2 colloidal solution, it was quickly adsorbed on the MA2 surface as adsorbate H₂O₂ (H₂O₂^{*}) (**Scheme 5.1. A**, right). With the abundance of the pre-adopted OH⁻ on the MA2 hierarchical surface, e.g., the surface of the Au (111) facet, the decomposition process of adsorbed H₂O₂^{*} tended to follow the acid-like decomposition strategy with calculated lower energy barriers of the first (0.13 eV) and second steps (0.80 eV)[37]. As a result, hydroperoxyl ligands (-OOH) were formed in terms of the H-OOH bond cleavage[38]. Released H⁺ ions then had rearrangement and conjugation with the adjacent -OH group, resulting in adsorbate H₂O (H₂O^{*}) formation as well (**Scheme 5.1. A**, right)[39]. The -OOH group was further stabilized by hydrogen bonds formed between the -OOH group and other polar groups and even H₂O^{*} on the MA2 surface, such as -F, =O, -OH, etc. According to the radical-trap experiment (**Appendix V, Figure S5.4.**), there is no color change in the MA2/TMB/H₂O₂ system in the presence of LAA, indicative of the superoxide anion (O₂^{-•}) importance in the H₂O₂ decomposition process[21]. The hydroxyl radical (•OH) is not the result of our experiment due to the UV-Vis absorbance peak of an ISO-contained enzyme nano-mimic system with similar intensity to that of the blank system. Moreover, it is important to note that the absorbance peak of the MA2 system with a much lower intensity was observed in the

presence EDTA•2Na. This demonstrates that h^+ is formed and plays a critical role in the colorimetric oxidation of TMB, leading to greenish blue TMBox product release. As mentioned earlier, abundant e^- remained on the surface of L-Ti₃C₂T_x NS due to the etching process, which provides e^- a rich surface environment with O₂^{-•}. In consideration of pH 3.6 external environment (H₃O⁺), O₂ gas was generated when rich in H₃O⁺ ions reacted with O₂^{-•} and surface e^- in the solution[40]. Furthermore, the synthesized MA2 has the Ti-O (TiO₂) composition on the surface as XPS shows. It is an energetical favorite to replace the final produced adsorbate H₂O molecules with H₂O₂ molecules due to higher magnitude adsorption energy of H₂O₂ on the TiO₂ surface[38]. Finally, the MA2 nanocomposites enters another catalytic cycle.



Scheme 5.1. A. Schematic illustration of a proposed mechanism in the MA2/TMB/H₂O₂ system, B. Schematic diagram of the mechanism of AMP and Pen G inhibitive effect on the MA2-triggered redox reaction between two substrates

5.3.4. Colorimetric detection of AMP and Pen G

As AMP or Pen G was able to suppress the color change of the enzyme mimic system (MA2/TMB/H₂O₂), it is possible to establish a colorimetric sensing methodology for AMP and Pen G analysis. We proposed the mechanism of colorimetric sensing of AMP and Pen G, though more details need to be further investigated. The color of the enzyme mimic system turned greenish-blue without adding AMP or Pen G, which can be confirmed in the measuring A₆₅₃ via UV-Vis spectroscopy (Shown in **Scheme 5.1.B UV spectra (Blank)**). In contrast, when AMP and Pen G were added into the system, the greenish-blue color of the solution cannot appear as **Scheme 5.1. B UV spectra (AMP and Pen G)** were shown, neither were measured by UV-Vis spectroscopy. Accordingly, AMP and Pen G can be adsorbed on the Au and TiO₂ surface via the Au-S conjugation bond and hydrogen bonds in an acidic solution[41, 42]. This may block the active sites of MA2 to TMB and inhibit the oxidation reaction of TMB, thus preventing color change. From an atomic-scale perspective, protonated AMP (pK_{a2} = 7.1) can be adsorbed on the Au surface via Au-S and N-Au conjugation bond in the form of a "direct" or "bridge" configuration with a higher magnitude of adsorption energy than that of the Au-S conjugation bond only [41, 42]. In other words, it is energetically preferable for AMP adsorption on the Au surface with two former configurations via Au-S and N-Au conjugation bonds (**Shown in Scheme 5.1. B**). Furthermore, the greenish-blue color of the antibiotic-involved mixture (MA2/TMB/H₂O₂) appeared slowly after overnight reaction (**Figure S5.5**), probably resulting from that two lactam antibiotics are hypothesized to be under degradation in this enzyme mimic system since [43].

Based on the color-inhibition strategy, we designed an MA2-based detection method to analyze AMP and Pen G qualitatively and quantitatively. The optimization of incubation time was carried out by mixing AMP and MA2 before TMB and H₂O₂ were introduced. The data was recorded in

Figure S5.7., where A_{653} is the absorbance peak of the final MA2 system measured under a wavelength of 653 nm. The lowest UV-Vis absorbance intensity at 10 min incubation time means the best inhibitive effect of AMP on the color-change reaction. Therefore, 10 min was used as the optimal incubation time for AMP and Pen G detection.

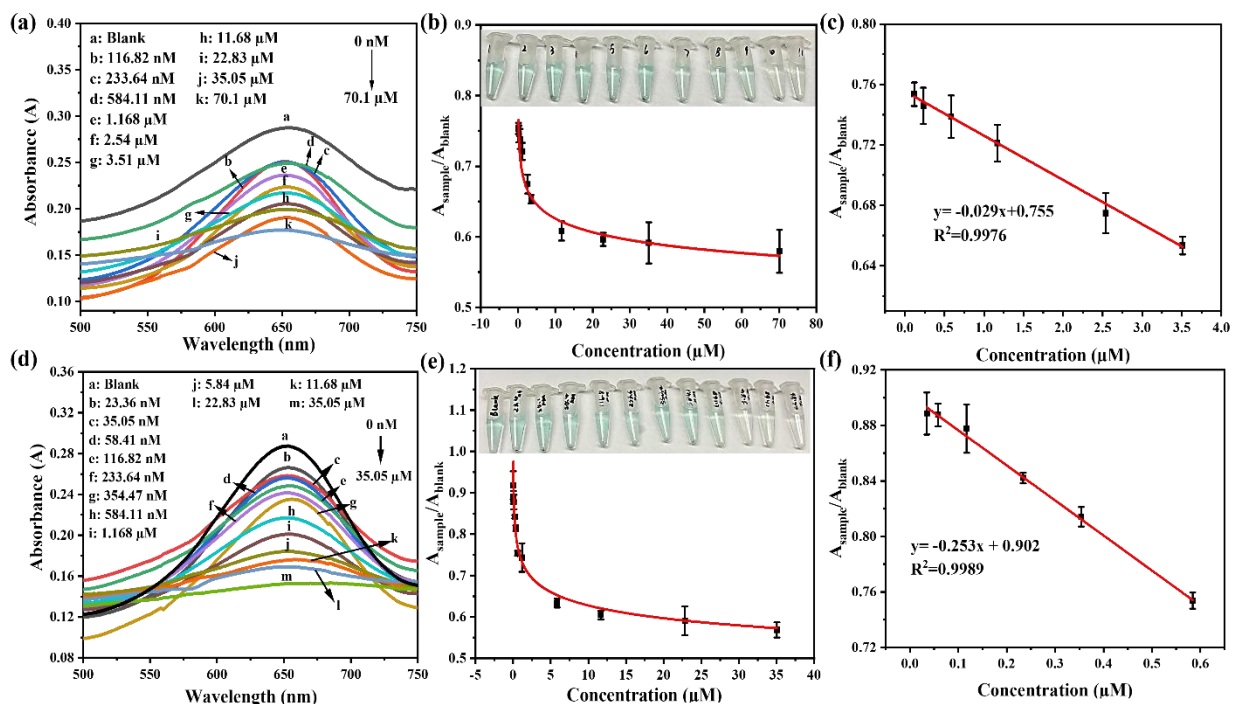


Figure 5.4. (a). and (d). UV-Vis absorption spectra for AMP and Pen G detection, respectively, by the enzymatic nano-mimic system, (b). and (e). Detection range of designed colorimetric method for AMP and Pen G, respectively, inset: digital photos for the visualized color change of MA2/TMB/H₂O₂ system in the presence of a corresponding concentration of AMP and Pen G, respectively, Linear-relationships between β -lactam antibiotics concentrations ((c). AMP and (f). Pen G concentration) and the relative response of UV-Vis absorbance peak.

Under the optimal reaction conditions, the sensing performance of the enzyme mimic system for discrimination of two β -lactam antibiotics was investigated using UV-Vis techniques. **Figure**

5.4. (a) and 5.4. (d) show the intensity of the UV-Vis absorbance peak at 653 nm of the enzyme mimic system in the presence of AMP-only and Pen G-only, respectively, which continuously reduces with the increasing amount of two antibiotics concentrations. Based on the UV-Vis spectra, the dynamic range of this method for AMP and Pen G analysis was plotted in **Figure 5.4. (b) and 5.4. (e)**. The y-axis was calculated as follows (Eq. 6):

$$\text{y-axis} = \frac{A_{\text{sample}}}{A_{\text{blank}}} \quad (6)$$

Where A_{sample} and A_{blank} mean the A_{653} values of the enzymatic nano-mimic system only and the AMP or Pen G-contained enzymatic nano-mimic system, respectively. Consequently, this method has relatively wide dynamic ranges for two antibiotics, from 116.82 nM to 70.1 μM and 23.36 nM to 35.05 μM for AMP and Pen G, respectively (**Figure 5.4. (b) and 5.4. (e)**). The inset photographs of **Figure 5.4. (b) and 5.4. (e)** depict the color fading from apparent greenish blue to colorless in the presence of corresponding AMP and Pen G concentrations, respectively. Thus, the MA2 catalase-mimic performance enables the naked eye semi-quantitative determination of AMP and Pen G in nano- and micromolar ranges. Besides, the high linearity of sensor response was calculated as 116.82 nM to 3.51 μM and 35.1 nM to 584 nM for AMP ($R^2 = 0.9976$) and Pen G ($R^2 = 0.9989$) detection (**Figure 5.4. (c) and (f)**), respectively. The calculated limit of detection (LOD) is 68.9 nM and 7.51 nM for AMP and Pen G, respectively, in regards to the formula of $L=3.3*S/R$, where S is the standard deviation of the intercept, and R reveals the slope of the calibration curve[44]. Although the LOD of AMP detection is higher than the MRL of the requirements, that of Pen G detection is smaller than the MRL of the requirement set by different international agencies (**Appendix V, Table S5.1.**). This may result from different AMP and Pen G degradation rates in the presence of MA2, where the AMP might be photodegraded faster than Pen G. Yet, this should be further investigated. Compared with other colorimetric methods, our method

exhibited better sensing performance in Pen G detection than most, though the sensitivity to AMP detection is lower (**Appendix V, Table S5.4**). Additionally, our method can detect two lactam antibiotics, AMP and Pen G, separately with relatively good results. To test the validation of our method in the existence of both antibiotics, we mixed AMP and Pen G in a 1:1 ratio as the β -lactam antibiotic mixture detected by this established method (**Appendix V, Figure S5.6**). The result presents that our method can also be available for AMP/Pen G mixture detection.

5.3.5. Selectivity and real sample application

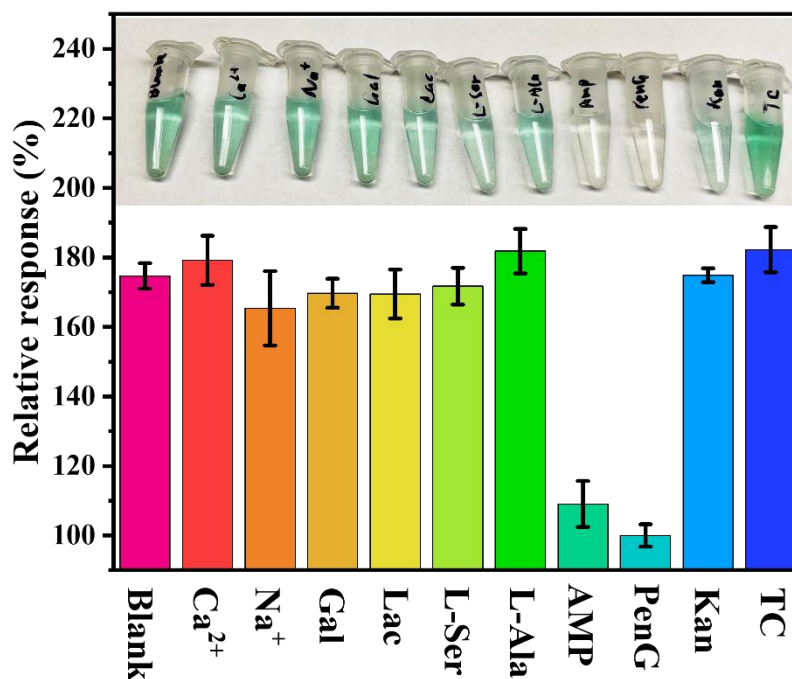


Figure 5.5. The selectivity experiment of MA2 towards 11 potential targets (35.05 μ M). Lac: lactose, L-Ser: L-serine, L-Ala: L-alanine, Kan: kanamycin, TC: tetracycline.

Eight different potential interferents were used to evaluate the specificity of this sensor, including ions, amino acids, and other antibiotic families (such as kanamycin and tetracycline). Under optimal conditions, the tests were performed with 35.05 μ M interferents in the above

enzyme nano-mimic system. As illustrated in the inset digital photo of **Figure 5.5.**, there is less greenish-blue color appearance in the MA2/TMB/H₂O₂ system containing AMP or Pen G compared to other interferents-involved solutions. To quantitatively measure the intensity of color change for selectivity determination, we calculated the relative response (%) as following Eq. 7:

$$\text{Relative Response (\%)} = \frac{A_{653}(\text{interferents})}{A_{653}(\text{Pen G})} * 100\% \quad (7)$$

Where $A_{653}(\text{interferents})$ and $A_{653}(\text{Pen G})$ are UV-Vis absorbance peaks of the solution containing interferents and Pen G, respectively. Here, the AMP-contained solution was calculated as an "interferent" in terms of lower sensitivity for AMP detection than that for Pen G. Higher relative response indicates a lower inhibitive effect on the color change of the enzyme nano-mimic system. It can be seen that the relative response is significantly lower for solutions treated by AMP or Pen G than other interferent-involved samples. This data suggests that this sensor has good analysis selectivity.

The applicability of this sensor was carried out to detect AMP and Pen G in tap water and skim milk products by the standard addition method. The measured concentrations of AMP and Pen G in tap water were lower than spiked concentrations, with recoveries ranging from 92.2% ~ 98.3% and 80.7 % ~ 92.2%, respectively, probably ascribed to the pretreatment (**Appendix V, Table S5.4.**). On the contrary, AMP and Pen G with higher measured concentrations were calculated from the skim milk, caused by the more complexity of milk sample matrices, where the organic flavors or proteins may influence the sensor activity. Overall, our colorimetric sensor presents an alternative approach to AMP and Pen G analysis and shows a promising way for agri-food system monitor.

5.4. Conclusions

In summary, a novel hierarchical nanocomposite, MA2, was constructed by using a one-step, facile method where Au precursor was directly reduced by L-Ti₃C₂T_x NS without adding any reductants. With remarkably boosting enzyme-like catalytic activity owing to the synergetic effect of Au and L-Ti₃C₂T_x NS, prepared-MA2 is capable of generating O₂^{-•} anion with the aid of H₂O₂ molecules, which plays an essential role in the redox reaction between two enzymatic substrates (H₂O₂ and TMB) and facilitates the color of the solution to turn greenish-blue. As AMP or Pen G was introduced into the system, both two β-lactam antibiotics were energetically adsorbed on the surface of MA2 by hydrogen bonds, N-Au absorption, and S-Au conjugation bonds, which can block the exposure of active sites of MA2 to external environments, specifically, TMB. Next, the adsorbed β-lactam antibiotics might further be degraded by consuming the generated O₂^{-•} from H₂O₂, consequently inhibiting the colorimetric oxidation of TMB and, finally, the system's color change. According to this strategy, the colorimetric detection assay was designed and established for qualitative and quantitative measurements of two antibiotics. The assay exhibited an excellent LOD (7.51 nM) for Pen G while lower sensitivity to AMP with a LOD of 68.9 nM in 40 min, probably due to the different degradation rates of AMP and Pen G. Our colorimetric method can provide a promising alternative in routine sensing practice for β-lactam antibiotics analysis in agri-food system monitoring.

5.5. Appendix V.

Table S5.1. Maximum residue limit of ampicillin and penicillin in milk

Antibiotics	International Agencies	MRL ⁵ ($\mu\text{g/L}$)	Ref. ⁶
AMP ¹	USFDA ³	10 (~30 nM)	[45]
	EU ⁴	4 (~12 nM)	[46]
PenG ²	USFDA	5 (~15 nM)	[47]
	E.U.	4 (~12 nM)	[46, 48]

Note: ¹ AMP: ampicillin, ² PenG: penicillin G, ³ USFDA: the U.S. Food and Drug Administration,

⁴ E.U.: the European Union, ⁵ MRL: maximum residue limit, ⁶ Ref.: reference.

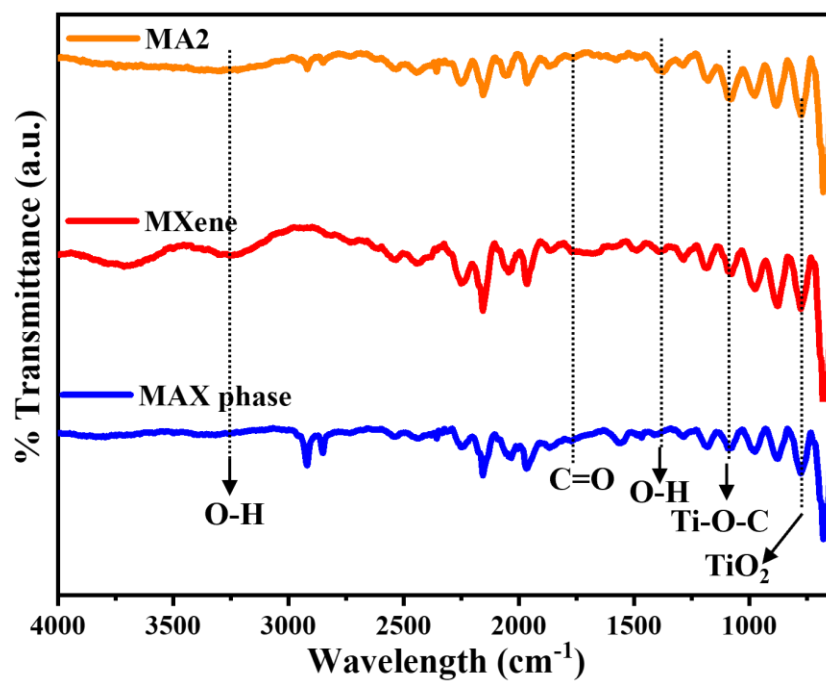


Figure S5.1. FT-IR spectra of MA2, L-Ti₃C₂T_x NS MXene, and MAX phase.

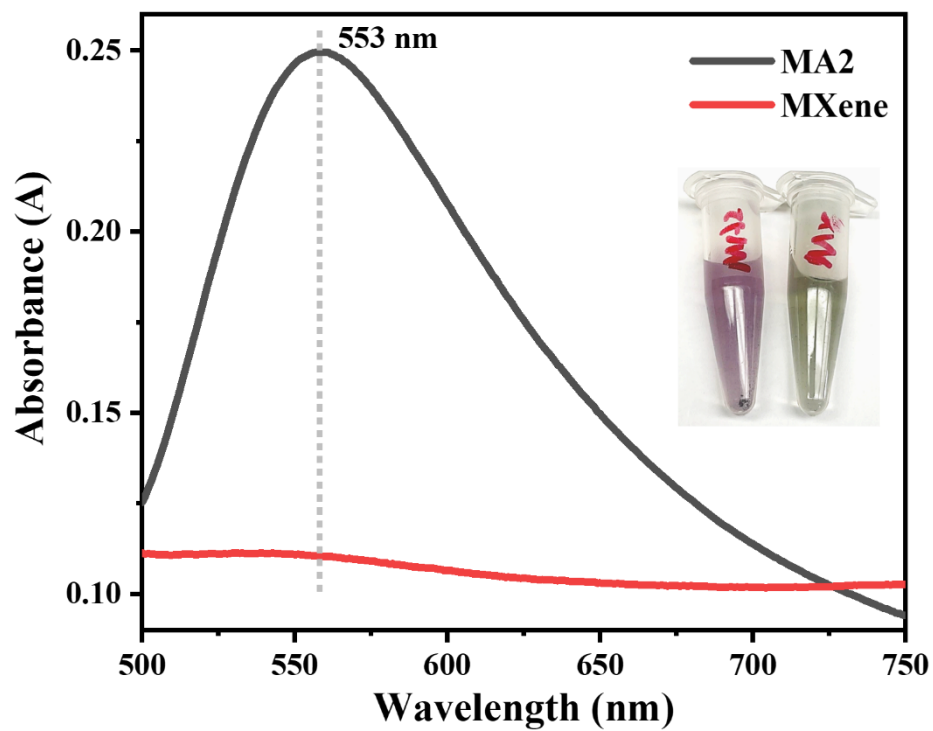


Figure S5.2. UV-Vis absorbance spectra of MA2 and L-Ti₃C₂T_x NS MXene. Inset: digital photo of concentrated MA2 (red) and L-Ti₃C₂T_x NS MXene solution (light grayish green).

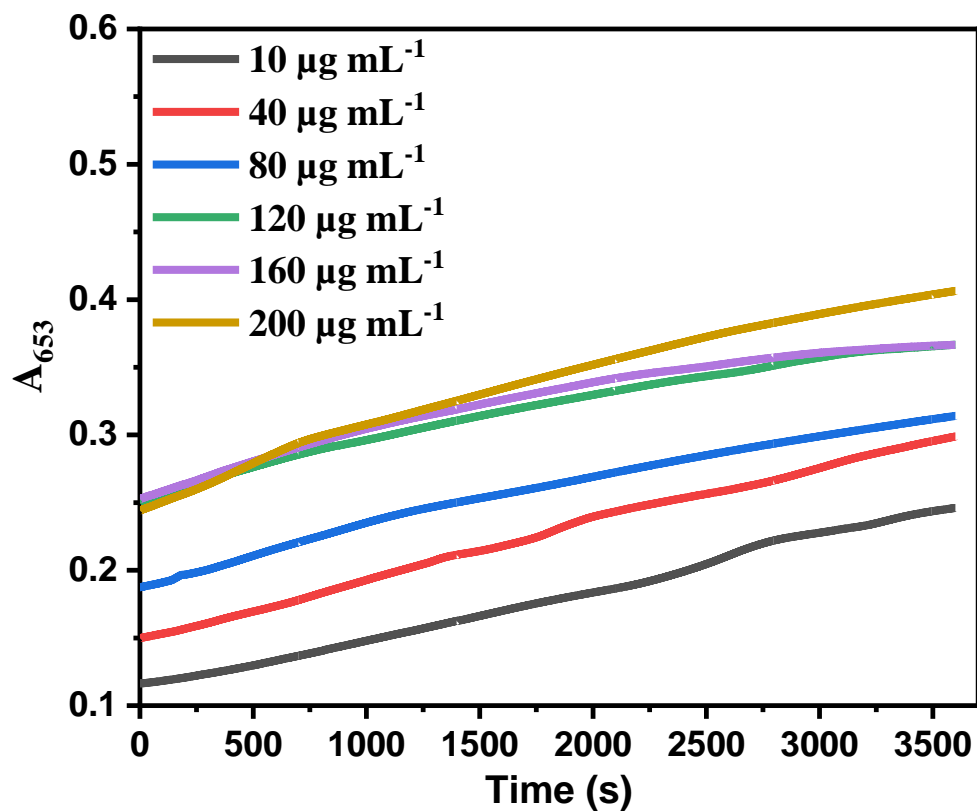


Figure S5.3. The time-drive curve for redox reaction of TMB/ H_2O_2 induced by various MA2 concentrations.

Table S5.2. Comparison of different catalase-like nano-mimics with their Michaelis-Menton kinetic parameters to H₂O₂ substrate

Catalase/catalase-like nano-mimic	K _m (mM)	V _{max} (nM/s)	Reference
Catalase	71.60	2.9*10 ⁵	[49]
Pt-Ft ^a	420.60	8.4*10 ⁵	
Fe ³⁺ /AMP CPs ^b	112.2	2.4*10 ³	[50]
2L-Fht ^c	40.60	3.04*10 ³	[51]
Multi-caged IrO _x NPs	187.95	5.64*10 ³	[52]
PBNCs@PEI ^d	0.21	415.6	[53]
HABT-C ^e	104.5	1.22 *10 ^{3 f}	[54]
Co-SAs@NC ^g	40.5	8.1*10 ⁴	[55]
Au ₂₄ Ag ₁ nanocluster	222.42	1.15*10 ³	[56]
MA2	39.35	13.82	This work

Note: a. ferritin-platinum nanoparticles, b. Fe³⁺ immobilized adenosine monophosphate (AMP), c. 2-line ferrihydrite, d. polyethyleneimine-modified Prussian blue nanocubes, e. Au nanoparticle doped carbon dots modified TiO₂ nanosphere, f. unit was converted from reported mg/L min to nM/s, g. Co-coated N-doped porous carbon

Table S5.3. Zeta potential of MA2 in different solutions

Solution	Zeta potential ^a	Standard error ^b
Water (pH 7.0)	-30.16	3.17
Buffer (pH 3.6)	-32.86	0.39

Note: a. zeta potential was repeated five times and calculated with mean value, b. standard error was calculated based on five repeated experiments.

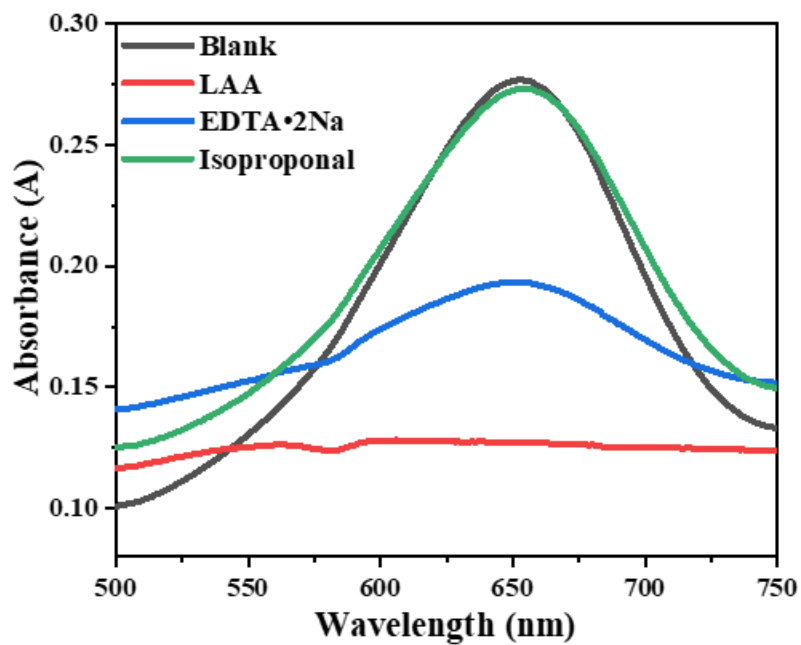


Figure S5.4. UV-Vis spectra for free radical-trapping experiment with various radical scavengers. LAA: L-ascorbic acid, EDTA•2Na: Ethylenediaminetetraacetic acid sodium salts.

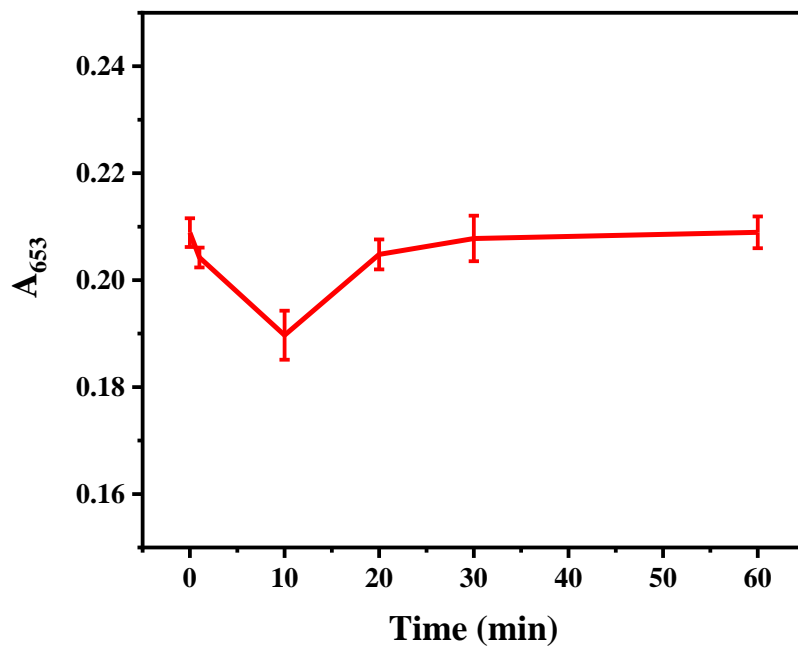


Figure S5.5. Optimization experiment for an incubation time of β -lactam antibiotics and MA2

Table S5.4. Comparison of different methods for AMP and PenG detection

Targets	Analysis method	Material composites	Linear range	LOD	Ref. ^a
AMP	Colorimetric	Au NPs	0.03 ~ 10 ng/mL	0.0013 ng/mL	[57]
	Colorimetric	Mo-CDs ^b	0.0500 ~ 100 µg/mL	12 ng/mL	[58]
	EC-SPR ^c	Aptasensor	2.5 ~ 1000 µM	1 µM	[59]
	ACV ^d	Methylene blue-aptasensor	5~ 5000 µM	1 µM	[60]
	SWV ^e		100 ~ 5000 µM	30 µM	
	Electrochemical	Aptasensor	100 ~ 10,000 µg/mL	10 µg/mL	[61]
	BIA ^f	Cu electrode	30 ~ 250 µM	7.11 µM	[62]
	Colorimetric	MA2	116.82 nM ~ 3.51 µM	68.9 nM	This work
Pen G	Fluorescence	ssDNA aptasensor	0 ~ 50 nM	9.2 nM	[63]
	SERS ^g	Ag platform	100 nM ~ 100 µM	100 nM	[64]
	Electrochemical	β-lactamase-based biosensor	0.26 ~ 0.66 µM	0.079 µM	[65]
	Electrochemical	CILE-TiO ₂ /IL ^h	3 ~ 1,000	2.09 nM	[66]
	Electrochemical	Al-p-Si-SiO ₂ -Ta ₂ O ₅ -virus (TMV) ⁱ	0.1 ~ 10 mM	50 µM	[67]
	Electrochemical	Pt/Au nanowire/nanoparticle array	20 ~ 310 µM	10.5 µM	[68]
	Colorimetric	Modified TMV nanorods with penicillinase	-	100 µM	[69]
	Colorimetric	MA2	35.1 nM ~ 584 nM	7.51 nM	This work

Note: a. Reference, b. molybdenum-coated carbon dots, c. Electrochemical surface plasmon resonance, d. alternating current voltammetry, e. square wave voltammetry, f. batch injection analysis, g. surface-enhanced Raman scattering, h. TiO₂ nanoparticles/ionic liquid coated carbon paste electrode, i. TMV: tobacco mosaic virus

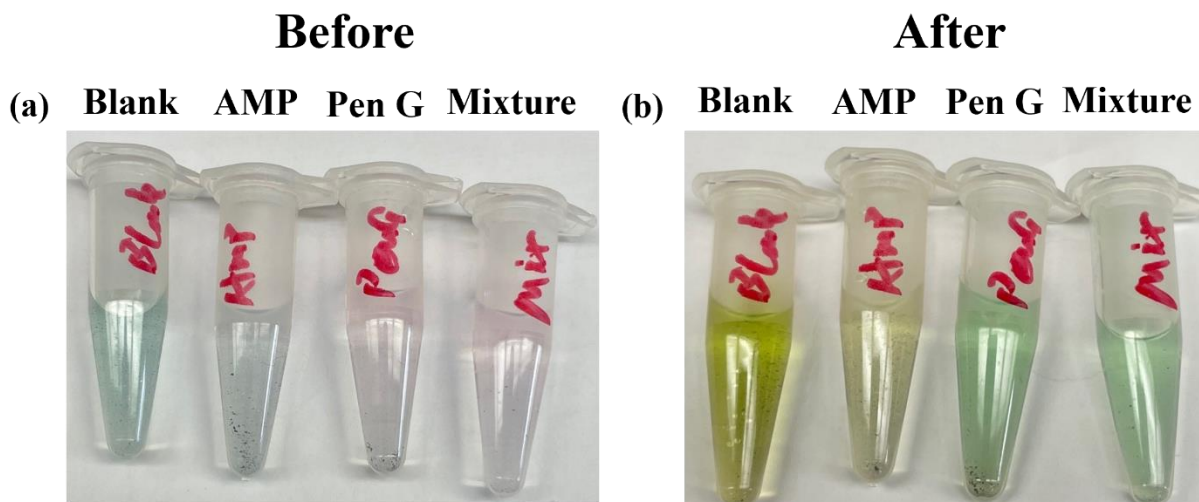


Figure S5.6. Overnight experiment of the inhibition effect of AMP, PenG, and their mixture (1:1) on the enzymatic nano-mimic system (MA2/TMB/H₂O₂).

Table S5.5. Results of AMP and PenG detection in the real sample matrices

Sample	Target	Spiked (μM)	Found (μM)	Recovery(%) ^a	STD ^b
Tape water	AMP	0.2	0.197	98.29	7.16
		0.5	0.46	92.22	13.27
	Pen G	0.08	0.074	92.26	8.74
		0.16	0.129	80.71	7.39
Skim milk	AMP	0.2	0.26	131.26	9.16
		0.5	0.52	104.75	11.89
	Pen G	0.08	0.099	124.09	9.05
		0.16	0.14	107.17	10.83

Note: a. Recovery: $\text{recovery} = \frac{\text{found concentration}}{\text{spiked concentration}} \times 100\%$, standard deviation error for three tests.

5.6. References

- [1] K.I. Mohr, History of antibiotics research, How to Overcome the Antibiotic Crisis: Facts, Challenges, Technologies and Future Perspectives (2016) 237-272.
- [2] I. Braschi, S. Blasioli, C. Fellet, R. Lorenzini, A. Garelli, M. Pori, D. Giacomini, Persistence and degradation of new β -lactam antibiotics in the soil and water environment, *Chemosphere* 93(1) (2013) 152-159.
- [3] V.K. Sharma, N. Johnson, L. Cizmas, T.J. McDonald, H. Kim, A review of the influence of treatment strategies on antibiotic resistant bacteria and antibiotic resistance genes, *Chemosphere* 150 (2016) 702-714.
- [4] M. Shirani, B. Akbari-Adergani, H. Rashidi Nodeh, S. Shahabuddin, Ultrasonication-facilitated synthesis of functionalized graphene oxide for ultrasound-assisted magnetic dispersive solid-phase extraction of amoxicillin, ampicillin, and penicillin G, *Microchimica Acta* 187 (2020) 1-11.
- [5] S. Nathanson, E. Moreau, C. Merlet-Benichou, T. Gilbert, In utero and in vitro exposure to β -lactams impair kidney development in the rat, *Journal of the American Society of Nephrology* 11(5) (2000) 874-884.
- [6] M.I. Hutchings, A.W. Truman, B. Wilkinson, Antibiotics: past, present and future, *Current opinion in microbiology* 51 (2019) 72-80.
- [7] K.M.S. Ana, J. Madriaga, M.P. Espino, β -Lactam antibiotics and antibiotic resistance in Asian lakes and rivers: An overview of contamination, sources and detection methods, *Environmental Pollution* 275 (2021) 116624.
- [8] M. Esmaelpourfarkhani, K. Abnous, S.M. Taghdisi, M. Chamsaz, A novel turn-off fluorescent aptasensor for ampicillin detection based on perylenetetracarboxylic acid diimide and gold nanoparticles, *Biosensors and Bioelectronics* 164 (2020) 112329.
- [9] W. Wang, S. Gunasekaran, Potential Toxicology of Nanozymes, *Nanozymes*, CRC Press 2021, pp. 377-401.
- [10] W. Wang, S. Gunasekaran, Nanozymes-based biosensors for food quality and safety, *TrAC trends in analytical chemistry* 126 (2020) 115841.
- [11] H. Wang, K. Wan, X. Shi, Recent advances in nanozyme research, *Advanced materials* 31(45) (2019) 1805368.
- [12] Q. Zhong, Y. Li, G. Zhang, Two-dimensional MXene-based and MXene-derived photocatalysts: Recent developments and perspectives, *Chemical Engineering Journal* 409 (2021) 128099.
- [13] M. Hu, H. Zhang, T. Hu, B. Fan, X. Wang, Z. Li, Emerging 2D MXenes for supercapacitors: status, challenges and prospects, *Chemical Society Reviews* 49(18) (2020) 6666-6693.
- [14] W. Wang, S. Gunasekaran, MXene-Based Nucleic Acid Biosensors for Agricultural and Food Systems, *Biosensors* 12(11) (2022) 982.
- [15] Y. Pei, X. Zhang, Z. Hui, J. Zhou, X. Huang, G. Sun, W. Huang, Ti₃C₂TX MXene for sensing applications: recent progress, design principles, and future perspectives, *ACS nano* 15(3) (2021) 3996-4017.
- [16] W. Wang, Y. Yin, S. Gunasekaran, Oxygen-terminated few-layered Ti₃C₂T_x MXene nanosheets as peroxidase-mimic nanozyme for colorimetric detection of kanamycin, *Biosensors and Bioelectronics* (2022) 114774.
- [17] M. Alhabeb, K. Maleski, B. Anasori, P. Lelyukh, L. Clark, S. Sin, Y. Gogotsi, Guidelines for synthesis and processing of two-dimensional titanium carbide (Ti₃C₂T_x MXene), *Chemistry of Materials* 29(18) (2017) 7633-7644.

- [18] E. Satheeshkumar, T. Makaryan, A. Melikyan, H. Minassian, Y. Gogotsi, M. Yoshimura, One-step solution processing of Ag, Au and Pd@ MXene hybrids for SERS, *Scientific reports* 6(1) (2016) 1-9.
- [19] J. Hu, F. Tang, L. Wang, M. Tang, Y.-Z. Jiang, C. Liu, Nanozyme sensor based-on platinum-decorated polymer nanosphere for rapid and sensitive detection of *Salmonella typhimurium* with the naked eye, *Sensors and Actuators B: Chemical* 346 (2021) 130560.
- [20] H. Wu, J. Liu, Z. Chen, P. Lin, W. Ou, Z. Wang, W. Xiao, Y. Chen, D. Cao, Mechanism and application of surface-charged ferrite nanozyme-based biosensor toward colorimetric detection of L-cysteine, *Langmuir* 38(27) (2022) 8266-8279.
- [21] Y. Wang, L. Rao, P. Wang, Z. Shi, L. Zhang, Photocatalytic activity of N-TiO₂/O-doped N vacancy g-C₃N₄ and the intermediates toxicity evaluation under tetracycline hydrochloride and Cr (VI) coexistence environment, *Applied Catalysis B: Environmental* 262 (2020) 118308.
- [22] B. Soledad-Rodríguez, P. Fernández-Hernando, R. Garcinuño-Martínez, J. Durand-Alegría, Effective determination of ampicillin in cow milk using a molecularly imprinted polymer as sorbent for sample preconcentration, *Food Chemistry* 224 (2017) 432-438.
- [23] L.H. Karlsson, J. Birch, J. Halim, M.W. Barsoum, P.O. Persson, Atomically resolved structural and chemical investigation of single MXene sheets, *Nano letters* 15(8) (2015) 4955-4960.
- [24] M. Shekhirev, C.E. Shuck, A. Sarycheva, Y. Gogotsi, Characterization of MXenes at every step, from their precursors to single flakes and assembled films, *Progress in Materials Science* 120 (2021) 100757.
- [25] T. Zhang, L.-Z. Zhang, Development of a MXene-based membrane with excellent anti-fouling for air humidification-dehumidification type desalination, *Journal of Membrane Science* 641 (2022) 119907.
- [26] L.-Å. Näslund, I. Persson, XPS spectra curve fittings of Ti₃C₂T_x based on first principles thinking, *Applied Surface Science* 593 (2022) 153442.
- [27] A.C. Khot, T.D. Dongale, J.H. Park, A.V. Kesavan, T.G. Kim, Ti₃C₂-based MXene oxide nanosheets for resistive memory and synaptic learning applications, *ACS Applied Materials & Interfaces* 13(4) (2021) 5216-5227.
- [28] X. Chang, Q. Wu, Y. Wu, X. Xi, J. Cao, H. Chu, Q. Liu, Y. Li, W. Wu, X. Fang, Multifunctional Au Modified Ti₃C₂-MXene for Photothermal/Enzyme Dynamic/Immune Synergistic Therapy, *Nano Letters* (2022).
- [29] Q. You, L. Zhuang, Z. Chang, M. Ge, Q. Mei, L. Yang, W.-F. Dong, Hierarchical Au nanoarrays functionalized 2D Ti₂CT_x MXene membranes for the detection of exosomes isolated from human lung carcinoma cells, *Biosensors and Bioelectronics* 216 (2022) 114647.
- [30] C. Liu, H. Zhang, R. Li, X. Li, P. Tang, Y. Wang, B. Yang, Z. Qiao, G. Yang, Laser triggered exothermic chemical reaction in Au nanoparticle@ Ti₃C₂ MXene membrane: A route toward efficient light to high-temperature pulse conversion, *Chemical Engineering Journal* 420 (2021) 127672.
- [31] X. Mi, H. Li, R. Tan, B. Feng, Y. Tu, The TDs/aptamer cTnI biosensors based on HCR and Au/Ti₃C₂-MXene amplification for screening serious patient in COVID-19 pandemic, *Biosensors and Bioelectronics* 192 (2021) 113482.
- [32] U. Rizal, S. Das, D. Kumar, B.S. Swain, B.P. Swain, Synthesis and characterization of TiO₂ nanostructure thin films grown by thermal CVD, *AIP Conference Proceedings*, AIP Publishing LLC, 2016, p. 020115.

- [33] E. Lee, A. VahidMohammadi, B.C. Prorok, Y.S. Yoon, M. Beidaghi, D.-J. Kim, Room temperature gas sensing of two-dimensional titanium carbide (MXene), *ACS applied materials & interfaces* 9(42) (2017) 37184-37190.
- [34] Z. Yu, L. Jiang, R. Liu, W. Zhao, Z. Yang, J. Zhang, S. Jin, Versatile self-assembled MXene-Au nanocomposites for SERS detection of bacteria, antibacterial and photothermal sterilization, *Chemical Engineering Journal* 426 (2021) 131914.
- [35] G.V. Lowry, R.J. Hill, S. Harper, A.F. Rawle, C.O. Hendren, F. Klaessig, U. Nobbmann, P. Sayre, J. Rumble, Guidance to improve the scientific value of zeta-potential measurements in nanoEHS, *Environmental Science: Nano* 3(5) (2016) 953-965.
- [36] A.J. Shnoudeh, I. Hamad, R.W. Abdo, L. Qadumii, A.Y. Jaber, H.S. Surchi, S.Z. Alkelany, Synthesis, characterization, and applications of metal nanoparticles, *Biomaterials and bionanotechnology*, Elsevier2019, pp. 527-612.
- [37] J. Li, W. Liu, X. Wu, X. Gao, Mechanism of pH-switchable peroxidase and catalase-like activities of gold, silver, platinum and palladium, *Biomaterials* 48 (2015) 37-44.
- [38] A. Thetford, G.J. Hutchings, S.H. Taylor, D.J. Willock, The decomposition of H₂O₂ over the components of Au/TiO₂ catalysts, *Proceedings of the Royal Society A: Mathematical, Physical and Engineering Sciences* 467(2131) (2011) 1885-1899.
- [39] D. Xu, L. Wu, H. Yao, L. Zhao, Catalase-Like Nanozymes: Classification, Catalytic Mechanisms, and Their Applications, *Small* 18(37) (2022) 2203400.
- [40] X. Li, C. Chen, J. Zhao, Mechanism of photodecomposition of H₂O₂ on TiO₂ surfaces under visible light irradiation, *Langmuir* 17(13) (2001) 4118-4122.
- [41] J.W. Peterson, L.J. Petrasky, M.D. Seymour, R.S. Burkhart, A.B. Schuiling, Adsorption and breakdown of penicillin antibiotic in the presence of titanium oxide nanoparticles in water, *Chemosphere* 87(8) (2012) 911-917.
- [42] N. Tarrat, M. Benoit, M. Giraud, A. Ponchet, M.-J. Casanove, The gold/ampicillin interface at the atomic scale, *Nanoscale* 7(34) (2015) 14515-14524.
- [43] T.C.M.V. Do, D.Q. Nguyen, K.T. Nguyen, P.H. Le, TiO₂ and Au-TiO₂ nanomaterials for rapid photocatalytic degradation of antibiotic residues in aquaculture wastewater, *Materials* 12(15) (2019) 2434.
- [44] M. Alafeef, K. Dighe, P. Moitra, D. Pan, Rapid, ultrasensitive, and quantitative detection of SARS-CoV-2 using antisense oligonucleotides directed electrochemical biosensor chip, *ACS nano* 14(12) (2020) 17028-17045.
- [45] T.A. Msagati, M.M. Nindi, Determination of β -lactam residues in foodstuffs of animal origin using supported liquid membrane extraction and liquid chromatography–mass spectrometry, *Food Chemistry* 100(2) (2007) 836-844.
- [46] M. Khaskheli, R. Malik, M. Arain, A. Soomro, H. Arain, Detection of β -lactam antibiotic residues in market milk, *Pakistan Journal of Nutrition* 7(5) (2008) 682-685.
- [47] C. Liu, H. Wang, Y. Jiang, Z. Du, Rapid and simultaneous determination of amoxicillin, penicillin G, and their major metabolites in bovine milk by ultra-high-performance liquid chromatography–tandem mass spectrometry, *Journal of Chromatography B* 879(7-8) (2011) 533-540.
- [48] A. Pennacchio, A. Varriale, M.G. Esposito, A. Scala, V.M. Marzullo, M. Staiano, S. D’Auria, A rapid and sensitive assay for the detection of benzylpenicillin (PenG) in milk, *PLoS One* 10(7) (2015) e0132396.

- [49] J. Fan, J.-J. Yin, B. Ning, X. Wu, Y. Hu, M. Ferrari, G.J. Anderson, J. Wei, Y. Zhao, G. Nie, Direct evidence for catalase and peroxidase activities of ferritin–platinum nanoparticles, *Biomaterials* 32(6) (2011) 1611-1618.
- [50] M. Jiao, Z. Li, X. Li, Z. Zhang, Q. Yuan, F. Vriesekoop, H. Liang, J. Liu, Solving the H₂O₂ by-product problem using a catalase-mimicking nanozyme cascade to enhance glycolic acid oxidase, *Chemical Engineering Journal* 388 (2020) 124249.
- [51] R. Zhang, L. Chen, Q. Liang, J. Xi, H. Zhao, Y. Jin, X. Gao, X. Yan, L. Gao, K. Fan, Unveiling the active sites on ferrihydrite with apparent catalase-like activity for potentiating radiotherapy, *Nano Today* 41 (2021) 101317.
- [52] W. Zhen, Y. Liu, W. Wang, M. Zhang, W. Hu, X. Jia, C. Wang, X. Jiang, Specific “unlocking” of a nanozyme-based butterfly effect to break the evolutionary fitness of chaotic tumors, *Angewandte Chemie International Edition* 59(24) (2020) 9491-9497.
- [53] H. Liang, Y. Liu, A. Qileng, H. Shen, W. Liu, Z. Xu, Y. Liu, PEI-coated Prussian blue nanocubes as pH-Switchable nanozyme: Broad-pH-responsive immunoassay for illegal additive, *Biosensors and Bioelectronics* 219 (2023) 114797.
- [54] N. Tao, H. Li, L. Deng, S. Zhao, J. Ouyang, M. Wen, W. Chen, K. Zeng, C. Wei, Y.-N. Liu, A cascade nanozyme with amplified sonodynamic therapeutic effects through comodulation of hypoxia and immunosuppression against cancer, *ACS nano* 16(1) (2021) 485-501.
- [55] S. Cai, J. Liu, J. Ding, Z. Fu, H. Li, Y. Xiong, Z. Lian, R. Yang, C. Chen, Tumor-Microenvironment-Responsive Cascade Reactions by a Cobalt-Single-Atom Nanozyme for Synergistic Nanocatalytic Chemotherapy, *Angewandte Chemie International Edition* 61(48) (2022) e202204502.
- [56] S. Sun, H. Liu, Q. Xin, K. Chen, H. Ma, S. Liu, X. Mu, W. Hao, S. Liu, Y. Gao, Atomic engineering of clusterzyme for relieving acute neuroinflammation through lattice expansion, *Nano Letters* 21(6) (2021) 2562-2571.
- [57] X. Zhang, W. Sun, Y. Cheng, Aptamer labeled nanozyme-based ELISA for ampicillin residue detection in milk, *Chemical Papers* 76(5) (2022) 3077-3085.
- [58] W. Lu, Y. Guo, Y. Yue, J. Zhang, L. Fan, F. Li, Y. Zhao, C. Dong, S. Shuang, Smartphone-assisted colorimetric sensing platform based on molybdenum-doped carbon dots nanozyme for visual monitoring of ampicillin, *Chemical Engineering Journal* (2023) 143615.
- [59] A. Blidar, B. Feier, M. Tertis, R. Galatus, C. Cristea, Electrochemical surface plasmon resonance (EC-SPR) aptasensor for ampicillin detection, *Analytical and bioanalytical chemistry* 411 (2019) 1053-1065.
- [60] Z.-g. Yu, R.Y. Lai, A reagentless and reusable electrochemical aptamer-based sensor for rapid detection of ampicillin in complex samples, *Talanta* 176 (2018) 619-624.
- [61] G. Rosati, M. Ravarotto, M. Scaramuzza, A. De Toni, A. Paccagnella, Silver nanoparticles inkjet-printed flexible biosensor for rapid label-free antibiotic detection in milk, *Sensors and Actuators B: Chemical* 280 (2019) 280-289.
- [62] W.B. Veloso, G.A.C. Ribeiro, C.Q. da Rocha, A.A. Tanaka, I.S. da Silva, L.M.F. Dantas, Flow-through amperometric determination of ampicillin using a copper electrode in a batch injection analysis system, *Measurement* 155 (2020) 107516.
- [63] A.-Y. Lee, N.-R. Ha, I.-P. Jung, S.-H. Kim, A.-R. Kim, M.-Y. Yoon, Development of a ssDNA aptamer for detection of residual benzylpenicillin, *Analytical biochemistry* 531 (2017) 1-7.
- [64] X. Jiang, X. Qin, D. Yin, M. Gong, L. Yang, B. Zhao, W. Ruan, Rapid monitoring of benzylpenicillin sodium using Raman and surface enhanced Raman spectroscopy, *Spectrochimica Acta Part A: Molecular and Biomolecular Spectroscopy* 140 (2015) 474-478.

- [65] T.M. do Prado, M.V. Foguel, L.M. Goncalves, T.S. Maria del Pilar, β -Lactamase-based biosensor for the electrochemical determination of benzylpenicillin in milk, *Sensors and Actuators B: Chemical* 210 (2015) 254-258.
- [66] M.R. Baezzat, Z. Pourghobadi, R. Pourghobadi, Nanomolar determination of Penicillin G potassium (PGK) salt using a Carbon Paste Electrode modified with TiO₂ nano particles/Ionic Liquids in real samples, *Materials Chemistry and Physics* 270 (2021) 124641.
- [67] A. Poghossian, M. Jablonski, C. Koch, T.S. Bronder, D. Rolka, C. Wege, M.J. Schöning, Field-effect biosensor using virus particles as scaffolds for enzyme immobilization, *Biosensors and Bioelectronics* 110 (2018) 168-174.
- [68] Z. Li, C. Liu, V. Sarpong, Z. Gu, Multisegment nanowire/nanoparticle hybrid arrays as electrochemical biosensors for simultaneous detection of antibiotics, *Biosensors and Bioelectronics* 126 (2019) 632-639.
- [69] C. Koch, A. Poghossian, M.J. Schöning, C. Wege, Penicillin detection by tobacco mosaic virus-assisted colorimetric biosensors, *Nanotheranostics* 2(2) (2018) 184.

Chapter VI.

Conclusions and Future Prospects

The revolutionary innovation in nanotechnology, where nanomaterials can function to mimic natural enzymes, facilitated the development of colorimetric sensing and biosensing methods that are rapid, inexpensive, and portable. As a newborn 2D nanomaterial, $\text{Ti}_3\text{C}_2\text{T}_x$ -based MXene has attracted much attention recently due to its unique properties, such as high conductivity, large surface area, excellent reductivity, lightweight, good surface modification, etc. These features make the $\text{Ti}_3\text{C}_2\text{T}_x$ -based MXene a successful nanomaterial candidate in sensing applications. In this dissertation oxygen-terminated few-layered $\text{Ti}_3\text{C}_2\text{T}_x$ -based MXene (OFL-Ti-MN) was used to mimic the enzymatic system ($\text{H}_2\text{O}_2/\text{TMB}$). The results indicate that OFL-Ti-MN can convert enzymatic substrates to their related products as would a natural peroxidase. This enzyme-mimicking behavior was adopted in the sensing and biosensing applications for detecting different antibiotics such as a kanamycin (KAN), tetracycline, ampicillin, and penicillin G..

Taking advantage of the unique enzyme-mimic property, in Chapter III the catalytic mechanism of OFL-Ti-MN in substrates (TMB and H_2O_2) was explored. The catalytic kinetics indicate that OFL-Ti-MN shows affinity to both TMB and H_2O_2 . Further investigation on the catalytic performance of OFL-Ti-MN exhibited that the OFL-Ti-MN can degrade H_2O_2 and help generate $\bullet\text{OH}$ into the solution. This reactive oxygen species can oxidize the TMB and produce a bluish-green product, altering the solution color. As kanamycin (KAN) is introduced into the reaction system, there is no color shown. Our proposed mechanism pointed out that the KAN molecules were adsorbed on the surface of OFL-Ti-MN in the form of hydrogen bonds and amine-metal coordinate bonds. Active sites of OFL-Ti-MN were then blocked, and the prevention of the reaction between the OFL-Ti-MN surface and H_2O_2 led to the inhibition of the redox reaction.

Therefore, the bluish-green color of the solution would not show up. By using this strategy, the OFL-Ti-MN-based enzymatic system was used for kanamycin antibiotic detection. The limit of detection (LOD) is 15.28 nM with a calculated linear range of 23.09 to 769 nM.

In addition, the presence of tetracycline (TC) can also inhibit the color change of the solution that contains the OFL-Ti-MN/TMB/H₂O₂ system (Chapter IV). TC could be degraded by the generated •OH competently to TMB, which will be finally transforming into CO₂ and H₂O in the environment. We used the inhibition effect of TC to color-change reaction as the basis and designed a colorimetric sensing method for TC analysis with LOD as 615.4 nM and detection dynamic range from 0.769 μM to 307.6 μM. Therefore, this is an alternative way for TC detection and simultaneous degradation.

In Chapter V, a hierarchical nanostructure of Au/layered Ti-based MXene (MA) was constructed in a one-step method. Layered Ti₃C₂T_x MXene (L-Ti₃C₂T_x NS) possesses excellent reducibility due to the chemically etching process, which facilitates reducing the Au precursor without additional reductant. Because of the synergistic effect of Au nanoparticles and L-Ti₃C₂T_x NS, the enzymatic kinetics of MA were significantly improved against H₂O₂ molecules. Besides, different from the role of OFL-Ti-MN in the catalytic reaction, the MA mimics the catalase in the presence of H₂O₂ and generates the superoxide ions (•O₂⁻) in the solution. However, ampicillin (AMP) and penicillin G (PenG) with lactam ring is capable of inhibiting the color-change reaction due to the strong adsorption between these two β-lactam antibiotics and the MA surface, covering the exposed active sites of MA to the external conditions (TMB/H₂O₂). Therefore, the color of the solution was inhibited. By adopting this idea, a colorimetric sensing strategy for these two antibiotics was developed with LOD to AMP and PenG as 68.9 nM and 7.51 nm, respectively.

There are several questions that should be further addressed:

1. Detailed information on the catalytic mechanism of OFL-Ti-MN and MA in triggering redox reaction between H_2O_2 and TMB should be further investigated, which may need support from a computational model;
2. Detailed degradation information of TC in the OFL-Ti-MN/TMB/ H_2O_2 system may need to be further provided;
3. The sensitivity of TC detection could be improved;
4. The final destiny of two β -lactam antibiotics in the MA/TMB/ H_2O_2 system should be investigated in the future to improve the mechanism;
5. Other real sample matrices (e.g., cheese, yogurt, etc.) may be used for testing spiked antibiotics by using these colorimetric detection techniques.
6. It is important to design and establish a complete sensing system that can differentiate KAN and TC by using OFL-Ti-MN/TMB/ H_2O_2 method when they exist simultaneously. Similarly, to identify AMP or PenG when they are both in the sample. A separate method may need to be developed.